2018

Amplified, Synergistic (Photo) Catalytic Water-Splitting by Thin- Film Conducting Polymer Composites

Mohammed Fathi Khaleel Alsultan
University of Wollongong

UNIVERSITY
OF WOLLONGONG
AUSTRALIA

Amplified, Synergistic (Photo) Catalytic Water-Splitting by Thin-Film Conducting Polymer Composites

Mohammed Fathi Khaleel Alsultan

Supervisors:
Prof Gerhard F. Swiegers and Dr. Pawel Wagner

This thesis is presented as part of the requirement for the conferral of the degree:
Doctor of Philosophy (Integrated) in Inorganic Chemistry

This research has been conducted with the support of the Iraqi Ministry of Higher Education and Scientific Research

The University of Wollongong
Intelligent Polymer Research Institute and ARC Centre of Excellence for Electromaterials Science

December 2018

Abstract

There is currently great interest in harnessing sunlight to generate hydrogen from water. Hydrogen may serve as a future energy carrier that could one day supplant fossil fuels like gasoline or diesel. One of the major challenges with implementing this concept is that, present-day photoelectrochemical (PEC) water splitting systems are either inefficient in their capacity to catalytically split water and/or subject to photocorrosion. The problem typically lies at the interface at which the water-splitting catalytic reaction occurs. One potential solution is to develop a thin-film, catalytic, interfacial layer that may lie between the photo-activated species (e.g. the semiconductor) and the aqueous, liquid phase. Such an interfacial layer could be designed to catalyse water-splitting at a more accelerated rate than is possible in its absence, whilst simultaneously suppressing photocorrosion. Ideally, such a thin-film interface would provide the greatest possible catalytic effect, preferably by synergistic amplification of the catalysis beyond what may be achieved by the catalyst species themselves.

This work aimed to study and develop thin-film composites, based on well-known conducting polymer supports, that may serve as such an interfacial layer and that display synergistically amplified water-splitting catalysis. Despite their potential for facilitating high activity, thin-film conducting polymer supports have, historically, expedited only relatively weak performances in, for example, catalytic water oxidation (with current densities in the $\mu A/cm^2$ range).

In Chapter 3, the conditions under which a thin-film conducting polymer, poly(3,4-ethylenedioxythiophene) (PEDOT), may synergistically amplify water oxidation catalysis have been investigated. A composite conducting polymer film was developed that, when overcoated on a bare Pt electrode, synergistically amplified its catalytic performance by an order of magnitude (into the mA/cm^2 range). Pt is the most active, industry-standard catalyst for water oxidation. When poised at 0.80 V (vs Ag/AgCl) at pH 12, a control, bare Pt electrode yielded a current density of 0.15 mA/cm^2 for catalytic water oxidation. When then overcoated

with a composite PEDOT film containing nanoparticulate Ni ('nano-Ni') catalyst and reduced graphene oxide (rGO) conductor in the specific molar ratio of 4.5 (C; PEDOT) : 1 (Ni) : 9.5 (C; other), the electrode generated water oxidation current densities of 1.10-1.15 mA/cm^2 under the same conditions (over >50 h of operation; including a photocurrent of 0.55 mA/cm^2 under light illumination of 0.25 sun). Control films containing other combinations of the above components, yielded notably lower currents. The conditions employed were the most favourable for water oxidation at which the PEDOT did not degrade. EIS and Tafel plot studies suggested that the above composite contained an optimum ratio of catalyst density to conductivity and thickness in which the PEDOT electrically connected the largest number of catalytic sites (thereby maximizing the catalytically active area) by the shortest, least-resistive pathway for electron conduction (thereby minimizing the Tafel slope). That is, the amplification appeared to be created by a synergistic matching of the connectivity, conductivity, and catalytic capacity of the film.

Chapter 4 tested whether this approach could also provide a possible means for more effectively deploying thin-film conducting polymers in hydrogen reduction catalysis. The Chapter reports a composite of PEDOT that is notably more catalytically active for hydrogen generation than the industry-standard benchmark catalyst, Pt, under the same conditions. A PEDOT thin-film containing nano-Ni and rGO, again, in a very specific molar ratio (namely, 5.6 (C; PEDOT) : 1 (Ni) : 5.2 (C; other)) photocatalytically generated H_2 at 3.6 mA/cm^2 (including ca. 0.2 mA/cm^2 due to the light illumination) after 3 h at -0.75 V (vs Ag/AgCl) in 0.05 M H_2SO_4/0.2 M Na_2SO_4 under 0.25 sun. A control bare Pt electrode produced only 2.2 mA/cm^2 under the same conditions. A control nano-Ni/rGO film containing the same quantities of nano-Ni and rGO but without any PEDOT, yielded 2.1 mA/cm^2, indicating that the PEDOT synergistically amplified the above result by 71%. Other ratios of the above PEDOT composite produced notably lower activities. Control PEDOT, PEDOT/nano-Ni, and PEDOT/rGO films were an order of magnitude less catalytically active. Studies showed that the synergistic amplification also involved the PEDOT electrically connecting the largest number of active sites by the shortest, most efficient pathways for charge transport, which, in

this case, involved hole (h^+) transport. These results confirmed the proposition that thin-film conducting polymers involving very specific, optimum ratios of catalyst density to thickness may synergistically amplify catalysis.

In Chapter 5, the developed approach was tested with a different conducting polymer, namely polypyrrole (PPy). Composite PPy films incorporating nano-Ni and rGO, on FTO glass and Pt-coated FTO glass were studied as photoelectrocatalysts of both the oxygen evolution reaction (OER) in alkaline media (0.2 M Na_2SO_4 with pH 12 at 0.8 V *vs* Ag/AgCl) and the hydrogen evolution reaction (HER) in acidic media (mixture of 0.05 H_2SO_4 and 0.2 M Na_2SO_4 at - 0.75 V *vs* Ag/AgCl). Thin films containing PPy: nano-Ni : rGO in a molar ratio of 1.0 (N; PPy) : 1.49 (Ni) : 7.07 (C; others) proved to be extremely OER active, generating current densities of 0.97-1.0 mA/cm^2 (including a photocurrent of 0.48 mA/cm^2 under constant light illumination of 0.25 sun), while films containing PPy: nano-Ni: rGO in a molar ratio of 1.00 (N; PPy): 1.95 (Ni): 8.63 (C; others) were highly HER active, generating current densities (2.38-2.60) mA/cm^2 including (200-400 μA/cm^2 from light illumination). For both OER and HER optimized films, GC studies confirmed that O_2 gas was generated in the OER system and H_2 gas was generated in the HER system. While the PPy-based thin-films were not as catalytically active as the earlier-examined PEDOT films, they, nevertheless, demonstrated that the principles of synergistic amplification developed in Chapters 3 and 4 were general and could be applied to other conducting polymers.

In Chapter 6, PEDOT thin films containing other catalysts (namely nanoparticulate Co_3O_4 ('nano-Co_3O_4')) and conductors (namely carbon nanotubes (CNTs)) were studied. PEDOT/nano-Co_3O_4/CNT films, prepared via vapour phase polymerisation onto a Pt electrode, proved to be the best water oxidation catalysts discovered in the course of this thesis. The films were studied as photoelectrocatalysts of water oxidation in 0.2 M Na_2SO_4, adjusted to pH 12, as an electrolyte. Films containing PEDOT : nano-Co_3O_4 : CNT in the specific molar ratio of 6.92 (C; PEDOT) : 1 (Co) : 5.13 (C; other) exhibited high performance activity, realising current densities of 2.34-2.46 mA/cm^2 at 0.80 V (vs Ag/AgCl) of (including a photocurrent of 0.51-0.53 mA/cm^2) after > 35 h of operation under light illumination of 0.25

sun. This contrasted sharply with the control bare Pt electrode that yielded only 0.15 mA/cm^2. An equivalent PEDOT control film yielded a negligible current. GC analysis demonstrated that oxygen (O_2) was the gas generated by the PEDOT/nano-Co_3O_4/CNT with and without light illumination. To the best of our knowledge, the PEDOT/nano-Co_3O_4/CNT film is the most active water oxidation catalyst ever reported, as a proportion of the activity of bare Pt.

Finally, Chapter 7 examined the use of a chemical (i.e. a concentration) bias as a means of driving spontaneous water-splitting, without need for an applied voltage bias. Such a chemical bias was created by using two separate electrolytes with different pHs in two half cells. An electrolyte with high pH was used in the anode half-cell with a low pH electrolyte in the cathode half-cell. A novel, mechanically durable, highly ion-conductive and flexible polyacrylamide CsCl hydrogel was developed to connect the two half-cells. The hydrogel was fixed in a U-tube and applied as a separator for the two water splitting half cells (cathode and anode). The cells spontaneously split water, without need for an applied voltage bias, upon being connected with the hydrogel, for up to 14 h of continuous testing. The feasibility of (and properties of) a chemical rather than an electrical potential to drive water splitting was thereby demonstrated, at least for a period of 14 h.

Acknowledgements

To my parents, for their unlimited support. Thank you for all that you have done with me. I will never forget your efforts throughout all my school and university days. I will tell my children, when they grow up, how you were great with me and with my other brothers and sisters.

To my wife Nadia, your love, support and patience with me and my horrible science talks at home, which made the last years fly by. Thank you, Nadia, for taking care of our three children that made our life so beautiful.

I would like gratefully thank my supervisors, Prof Gerhard Swiegers and Dr Pawel Wagner, for their fantastic help, great guidance in the lab, and for scientifically discussing the results, as well as proofreading and valuable feedback for both thesis and research papers. Nothing would have been done without their encouragement throughout my research time. I also thank them for their understanding of my difficult circumstances between 2014 and 2017, when radical Islamic military groups invaded my home city of Mosul, Iraq, and I lost contact with my big family for more than three years. I was so worried about them, as well as my city and its people at same time.

I would like to thank all of the staff and students at IPRI for their support especially Dr Ali Jalili, Prof. Attila Mozer, Prof. Marc in het Panhuis, Dr Klaudia Wagner, Dr Danijel Boskovic, Dr Prerna Tiwari, Dr Holly Warren, Jaecheol Choi, Khalid W. Zainulabdeen and Amar Al-Kaisy for their help in my first practical experiments.

Finally, I would like to thank the Ministry of Higher Education and Scientific Research in Iraq for their education program providing funding and support to send students like myself overseas.

Certification

I, Mohammed Fathi Khaleel Alsultan, declare that this thesis submitted in fulfilment of the requirements for the conferral of the degree Doctor of Philosophy in Science, from the University of Wollongong, is wholly my own work unless otherwise referenced or acknowledged. This document has not been submitted for qualifications at any other academic institution.

_____

Mohammed Fathi Khaleel Alsultan
10 December 2018

Publications

Book Chapters:

Mohammed Alsultan, Abbas Ranjbar, Gerhard F. Swiegers, Gordon G. Wallace, Sivakumar Balakrishnan, and Junhua Huang. *Chapter 11. Application of Conducting Polymers in Solar Water-Splitting Catalysis*, in *Industrial Applications for Intelligent Polymers and Coatings* (M. Hosseini, A.S.H. Makhlouf (eds.)), Springer International Publishing, Switzerland, 2016 (DOI: 10.1007/978-3-319-26893-4_11)

Peer-Reviewed Journal Papers:

Mohammed Alsultan, Sivakumar Balakrishnan, Jaechol Choi, Rouhollah Jalili, Prerna Tiwari, Pawel Wagner, Gerhard F. Swiegers. *Synergistic Amplification of Water Oxidation Catalysis on Pt by a Thin-Film Conducting Polymer Composite*.
ACS Applied Energy Materials, **2018**, *1*, 4235-4246 (DOI: 10.1021/acsaem.8b00728)

Mohammed Alsultan, Jaechol Choi, Rouhollah Jalili, Pawel Wagner, Gerhard F. Swiegers. *Synergistic Amplification of Catalytic Hydrogen Generation by a Thin-Film Conducting Polymer Composite.*
Catalysis Science and Technology, **2018**, 8, 4169-4179 (DOI: 10.1039/c8cy00780b).

Mohammed Alsultan, Pawel Wagner, Gerhard F. Swiegers. *Synergistic Amplification of Catalytic Oxygen and Hydrogen Generation from Water by Thin-Film Polypyrrole Composites.* In Preparation

Mohammed Alsultan, Pawel Wagner, Gerhard F. Swiegers. *Synergistic Amplification of Catalytic Oxygen Generation by a PEDOT/Nano-Co_3O_4/CNT Thin-Film Composite.* In Preparation

Mohammed Alsultan, Pawel Wagner, Gerhard F. Swiegers. *Novel Hydrogel Separator for Bifunctional Oxygen and Hydrogen Evolution Reactions by Composite PEDOT/nano-Ni/rGO Films.* In Preparation

Peer-Reviewed Conference Papers:

Photocatalytic, Oxygen-Generating PEDOT/Nano-Ni Composite film with Sustained High Activity. Published in: *Proceedings of the First MoHESR and HCED Iraqi Scholars Conference in Australasia, 5-6 December 2017*.

Posters:

A Composite PEDOT/Nano-Ni/rGO Photocatalyst that is more Active than Pt for Hydrogen Generation. Poster presented at the International Conference on Nanoscience and Nanotechnology 29 Jan - 2 Feb 2018 (ICCON 2018).

Photocatalytic Water Oxidation by Composites of Ni Nanoparticles, reduced Graphene Oxide (rGO) and Poly (3,4-ethylenedioxythiophene) (PEDOT). Poster presented at the International Electromaterials Science Symposium, 8-10 February 2017.

List of Names or Abbreviations

AEL	anion-exchange layer
APS	3-(aminopropyl) triethoxysilane
BHJ	bulk heterojunction
BPMs	bipolar passive membrane
CB	conduction band
Cct	double layer capacitance
CNT	carbon nanotube
Co-MOF	cobalt-based metal-organic framework
CP	conducting polymer
CPE	constant phase element
CV	cyclic voltammetry
CVD	chemical vapour deposition
DLH	double-layer hydroxide
dpbyl	$[(2,2'\text{-bipyridine})(4,4'\text{-diphosphonate-}2,2'\text{-bipyridine})\text{-}(CO)_2]^{2+}$
DSC	dye sensitized solar cell
ErGO	electrochemically reduced graphene oxide
EEC	equivalent electric circuit
EIS	electrochemical Impedance Spectroscopy
EtOH / Eth.	Ethanol
Fe(III)-*P*TS	iron(III) *p*-toluenesulfonate hexahydrate
FP	fluorine and phosphorous process
FTIR	Fourier transform infrared spectroscopy
FTO	fluorine-doped tin oxide
GC	gas chromatography
GC	glassy carbon
GCE	glassy carbon electrode
GIO	graphene inverse opal
GNS	graphene nano sheet
GO	graphene oxide
GQDs	graphene quantum dots
GR	graphene
h	hour
h^+	hole (in the valence band)
HER	hydrogen evolution reaction

HOMO	highest occupied molecular orbital
ITO	indium tin oxide
IPCE	incident photon to current conversion efficiency
LCD	liquid crystal display
LDH	layered double hydroxides
LSV	linear sweep voltammogram
LUMO	lowest unoccupied molecular orbital
min	minute
MeOH / Meth.	Methanol
MMA	Mini-Materials Analyzer
MnTPPS	5,10,15,20-tetrakis(4-sulfonatophenyl)porphyrinatomanganese (III) chloride
MOF	metal–organic framework
MPSA	self-assembled melamine,phytic acid
NAs	nanowire arrays
NC_S	nanocrystals
NHE	normal hydrogen electrode
NOSC	N-, O-, and S-tridoped carbon-encapsulated Co_9S_8 nanomaterials
NP	nanoparticles
NPC	N, P-codoped carbon shells
NPG	nanoporous gold
NPRGO	N, P-codoped rGO
NW	nanowire
OEC	oxygen-evolution catalyst
OER	oxygen evolution reaction
ORR	oxygen reduction reaction
OSC	organic thin-film solar cells
R_Ω	Ohmic resistance
R_{ct}	charge transfer resistance
RDE	ring-disk electrode
rGO	reduced graphene oxide
RHE	reversible hydrogen electrode
RuP	tris(bipyridine)(2,2' –(bipyridine-4,4'-di(methylphosphonic acid) ruthenium (II) hexaflorophosphonium
rpm	revolutions per minute
SEM	scanning electron microscopy
SG	sulfonated graphene

SOM	soft-oxometalate
TCPP	tetrakis(4-carboxyphenyl)porphyrin
TEM	transmission electron microscopy
TEOA	triethanolamine
TLC	Thin Layer Chromatography
TLCC	Thin Layer Chromatography Chamber
TOF	turnover frequency
TON	turnover numbers
TNTs	TiO_2 nanotube arrays hybrids
TNT	titanate nanotube
PANI	polyaniline
PBTH	poly(2,2 '-bithiophene)
PEC	photoelectrochemical cell
PEDOT	poly (3,4-ethylenedioxythiophene)
PEDOT-PEG	poly (3,4-ethylenedioxythiophene)-poly(ethylene glycol)
PEDOT:PSS	poly(3,4-ethylenedioxythiophene)-polystyrene sulfonate
PEM	proton exchange membrane
PEG	poly(ethylene glycol)
PDTT	poly[dithieno(3,2-b:2',3'-d)]thiophene.
PI-*b*-PAA	amphiphilic block copolymer poly(isoprene-b-acrylic acid)
PPD	*p*-phenylenediamine
PSC	polymer solar cell
PSGM	poly-(styrene/glycidylmethacrylate)
PSS	polystyrene sulfonate
PTh	polythiophene
PTT	poly[dithieno(3,2-b)]thiophene]
p-TS	*p*-toluene sulfonate
QE	quantum efficiency
TCO	transparent conductive oxide
VB	valence band
VPP	vapour phase polymerization
XRD	X-ray powder diffraction (XRD)
WOR	water oxidation reaction

List of Contents

Chapter 1

Chapter 2

Chapter 3

Chapter 4

Chapter 5

List of Figures

Note: The term "license no." in the Figure captions below refers to the relevant identification number of the license provided by the Copyright Clearance Centre (copyright.com) for reproduction of the material referred to.

List of Tables

Chapter 1

Introduction

Declaration: Portions of this chapter are drawn from a published book chapter entitled: "Application of Conducting Polymers in Solar Water-Splitting Catalysis", for which I, Mohammed Alsultan, was the first author, along with co-authors: Abbas Ranjbar, Gerhard F. Swiegers, Gordon G. Wallace, Sivakumar Balakrishnan, and Junhua Huang (Chapter 11 in Industrial Applications for Intelligent Polymers and Coatings, M. Hosseini, A.S.H. Makhlouf (eds.), Springer International Publishing, Switzerland, 2016 (DOI 10.1007/978-3-319-26893-4_11). My contribution involved: (i) researching the scientific literature, (ii) identifying the publications of interest, (iii) writing short summaries of each publication, and (iv) writing the first draft of the book chapter.

1.1 Background: Demand for Renewable Energy

On Earth, there are two main types of energy available for use: renewable energy and non-renewable energy. When the source of energy is, effectively, unlimited, it is called renewable energy; examples include sunlight, tidal and wave energy, wind power, hydropower energy, geothermal energy and biofuel production from carbon neutral materials with low CO_2 emissions. If the source of the energy may be depleted, it is called non-renewable energy; the main example is fossil fuels. A key advantage of renewable energy is that this source does not result in CO_2 emissions to the atmosphere (CO_2 is a so-called "greenhouse gas"). By contrast, non-renewable energy contributes to greenhouse gases and climate change. Increasing population growth, standards of living, development and urbanization have resulted in a

growing requirement for supplied power. In addition, the sources of many non-renewable energy types, such as oil, are decreasing in number and becoming more difficult to find. In most countries, fossil fuels supply 80% of energy needs. Questions have been raised as to whether fossil oil will be enough for the long term. Studies have shown that current oil reserves will last for the next 40 years, gas for the next 60 years and coal for the next 200 years.[1] Scientists have estimated that the total energy required by 2050 will be 13 tetrawatt (TW) per annum.[2] These factors have encouraged governments, communities and energy companies to support efforts aimed at developing alternative energies like solar cells, geothermal energy, wind power and nuclear fusion.[3-5]

Sunlight could provide us with 3.8 x 10^{23} kW of energy per hour. [6] This means that sunlight could supply 100,000 times more energy than is used by the current population.[6] If only 0.1% the earth's surface were to be covered with solar cells that have conversation efficiency 10%, this will satisfy the energy needs of the current world population.[7] Thus, the renewable energy industry is in a position to grow rapidly to provide for future energy needs.[8]

1. 2 Water Electrolysis and Photochemical Cell Water Splitting: A Brief Description

Hydrogen (H_2) and oxygen (O_2) gases have been successfully produced in large scale using water splitting electrochemical systems (known as water electrolyzers) since the 1930's. Much research has since been devoted to the development of water splitting systems utilizing both biological (e.g. algae, plant and certain bacteria) and physical methods (e.g. catalysts and semiconductors).[9]

In 1972, Fujishima and Honda developed the first photoelectrochemical cell (PEC) that split water under light, using a TiO_2 *n*-type semiconductor as anode connected to a platinum black cathode, operating in aqueous electrolyte at pH 4.7 and a bias of -5 V (*vs* SCE). When the PEC was illuminated with light, O_2 and H_2 were generated at the anode and the cathode respectively.[10] Later, PEC technology was developed to be capable of directly converting water to O_2 and H_2 under sunlight, without need for an applied voltage. An

extensive effort has been made to combine water electrolysis with solar power, as that can provide an attractive approach to producing sustainable H_2 and O_2. [11, 12]

Thermodynamically, a minimum potential of 1.23 V *vs* NHE at pH 0 is required to achieve water decomposition into H_2 and O_2 (eq. 1.1) with a Gibbs free energy (ΔG^o) for the reaction of 237 kJ/mol, at standard condition of temperature and pressure (STP).[9]

$$H_2O_{(l)} + electricity + heat \rightarrow H_{2(g)} + \frac{1}{2}O_{2(g)} \quad \ldots (1.1)$$

ΔG^o = 237 kJ/mol and $E^\circ_{cell} = 1.23\ V$ … (1.2)

The actual minimum cell potential (E) decreases as the pH increases according to the Nernst equation: [13]

$$E = E^\circ_{cell} - 0.0591(pH) \quad \ldots (1.3)$$

where E represents the actual cell potential and E°_{cell} is the standard cell potential. These minimum potentials represent the smallest amount of electrical energy needed to drive the reaction.

In practice, higher potentials than 1.23 V vs NHE must be applied to drive the water splitting reaction. The higher potentials are needed to provide heat to the reaction, which is formally endothermic. Thus, up to a voltage of 1.48 V *vs* NHE (known as the '*thermoneutral voltage'*, or E_{TN}), the additional voltage provides the heat required by the reaction. At 1.48 V, the electrical energy needs and the thermal (heat) needs of the reaction are, in theory, fully provided for, so that water electrolysis at 1.48 V is considered to have an energy efficiency of 100%.[9] Above 1.48 V, the additional voltage generates additional heat that is irradiated into the external environment in an exothermic manner.

Additional voltage must also be applied to overcome kinetic phenomenon during water splitting, such as loss of Ohmic voltage and mass transport (i.e. the needs to move reactants to the catalysts and products away from them); this voltage is known as the "*overpotential"*.[14] The activity of water splitting electrocatalytic systems, typically, depend on several parameters, including: (a) surface area, shape and size of the catalysts materials,[15] (b) the conduction pathway and electrical resistance,[16] (c) the local pH and the external bias that is applied,[17-18] and (d) the use of sunlight as an energy source (if the catalysts employed have wide visible absorption bands).[19-20]

In an electrochemical cell, water splitting involves two half-cell reactions. At the cathode, water reduction occurs leading to the '*hydrogen evolution reaction'* (HER). At the anode, the water oxidation half-cell reaction occurs, leading to the *'oxygen evolution reaction'* (OER). In alkaline solution, the equations for the half-cells are:[14]

Cathode (reduction) $4H_2O + 4e^+ \rightarrow 2H_2 + 4OH^-$ … (1.4)

Anode (oxidation) $4OH^- \rightarrow O_2 + 2H_2O + 4e^+$ … (1.5)

In the acidic media the corresponding reactions are:

Cathode (reduction) $4H^+ + 4e^- \rightarrow 2H_2$ … (1.6)

Anode (oxidation) $2H_2O \rightarrow O_2 + 4H^+ + 4e^-$ … (1.7)

Water oxidation (or the OER) requires a higher potential than water reduction (or the HER). The greater potential is needed for the four electron process of forming the O-O bond. The HER requires a 2-electron process to form the H-H bond, so that it is easier than the OER. Figure 1.1 depicts a comparison in potential of both HER and OER (η_a and η_c refer to the potential of OER and HER respectively.)[21]

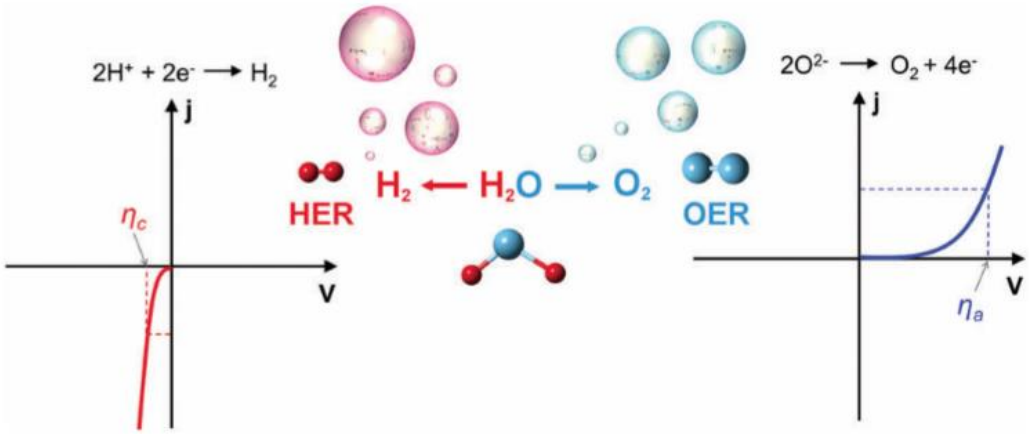

Figure 1.1: *Comparison of the potentials (V) and electrical currents (j) involved in the HER and OER. The values η_a and η_c refer to the potential of OER and HER respectively. Reproduced with permission from ref. 21 (license no. 4466800227002).*

Noble-metals themselves, like Pt, and noble metal oxides, such as RuO_2, IrO_2, RhO_2, PtO_2, have high activities as catalysts of both the OER and the HER in alkaline and acidic media. However, due to their high cost and scarcity, much effort has been devoted to catalysis by earth-abundant transition metals or their alloys, including Ni, Co and Fe, as alternative catalysts for OER and HER water electrolysis. These efforts highlight the attractive properties of transition metals for PEC water splitting, such as: high activity, durability and stability (some of them have higher performance than noble materials, especially when they are interfaced with other materials that can improve the catalyst performance, such as nitrides, carbides, sulfides, phosphides, selenides and carbon-based graphene, reduced graphene oxide, and carbon nanotubes).[22]

Photocatalysis involves a chemical reaction that occurs *via* a catalyst under photoirradiation. Photosystem II is a natural biological system found in all photosynthetic organisms that is a natural source of energy on earth. It splits water into oxygen under the influence of sunlight, generating energetic electrons in the process. Photosynthesis uses these electrons, effectively, to power the plant or microbe in which it occurs.[15, 23]

The fundamental principle of artificial water splitting under light includes three steps;

a) electrons (e^-) in the valence band (VB) of the photocatalyst absorb light and transfer to the conduction band (CB) leaving holes (h^+) in the VB,
b) both the h^+ and e^- transfer to different locations on the surface of the photocatalyst, and
c) when the h^+ and e^- reach the surface, they create the processes of water reduction (HER) and water oxidation (OER), respectively, at their different locations.

Ideally, the VB should be 1.23 V or more in order to ensure O_2 evolution while the CB should be at 0.00 V or less to ensure H_2 evolution. [24]

The success of a photoelectrochemical cell (PEC) in water splitting also depends on various technical and economic parameters, including that the cell contents should be low cost, non-toxic to the environment, have high durability, and should easily harness sunlight. Nanotechnology has also played a crucial role in the development of the photochemical solar cell, by, for example, allowing for tuning of the VB-CB bandgap of the photocatalyst and /or interfacing with other catalytic materials for water splitting able to increase its efficiency, durability, and stability.[25-27]

1.3 Applications of Conducting Polymers in PEC Water-Splitting

In 1978, Shirakawa and colleagues demonstrated that polyacetylene becomes electrically conductive after being treated with electron-accepting (*p*-doped) or electron donating dopants (*n*-doped).[28-29] Since that time, an entire class of polymeric conductors has been developed, including polypyrroles (PPy), poly(3,4-ethylenedioxythiophenes) (PEDOT), polythiophenes, polyanilines and many more; Figure 1.2 shows the parent forms of these polymers.[30] Conducting polymers (CPs) have two broad potential application areas.[31] The first utilizes the conductivity of CPs in, for example electrostatic materials, conducting adhesives, electromagnetic shielding, printed circuit

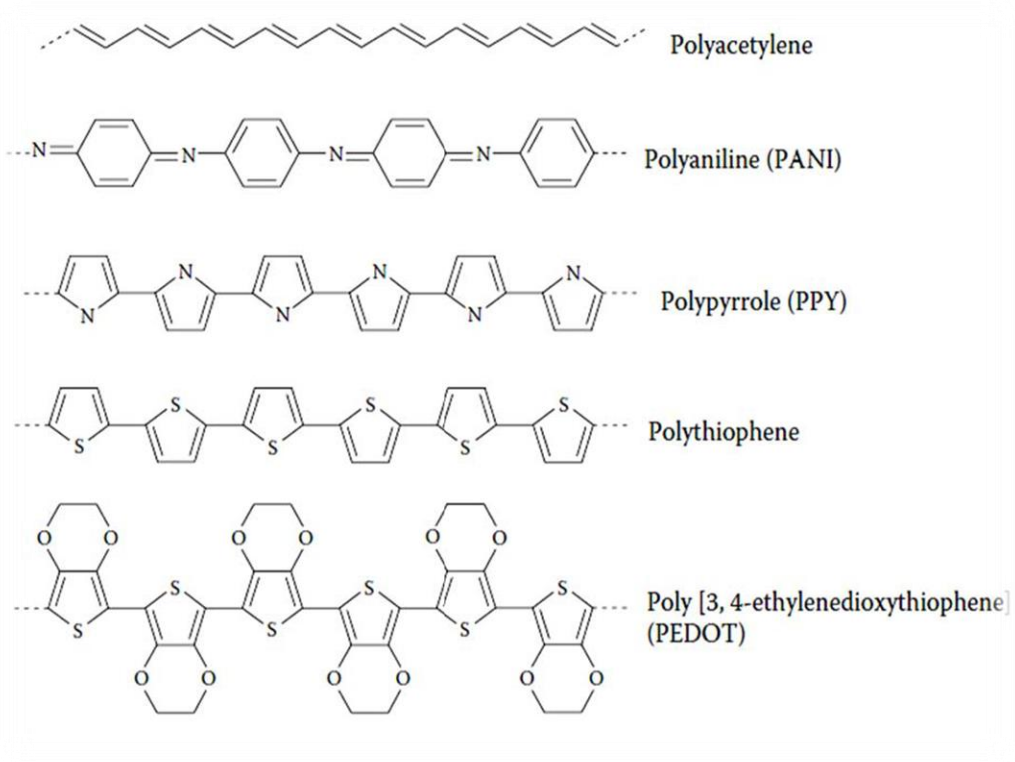

Figure 1.2: *Common conducting polymers*

boards, artificial nerves and electronics (diodes, transistors). The second makes use of their electroactivity in, for example, molecular electronics, biochemical and thermal sensors, optical computers, rechargeable batteries and solid electrolytes, drug release systems and ion-exchange membranes.

CPs are extensively conjugated molecules that have backbones of π-electrons due to C=C conjugated bonds that are able to inter-convert between single and double bonds. In these molecules, electrons are able to move through the extended π – orbital system. This feature imparts CPs with interesting properties, including low ionization potential, low-energy optically transitions, and high electron affinity, which allow the polymer to be oxidized and reduced relatively easily.[32] Conducting polymers are typically insulators in their neutral state but when they are doped their behaviour changes to the conducting state.[33] Doping of conducting polymers can be viewed as a charge transfer reaction, which results in oxidation or reduction of sites along the polymer chains. This induces upward shifts in the energy of the *highest occupied molecular orbital* (HOMO) of the valence band (VB) and downward shifts in the energy of the *lowest unoccupied molecular orbital* (LUMO) of the conducting band

(CB), decreasing the bandgap in the process.[34] By contrast, the doping reaction in solid-state semiconductors creates either electron rich or electron deficient sites with no charge transfer between these sites. The general doping reaction process of CPs follows the equations.[35]

$$\text{Polymer} + X \rightleftharpoons (\text{Polymer})^{n+} + X^{n-} \quad p\text{-doping reaction (X = oxidising agent)} \ldots (1.8)$$

$$\text{Polymer} + M \rightleftharpoons (\text{Polymer})^{n-} + X^{n+} \quad n\text{-doping reaction (M = reducing agent)} \ldots (1.9)$$

(X includes I, Br, As F while M = Na, Li).[32]

The conductivity of a polymer depends on the level of doping, the relative alignment of the polymer chains, the conjugated chain length and the sample purity, amongst others.[32] The conductivity can be measured using the equation:

$$\sigma = 1/R = n\, e\, \mu \quad \ldots (1.10)$$

where σ = conductivity ($\Omega^{-1}\ m^{-1}$ or $S\ m^{-1}$, typically reported as $S\ cm^{-1}$), n = number of charge carriers (electrons or holes [e^-, h^+]), e = electron charge and μ = charge carrier mobility. CPs can be controlled if the nature of the process that regulates them can be understood [31]

CPs have other unique properties such as tunable conductivity between insulating and metallic regions, adjustable permeability, are relatively low cost, have readily available processing capacities and have controllable microwave absorption properties, which make them significant for industrial applications.[36]

Solar cell applications involving CPs have attracted broad research interest due to their potential utility in the fabrication of low-cost, flexible and large area electrochemical devices. The conversion efficiency of such "polymer" solar cells is, however, still low when compared with inorganic semiconductors. A key challenge is therefore to find polymers that display the properties needed for high conversion efficiency, such as broad/intense absorptions, and high charge carrier mobility at appropriate energy levels.[37] One possible way to increase the

conversion efficiency involves utilizing two or more chemical materials with different spectral responses to achieve a higher overall utilization of solar energy.[38] This principle has been applied to modify, for example, photoelectrochemical (PEC) anodes with conducting polymers to thereby render them capable of splitting water when illuminated with sunlight.

1.3.1 PEC Water-Splitting Utilizing Polypyrrole (PPy)

Polypyrrole (PPy) is commercially inexpensive and processable (conductivity approximately 10-50 S cm^{-1}). It is thermodynamically stable and can be readily prepared by polymerization of its monomer; using a chemical oxidant such as $FeCl_3$, or via its electrochemical synthesis, with the incorporation of counter-ions into the polymer matrix. PPy has high conductivity due to its charge carrier mechanism.[39-41]

PPy was studied as a nanoparticle coating for water oxidation catalysis by Arthur and Honda more than 30 years ago.[42] They reported that when CdS nanoparticles were modified with a PPy layer, the PEC performance in the oxidation of water to O_2 gas was improved. They also reported that the presence of the PPy stabilized the semiconductor surface against photodegradation. By contrast, when polystyrene was used as a coating instead of PPy, it reduced the ΔG for solvation of the CdS lattice, resulting in photocorrosion of the CdS semiconductor surface.

Recently, Tan and colleagues[43] fabricated a new PEC for hydrogen (H_2) evolution under visible light using TiO_2 modified with PPy. PPy/TiO_2 nanoparticles (NPs) were prepared with two different morphologies: particles and film. PPy was combined with TiO_2 nanoparticles through *in situ* polymerization using water-trihexyl(tetradecyl)phosphonium dicyanamide in ionic liquid/water or toluene/water. The film generated from toluene displayed a higher H_2 generation rate compared to the particle morphology, which yielded lower H_2 production but higher thermal stability. As PPy coats the surface of TiO_2 nanoparticles, the PPy/TiO_2 NPs have a core-shell structure. The low band gap of PPy (2.6 eV) allowed the absorption of visible light and the transfer of an excited electron into the conduction band of

TiO_2 (3.2 eV), resulting in an electron-hole pair, which was able to split water into H_2 at the TiO_2 interface and O_2 at the PPy interface. The transfer of the excited electrons into the conduction band (CB) of, first PPy and then TiO_2, which has a lower energy than the excited state of PPy, diminished the rate of electron-hole recombination in PPy. The electrons on the surface of TiO_2 are sufficiently energetic to reduce water to hydrogen gas. The holes that remain on the PPy are able to oxidize water. The mechanism is shown schematically in Figure 1.3. In addition, the PPy/TiO_2 photoelectrode, which generated 0.04 mmol min^{-1} of hydrogen, was non-toxic and inexpensive when compared with other inorganic materials such as $InTaO_4$ (band gap 2.25 eV) and $YBiWO_6$ (band gap 2.71 eV), which produce similar rates of H_2 (0.05 mmol min^{-1} and 0.07 mmol min^{-1}, respectively, under light of wavelength >420 nm).

Furthermore, the combined PPy/TiO_2 appeared to be better than other systems based on Pt or shuttle redox mediators such as IO^{3-}/I^{-1} and $Fe^{3+/2+}$.[44-46] Other, similar, core-shell systems have been described elsewhere.[47]

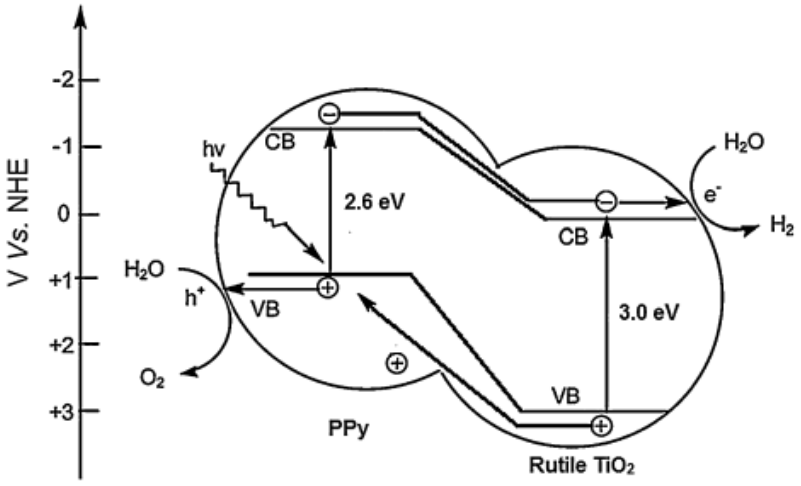

Figure 1.3: *The mechanism of electron transfer to the CB of TiO_2, which assisted H_2 and O_2 evolution in PPy/TiO_2 nanoparticles. It should be noted that the CB in the PPy component is actually an excited electronic state (LUMO). Reproduced with permission from ref. 43 (written agreement).*

Perhaps the best known polymerization technique for semiconductor modification is in situ polymerization, which includes sol-gel, blending and vapour phase polymerization methods. Simple operation and mild reaction conditions are required.

Wang and co-workers[48] used *in situ* polymerization to modify TiO_2 with PPy. The resulting TiO_2 /PPy (core/shell) had higher photoactivity under irradiation than TiO_2 modified with methyl orange. Moreover, higher conductivity and better absorption of visible light could be achieved by treating the PPy with dopants such as anthraquinone-2-sulfonic acid, iron (III) sulfate, and iron(III) *p*-toluenesulfonate hexahydrate.

The chemical structure and the doping method played a significant role in determining the properties of PPy in such fabricated photoanodes.[49] CdS is, in theory, an excellent semiconductor for water splitting since it has a near-ideal band gap (2.4 eV) with the energy of the conduction band CB well placed for water oxidation.[50] Zhang *et al.*[51] used *in situ* polymerization to improve the conductivity and the absorbance of PPy on CdS. Sodium dodecylbenzene sulfonate (DBSNa), hexadecyl trimethyl ammonium bromide (CTAB) and sodium *p*-toluenesulfonate (TSNa) were employed as dopants. Na_2S and Na_2SO_3 acted as sacrificial reagents to diminish recombination. The results revealed that PPy/CdS displayed higher performance than CdS alone, with larger H_2 generation rates observed. The use of TSNa as dopant yielded the best photoactivity for H_2 generation, while samples doped by CTAB displayed lower photoactivity (Figure 1.4).

PPy is a promising conductive polymer that generates excited electrons in direct response to visible light. Nanoparticles modified with PPy may display amplified photocurrents and improved conversion efficiencies when used as a photoelectrode in a PEC application.[52] PPy is also stable in acidic and neutral solutions, helping to prevent electron-hole recombination reactions (backward reactions). These properties encouraged Wang *et al.*[53] to combine PPy with the semiconductor ZnO, which is a promising photoanode for PEC water splitting. ZnO is also commercially inexpensive and its band gap is more suitable than other

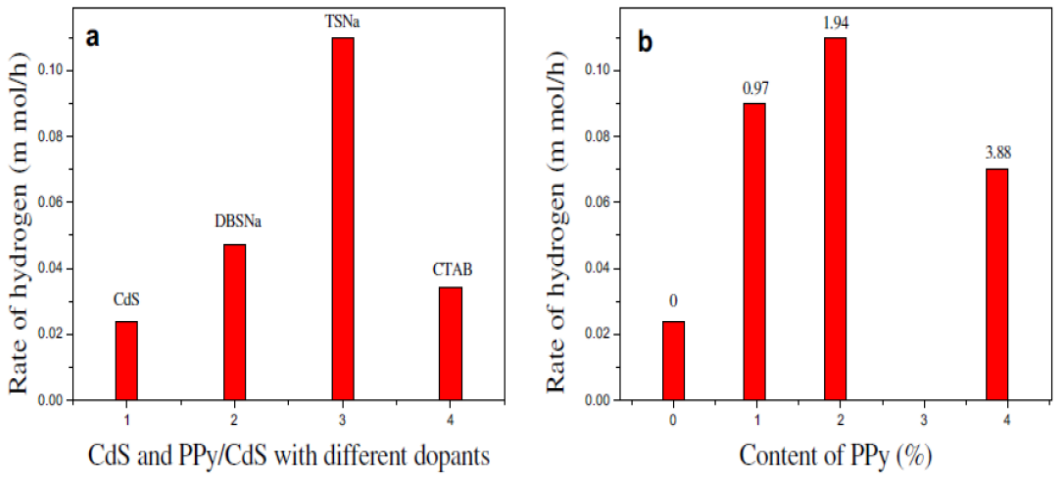

Figure 1.4: *Hydrogen evolution rates of: (a) CdS and PPy/CdS with different dopants; DBNa, TSNa and CTAB, and (b) PPy/CdS doped by TSNa having different levels of PPy. Reproduced with permission from ref. 51 (license no. 4466750304402).*

semiconductors such as TiO_2.[54] PPy/ZnO core-shell nanoparticles were synthesized on indium tin oxide (ITO) by a chemical oxidation method, which included using boric acid as a buffer solution containing potassium chloride and sodium dodecylsulfate. $FeCl_3$ was used as oxidant. Figure 1.5 a schematically shows the structure of the combined PPy/ZnO NPs.[53]

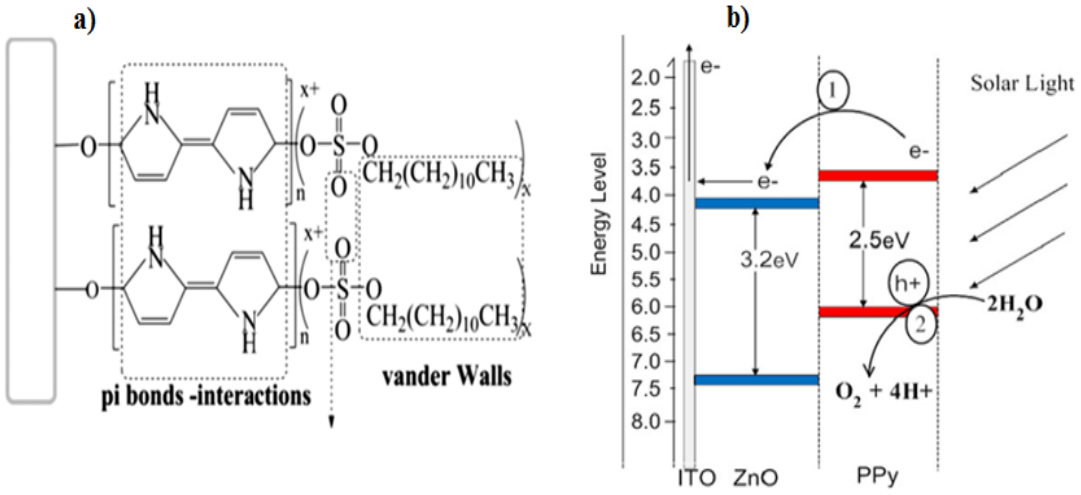

Figure 1.5: *a) Schematic of the structure of PPy/ZnO on the surface of ZnO nanorods (NRs). b) Illustration of PPy/ZnO NPs mechanism as PEC catalyst for water splitting under visible light. Reproduced with permission from ref. 53 (license no. 4466740456316).*

Wang's work highlighted three important features of PPy which make it useful in catalytic water-splitting applications when combined with a conventional semiconductor, namely: (i) PPy has a band gap that enhances PEC performance under visible light, (ii) the conductivity of PPy accelerates the transfer of electrons during the creation of holes, and (iii) the stability of PPy in water suppresses photo-corrosion of the solid-state semiconductor to thereby enhance the stability of the PEC system toward water oxidation. Figure 1.5(b) illustrates the mechanistic steps for PEC performance as described in Wang's work. The holes are generated at the PPy film by light excitation of electrons to the VB of the PPy. The excited electrons are then injected into the CB of ZnO. The holes in the CB of PPy oxidize water. The PEC was improved by increasing the gap in the Fermi levels to facilitate electron transfer from PPy to ZnO. Polypyrrole oligomers and molecular materials have also been investigated in water splitting.[55-56]

1.3.2 PEC Water-Splitting Utilizing Poly(3,4-ethylenedioxythiophene) (PEDOT)

While PEDOT is formally a functionalized thiophene, it will be addressed separately in this work because PEDOT is widely considered to be the best available CP in terms of conductivity, processability, transparency to visible light, stability, and fast electrochemical switching.[57-60] PEDOT can be combined with dispersions which act as counter ions, such as poly(styrene sulfonic acid) (PSS). The presence of a counter ion enhances the positive charge in oxidized PEDOT, increasing its dispensability and yielding PEDOT: PSS.[59] The properties of PEDOT encouraged researchers to use it to enhance the performance of PECs for both the Oxygen Evolution Reaction (OER) and the Hydrogen Evolution Reaction (HER) from water.

Thin films of PEDOT and poly(ethylene glycol) (PEG) have been synthesized on gold (Au), glassy carbon (GC) and titanium foil (Ti) substrates.[61-63] Li and colleagues have also fabricated a hybrid Si-APS/PEDOT core-shell nanowire system by vapour phase polymerization (VPP) (APS = 3-aminopropyltriethoxysilane).[64] APS was used as the initial

monolayer coating on the Si nanowire surface. Subsequent vapour phase polymerization of the monomer EDOT produced a strong, mechanically adhered PEDOT coating on the Si nanowire. PEDOT has a high selectivity for this application and could be finely patterned onto the nanoparticles due to the strong interaction between the N-H group on APS and PEDOT. The use of $FeCl_3$ as oxidant also dramatically improved the adhesion between the PEDOT film and the combined substrate.[65] The resulting hybrid photoelectrode Si-APS/PEDOT exhibited a notable catalytic performance in water splitting, generating high relative current densities (as shown in Figure 1.6(A)). It also displayed improved corrosion stability.

The mechanism of H_2 generation in this system was investigated. The Si nanowire absorbed the incident light, since the transparency of the PEDOT film was high in the visible light range. Electron–hole pairs could be diffused from the Si nanowire to the Si/PEDOT interface and then be separated by the Schottky junction effect. As depicted in Figure 1.6(B), thanks to the external bias, the electrons moved toward the aluminium (Al) circuit contact and then, *via* the external circuit, on to the Pt cathode, where they reduced water to form hydrogen. The holes (h^+) transferred to the PEDOT film, facilitating water oxidation on the surface to generate oxygen gas. Short nanowires suppressed the recombination of the generated electron-hole pairs but yielded lower activity toward hydrogen reduction. Long nanowires were better from an activity point of view, but resulted in increased recombination reactions.

PEDOT can also be combined with sensitizers and with other nonconductive or conducting polymers, such as polyethylene glycol (PEG) and polythiophene (PTh), to exhibit significant electrocatalytic properties. For example, PEDOT-PEG has been reported to catalyse water reduction to hydrogen at rates higher than classical catalysts like Pt.[66] The PEG was believed to facilitate ion diffusion in the interior of the polymer materials. The VPP method was said to enhance the incorporation of PEG to thereby ensure that the polymer structure has an open morphology which allowed electrolyte access. Thus, the main role of the conductive polymer in water reduction was to provide a source of electrons.[66]

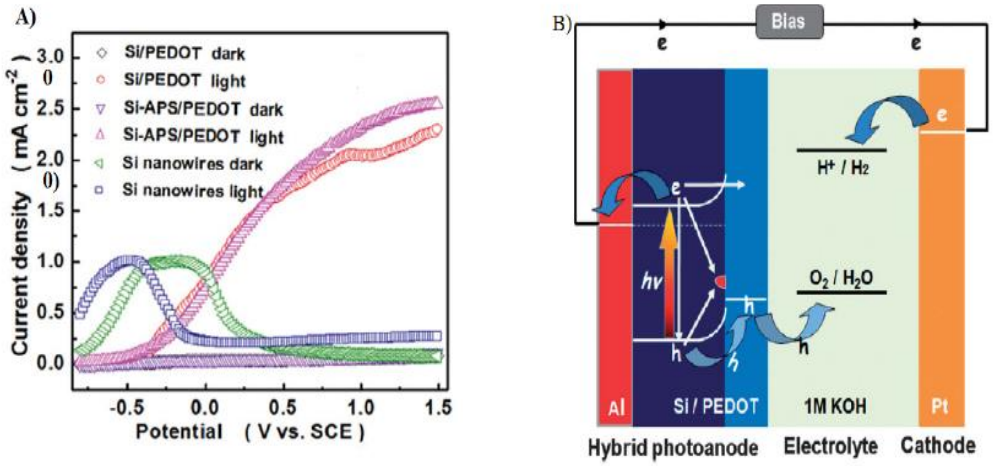

Figure 1.6: *(A) Current density of hybrid Si-APS/PEDOT compared to Si/PEDOT or Si nanowire as control. (B) The proposed mechanism of water oxidation using Si-APS /PEDOT as photoanode. Reproduced with permission from ref. 64 (license nos. 4466390650873 and 4466390994734).*

Studies have also examined PEDOT combined with other polymers in such PEC systems. For example, Kolodziejczyk and co-workers[67] studied a new hetero-junction design involving alloys of two conjugated polymers, PEDOT and poly(*ter*-thiophene) (PTTh), as a light-assisted catalyst of: (i) oxygen reduction (to form water), and (ii) water oxidation (to form oxygen). In acting as an oxygen reduction photocatalyst, the mixed polymers, deposited using the VPP method on either bulk gold or on Gore-Tex sputter-coated with gold, exhibited excellent performance, with stability lasting up to 98 h. However this photocatalyst did not display a notable water-oxidation effect, likely due to the recombination reactions.

Gustafson et al.[68] investigated the performance of conjugated polymers for water oxidation under illumination by UV light. Four sets of mixtures were prepared by VPP; namely, PEDOT: poly(thieno[3,2-b]thiophene) (PTT), PEDOT: poly(dithieno[3,2-b:2′,3-d]thiophene) (PDTT). PDTT, PEDOT: PEG: PTT and PEDOT: PEG: PDTT, with different ratios. It was observed that PEDOT: PEG: PDTT in the ratio 1:2:2 achieved the highest current density under illumination followed by PEDOT: PEG (1:1) and PEDOT: PDTT (1:2) respectively. The reasons for this behaviour were not explored in detail. However, it was suggested that the behaviour may arise from a higher degree of order or alignment in the

PEDOT. The interesting thing that was observed was that the active junction could potentially be enhanced to achieve a relative photovoltage and photocurrent increase under illumination.

As noted earlier, PEDOT may display anticorrosion properties in water due to the Schottky junction between the PEDOT layer and its substrate. The junction facilitates the transfer of holes to the solution. [69-70]These properties encouraged Duan et al.[71] to select PEDOT as the coating for Ag nanoparticles (AgNPs) modified with core-shell Si nanowires (SiNW). Water/methanol was used as the electrolyte. The PEDOT film was deposited on the surface of the SiNWs by electro-polymerization. The resulting AgNPs/PEDOT/SiNW arrays displayed stronger light absorbance than unmodified PEDOT/SiNWs, AgNP/SiNWs or SiNWs (Figure 1.7(A)). In addition, the PEDOT layer assists to release the lattice mismatch between the AgNPs and SiNWs, which: (i) encouraged the charge carriers to diffuse with higher efficiency, (ii) improved the photocatalysis in aqueous solution, (iii) increased stability, and (iv) reduced the onset potential (Figure 1.7(B)). The conversion efficiency for this system reached 2.86%. Similar designs made by Jeong et al. used Si nanocones with poly(styrenesulfonate) (PEDOT:PSS).[72]

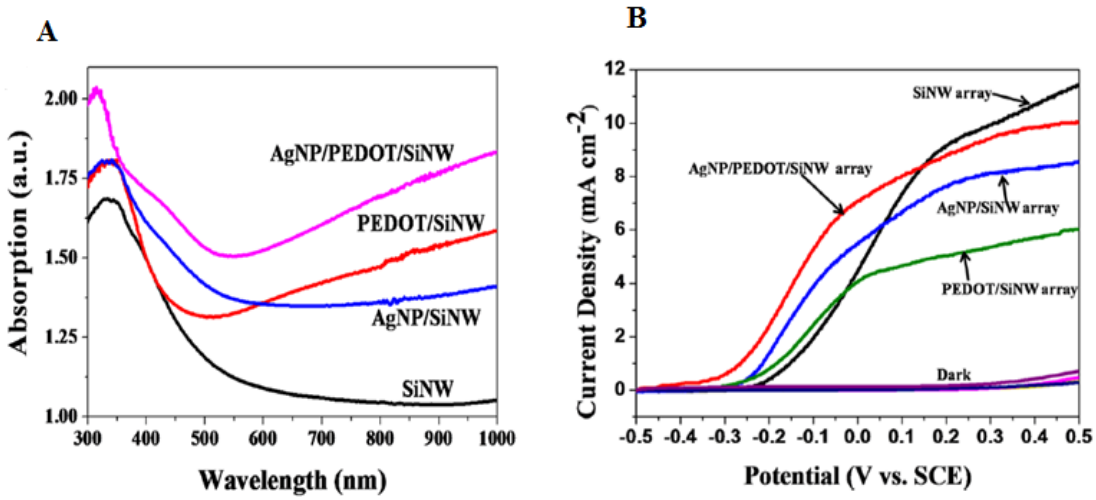

Figure 1.7: *(A) UV−visible absorption spectra of AgNPs/PEDOT/SiNW arrays, PEDOT/ SiNW, AgNP/ SiNW arrays, and AgNPs /SiNW arrays. (B) Current-potential characteristics of the different photoanodes in the dark and under illumination, collected at a scan rate of 50 mV/s from −0.5 to +0.5 V (vs SCE). Reproduced with permission from ref. 71 (license granted by written document).*

In order to be useful in solar water-splitting, CP coatings need to display notable electrocatalytic properties. Several studies have examined the electrocatalytic capabilities of PEDOT-based coatings and their application in, for example, gas diffusion electrodes.

Chowdhury and co-workers[73] fabricated highly active catalysts that were inexpensive relative to Pt/C and bifunctional electrocatalysts for oxygen reduction (ORR) and the oxygen evolution reactions (OER). Their PEDOT-$CoMnO_4$ nanocomposites were prepared by polymerization of the aqueous micellar dispersion consisting of dodecyl benzene sulfonic acid (DBSA) as the surfactant, EDOT as the monomer, and $CoMn_2O_4$ nanoparticles. The resulting, dark blue coloured nanocomposites were dropcast directly from alcoholic slurries onto a rotating disk glassy carbon electrode (GCE), which was air-dried to allow solvent evaporation. The GCE/PEDOT-$CoMn_2O_4$ nanocomposites catalyzed H_2 evolution in the higher potential range. The electrode was immersed in a KOH solution saturated with O_2. For LSV measurements, the non-conducting α-MnO_2 and $CoMn_2O_4$ spinel was mixed with conductive carbon powder or acetylene black and Teflon binder to create a well-mixed paste.

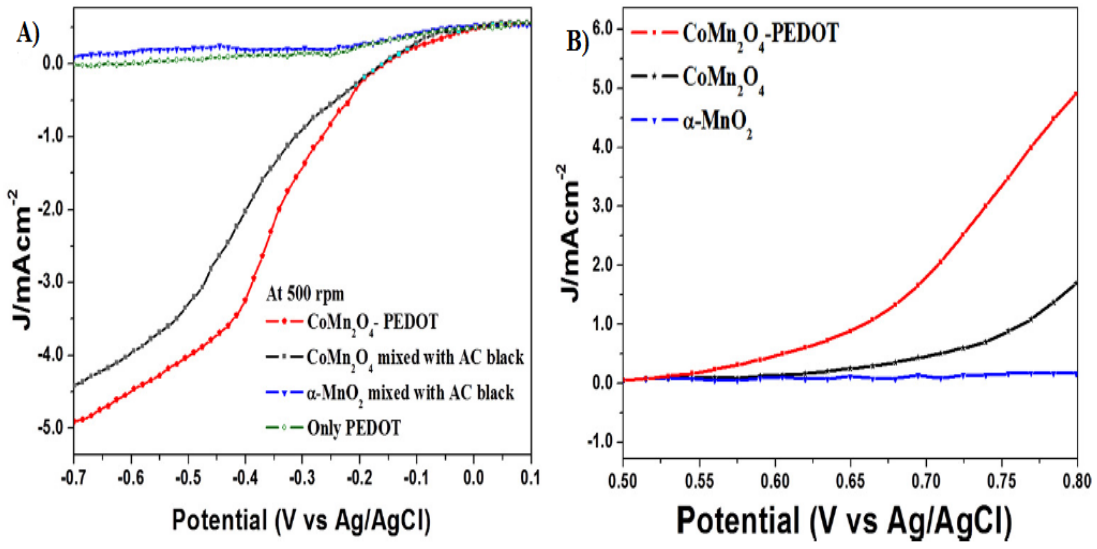

Figure 1.8: *Voltammetric curves of the OER measured at different rotation rates in the potential window of 0.5-0.8 V. Electrochemical comparison of $CoMn_2O_4$-PEDOT nanocomposites with $CoMn_2O_4$, PEDOT and π-MnO_2 as (A) ORR and (B) OER electrocatalysts. Reproduced with permission from ref. 73 (license no 4466760035499).*

The results revealed that PEDOT-based $CoMn_2O_4$ had better ORR catalytic activity compared to the spinel itself. The catalytic activity of the $CoMn_2O_4$ spinel was reduced when it was mixed mechanically with the acetylene black. However, it displayed better performance in the form of nanocomposites with the conducting PEDOT polymer (see Figure 1.8(a)). Figure 1.8(b) shows the activity for the OER reaction, which can be viewed as a reverse process of the ORR. In 0.1 M KOH, the $CoMn_2O_4$-PEDOT nanocomposites displayed higher OER currents than either free α-MnO_2 nanorod or $CoMn_2O_4$ nanocrystals. The α-MnO_2 nanorod did not show any OER/ORR activity.

Inherently conducting polymers (ICPs) such as PEDOT have also been used to fabricate electrodes that contain three-phase gas-solid-liquid interfaces. Gore-Tex membranes are well-known porous, hydrophobic materials that prevent aqueous electrolytes from passing through it. Its porous structure is however highly permeable to gas. When Gore-Tex is coated with Au and then with PEDOT: *p*-toluenesulfonic acid (by VPP), a high surface area gas diffusion electrode is created. The layer of PEDOT: PTS then lies at the interface of the gas and the liquid electrolyte phases, where it may catalyze water splitting as shown in Figure 1.9.

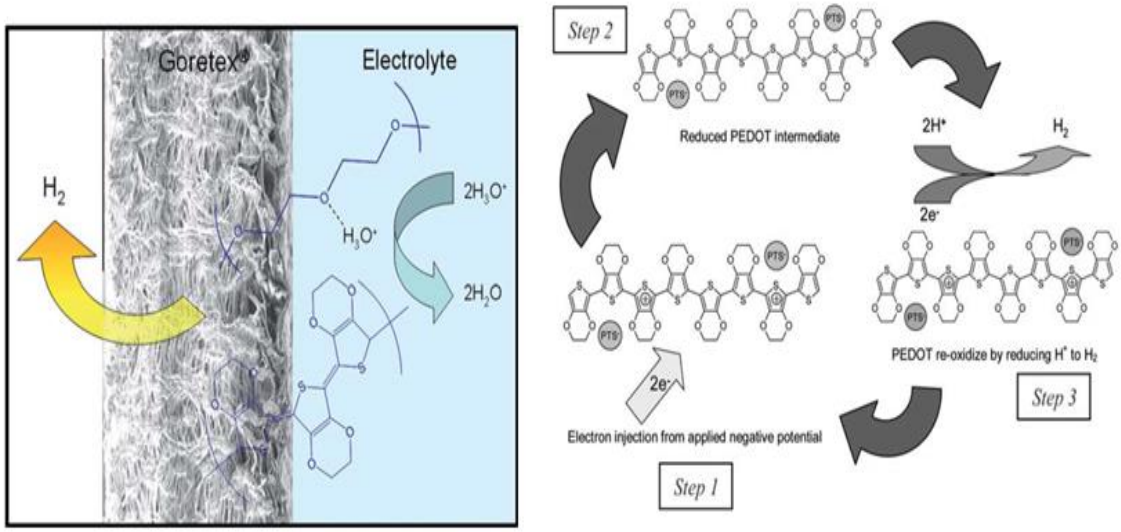

Figure 1.9: *Left diagram: The synthesis of PEDOT:PTS-coated Goretex-Au for water splitting. Right diagram: the proposed mechanism for hydrogen production by the PEDOT. Reproduced with permission from ref. 75 (license no 4466441066917).*

At negative potentials, electrons are injected into the oxidized PEDOT: PTS, generating an intermediate reduced PEDOT:PTS. The reduced PEDOT:PTS is not stable in the presence of H^+ and therefore readily re-oxidizes by reducing $2H^+$ to H_2.[74-75]

A significant study wherein PEDOT was used as a "stand-alone", light–assisted water oxidation catalyst has been carried out by Chen and co-workers.[76] In their investigation, PEDOT films were deposited on ITO-PET sheets by VPP, with and without the incorporation of the anionic sulfonated Mn-porphyrin **1** (Figure 1.10). PEDOT without **1** exhibited a blue-white color while PEDOT-**1** displayed a green colour. PEDOT-**1** also exhibited large light absorption peaks between 350-450 nm corresponding to the electronic structure of porphyrin. Energy-dispersive X-ray spectroscopy (EDX) revealed that the porphyrin in the PEDOT films was uniformly distributed in a ratio of 1:3 (1 Mn porphyrin: 3 EDOT monomer).

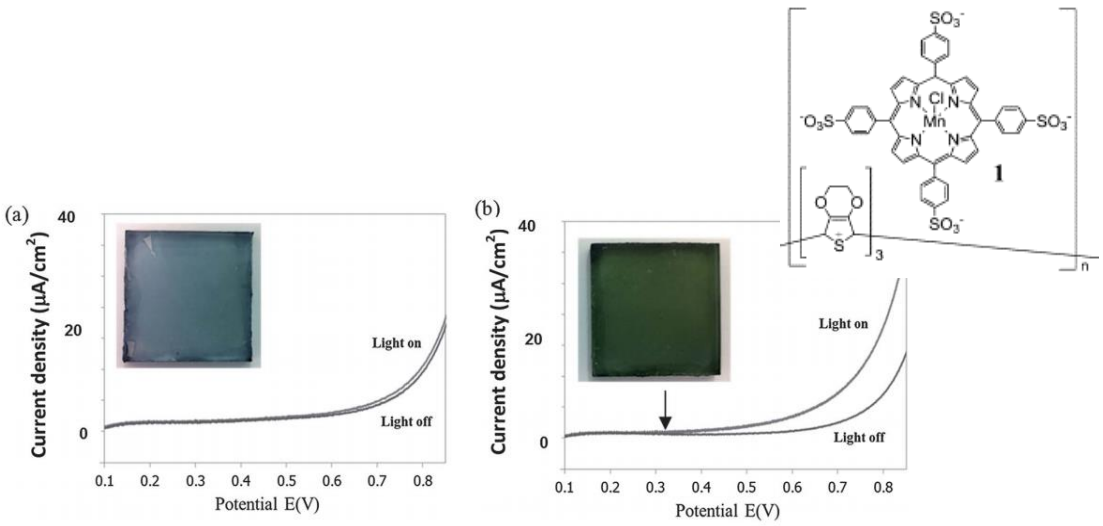

Figure 1.10: *Current density plot as a function of applied voltage with and without light illumination (vs. Ag/AgCl) (scan rate: 5 mV s^{-1} using aqueous 0.1 M Na_2SO_4 and pH 7) of: (a) PEDOT and (b) PEDOT-**1**. The arrow in (b) shows the earlier onset potential for light assisted water oxidation catalysis the inset in b shows the structure of PEDOT-**1**. Reproduced with permission from ref. 76 (license no. 4466450277303).*

Linear sweep voltammograms (LSV) were carried out at a slow scan rate (5 mVs^{-1}) to study the performance as water oxidation catalysts, of photoanodes based on PEDOT and PEDOT-**1** films in aqueous solutions, with and without light illumination. The results showed a clear photocurrent associated with O_2 formation from water, starting from ca. 0.32 V vs. Ag/AgCl (0.55 V vs. NHE) (Figure 1.10). This was substantially below the onset potential for poly(terthiophene)-**1** (0.91 V vs. NHE). It was also negative of the theoretical minimum.

Further work investigated light illumination of PEDOT-**1**/ITO-glass electrode at a constant potential of 0.70 V vs. Ag/AgCl (0.93 V vs. NHE) in aq. 0.1 M Na_2SO_4. The results indicated an immediate photocurrent under visible light. When the light was switched off, the photocurrent reduced rapidly. The mechanism for this system was investigated and proposed to involve light being absorbed by Mn porphyrin **1** with the excited electrons injected into the PEDOT, which was reduced from the oxidized to the neutral form. The neutral form was then immediately re-oxidized, where afterwards the hole in the remaining $\mathbf{1}^+$ interacted with an adjacent, cofacial *face to face* Mn porphyrin in its clusters leading to the extraction of electrons from two water molecules to create O_2.

1.3.3 Other Examples of PEC Water-Splitting Utilizing Conducting Polymers

Table 1 in the Appendix of this work provides a comprehensive list of recent research that has been done for water splitting used PEDOT, PPy and polythiophene (PTh). The role of the CP in these systems have been highlighted. Other CPs, such as polythiophene and polyaniline, have been discussed thoroughly in our book chapter entitled: "*Application of Conducting Polymers in Solar Water-Splitting Catalysis* in *Industrial Applications for Intelligent Polymers and Coatings*" (Mohammed Alsultan, Abbas Ranjbar, Gerhard F. Swiegers, Gordon G. Wallace, Sivakumar Balakrishnan, and Junhua Huang, Chapter 11 in *Industrial Applications for Intelligent Polymers and Coatings*, M. Hosseini, A.S.H. Makhlouf

(eds.), Springer International Publishing, Switzerland, 2016 (DOI 10.1007/978-3-319-26893-4_11).

1.4 Applications of Carbon Materials in PEC-Based Water- Splitting

Carbon based materials such as (modified) graphene oxide, graphene itself, carbon nanotubes and graphite have been widely used in water splitting application. As much of the following work has studied modified graphene oxide and CNTs, we highlight some of their interesting properties.

1.4.1 Applications of Graphene /Oxide in PEC Water-Splitting

The unique structure of graphene is attributed to its high transparency (97.7% per layer reduced to 94.3 % if five layers are applied together) and mechanical strength, inherent flexibility, large specific surface area (2630 m^2g^{-1}), high chemical and electrochemical stability, high conductivity (10^6 S cm^{-1}) and room-temperature mobility of charge carriers at (200000 cm^2 V^{-1} s^{-1}). In addition, graphene can be functionalized at low cost, which makes it attractive for commercial applications. Therefore, graphene and its derivatives have been widely investigated in the past several years in a variety of scientific fields, such as energy storage materials, microelectronic and optoelectronic devices, electrocatalysts, polymer composites, ultrastrong paper-like materials, graphene based nanomaterials for applications in the PEC and photocatalytic hydrogen production.[77-80]

Modified graphene oxide can play a vital role in water splitting, as a photocatalyst for O_2 and H_2 production.[81-82] It can accept and transfer electrons[83] as a redox mediator or as redox-mediator factors[84] in dye-sensitized solar cells (DSSCs)[85] and as a cocatalyst.[86] In the last 10 years a significant amount of research was conducted using modified GO for water electrolysis

or PEC water splitting. Table 2 in the Appendix highlights some of those studies and the roles of modified GO therein.

Graphene oxide (GO) can be produced by oxidizing graphene through a strong oxidization reaction involving HNO_3, H_2SO_4 and $KMnO_4$ (modified Hummers' method). The resultant GO is considered to be an intermediate state between graphene and graphite. Because it has sp^3 hybridized carbon atoms that obstruct delocalization of π –conjugation electrons in the graphene system, it is an insulator.[87] Tuning of its band gap from an insulating to conductive state can be achieved by chemical reduction of GO to reduced GO (rGO). The band gap of rGO depends strongly on the how the GO is oxidized.[88] However, some researchers have reported that rGO has a more negative reduction potential than the H_2 reduction potential and rGO has sufficient ability to generate H_2 from solar water splitting.[89-90] rGO incorporates various oxygen-containing functional groups (such as hydroxyl, epoxy, and carboxyl) on both its basal and edge planes and when recombined with other nanocomposites through various techniques such as hydrothermal, solvothermal, or photocatalytic methods, the system showed higher performance toward H_2 or O_2 production.[91-92]

1. 4. 2 Carbon Nanotube-Based Water Splitting

Since the discovery of carbon nanotubes (CNTs) in 1991[93] and the recognition of spherical molecules composed entirely of carbon atoms in fullerenes, single and multi carbon nanotubes,[94-96] the unique properties of CNTs have been found to include large specific surface areas (e.g. of 1315 $m^2 g^{-1}$),[97-98] high conductivity (up to 5000 S cm^{-1}) and excellent mechanical properties. [99-101, 98] CNTs have been studied in many applications including solar cells,[102-104] water splitting,[105-106] fuel cell, [107-108]sensors,[109-110] optical devices,[111] and biomedicine.[112]

Single and multi-walled CNTs can be formed by folding graphene layers into cylinder shapes, then capping both ends to form nanotubes. CNTs can have one of the three chiralities: armchair, zigzag and a chirality that depends on the rolling angle of the graphene sheet. The type of chirality may have a significant impact on the electrical properties. CNTs are also rich

with sp^2 carbon–carbon chemical bonds which are stronger than sp^3 bonds. Thus, CNTs have excellent mechanical properties.[113-115]

There are four methods for CNT production including; arc-discharge deposition, chemical vapour deposition (CVD), laser ablation, and disproportionation of carbon monoxide at high pressure. CNTs can be functionalized *via* covalent and non-covalent modifications to be potentially useful in their specific applications. Covalent modification means that functional groups can be attached onto the side wall or ends of the carbon nanotube; this modification mostly results in a disruption of the sp^2 carbon hybridization because of σ-bond formation, while non-covalent modification allows for various interaction adsorptions (e.g. hydrogen bond, Van der Waals force and π–π stacking interaction).[116]

CNTs may act as stand-alone electrocatalysts for the OER[117-118] and HER[119]or even as photoelectrocatalysts for the HER. [120] However, it can play a similar role to that of rGO in water splitting catalyst systems. For example, hybridization or doping of nano catalytic materials with CNTs can produce an efficient, durable electrocatalysts with comparable performance to noble metals such as Pt, Ir, and Ru. [121-125] CNTs and modified graphene oxide can increase the active surface area of the catalyst, help prevent dissolution during catalysis, [126] improves the conductivity of the cataysts,[127] enhance the mobility of both photogenerated charge carriers (e^-, h^+), restrict recombination reactions,[128] increase electron lifetime during the photocatalytic operation,[129] enhances visible light absorption, and act as a solid-state electron mediator in Z-scheme systems facilitating water splitting.[130]

1.5 Transition Metal-Based Catalyst for Water-Splitting

As noted above, transition metals are considered to be alternatives to precious metal catalysts, especially when they are interfaced with other catalyst materials. Transition metals can be utilized in nanoparticle, metal oxide or hydroxide forms, as electrocatalyst materials in acidic, neutral or alkaline media. In some research, their activity has been found to be greater than the noble metals. Thus, they have been gained significant attention in the last several

decades and much research has highlighted their potential in composites, for water splitting catalysis. This work has concentrated on using nano- cobalt oxide and nano- nickel.

1.5.1 Solar and Non-Solar Water-Splitting with Co_3O_4 and Nickel Catalysts

The cobalt oxides present a well-known class of water oxidation catalysts that do not require illumination with sunlight in order to operate. One of the most active such catalysts is Co_3O_4 in the spinel phase. While such catalysts do not require sunlight illumination *per se*, it is often useful to incorporate them and adapt them for use in solar water-splitting because they provide the resulting device with enhanced catalytic properties. For example, ZnO is a semiconductor that is relatively useful as in DSSCs, but less useful for solar water–splitting. Incorporation of Co_3O_4 on its surface however, allows it to split water under illumination. One of the best strategies of increasing the catalytic effect of Co_3O_4, is tuning its nanoparticle size to provide high surface areas with more active sites during the catalytic reaction.[131] For example, Esswein et al. investigated the loading of Co_3O_4 nanoparticles that have different sizes of 5.9 nm, 21.1 nm and 46.9 nm, on Ni foam. They reported that the catalytic surface area increased by an order of the magnitude when the smallest Co_3O_4 nanoparticle was used under the same conditions, showing a lower overpotential of 50 mV at a current density of 10 mA/cm^2.[132] However, Chou et al. reported that, using the same size of different cobalt oxides such as Co_3O_4 and CoO of 10 nm showed very similar activity for water splitting.[133] Another approach to enhance the activity performance of Co_3O_4 is to produce a more mesoporous structure by incorporating its nanoparticles with other mesoporous nanomaterials. For example, Qu et al. prepared highly ordered mesoporous 3D Pd-Co_3O_4; the results show that the mesoporous structure had a 1.6-times higher OER activity, stability, and a current density of 9.2 mA cm^{-2}, than mesoporous Co_3O_4 electrode alone.[134]

Further water splitting enhancement activity could be achieved by combining Co_3O_4 with conductive substrates. Carbon based materials (e.g. CNT, rGO and graphene) have been

employed as conductive substrates yielding higher conductivity and larger specific surface area of catalysis. For example, Co_3O_4 /rmGO (reduced mildly oxidized graphene oxide) prepared via hydrothermal reaction, exhibits high bifunctional electrocatalytic activity for the OER and ORR.[135] Co_3O_4 (NP)/graphene composites fabricated by layer-by-layer assembly exhibited remarkable electrocatalytic activity toward the OER.[136] A Co_3O_4/SWNTs-loaded ITO anode prepared *via* a chemical approach achieved 4-times higher performance than pristine Co_3O_4 at same condition. [137] Graphene(G)-Co_3O_4 was fabricated via an oleic acid assisted method followed by thermal treatment with the resulting electrocatalyst showing remarkable stability in both alkaline and neutral electrolytes. In this study it was observed also that the current density increased rapidly when the electrolyte was changed from neutral to 0.1 M KOH and 1 M KOH.[138] Islam et al. fabricated a bifunctional composite for both OER and HER photocatalysis, comprising of 3D atomic-cobalt(Co)/Co_3O_4-rGO) composite, via a chemical and hydrothermal approach, with the electrocatalyst exhibiting comparable activity to Ru/C and Pt/C for OER and HER.[139]

Numerous successful applications of PEC water splitting based on Co_3O_4 catalyst have been investigated. Peicheng et al deposited a mesoporous TiO_2 film on FTO substrate. The FTO glass was then immersed in an aqueous solution of ruthenium photosensitizer (RuP), followed by an ethanolic solution of 4-formylbenzoic acid and a methanolic solution of amino-functionalized Co_3O_4 respectively. The resulting photocurrent density was enhanced by more than 8-times over the catalyst without Co_3O_4.[140] Chua et. al.[141] fabricated Co_3O_4/WO_3 *via* sol gel, spin coating and hydrothermal methods, and the resulting photocurrent was enhanced by 40% with hydrogen evolution improved by 34%. Gupta et al.[142] fabricated a Co_3O_4-rGO nanocomposite *via* (γ)-radiolysis technique using alcoholic solution (isopropanol) containing cobalt ions with and without a suspended GO nanoparticles. The reported results showed that the hydrogen evolution rate reached 30 μmol h^{-1} g^{-1}, which means the hydrogen evolution rate was enhanced by 10-times over pure Co_3O_4. A $Co_3O_4/BiVO_4$ photoanode, fabricated *via* a drop-casting technique, produced a photocurrent of 2.71 mA/cm^2 at 1.23 V vs RHE, which represents the highest photocurrent thus far reported for Co-catalysed undoped $BiVO_4$ (with

photo conversion efficiency reaching 0.659%).[143] Liu et al.[144] fabricated a Co_3O_4-GaN photoanode *via* aerosol deposition of Co_3O_4 nanoparticles, and directly deposited on GaN nanowires on FTO glass. The results demonstrated a lower onset potential than GaN and improved the photocurrent by nearly 2-times after 300 s of operation in 1 M NaOH and 1 V vs RHE.

Nickel, its oxide and hydroxide have previously proved to be effective co-catalysts in water splitting applications. Ni-based nanomaterials have gained a growing interest for different applications, due to its features such as earth abundance, high chemical stability, high surface area, and its remarkable electrochemical properties.[145-146] For water splitting, recent research has investigated interfaces of Ni (based on the nanoparticle form) with other active materials, as an electrocatalyst for water splitting. For example, Ai et al.[147] fabricated a highly effective, bifunctional electrocatalyst with excellent stability consisting of Ni (NP) encapsulated in nitrogen-doped graphene Ni@NC *via* hydrothermal annealing. A current density of 10 mA/cm^2 was achieved for the OER at 1.6 V *vs* RHE in 1.0 M KOH and for the HER at -205 mV. Ai et al.[148] fabricated a highly active bifunctional electrocatalyst Ni@G for both OER and HER prepared via hydrothermal treatment and exhibits similar interesting results of Xu group.

Recent research reported that Ni based NP as catalyst can interact with semiconductors to enhance photocatalyst water splitting system. For example, in 2014 Li et al.[149] fabricated Ni/CdS photocatalysts for the HER *via* chemical reduction of $NiCl_2$ by $NaBH_4$ in the presence of polyvinylpyrolidone (PVP). The nano-Ni was then loaded onto the surface of CdS nanoparticles via a photo-induced electron technique. The photocatalyst was found to increase the H_2 evolution rate with an increase of Ni (NP) to a maximum at 2.5 % (mass fraction), when 9050 μmol h^{-1} g^{-1} QE of 9.4% at λ = 420 nm were achieved under 300 W Xe lamp. Wang et al.[150] fabricated a similar Ni/CdS photocatalyst in a similar preparation method utilizing $N_2H_4.H_2O$ as reducing agent for $NiCl_2$ to prepare Ni(NP) and used Cd $(NO_3)_2.4H_2O$ to prepare CdS. The loading of Ni(NP) was maximized at 4% (mass fraction) to produce a hydrogen evolution rate of 25.848 mmol/h.g and QE of 26.8% at 420 nm. 200. Cheng et al.[151]

introduced a layer of Ni(NP) on SnS_2 nanosheet via a hydrothermal method. The resulting photocatalyst exhibited higher visible light absorption, and its current density doubled to reach 45 μA/cm^2 at zero bias *vs* SCE for oxygen evolution of up to 3.2 mmol. g^{-1} after 3 h of operation. Finally, polyvinylpyrrolidone-coated carbon PVP-CQD/$Ni_{(NP)}$ composites were synthesized *via* a chemical method.[152]The resulting photocatalyst exhibited a hydrogen evolution rate of 330 mmol H_2.g^{-1} under 470 nm light, which was significantly higher than both CQDs and NiNPs that registered only 68 and 6 μgml^{-1} respectively.

1.6 Conclusion: Literature Review

CPs have unique properties that make them suitable for solar water-splitting applications. These properties include: conductivity, permeability to water, low-cost, environmental non-toxicity, electrochemical stability, useful light absorption, ready combination with other materials, excellent electron transfer properties, and uncomplicated preparative methods. This diversity and utility impart CPs with great promise in the catalytic generation of hydrogen and/or oxygen from water under illumination by sunlight.

Due to properties like high surface area, good dispersion in aqueous media, an excellent conductivity that enhances electron mobility, easy factionalized with active groups that boosts overall activity in water splitting, stability and durability in neutral, acidic and alkaline media, and excellent synergetic effects or interfaces with other materials, carbon based materials such as rGO and CNT have been extensively researched to develop water splitting system for both O_2 and H_2 production.

Co_3O_4 nanoparticles and Ni (NP) as cheap metals, offer an alternative to precious metal electrocatalyst materials such as Pt, Pd, IrO_2 and RuO_2 when interfaced with other active materials. However, studies of Ni- based nanomaterials and Co_3O_4 forms for water splitting are still limited and need more investigation, especially when interfaced with CP, rGO, and CNTs.

1. 7 The Aims of this Work: Studies of Thin-Layer Conducting Polymer Composites as (Photo) Catalytic Interfacial Materials

While the concept of harnessing sunlight to generate hydrogen as an energy carrier, may seem attractive, one of the major challenges with implementing it is that, at the present time, most PEC solar water splitting systems are either highly inefficient in their capacity to catalytically split water, or they are not durable when placed in water and then used for water-splitting. Non-functional, insulating coatings may also be formed.

The problem typically lies at the interface at which the water-splitting catalytic reaction occurs; for example, the interface between a photoactive semiconductor and the water that is to split. A key feature of any PEC cell is the interface/s between the different substances involved. It is here that significant inefficiencies and technical issues frequently arise. What is typically needed is a thin-film interfacial layer that lies between the photocatalyst and the aqueous liquid phase. The interfacial layer would then, effectively, connect and mediate the physical properties of the substrate photocatalyst/catalyst with the liquid water phase. Interfaces of this type need to be tailored to that task however. They need to maximise the advantageous properties of the photocatalyst in respect of harnessing illumination by sunlight and providing a driving force, whilst simultaneously providing a highly efficient, durable catalyst for splitting the water in the liquid phase into hydrogen or oxygen.

This work aims to study and develop various mixtures of materials that are, or could be suitable interfaces in water-splitting catalysis. Some of the mixtures will aim to provide a light-driven or -assisted catalytic effect. Others will seek only a catalytic effect, opting to rely on the intrinsic light harvesting capabilities of the materials to which the catalytic interface will be applied. All of the systems to be studied and developed will be of the 'thin-film' type that can be conveniently employed to enhance existing or new solar cells, or electrochemical cells. The aim is to develop powerful, readily-processable, and easily applied interfacial materials that could be useful to scientists working in other fields, such as on novel solar cells.

While a not insignificant amount of work has already been done on the development and study of catalytic coatings, such as Nocera's cobalt-phosphate (Co-Pi) materials,[153] there clearly is a lot more that can be done. Most such studies have examined specific semiconductors with specific catalytic coatings. Few studies have focussed on and considered the general nature of such interfacial thin-films and how they should be applied in order to maximally improve upon the performance of PECs involving both inorganic and organic thin-film coatings.

The most critical feature required in such an interfacial thin-film coating will, undoubtedly, be electrical conductivity. A secondary feature will be ready processability in a thin-film form, thereby allowing their application to the widest possible variety of potential substrates. Preferably, such thin films should be able to be deposited in a uniformly thin layer that is cohesive, adhesive to the substrate, and robust during operation. A third feature is that such thin films should act to not only transmit and harness a voltage generated by an underlying substrate but to maximise the (photo)catalytic effect that can be achieved from such a voltage. That is, the thin film should, ideally, be capable of amplifying the catalytic effect. This should occur even under mild reaction conditions, such as at near-neutral pHs at low applied voltages.

As discussed in the example above, conducting polymers have, in one way or another, been shown to demonstrate all of these properties. Indeed, conducting polymers are, arguably, one of the only materials that are potentially capable of meeting all of these requirements.

Moreover, conducting polymers may be infused with nano- or micro-particulate catalysts and / or conductors to modify and improve their properties in this respect. The resulting *composite* thin-films can potentially be made to exhibit synergistically amplified catalytic performances. That is, they can potentially be formulated so as to accelerate (photo)catalysis beyond what may normally be expected, including at moderate applied voltages and under mild pH conditions.

This work will address these challenges. It will investigate thin-layer conducting polymer composites and how they may be best tailored and applied in order to achieve the

above objectives. In particular, the work will examine if thin-film conducting polymer composites can be induced to synergistically amplify water-splitting catalysis itself and, if so, how they should be applied. This topic is, itself, of fundamental importance in the field of catalyst immobilization using conducting polymers.

1.8 Scope of this Work: Conducting Polymer Organic-Inorganic Composites as Thin Film Layers that Synergistically Amplify Catalysis

Many solar cells architectures can be adapted to water-splitting using suitable catalysts. Rather than focussing on one particular class of solar cell, this study will examine various conducting polymer composites as inorganic-organic thin films that:

(i) act as "stand-alone" catalytic water-splitting layers, or solar-driven / assisted water-splitting layers, when applied as uniformly thin films (<1 mm thick) on substrates that generate a voltage, whether that be a light-induced voltage or an electrically-induced voltage; and

(ii) Synergistically amplify the (photo) catalytic effect by optimizing the contents of the film itself. If such synergistic amplification can be achieved, studies will seek to develop methods of applying such thin films that generally bring about synergistic amplifications.

The following organic and inorganic materials will be examined. The conducting polymers PEDOT and polypyrrole will be studied as thin film substrates. The technique of vapour-phase polymerisation will generally be used, as it has been found to reliably provide uniformly thick layers of high density with strong cohesion and adhesion to substrates. PEDOT and polypyrrole are generally considered the best conductive polymers due to their conductivity, permeability to water, low-cost, environmental non-toxicity, electrochemical

stability, useful light absorption, capacity to be readily combined with other materials, excellent electron transfer properties, and uncomplicated preparative methods. This diversity and utility offer great promise in respect of the catalytic generation of hydrogen and/or oxygen from water with or without illumination by light.

The organic materials that will be incorporated into the thin film conducting polymers as a conductor (or, at least, a modifier of electrical conduction) will be modified graphene oxides, including mildly reduced graphene oxide (mrGO), and carbon nanotubes. This choice has been dictated by the fact that the thin-films will be studied for catalytic oxygen generation. Oxygen is a highly aggressive product that is known to rapidly oxidise and degrade most carbon-based conductors. However, mildly reduced graphene oxide (mrGO) is a form of carbon that has high degree of oxidation and cannot be easily oxidized so that it is therefore highly resistant to further oxidation. As such, it should not be affected by the production of oxygen gas. The reduced part - graphene, may enhance: (i) the mobility of photogenerated electrons and holes, (ii) photocurrent density, (iii) mechanical stability and durability of the proposed thin films, and (iv) H_2 and O_2 evolution rates. Carbon nanotubes are also a form of carbon that appear to be generally impervious to oxidation, albeit for largely kinetic reasons.

The following inorganic materials will be incorporated into the thin film conducting polymers as catalysts (or modifier of catalytic capability): (i) nanoparticulate nickel (Ni) and (ii) Co_3O_4. These choices have been dictated by the need for powerful water-splitting catalysts that can be readily incorporated into, and interface well with thin film conducting polymers. Nanoparticulate Ni will, initially, be studied as it is capable of catalysing both water oxidation and hydrogen reduction. It is also intrinsically conductive in its own right, which may help amplify the catalytic properties of the thin films. Thereafter, Co_3O_4, which is well known to be an excellent water oxidation catalyst, will be examined. This material is an insulator and may therefore not be as well suited to the objectives of this work.

The following specific topics will be discussed (Chapters in this thesis):

(Chapter 3) Investigate the interfacial catalytic properties of thin-film composites compincreased of Ni nanoparticles (nano-Ni), PEDOT and mildly reduced graphene oxide (rGO) in alkaline media for catalytic water oxidation;

(Chapter 4) Investigate the interfacial catalytic properties of thin-film composites compincreased of nano-Ni, PEDOT and rGO in acidic media for catalytic hydrogen evolution from water;

(Chapter 5) Investigate the interfacial catalytic properties of thin-film composites compincreased of nano-Ni, polypyrrole (PPy) and rGO in alkaline media for catalytic water oxidation;

Investigate the interfacial catalytic properties of thin-film composites compincreased of nano-Ni, PPy and rGO in acidic media for catalytic hydrogen evolution from water;

(Chapter 6) Investigate the interfacial catalytic properties of thin-film composites compincreased of Co_3O_4, PEDOT, and rGO in alkaline media for catalytic water oxidation;

(Chapter 7) Investigate the design of a hydrogel separator for bifunctional electrochemical and photoelectrochemical water-splitting catalysis based on thin-film composites compincreased of Ni nanoparticles (nano-Ni), PEDOT and mildly reduced graphene oxide (rGO)

1.9 References

1. Züttel, A.; Remhof, A.; Borgschulte, A.; Friedrichs, O. Hydrogen: The Future Energy Carrier. *Philos. Trans. R. Soc. A-Math Phys. Eng. Sci.* **2010**, *368*, 3329-3371.
2. Parida, B.; Iniyan, S.; Goic, R. A Review of Solar Photovoltaic Technologies. *Renew. Sust. Energy Rev.* **2011**, *15* (3), 1625-1636.
3. Dresselhaus, M. S.; Thomas, I. L. Alternative Energy Technologies. *Nat.* **2001**, *414*, 332-337.
4. Luca, R. D.; Romeo, F.; Zozzaro, P. Capturing Sunlight. *Eur. J. Phys.* **2006**, *27* (2), 347-352.
5. Li, C.; Liu, M.; Pschirer, N. G.; Baumgarten, M.; Müllen, K. Polyphenylene-Based Materials for Organic Photovoltaics. *Chem.Rev.* **2010**, *110* (11), 6817-6855.
6. Li, B.; Wang, L.; Kang, B.; Wang, P.; Qiu, Y. Review of Recent Progress in Solid-State Dye-Sensitized Solar Cells. *Sol. Energy Mater. Sol. Cells* **2006**, *90* (5), 549-573.
7. Colligon, J. S. The world energy crisis: Some vacuum-based solutions. *Vac.* **2006**, *80* (10), 1047.
8. Li, C.; Wang, F.; Yu, J. C. Semiconductor/Biomolecular Composites for Solar Energy Applications. *Energy Environ Sci.* **2011**, *4* (1), 100-113.
9. Neelu Chouhan, R.-S. L., Jiujun Zhang Concept in Photochemical Water Splitting. In *Photochemical Water Splitting: Materials and Applications*, Taylor & Francis Group, CRC Press: London, New York, **2017**; pp 41-80.
10. Fujishima, A.; Honda, K. Electrochemical Photolysis of Water at a Semiconductor Electrode. *Nat.* **1972**, *238*, 37-38.
11. Nozik, A. J. Photoelectrochemistry: Applications to Solar Energy Conversion. *Annu. Rev. Phys.Chem.* **1978**, *29* (1), 189-222.
12. Abe, R. Recent Progress on Photocatalytic and Photoelectrochemical Water Splitting Under Visible Light Irradiation. *J. Photochem. Photobiol. C: Photochem. Rev.* **2010**, *11* (4), 179-209.
13. Galvanic and Electrolytic Cells and the Standard Hydrogen Electrode. http://www4.ncsu.edu/~franzen/public_html/CH201/module/lec17/lec17.html (accessed 20 June 2018).
14. Doyle, R. L.; Lyons, M. E. G. The Oxygen Evolution Reaction: Mechanistic Concepts and Catalyst Design. In *Photoelectrochemical Solar Fuel Production: From Basic Principles to Advanced Devices*, Giménez, S.; Bisquert, J., Eds. Springer Int. Publishing: Switzerland, **2016**; pp 41-104.

15. Liao, C.-H.; Huang, C.-W.; Wu, J. C. S. Hydrogen Production From Semiconductor-Based Photocatalysis via Water Splitting. *Catal.* **2012**, *2*, 490-516.
16. Kuo, D.-Y.; Kawasaki, J. K.; Nelson, J. N.; Kloppenburg, J.; Hautier, G.; Shen, K. M.; Schlom, D. G.; Suntivich, J. Influence of Surface Adsorption on The Oxygen Evolution Reaction on IrO_2(110). *J. Am. Chem. Soc.* **2017**, *139* (9), 3473-3479.
17. Zhang, G.; Zhang, W.; Minakata, D.; Chen, Y.; Crittenden, J.; Wang, P. The pH effects on H_2 Evolution kinetics for Visible Light Water Splitting Over The $Ru/(CuAg)_{0.15}In_{0.3}Zn_{1.4}S_2$ *Photocatal*. *Int. J. Hydrogen Energy* **2013**, *38* (27), 11727-11736.
18. Bledowski, M.; Wang, L.; Ramakrishnan, A.; Beranek, R. TiO_2-Polyheptazine Hybrid Photoanodes: Effect of Cocatalysts and External Bias on Visible Light-Driven Water Splitting. *J. Mater. Res.* **2013**, *28* (3), 411-417.
19. Jafari, T.; Moharreri, E.; Amin, S. A.; Miao, R.; Song, W.; Suib, L. S. Photocatalytic Water Splitting—The Untamed Dream: A Review of Recent Advances. *Mol.* **2016**, *21*, 900-929.
20. Li, X.; Yu, J.; Low, J.; Fang, Y.; Xiao, J.; Chen, X. Engineering Heterogeneous Semiconductors for Solar Water Splitting. *J. Mater. Chem. A* **2015**, *3* (6), 2485-2534.
21. Suen, N.-T.; Hung, S.-F.; Quan, Q.; Zhang, N.; Xu, Y.-J.; Chen, H. M. Electrocatalysis for the Oxygen Evolution Reaction: Recent Development and Future Perspectives. *Chem. Soc. Rev.* **2017**, *46* (2), 337-365.
22. Zhang, L.; Xiao, J.; Wang, H.; Shao, M. Carbon-Based Electrocatalysts for Hydrogen and Oxygen Evolution Reactions. *ACS Catal.* **2017**, *7* (11), 7855-7865.
23. El-Khouly, M. E.; El-Mohsnawy, E.; Fukuzumi, S. Solar Energy Conversion: From Natural to Artificial Photosynthesis. *J. Photochem. Photobiol. C: Photochem. Rev.* **2017**, *31*, 36-83.
24. Maeda, K.; Domen, K. New Non-Oxide Photocatalysts Designed for Overall Water Splitting Under Visible Light. *J. Phys. Chem. C* **2007**, *111* (22), 7851-7861.
25. Walter, M. G.; Warren, E. L.; McKone, J. R.; Boettcher, S. W.; Mi, Q.; Santori, E. A.; Lewis, N. S. Solar Water Splitting Cells. *Chem. Rev.* **2010**, *110* (11), 6446-6473.
26. Huang, X.; Woo, H.; Wu, P.; Jin Hong, H.; Jung, W.; Kim, B.-J.; Vanel, J.-C.; Woo Choi, J. Simple Eco-Friendly Synthesis of the Surfactant Free SnS Nanocrystal Toward the Photoelectrochemical Cell Application. *Sci. Rep.* **2017**, *7*, 16531 (1-9).
27. Wang, J.; Sun, H.; Huang, J.; Li, Q.; Yang, J. Band Structure Tuning of TiO_2 for Enhanced Photoelectrochemical Water Splitting. *J. Phys.Chem. C* **2014**, *118* (14), 7451-7457.

28. Chiang, C. K.; Druy, M. A.; Gau, S. C.; Heeger, A. J.; Louis, E. J.; MacDiarmid, A. G.; Park, Y. W.; Shirakawa, H. Synthesis of Highly Conducting Films of Derivatives of Polyacetylene, $(CH)_x$. *J. Am. Chem. Soc.* **1978**, *100* (3), 1013-1015.
29. Basescu, N.; Liu, Z. X.; Moses, D.; Heeger, A. J.; Naarmann, H.; Theophilou, N. High Electrical Conductivity in Doped Polyacetylene. *Nat.* **1987**, *327*, 403-405.
30. Yahyaie, I.; Ardo, S.; Oliver, D. R.; Thomson, D. J.; Freund, M. S.; Lewis, N. S. Comparison Between the Electrical Junction Properties of H-Terminated and Methyl-Terminated Individual Si Microwire/Polymer Assemblies for Photoelectrochemical Fuel Production. *Energy Environ. Sci.* **2012**, *5* (12), 9789-9794.
31. Pratt, C. Conductive Polymers. http:ntlworld.com/colin.pratt/home.html (accessed 20 June 2018).
32. M. Molapo, K.; Ndangili, P. M.; F. Ajayi, R.; Mbambisa, G.; M. Mailu, S.; Njomo, N.; Masikini, M.; Baker, P.; I. Iwuoha, E. Electronics of Conjugated Polymers (I): Polyaniline. *Int. J. Electrochem. Sci.* **2012**, *7*, 11859-11875.
33. Ziadan, K. *Conducting Polymers Application*. **2012**, pp 1-26.
34. Chandrasekhar, P. *Conducting Polymers, Fundamentals and Applications: A Practical Approach*. Kluwer Academic: Boston , London **1999**; pp 3-22.
35. Bakhshi, A. K.; Bhalla, G. Electrically conducting polymers: Materials of The Twentyfirst Century. *J. Sci. Indust. Res.* **2004**, *63*(9), 715-728.
36. Saini, P.; Arora, M. Microwave Absorption and EMI Shielding Behavior of Nanocomposites Based on Intrinsically Conducting Polymers, Graphene and Carbon Nanotubes In *New Polymers for Special Applications*, Gomes, A. D. S., Ed. InTech: Rijeka, Croatia **2012**; pp 72-112.
37. Miomandre, F.; Pierre, A. *Basics and New Insights in the Electrochemistry of Conducting Polymers*. Nova, New York, **2013**; pp 53-90.
38. Tributsch, H. *Photovoltaic Hydrogen Generation*. *In. J. Hydrogen Energy* **2008**, *33* (21), 5911-5930.
39. Tat'yana, V. V.; Oleg, N. E. Polypyrrole: a Conducting Polymer; its Synthesis, Properties and Applications. *Russ. Chem.Rev.* **1997**, *66* (5), 443-457.
40. Kassim, A.; Basar, Z. B.; Mahmud, H. N. M. E. Effects of Preparation Temperature on the Conductivity of Polypyrrole Conducting Polymer. *J. Chem. Sci.* **2002**, *114* (2), 155-162.
41. Ilicheva, N. S.; Kitaeva, N. K.; Duflot, V. R.; KabanovaV. I. Synthesis and Properties of Electroconductive Polymeric Composite Material Based on Polypyrrole. *Annu. Rev. Phys. Chem.* **1978**, *2012*, 320316 (1-7).
42. Frank, A. J.; Honda, K. Polymer-Modified Electrodes, Catalysis and Water-Splitting Reactions. *J. Photochem.***1985**, *29* (1), 195-204.

43. Tan, Y.; Chen, Y.; Mahimwalla, Z.; Johnson, M. B.; Sharma, T.; Brüning, R.; Ghandi, K. Novel Synthesis of Rutile Titanium Dioxide–Polypyrrole Nano Composites and Their Application in Hydrogen Generation. *Synth. Met.* **2014**, *189*, 77-85.
44. Zou, Z.; Ye, J.; Sayama, K.; Arakawa, H. Direct Splitting of Water Under Visible Light Irradiation with an Oxide Semiconductor Photocatalyst. *Nat.* **2001**, *414*, 625-627.
45. Liu, H.; Yuan, J.; Shangguan, W.; Teraoka, Y. Visible-Light-Responding $BiYWO_6$ Solid Solution for Stoichiometric Photocatalytic Water Splitting. *J. Phys. Chem.C* **2008**, *112* (23), 8521-8523.
46. Abe, R.; Takata, T.; Sugihara, H.; Domen, K. Photocatalytic Overall Water Splitting Under Visible Light by TaON and WO_3 with an IO_3^-/I^- Shuttle Redox Mediator. *Chem. Commun.* **2005**, (30), 3829-3831.
47. Gu, S.; Li, B.; Zhao, C.; Xu, Y.; Qian, X.; Chen, G. Preparation and Characterization of Visible Light-Driven AgCl/PPy Photocatalyst. *J. Alloys Compd.* **2011**, *509* (18), 5677-5682.
48. Wang, D.; Wang, Y.; Li, X.; Luo, Q.; An, J.; Yue, J. Sunlight Photocatalytic Activity of Polypyrrole–TiO_2 Nanocomposites Prepared by 'in situ' Method. *Catal. Commun.* **2008**, *9* (6), 1162-1166.
49. Håkansson, E.; Lin, T.; Wang, H.; Kaynak, A. The Effects of Dye Dopants on The Conductivity and Optical Absorption Properties of Polypyrrole. *Synth.Met.* **2006**, *156* (18), 1194-1202.
50. Zhang, S.; Chen, Q.; Jing, D.; Wang, Y.; Guo, L. Visible Photoactivity and Antiphoto corrosion Performance of PdS–CdS Photocatalysts Modified by Polyaniline. *Int. J. Hydrogen Energy* **2012**, *37* (1), 791-796.
51. Zhang, S.; Chen, Q.; Wang, Y.; Guo, L. Synthesis and Photoactivity of CdS Photocatalysts Modified by Polypyrrole. *Int. J. Hydrogen Energy* **2012**, *37* (17), 13030-13036.
52. Zhang, Z.; Yuan, Y.; Liang, L.; Cheng, Y.; Xu, H.; Shi, G.; Jin, L. Preparation and Photoelectrochemical Properties of a Hybrid Electrode Composed of Polypyrrole Encapsulated in Highly Ordered Titanium Dioxide Nanotube Array. *Thin Solid Films* **2008**, *516* (23), 8663-8667.
53. Wang, Z.; Xiao, P.; Qiao, L.; Meng, X.; Zhang, Y.; Li, X.; Yang, F. Polypyrrole Sensitized ZnO Nanorod Arrays for Efficient Photo-Electrochemical Splitting of Water. *Phys. B: Conden. Matter* **2013**, *419*, 51-56.
54. Liu, M.; Nam, C.-Y.; Black, C. T.; Kamcev, J.; Zhang, L. Enhancing Water Splitting Activity and Chemical Stability of Zinc Oxide Nanowire Photoanodes with Ultrathin Titania Shells. *J. Phys. Chem. C* **2013**, *117* (26), 13396-13402.

55. Mola, J.; Mas-Marza, E.; Sala, X.; Romero, I.; Rodríguez, M.; Viñas, C.; Parella, T.; Llobet, A. Ru-Hbpp-Based Water-Oxidation Catalysts Anchored on Conducting Solid Supports. *Angew. Chem. Int. Ed.* **2008**, *47* (31), 5830-5832.
56. Brimblecombe, R.; Dismukes, G. C.; Swiegers, G. F.; Spiccia, L. Molecular Water-Oxidation Catalysts for Photoelectrochemical Cells. *Dalton Trans.* **2009**, (43), 9374-9384.
57. Andreas Elschner; Stephan Kirchmeyer; Wilfried Lovenich; Udo Merker; Reuter, K. *PEDOT: Principles and Applications of an Intrinsically Conductive Polymer*. Taylor & Frances Group: London , New York **2010**, pp 57-63
58. Pyshkina, O.; Kubarkov, A.; Sergeyev, V. Poly(3,4-ethylenedioxythiophene): Synthesis and Properties. *Sci. J. Riga Techn. Univ. Mater. Sci. Appl. Chem.* **2010**, (21), pp 51-54.
59. Kros, A.; Sommerdijk, N. A. J. M.; Nolte, R. J. M. Poly(pyrrole) Versus Poly(3,4-ethylenedioxythiophene): Implications for Biosensor Applications. *Sens. Actuators B: Chem.* **2005**, *106* (1), 289-295.
60. Carlberg, C.; Chen, X.; Inganäs, O. Ionic Transport and Electronic Structure in Poly (3,4ethylenedioxythiophene). *Solid State Ionics* **1996**, *85* (1), 73-78.
61. Wei, W.; Wang, H.; Hu Yun, H. A review on PEDOT-Based Counter Electrodes for Dye-Sensitized Solar Cells. *Int. J. Energy Res.* **2014**, *38* (9), 1099-1111.
62. Gu, C.; Norris, B. C.; Fan, F.-R. F.; Bielawski, C. W.; Bard, A. J. Is Base-Inhibited Vapor Phase Polymerized PEDOT an Electrocatalyst for the Hydrogen Evolution Reaction? Exploring Substrate Effects, Including Pt Contaminated Au. *ACS Catal.* **2012**, *2* (5), 746-750.
63. Metsik, J.; Saal, K.; Mäeorg, U.; Lõhmus, R.; Leinberg, S.; Mändar, H.; Kodu, M.; Timusk, M. Growth of Poly(3,4-ethylenedioxythiophene) Films Prepared by Base-Inhibited Vapor Phase Polymerization. *J. Polym. Sci. Part B: Polym.Phys.* **2014**, *52* (8), 561-571.
64. Li, X.; Lu, W.; Dong, W.; Chen, Q.; Wu, D.; Zhou, W.; Chen, L. Si/PEDOT Hybrid Core/Shell Nanowire Arrays as Photoelectrodes for Photoelectrochemical Water-Splitting. *Nanoscale* **2013**, *5* (12), 5257-5261.
65. Kim, S.; Pang, I.; Lee, J. Aminosilane SAM-Assisted Patterning of Poly(3,4-ethylene dioxythiophene) Nanofilm Robustly Adhered to SiO_2 Substrate. *Macromol. Rapid Commun.* **2007**, *28* (15), 1574-1580.
66. Swiegers, G. F.; MacFarlane, D. R.; Officer, D. L.; Ballantyne, A.; Boskovic, D.; Chen, J.; Dismukes, G. C.; Gardner, G. P.; Hocking, R. K.; Smith, P. F.; Spiccia, L.; Wagner, P.; Wallace, G. G.; Winther-Jensen, B.; Winther-Jensen, O. Towards

Hydrogen Energy: Progress on Catalysts for Water Splitting. *Aust. J. Chem.* **2012**, *65* (6), 577-582.

67. Kolodziejczyk, B.; Winther-Jensen, O.; MacFarlane, D. R.; Winther-Jensen, B. Conducting Polymer Alloys for Photo-Enhanced Electro-Catalytic Oxygen Reduction. *J. Mater. Chem.* **2012**, *22* (21), 10821-10826.
68. Gustafson, M. P.; Matsumoto, K.; MacFarlane, D. R.; Winther-Jensen, B. An Investigation of the Properties of Conducting Polymer Alloys for Water Oxidation. *Electrochem. Acta* **2014**, *122*, 166-172.
69. Winther-Jensen, B.; Fraser, K.; Ong, C.; Forsyth, M.; MacFarlane Douglas, R. Conducting Polymer Composite Materials for Hydrogen Generation. *Adv. Mater.* **2010**, *22* (15), 1727-1730.
70. Yang, T.; Wang, H.; Ou, X. M.; Lee, C. S.; Zhang, X. H. Iodine-Doped-Poly(3,4-Ethylenedioxythiophene)-Modified Si Nanowire 1D Core-Shell Arrays as an Efficient Photocatalyst for Solar Hydrogen Generation. *Adv. Mater.* **2012**, *24* (46), 6199-6203.
71. Duan, C.; Wang, H.; Ou, X.; Li, F.; Zhang, X. Efficient Visible Light Photocatalyst Fabricated by Depositing Plasmonic Ag Nanoparticles on Conductive Polymer-Protected Si Nanowire Arrays for Photoelectrochemical Hydrogen Generation. *ACS Appl. Mater. Interfaces* **2014**, *6* (12), 9742-9750.
72. Jeong, S.; Garnett, E. C.; Wang, S.; Yu, Z.; Fan, S.; Brongersma, M. L.; McGehee, M. D.; Cui, Y. Hybrid Silicon Nanocone–Polymer Solar Cells. *Nano Lett.* **2012**, *12* (6), 2971-2976.
73. Chowdhury, A. D.; Agnihotri, N.; Sen, P.; De, A. Conducting $CoMn_2O_4$ - PEDOT Nanocomposites as Catalyst in Oxygen Reduction Reaction. *Electrochim. Acta* **2014**, *118*, 81-87.
74. Winther-Jensen, B.; Winther-Jensen, O.; Forsyth, M.; MacFarlane, D. R. High Rates of Oxygen Reduction over a Vapor Phase–Polymerized PEDOT Electrode. *Sci.* **2008**, *321*, 671-675.
75. Winther-Jensen, B.; MacFarlane, D. R. New Generation, Metal-Free Electrocatalysts for Fuel Cells, Solar Cells and Water Splitting. *Energy Environ. Sci.* **2011**, *4* (8), 2790-2798.
76. Chen, J.; Wagner, P.; Tong, L.; Boskovic, D.; Zhang, W.; Officer, D.; Wallace, G. G.; Swiegers, G. F. A Light-Assisted, Polymeric Water Oxidation Catalyst that Selectively Oxidizes Seawater with a Low Onset Potential. *Chem. Sci.* **2013**, *4* (7), 2797-2803.
77. Sun, Y.; Wu, Q.; Shi, G. Graphene Based New Energy Materials. *Energy Environ. Sci.* **2011**, *4* (4), 1113-1132.

78. Zhu, Y.; Murali, S.; Cai, W.; Li, X.; Suk, J. W.; Potts, J. R.; Ruoff, R. S. Graphene and graphene oxide: Synthesis, Properties, and Applications. *Adv. Mater.* **2010**, *22* (35), 3906–3924.
79. Wang, S.; Ábrahám, D.; Vallejos-Burgos, F.; László, K.; Geissler, E.; Takeuchi, K.; Endo, M.; Kaneko, K. Distorted Graphene Sheet Structure-Derived Latent Nano porosity. *Langmuir*. **2016**, *32* (22), 5617-5622.
80. Avouris, P. Graphene: Electronic and Photonic Properties and Devices. *Nano Lett.* **2010**, *10* (11), 4285-4294.
81. Ng, Y. H.; Iwase, A.; Kudo, A.; Amal, R. Reducing Graphene Oxide on a Visible-Light $BiVO_4$ Photocatalyst for an Enhanced Photoelectrochemical Water Splitting. *J. Phys. Chem. Lett.* **2010**, *1* (17), 2607-2612.
82. Guo, J.; Li, Y.; Zhu, S.; Chen, Z.; Liu, Q.; Zhang, D.; Moon, W.-J.; Song, D.-M. Synthesis of WO_3@Graphene Composite for Enhanced Photocatalytic Oxygen Evolution From Water. *RSC Adv.* **2012**, *2* (4), 1356-1363.
83. Zhang, Y.; Zhang, N.; Tang, Z.-R.; Xu, Y.-J. Graphene Transforms Wide Band Gap ZnS to a Visible Light Photocatalyst. The New Role of Graphene as a Macromolecular Photosensitizer. *ACS Nano* **2012**, *6* (11), 9777-9789.
84. Iwase, A.; Yoshino, S.; Takayama, T.; Ng, Y. H.; Amal, R.; Kudo, A. Water Splitting and CO_2 Reduction Under Visible Light Irradiation Using Z-Scheme Systems Consisting of Metal Sulfides, CoOx-Loaded $BiVO_4$, and a Reduced Graphene Oxide Electron Mediator. *J. Am. Chem. Soc.* **2016**, *138* (32), 10260-10264.
85. Li, Z.; Gong, F.; Zhou, G.; Wang, Z.-S. NiS_2/Reduced Graphene Oxide Nanocom posites for Efficient Dye-Sensitized Solar Cells. *J. Phys.Chem.C* **2013**, *117*(13), 6561-6566.
86. Yeh, T.-F.; Cihlář, J.; Chang, C.-Y.; Cheng, C.; Teng, H. Roles of Graphene Oxide in Photocatalytic Water Splitting. *Mater. Today* **2013**, *16* (3), 78-84.
87. Eda, G.; Mattevi, C.; Yamaguchi, H.; Kim, H.; Chhowalla, M. Insulator to Semimetal Transition in Graphene Oxide. *J. Phys. Chem. C* **2009**, *113* (35), 15768-15771.
88. Xie, G.; Zhang, K.; Guo, B.; Liu, Q.; Fang, L.; Gong Jian, R. Graphene-Based Materials for Hydrogen Generation From Light-Driven Water Splitting. *Adv. Mater.* **2013**, *25* (28), 3820-3839.
89. Li, F.; Jiang, X.; Zhao, J.; Zhang, S. Graphene oxide: A promising Nanomaterial for Energy and Environmental Applications. *Nano Energy*, **2015**, *16*, 488-515.
90. Sutar, D.; Singh, G.; Botcha, V. D. Electronic Structure of Graphene Oxide and Reduced Graphene Oxide Monolayers. *Appl. Phys. Lett*. **2013**, *101*, 103103-103108.
91. Adan Mas, A.; Wei, D. Photoelectrochemical Properties of Graphene and Its Derivatives. *Nanomater*. **2013**, *3* (3), 325-356.

92. Zhao, J.; Liu, L.; Li, F. *Graphene Oxide: Physics and Applications*. Springer: New York, U.S.A, **2015**; pp 31-56
93. Iijima, S. Helical Microtubules of Graphitic Carbon. *Nat.* **1991**, *354*, 56-58.
94. Aqel, A.; El-Nour, K. M. M. A.; Ammar, R. A. A.; Al-Warthan, A. Carbon Nanotubes, Science and Technology part (I) Structure, Synthesis and Characterisation. *Arab. J. Chem.* **2012**, *5* (1), 1-23.
95. Rümmeli, M. H.; Ayala, P.; Pichler, T. Carbon Nanotubes and Related Structures: Production and Formation. In *Carbon Nanotubes and Related Structures*, Guldi, D. M.; Martín, N., Eds. **2010**; pp 1-21.
96. Chavan, R.; Desai, U.; Mhatre, P.; Chinchole, R. A Review : Carbon Nanotubes. *Int. J. Pharm.Sci. Rev. Res.* **2012**, *13*, 124-134.
97. Niu, J. J.; Wang, J. N.; Jiang, Y.; Su, L. F.; Ma, J. An Approach to Carbon Nanotubes with High Surface Area and Large Pore Volume. *Microporous Mesoporous Mater.* **2007**, *100* (1), 1-5.
98. Peigney, A.; Laurent, C.; Flahaut, E.; Bacsa, R. R.; Rousset, A. Specific Surface Area of Carbon Nanotubes and Bundles of Carbon Nanotubes. *Carbon* **2001**, *39* (4), 507-514.
99. Baik, S. H.; Lim, B. S.; Ryu, S. J.; Choi, D. H.; Kim, B. J.; Oh, S. Y.; Sung, B. H.; Choi, J. H.; Kim, C. J. Mechanical and Electrical Properties of Carbon Nanotubes in Copper-Matrix Nanocomposites. *Solid State Phenom.* **2007**, *120*, 285-288.
100. J. Bernholc; D. Brenner; M. Buongiorno Nardelli; V. Meunier; Roland, C. Mechanical and Electrical Properties of Nanotubes. *Annu. Rev. Mater. Res.* **2002**, *32* (1), 347-375.
101. Dai, L.; Chang Dong, W.; Baek, J. B.; Lu, W. Carbon Nanomaterials for Advanced Energy Conversion and Storage. *Small* **2012**, *8* (8), 1130-1166.
102. Alturaif, A. H.; Alothman, A. Z.; Shapter, G. J.; Wabaidur, M. S. Use of Carbon Nanotubes (CNTs) with Polymers in Solar Cells. *Mol.* **2014**, *19* , 17329-17344.
103. Colin Klinger; Yogeshwari Patel; Postma, H. W. C.; Xiao, J.; Wang, H.; Shao, M. Carbon Nanotube Solar Cells. *PloS ONE* **2012**, *27* (5), 37806 -73815.
104. Li, X.; Lv, Z.; Zhu, H. Carbon/Silicon Heterojunction Solar Cells: State of the Art and Prospects. *Adv. Mater.* **2015**, *27* (42), 6549-6574.
105. Xu, Y.; Kraft, M.; Xu, R. Metal-Free Carbonaceous Electrocatalysts and Photocatalysts for Water Splitting. *Chem. Soc. Rev.* **2016**, *45* (11), 3039-3052.
106. Georgakilas, V.; Tiwari, J. N.; Kemp, K. C.; Perman, J. A.; Bourlinos, A. B.; Kim, K. S.; Zboril, R. Noncovalent Functionalization of Graphene and Graphene Oxide for Energy Materials, Biosensing, Catalytic, and Biomedical Applications. *Chem. Rev.* **2016**, *116* (9), 5464-5519.

107. Wang, Q.; Wang, X.; Chai, Z.; Hu, W. Low-Temperature Plasma Synthesis of Carbon Nanotubes and Graphene Based Materials and Their Fuel Cell Applications. *Chem. Soc. Rev.* **2013**, *42* (23), 8821-8834.
108. Benipal, N.; Qi, J.; Liu, Q.; Li, W. Carbon Nanotube Supported PdAg Nanoparticles for Electrocatalytic Oxidation of Glycerol in Anion Exchange Membrane Fuel Cells. *Appl. Catal. B: Environ.* 20**17**, *210*, 121-130
109. Abdulla, S.; Mathew, T. L.; Pullithadathil, B. Highly Sensitive, Room Temperature Gas Sensor Based on Polyaniline-Multiwalled Carbon Nanotubes (PANI/MWCNTs) Nanocomposite for Trace-Level Ammonia Detection. *Sens. Actuators B: Chem.* **2015**, *221*, 1523-1534.
110. Hwa, K.-Y.; Subramani, B. Synthesis of Zinc oxide Nanoparticles on Graphene–Carbon Nanotube Hybrid for Glucose Biosensor Applications. *Biosens. Bioelectron.* **2014**, *62*, 127-133.
111. Rupasinghe, C.; Rukhlenko, I. D.; Premaratne, M. Spaser Made of Graphene and Carbon Nanotubes. *ACS Nano* **2014**, *8* (3), 2431-2438.
112. Wang Julie, T. W.; Cabana, L.; Bourgognon, M.; Kafa, H.; Protti, A.; Venner, K.; Shah Ajay, M.; Sosabowski Jane, K.; Mather Stephen, J.; Roig, A.; Ke, X.; Van Tendeloo, G.; de Rosales Rafael, T. M.; Tobias, G.; Al-Jamal Khuloud, T. Magnetically Decorated Multiwalled Carbon Nanotubes as Dual MRI and SPECT Contrast Agents. *Adv. Funct. Mater.* **2013**, *24* (13), 1880-1894.
113. Khan, Z. H.; Husain, M. Carbon Nanotubes and its Possible Applications. *Ind. J. Eng. Mater. Sci.* **2005**, *12*, 529-551.
114. Lei, X.; Natsuki, T.; Shi, J.; Ni, Q.-Q. Analysis of Carbon Nanotubes on The Mechanical Properties at Atomic Scale. *J. Nanomater.* **2011**, *2011*, 805313 (1-10).
115. Zaporotskova, I. V.; Boroznina, N. P.; Parkhomenko, Y. N.; Kozhitov, L. V. Carbon Nanotubes: Sensor Properties. A Review. *Mod. Electron. Mater.* **2016**, *2* (4), 95-105.
116. Karousis, N.; Tagmatarchis, N.; Tasis, D. Current Progress on the Chemical Modification of Carbon Nanotubes. *Chem. Rev.* **2010**, *110* (9), 5366-5397.
117. Wang, Z.; Jia, R.; Zheng, J.; Zhao, J.; Li, L.; Song, J.; Zhu, Z. Nitrogen-Promoted Self-Assembly of N-Doped Carbon Nanotubes and Their Intrinsic Catalysis for Oxygen Reduction in Fuel Cells. *ACS Nano* **2011**, *5* (3), 1677-1684.
118. Li, L.; Yang, H.; Miao, J.; Zhang, L.; Wang, H.-Y.; Zeng, Z.; Huang, W.; Dong, X.; Liu, B. Unraveling Oxygen Evolution Reaction on Carbon-Based Electrocatalysts: Effect of Oxygen Doping on Adsorption of Oxygenated Intermediates. *ACS Energy Lett.* **2017**, *2* (2), 294-300.
119. Pal, S.; Sahoo, M.; Veettil, V. T.; Tadi, K. K.; Ghosh, A.; Satyam, P.; Biroju, R. K.; Ajayan, P. M.; Nayak, S. K.; Narayanan, T. N. Covalently Connected Carbon

Nanotubes as Electrocatalysts for Hydrogen Evolution Reaction Through Band Engineering. *ACS Catal.* **2017**, *7* (4), 2676-2684.

120. Murakami, N.; Tango, Y.; Miyake, H.; Tajima, T.; Nishina, Y.; Kurashige, W.; Negishi, Y.; Takaguchi, Y. SWCNT Photocatalyst for Hydrogen Production From Water upon Photoexcitation of (8,3) SWCNT at 680-nm Light. *Sci. Rep.* **2017**, *7*, 43445 (1-7).
121. Gong, M.; Li, Y.; Wang, H.; Liang, Y.; Wu, J. Z.; Zhou, J.; Wang, J.; Regier, T.; Wei, F.; Dai, H. An Advanced Ni–Fe Layered Double Hydroxide Electrocatalyst for Water Oxidation. *J. Am. Chem. Soc.* **2013**, *135* (23), 8452-8455.
122. Zhang, X.; Zhang, X.; Xu, H.; Wu, Z.; Wang, H.; Liang, Y. Iron-Doped Cobalt Monophosphide Nanosheet/Carbon Nanotube Hybrids as Active and Stable Electrocatalysts for Water Splitting. *Adv. Funct. Mater.* **2017**, *27*, 1606635 (1-12).
123. Qu, K.; Zheng, Y.; Jiao, Y.; Zhang, X.; Dai, S.; Qiao, S. Z. Polydopamine-Inspired, Dual Heteroatom-Doped Carbon Nanotubes for Highly Efficient Overall Water Splitting. *Adv. Energy Mater.* **2016**, *7* (9), 1602068 (1-8).
124. Pi, Y.; Shao, Q.; Wang, P.; Lv, F.; Guo, S.; Guo, J.; Huang, X. Trimetallic Oxyhydroxide Coralloids for Efficient Oxygen Evolution Electrocatalysis. *Angew. Chem. Int. Ed.* **2017**, *56* (16), 4502-4506.
125. Yu, J.; Zhou, W.; Xiong, T.; Wang, A.; Chen, S.; Chu, B. Enhanced Electrocatalytic Activity of Co@N-doped Carbon Nanotubes by Ultrasmall Defect-Rich TiO_2 Nanoparticles for Hydrogen Evolution Reaction. *Nano Res.* **2017**, *10* (8), 2599-2609.
126. Cheng, H.; Su, C.-Y.; Tan, Z.-Y.; Tai, S.-Z.; Liu, Z.-Q. Interacting $ZnCo_2O_4$ and Au Nanodots on Carbon Nanotubes as Highly Efficient Water Oxidation Electrocatalyst. *J. Power Sources* **2017**, *357*, 1-10.
127. Liang, Y.; Li, Y.; Wang, H.; Dai, H. Strongly Coupled Inorganic/Nanocarbon Hybrid Materials for Advanced Electrocatalysis. *J. Am. Chem. Soc.* **2013**, *135* (6), 2013-2036.
128. Chaudhary, D.; Singh, S.; Vankar, V. D.; Khare, N. A Ternary Ag/TiO_2/CNT Photoanode for Efficient Photoelectrochemical Water Splitting Under Visible Light Irradiation. *Int. J. Hydrogen Energy* **2017**, *42* (12), 7826-7835.
129. Yousefzadeh, S.; Reyhani, A.; Naseri, N.; Moshfegh, A. Z. MWCNT/WO_3 Nanocomposite Photoanode for Visible Light Induced Water Splitting. *J. Solid State Chem.* **2013**, *204*, 341-347.
130. Ng, B.-J.; Putri, L. K.; Tan, L.-L.; Pasbakhsh, P.; Chai, S.-P. All-Solid-State Z-Scheme Photocatalyst with Carbon Nanotubes as an Electron Mediator for Hydrogen Evolution Under Simulated Solar Light. *Chem. Eng. J.* **2017**, *316*, 41-49.
131. Deng, X.; Tüysüz, H. Cobalt-Oxide-Based Materials as Water Oxidation Catalyst: Recent Progress and Challenges. *ACS Catal.* **2014**, *4* (10), 3701-3714.

132. Esswein, A. J.; McMurdo, M. J.; Ross, P. N.; Bell, A. T.; Tilley, T. D. Size-Dependent Activity of Co_3O_4 Nanoparticle Anodes for Alkaline Water Electrolysis. *J.Phys. Chem. C* **2009**, *113* (33), 15068-15072.

133. Chou Nam, H.; Ross Philip, N.; Bell Alexis, T.; Tilley, T. D. Comparison of Cobalt-based Nanoparticles as Electrocatalysts for Water Oxidation. *ChemSusChem* **2011**, *4* (11), 1566-1569.

134. Qing, Q.; Zhang, J.-H.; Wang, J.; Li, Q.-Y.; Xu, C.-W.; Lu, X. Three-Dimensional Ordered Mesoporous Co_3O_4 Enhanced by Pd for Oxygen Evolution Reaction. *Sci. Rep.* **2017**, 7, 41542 (1-9).

135. Liang, Y.; Li, Y.; Wang, H.; Zhou, J.; Wang, J.; Regier, T.; Dai, H. Co_3O_4 Nanocrystals on Graphene as a Synergistic Catalyst for Oxygen Reduction Reaction. *Nat. Mater.* **2011**, *10*, 780-786.

136. Suryanto, B. H. R.; Lu, X.; Zhao, C. Layer-by-layer Assembly of Transparent Amorphous Co_3O_4 Nanoparticles/Graphene Composite Electrodes for Sustained Oxygen Evolution Reaction. *J. Mater. Chem. A* **2013**, *1* (41), 12726-12731.

137. Wu, J.; Xue, Y.; Yan, X.; Yan, W.; Cheng, Q.; Xie, Y. Co_3O_4 Nanocrystals on Single-Walled Carbon Nanotubes as a Highly Efficient Oxygen-Evolving Catalyst. *Nano Res.* **2012**, *5* (8), 521-530.

138. Zhao, Y.; Chen, S.; Sun, B.; Su, D.; Huang, X.; Liu, H.; Yan, Y.; Sun, K.; Wang, G. Graphene-Co_3O_4 Nanocomposite as Electrocatalyst with High Performance for Oxygen Evolution Reaction. *Sci. Rep.* **2015**, *5*, 6729 (1-7).

139. Islam, M. M.; Faisal, S.; Akhter, T.; Roy, A. K.; Minett, A.; Konstantinov, K.; Xue Dou, S. Liquid-Crystal-Mediated 3D Macrostructured Composite of Co/Co_3O_4 Embedded in Graphene: Free-Standing Electrode for Efficient Water Splitting. *part. part. syst. character.* **2017**, 34, 1600386 (1-6).

140. Wei, P.; Hu, B.; Zhou, L.; Su, T.; Na, Y. New Strategy to Incorporate Nano-Particle Sized Water Oxidation Catalyst into Dye-Sensitized Photoelectrochemical Cell for Water Splitting. *J. Energy Chem.* **2016**, *25* (3), 345-348.

141. Chua, C. S.; Ansovini, D.; Lee, C. J. J.; Teng, Y. T.; Ong, L. T.; Chi, D.; Hor, T. S. A.; Raja, R.; Lim, Y.-F. The Effect of Crystallinity on Photocatalytic Performance of Co_3O_4 Water-Splitting Cocatalysts. *Phys. Chem. Chem. Phys.* **2016**, *18* (7), 5172-5178.

142. Bhavana, G.; Ambrose, A. M.; Tom, M.; Dash, S.; Tyagi, A. K. Facile Gamma Radiolytic Synthesis of Synergistic Co_3O_4-rGO Nanocomposite: Direct Use in Photocatalytic Water Splitting. *Mater. Res. Express* **2014**, *1*, 1-12.

143. Chang, X.; Wang, T.; Zhang, P.; Zhang, J.; Li, A.; Gong, J. Enhanced Surface Reaction Kinetics and Charge Separation of p–n Heterojunction $Co_3O_4/BiVO_4$ Photoanodes. *J. Am. Chem. Soc.* **2015**, *137* (26), 8356-8359.
144. Liu, G.; Karuturi Siva, K.; Simonov Alexandr, N.; Fekete, M.; Chen, H.; Nasiri, N.; Le Nhien, H.; Reddy Narangari, P.; Lysevych, M.; Gengenbach Thomas, R.; Lowe, A.; Tan Hark, H.; Jagadish, C.; Spiccia, L.; Tricoli, A. Robust Sub-Monolayers of Co3O4 Nano-Islands: A Highly Transparent Morphology for Efficient Water Oxidation Catalysis. *Adv. Energy Mater.* **2016**, *6* (15), 1-9.
145. Zhang, R.; Wei, H.; Si, W.; Ou, G.; Zhao, C.; Song, M.; Zhang, C.; Wu, H. Enhanced Electrocatalytic Activity for Water Splitting on NiO/Ni/Carbon Fiber Paper. *Mater.Commun.* **2017**, *10* (1). 2-8
146. Gong, M.; Wang, D.-Y.; Chen, C.-C.; Hwang, B.-J.; Dai, H. A Mini Review on Nickel-Based Electrocatalysts for Alkaline Hydrogen Evolution Reaction. *Nano Res.* **2016**, *9* (1), 28-46.
147. Xu, Y.; Tu, W.; Zhang, B.; Yin, S.; Huang, Y.; Kraft, M.; Xu, R. Nickel Nanoparticles Encapsulated in Few-Layer Nitrogen-Doped Graphene Derived From Metal–Organic Frameworks as Efficient Bifunctional Electrocatalysts for Overall Water Splitting. *Adv. Mater.* **2017**, *29* (11), 1-8.
148. Ai, L.; Tian, T.; Jiang, J. Ultrathin Graphene Layers Encapsulating Nickel Nanoparticles Derived Metal–Organic Frameworks for Highly Efficient Electrocatalytic Hydrogen and Oxygen Evolution Reactions. *ACS Sust. Chem. Eng.* **2017**, *5* (6), 4771-4777.
149. Li, X.; Wang, H.; Chu, T.; Li, D.; Mao, L. Synthesis and Peferentially Loading of Nickel Nanoparticle on CdS Surface and its Photocatalytic Performance for Hydrogen Evolution under Visible Light. *Mater. Res. Bull.* **2014**, *57*, 254-259.
150. Wang, H.; Chen, W.; Zhang, J.; Huang, C.; Mao, L. Nickel Nanoparticles Modified CdS – A Potential Photocatalyst for Hydrogen Production Through Water Splitting under Visible Light Irradiation. *Int. J. Hydrogen Energy* **2015**, *40* (1), 340-345.
151. Cheng, Z.; Wang, F.; Shifa, T. A.; Liu, K. Carbon Dots Decorated Vertical SnS_2 Nanosheets for Efficient Photocatalytic Oxygen Evolution. *Appl. Phys. Lett.* **2016**, *109* (5), 53905 -53909.
152. Virca, C. N.; Winter, H. M.; Goforth, A. M.; Mackiewicz, M. R.; McCormick, T. M. Photocatalytic Water Reduction Using a Polymer Coated Carbon Quantum Dot Sensitizer and a Nickel Nanoparticle Catalyst. *Nanotechnol.* **2017**, *28* (19), 195402 (1-9).
153. Kanan, M. W.; Yano, J.; Surendranath, Y.; Dincă, M.; Yachandra, V. K.; Nocera, D. G. Structure and Valency of a Cobalt−Phosphate Water Oxidation Catalyst

Determined by in Situ X-ray Spectroscopy. *J. Am. Chem. Soc.* **2010**, *132* (39), 13692-13701.

Chapter 2

Experimental

2.1 Materials

Chemicals and reagents used in this study are listed below:

Reagent Name	Grade/Batch/ Size	Supplier (Company)
Fluorine-doped tin oxide (FTO) slides	100 mm x 100 mm x 1.6 mm	Zhuhai Kaivo Electronic Components Co
Glass microscope slides		AkzoNobel
Iron(III) p-toluenesulfonate (Fe(III)-pTS)		Sigma-Aldrich
3,4-ethylenedioxythiophene (EDOT)		Sigma-Aldrich
Graphite flakes (3772)		Asbury Graphite Mills USA
Ni nanoparticles (20 nm)		Skyspring Nanomaterials
Multi-walled carbon nanotube (CNT)		Chengdu Organic Chemicals Co. Ltd
Co_3O_4 nanoparticles	25 nm	Skyspring Nanomaterials
Pyrrole (py)		Sigma Aldrich
Ethanol		Chem-Supply Pty Ltd
Acetone		Chem-Supply Pty Ltd
KOH (90% flakes)	Reagent grade	Sigma-Aldrich
HCl 36% (w/v) solution in water	Analytical grade	Univar
Sodium Sulfate (Na_2SO_4) anhydrous		Sigma-Aldrich
Sulfuric acid, 98 % conc. and 0.05 M		VS Chem House
Potassium chloride (KCl)		Sigma-Aldrich
Epoxy Glue Araldite	Part a) 100 ml epoxy resin liquid Part b) 80 ml alphatic amines	Selleys Dulux Group Pty Ltd
Copper (Cu) wires		
Hydrogen peroxide (H_2O_2), 30% (w/v)		Sigma-Aldrich
Potassium permanganate ($KMnO_4$)		Sigma-Aldrich

Table 2.1: *The chemicals and reagents used in this study*

2.2 Characterization Techniques and Materials

2.2.1 Characterization Techniques

Physical characterization and testing included a variety of techniques were utilized, including measuring thickness, conductivity, UV-Visible Spectroscopy, X-ray powder diffraction (XRD), X-Ray Photoelectron spectroscopy (XPS), Transmission electron microscopy (TEM), Scanning electron microscopy (SEM) and Energy dispersive X-Ray spectroscopy (EDX), Transmission electron microscopy (TEM), sputter coating, UV Centrifugation, pH measurement, Gas Chromatography, and Elemental analysis.

2.2.1.1 Thickness and Conductivity of Films

Thickness measurements were made using a Vccco Dektak 150 profilometer (Figure 2.1 and inset). In order to determine the film's thickness, a small line of the film (deposited on normal glass) was removed gently and completely with a thin wood stick to form a valley shape on the glass surface (see Figure 2.1(b) inset)). The software parameters of the profilometer program were set (Figure 2.1(c) inset)). Figure 2.1(d) inset depicts the data recorded *via* the tip of profilometer scan while Figure 2.1(e) refers to the data of film surface region and the zig- zag shape in it attributed to the film's surface. Figure 2.1(f) shows the glass surface region without film materials because it was removed via the wood stick. The difference between (e) and (f) represents the film's thickness. The film's thickness was scanned four times, and the average of these readings taken as film's thickness.

The film resistance was measured with a JANDEL RM3 four point probe (Jandel Engineering Ltd, UK) (Figure 2.2(a)). The principle of the four point probe is illustrated in Figure 2.2(b): the outer pair of point probes supply a current while the two inner pair measure the voltage. The electrical resistivity ρ can be calculated with the formula:

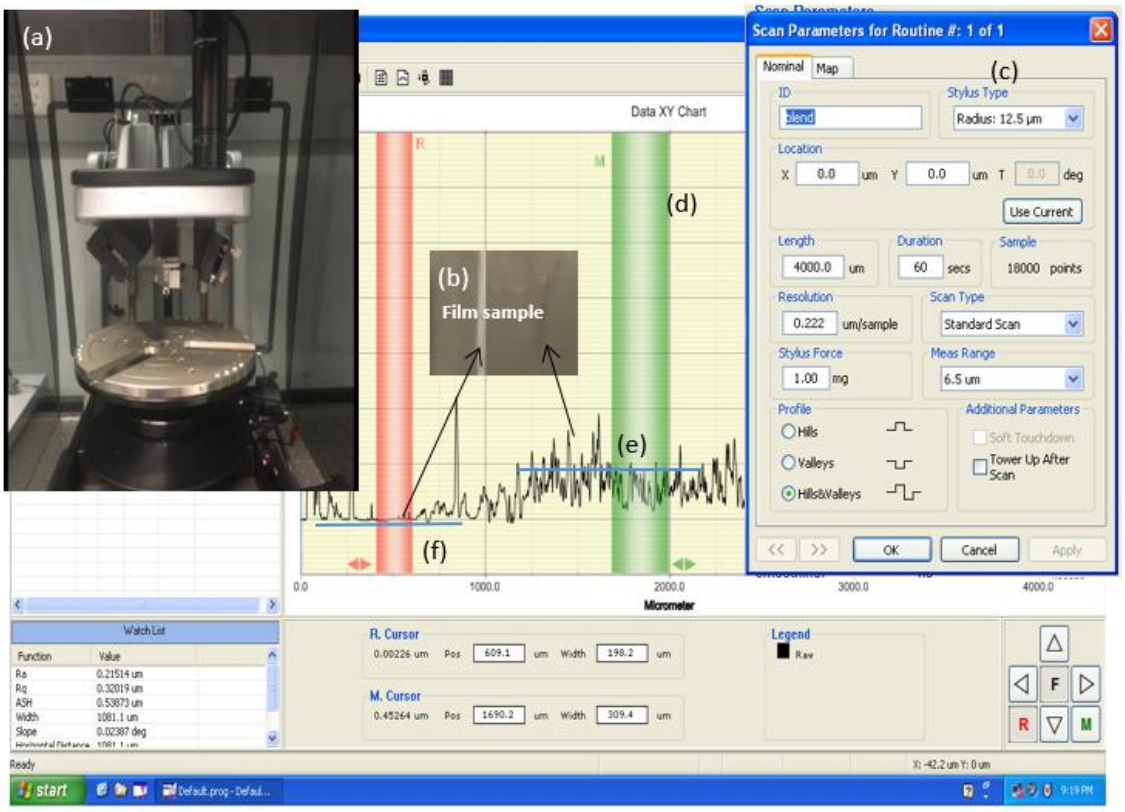

Figure 2.1: *(a) Vccco Dektak 150 profilometer, (b) Sample surface on glass that has line removed from the film material (film has valley shape), (c) Software parameters of the profilometer's program, (d) Data recorded via the profilometer's tip, (e) Surface thickness with film and (f) Surface thickness without film material (control reference).*

$$\rho = K\left(\frac{V}{I}\right) * t \qquad \ldots (2.1)$$

where K is a geometric factor equal to 4.5324 while V is the electric potential across the two inner probes, I is the applied current, and t is the sheet thickness. The electrical conductivity (S/cm) of the films samples was calculated using the equation $\sigma = 1/\rho$. Both FWD and REV measurements of the film's resistivity were made. FWD refers to the forward direction of current input (in relation to the voltage reading probes) while REV refers to the reverse direction of the current. If FWD and REV resistivity readings were similar, this means the resistance of the film is more stable.[1]

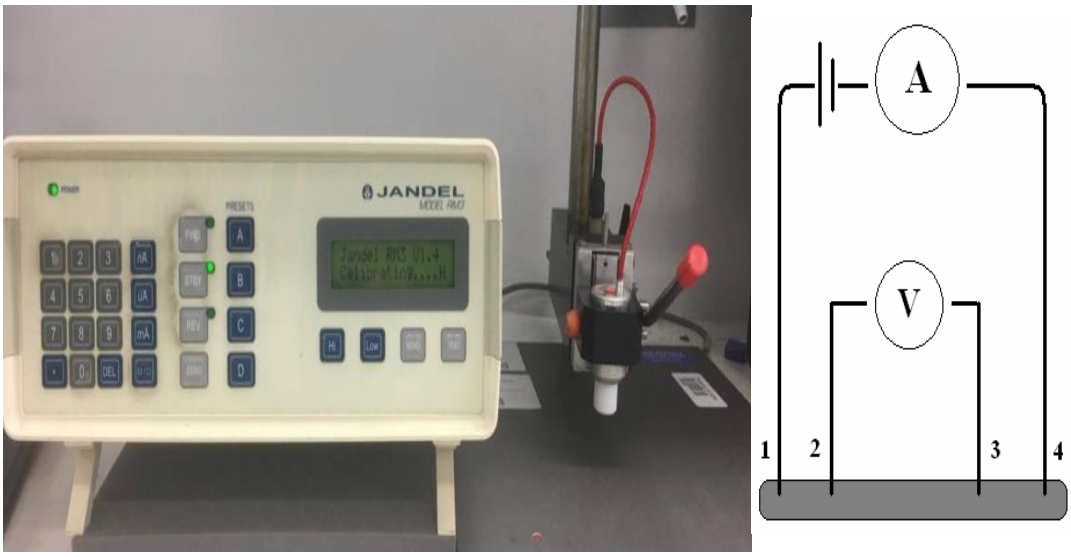

Figure 2.2: *(a) JANDEL RM3 four point probe, (b) diagram illustrating four probe operation.*

2.2.1.2 UV-Visible Spectroscopy

Films were deposited on a glass slide (not FTO glass films) and their UV-Visible spectra recorded with a UV-1800 SHIMADZU[2] in range 400 nm-800 nm (Figure 2.3).

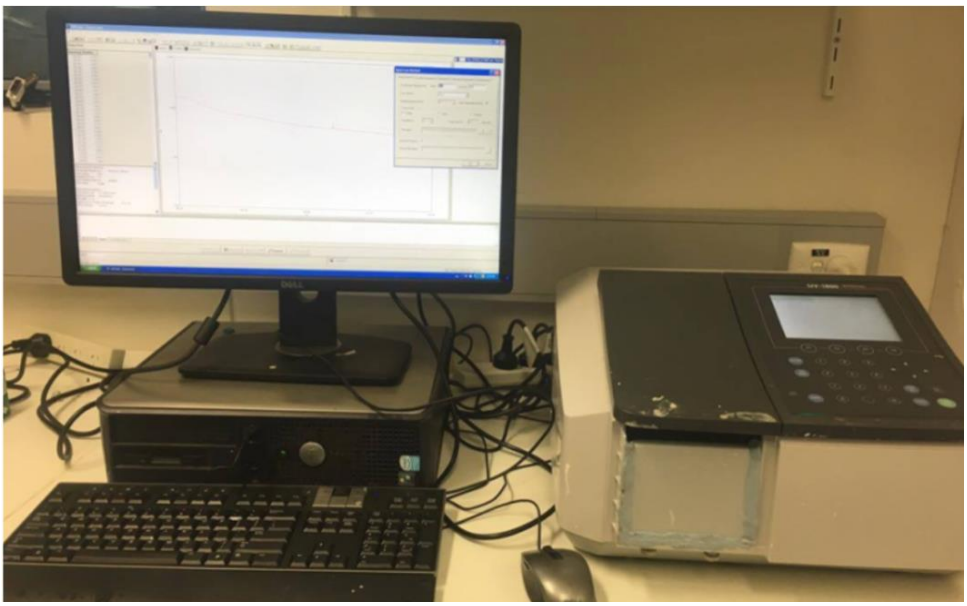

Figure 2.3: *UV-Visible spectroscopy UV-1800 SHIMADZU*

2.2.1.3 X-ray Powder Diffraction (XRD)

X-ray powder diffraction (XRD) is a qualitative technique which can be used to identify the phase type of a crystalline material. Briefly, when the surface of the material is exposed to monochromatic X-ray beam, the incident light will be diffracted by the electron clouds that sit around the atoms causing portion of the incident beam light to scatter/diffract.[2] The diffraction beam undergoes constructive and destructive interfaces. However, the constructive interfaces occurred when conditions satisfy Bragg's Law ($n\lambda=2d \sin \theta$). The diffraction direction beam depends on the size and shape of the unit cell of material, while the intensity of the diffracted beam depends on both the type and atom arrangement in the crystal structure. The direction of the beam angle is 2θ compared to incident beam angle that has only θ as can be seen see Figure 2.4(a). XRD is considered to offer a fast analytical technique used to determine the phase identification of a crystalline material and provide information on unit cell dimensins.[3] XRD was carried using (if needed) using a GBC Mini-Materials Analyzer (MMA) X-ray powder diffraction (XRD) (λ=1.54 Å). The supplied voltage and current kept at -40 kV and 25 mA respectively.

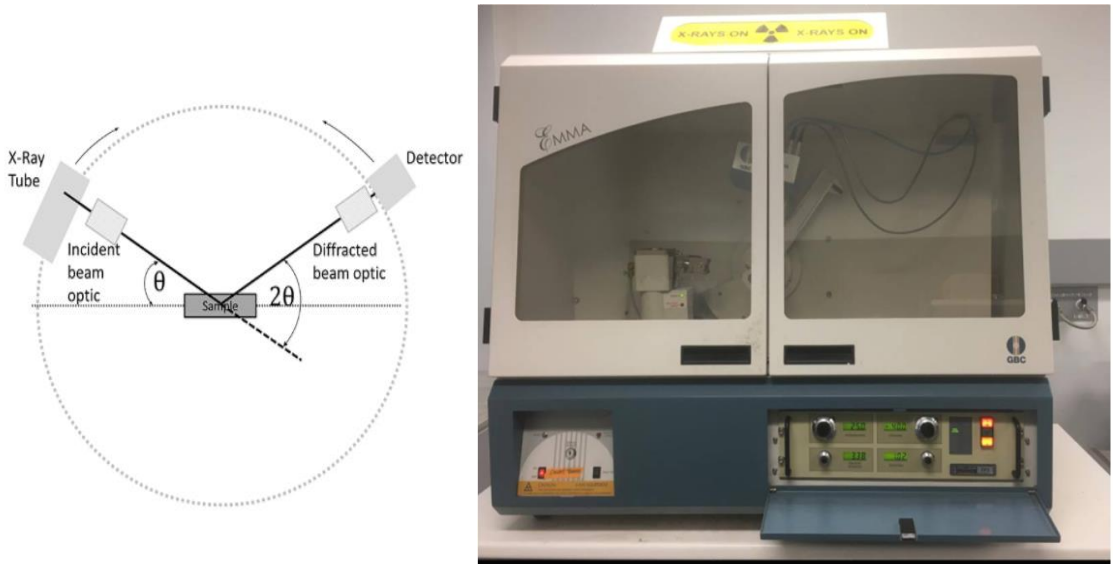

Figure 2.4: (a) *Scheme illustrating x-Ray diffraction, (b) X-ray diffraction machine type GBC MMA XRD (λ=1.54* Å*).*

2.2.1.4 X-Ray Photoelectron Spectroscopy (XPS)

XPS is a quantitative spectroscopic technique. The spectrum is collected via irradiation of the sample with an X-Ray beam (see Figure 2.5(a)). The energy emitted by the electrons describes their nature. XPS experiments carried out on PHI660 using a monochromatic Mg K_α X-ray as a beam source.[3]

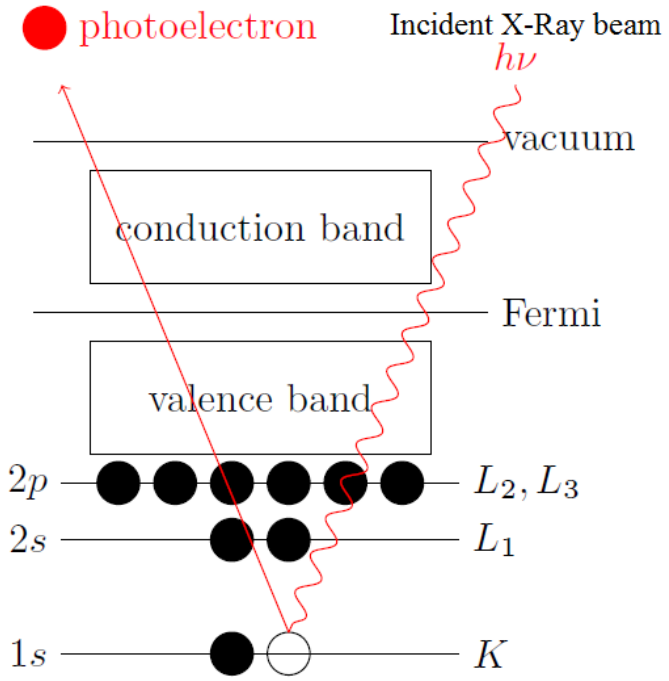

Figure 2.5: *Schematic showing the operation of XPS.*

2.2.1.5 Scanning Electron Microscopy (SEM) and Energy Dispersive X-Ray Spectroscopy (EDX).

A Jeol 7500 field emission scanning electron microscope [4-5] was utilized to study the surface morphology of film samples (Figure 2.6). SEM settings included: accelerating voltage of 5 kV; emission current of 10 µA; probe current of 8 mA and working distance of 8 mm. In addition, the sample were coated with 7 nm Pt via sputter coating to increase SEM signals.[6]

For EDX setting were changed to an accelerating voltage of 15 kV; emission current of 20 µA; probe current of 14 mA and working distance of 10 mm.

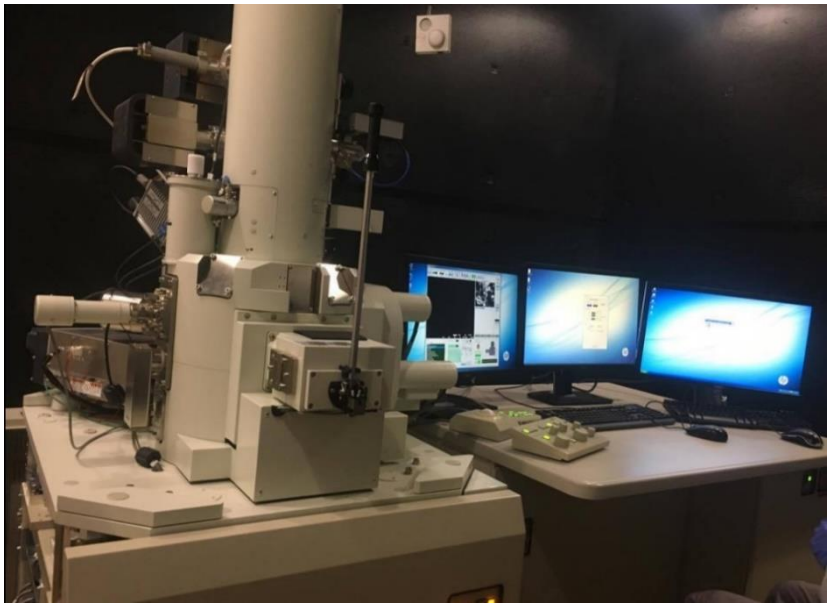

Figure 2.6: *Jeol 7500 field emission scanned electron microscope utilized in the study.*

2.2.1.6 Transmission Electron Microscopy (TEM)

In TEM technique, the sample has to be ultrathin (less than 100 nm thick) or a suspension on a grid. When the beam of electrons passes through the sample surface, the electrons will interact with the sample resulting in signals that form TEM images. These images can be magnified and focused onto an imaging device with higher resolution than light microscopy, obtaining fine details about the material even if as small as a single column of atoms. Typically, the sample's powder was collected from the glass substrate to gain a reasonable amount of the sample, with the sample then sonicated with 3 ml of ethanol. A drop of that suspension was dropcast on a TEM grid and imaged. TEM model JEOL JEM-2010 was used.[7]

Figure 2.7: *TEM model JEOL JEM-2010 used.*

2.2.1.7 Sputter-Coating

Platinum (Pt) sputter coating was performed with an EDWARDS FTM6 Auto 306 (Figure 2.7).

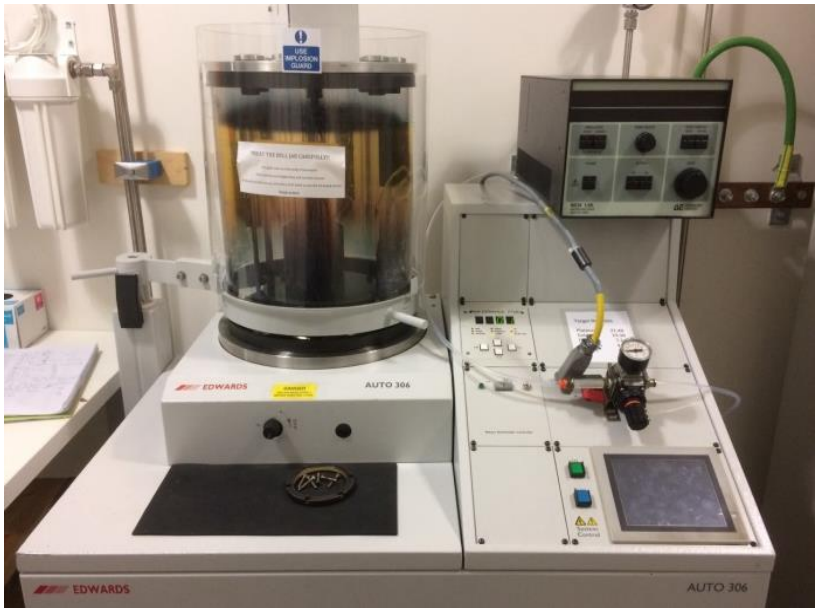

Figure 2.8: *EDWARDS FTM6 Auto 306 sputter coater.*

2.2.1. 8 UV Ozone and Plasma Cleaners

During preparation of fabricated electrodes, all FTO substrates underwent ozone cleaning for 20 min using PSD Pro SERIES Digital UV Ozone System.[8] A PDC plasma cleaner was used for plasma cleaning.

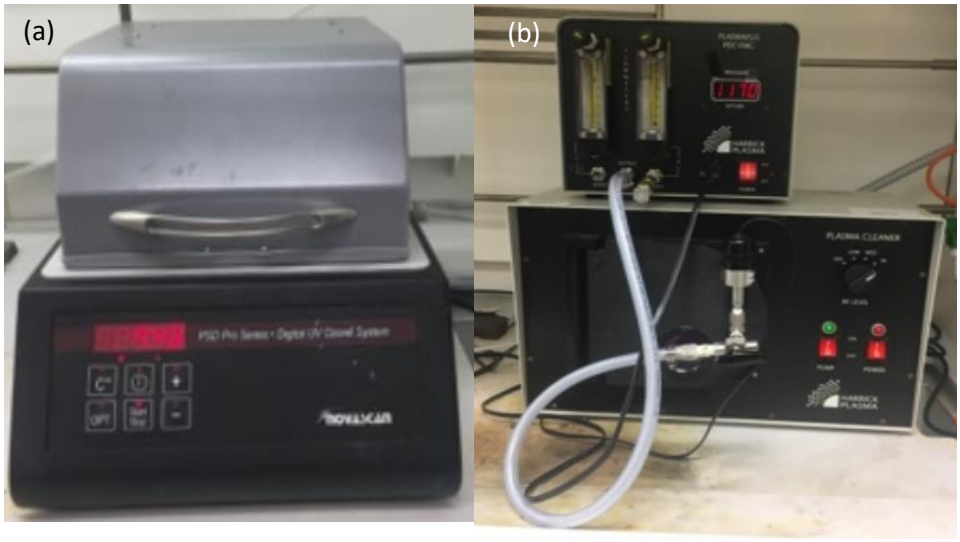

Figure 2.9: *(a) PSD Pro SERIES Digital UV Ozone System; (b) PDC plasma cleaner.*

2.2.1.9 Sonication

Sonication was carried out using a B2500R-MTH sonicator.

Figure 2.10: *B2500R-MTH sonicator.*

2.2.1.10 Centrifugation

Centrifugation was used in preparing graphene oxide with an Eppendorf centrifuge 5702 (Figure 2.11).

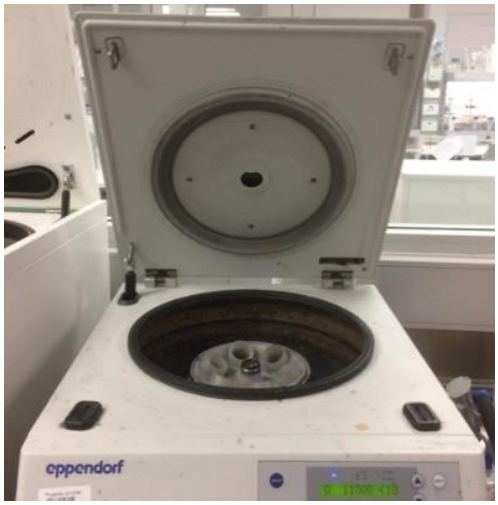

Figure 2.11: *Eppendorf 5702 centrifuge used in this study.*

2.2.1.11 pH Measurements

A pH meter was used measure the concentration of H^+ in water-based solutions. A variety of buffer solutions for both acidic and alkaline media provided via Ajax Pty Ltd were used to calibrate pH meter.

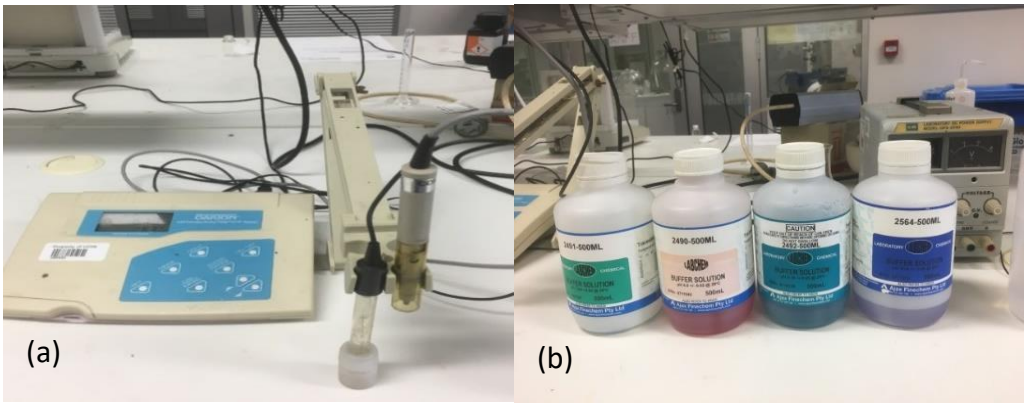

Figure 2.12: *(a) OAKTON pH/Conductivity/TDS/°C/°F meter, (b) variety of buffer solutions for both acidic and alkaline media provided by Ajax Pty Ltd.*

2.2.1.12 Photoelectrochemical Cell and Light Source

A fully-enclosed quartz cell (5 x 5 x 5 cm) was placed inside a closed cabinet that comprised a Faraday cage. A Pt mesh (1 x 2 cm) was used as the counter electrode (CE). A BASi Ag/AgCl aqueous salt bridge (KCl, 3 M) served as reference electrode (RE) while the prepared sample coated on FTO, were used as working electrode (WE). For an OER system, 0.2 M Na_2SO_4 aqueous solution was used, adjusted to pH as required by adding NaOH. The electrolyte for HER was 0.2 M Na_2SO_4 aqueous solution adjusted to pH by adding dilute 0.05 M H_2SO_4. In some experiments, a 0.05 M H_2SO_4 was used as an electrolyte (without Na_2SO_4 solution). The electrolyte was bubbled with N_2 gas for 30 min before each experiment and maintained under an N_2 atmosphere during the experiments. In experimental work, the photoelectrochemical cell was tested with linear sweep voltammetry (LSV), cyclic voltammetry (CV), chronoamperograms and EIS. The testing was carried out with and without light illumination from a SoLux daylight MR16 halogen light bulb (ca. 0.25 sun intensity). A Thorlabs visible-light bandpass filter (315-710 nm) was placed 1.5 cm in front of the light source. The bandpass filter removed any heat (infra-red wavelengths) generated by the light source (see Figure 2.13).

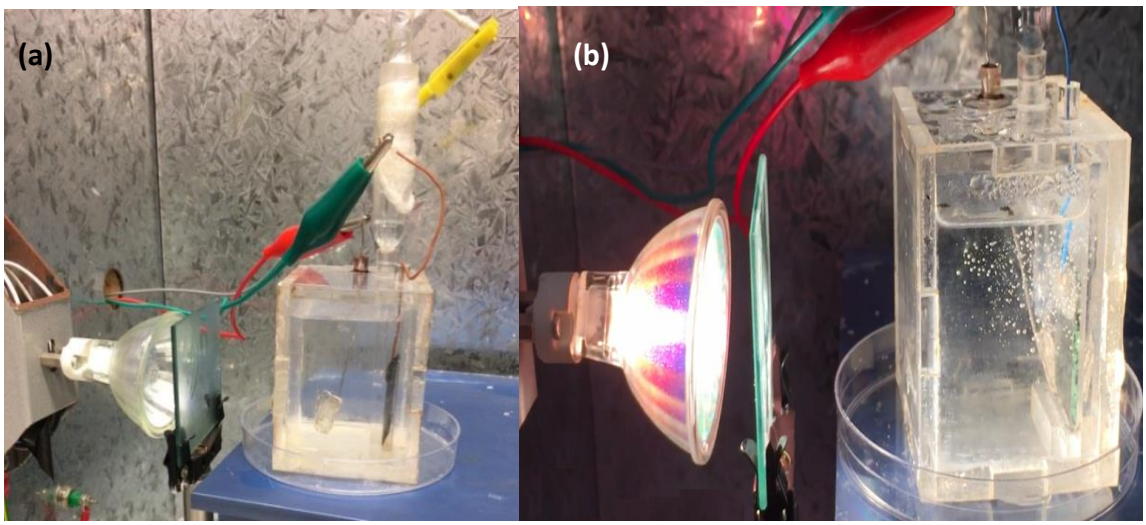

Figure 2.13: *Setup of photoelectrochemical cell (a) before running the experiment and (b) while running experiment when the light was switched on.*

2.2.1.13 Gas Chromatography

High performing samples on FTO glass were subjected to photocurrent testing with simultaneous gas analysis, using a custom-built apparatus. The apparatus, which is depicted in Figure 2.14, comprised of a fully-enclosed electrochemical cell containing two sealed, half-cells whose electrolytes were separated only by a Nafion 117 proton exchange membrane (5 x 4 cm). The one half cell contained the working electrode sample and the Ag/AgCl reference electrode. The other half-cell contained the Pt mesh counter electrode. One wall of the former half-cell was a quartz sheet. Illuminating light was passed through the above visible-light bandpass filter then through the quartz sheet wall onto the working electrode (Figure 2.14(l)).

The electrodes were connected to a CHI potentiostat. The gas outlets for the working and counter electrode half -cells were connected with gas-tight polymer and stainless steel tubing to sample loops connected to a dedicated Shimadzu GC-8A gas chromatograph (Figure 2.14).

After fitting the electrodes, both half cells were filled with electrolyte. The electrolyte in each half-cell was then separately purged with Ar gas overnight to remove all air inside the cell (without a voltage or light-illumination being applied to the cell). Thereafter, the Ar passing through each half cell was sampled, injected and analysed using the attached gas chromatograph, with the results plotted over 30 min of elution time.

The analyses verified that there was no gas other than Ar detected in the gas streams passing through each half-cell. The Ar gas, which was continuously bubbled through the electrolyte throughout the photocurrent experiment, acted as a carrier gas for the connected GC.

In the case of OER tests, a voltage bias of 0.8 V (vs. Ag/AgCl) was applied and, in case of HER tests a voltage bias of -0.75 V (vs. Ag/AgCl) was applied, with and without light-illumination to the cell, whereafter the carrier gas was tested as described above, for electrocatalysis product gases using the GC. The identities of the gases in the carrier Ar were determined by their retention times. Their relative proportions were determined by integrating

the area under their respective peaks. GC testing of this type, after illumination and biasing, provided a well-founded estimate of the proportions of gases produced by the films. The GC was equipped with a 6-foot Molecular Sieve 5 Å column connected with a thermal conductivity detector (TCD). The column was kept at 90°C while the detector was at 100°C.

2.2.1.14 Elemental Analysis

Elemental analysis of films was determined by the Campbell Microanalytical laboratory at the University of Otago, New Zealand. We collected the required amount of the optimized film, then it was sent to Microanalytical laboratory to determine % (w/w) of film's elemental contents.

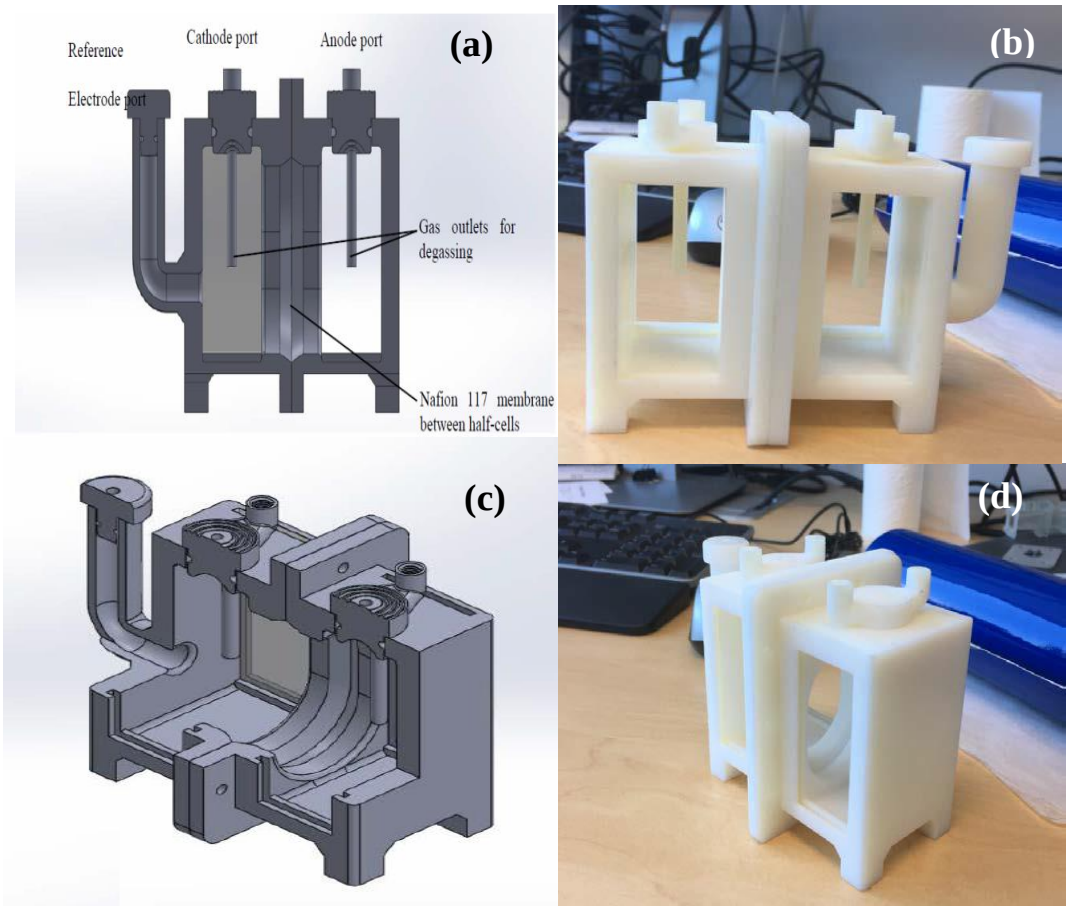

Figure 2.14 (Initial): (a) and (c) *Computer-drawn image of the GC Cell. (b), (d), Photographs of the GC Cell prior to fitting the quartz windows. Figure continued overleaf*

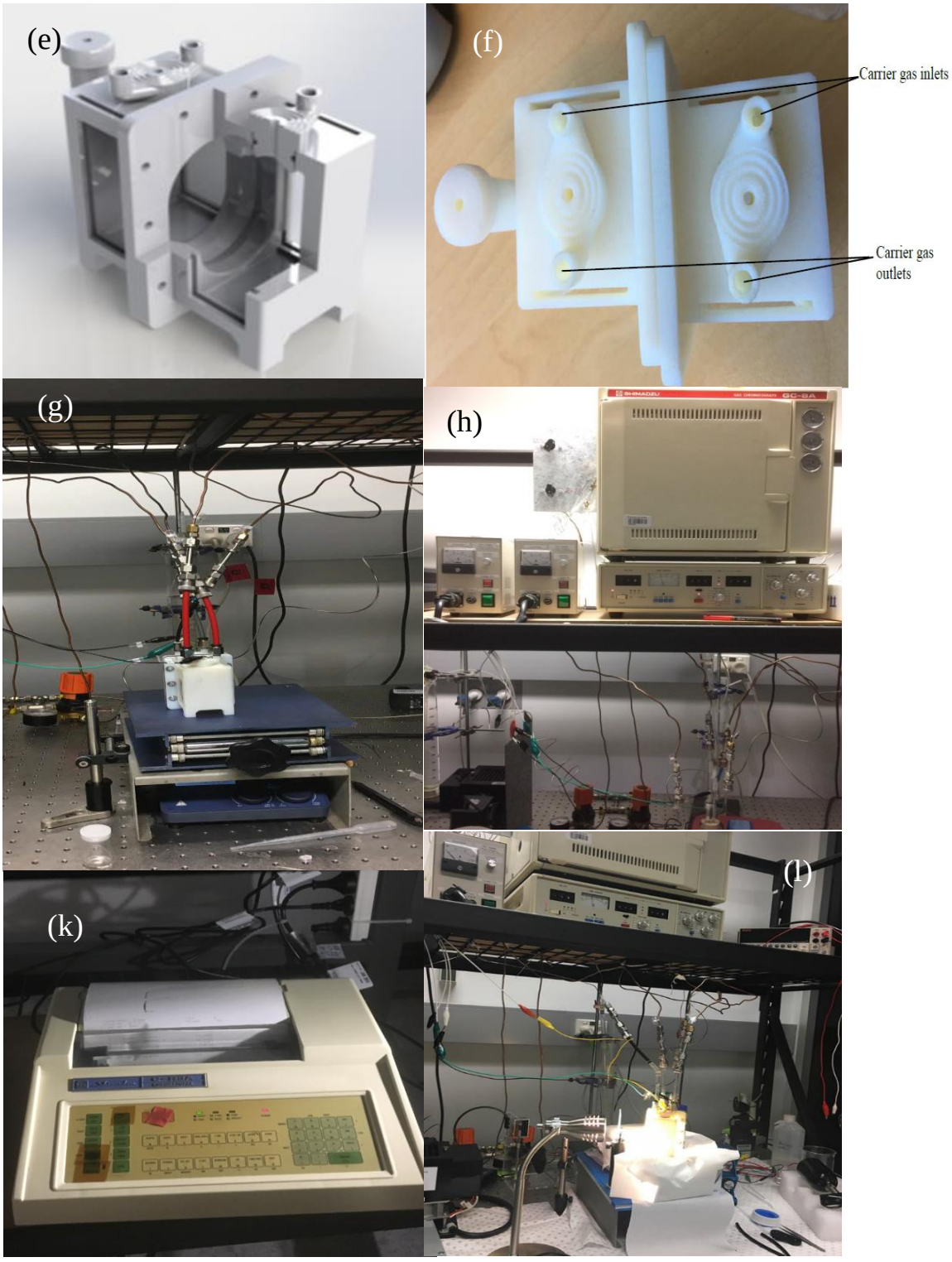

Figure 2.14 (Continued) *(e) Computer-drawn image of the GC Cell (g) Photograph of the GC cell during the experiments, (h) Shimadzu GC-8A Gas Chromatograph used in this study, (k) the detector recording the GC signals, (l) Photograph of the GC cell during the experiments with light illumination.*

2.2.2 Electrochemical Analysis Techniques

Electrochemical Analysis Techniques included cyclic voltammetry (CV), linear sweep voltammetry (LSV), Electrochemical Impedance Spectroscopy (EIS).

2.2.2.1 Cyclic voltammetry (CV) and linear sweep voltammetry (LSV)

Cyclic Voltammetry (CV) is a potentiodynamic electrochemical technique. The potential on the working electrode is swept forward and backward between two pre-set potential values. CV provides a rapid, simple and powerful technique to investigate electrochemical behavior. Figure 2.15(a) shows a CV waveform. The working electrode's potential is controlled relative to the reference electrode, producing a waveform signal. The (negative scan starts from greater potential (a) and ends at a lower potential (d). The potential at (d) is known as the "switching potential", which represents the potential value sufficient to cause oxidation or reduction of an analyte. After the point (d) the positive scan scan starts from (d) and goes to (g). Reduction occurs from (a) to (d) while oxidation occurs from (d) to (g). In some cases it is important that the working electrode is first has been scanned negative and then positive scan. The cycle can be repeated to determine the stability of the working electrode film.

Figure 2.15(b) shows the cyclic voltammogram from a single electron reduction and oxidation. The current that reported due to the negative scan, is known as the "cathodic current" (i_{pc}); the corresponding potential peak at (c) when the working film is reduced is called the cathodic peak potential (E_{pc}). After the potential is switched at (d), the positive scan occurs, with the resulting current known as anodic current (I_{pa}); the corresponding potential peak at (f) is called the anodic peak potential (E_{pa}) when the film starts to oxidize.[9]

Linear sweep voltammetry (LSV) is similar to the CV technique but measures the current on the working electrode by sweeping the voltage in either the negative or positive direction only; it can be considered to be half of a CV.[10]

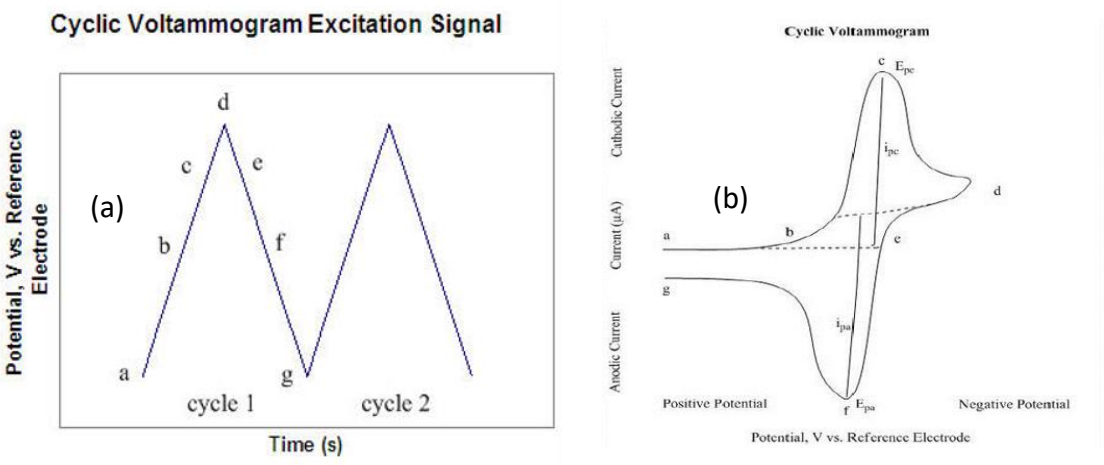

Figure 2.15: (a) *CV excitation signal, (b) cyclic voltammogram of a reversible single electron oxidation-reduction couple. ref. 9*

In this work, a potential was supplied between the working electrode and the reference electrode. The resulting current was measured between the working electrode and the counter electrode. The rate of change of the voltage over the time is called the "scan rate" (V/s). Each prepared thin film on FTO was tested as the working electrode, while a Pt mesh (1 x 2 cm) was used as the counter electrode. A BASi Ag/AgCl aqueous salt bridge (KCl, 3 M) served as reference electrode. For CV and LSV studies an EDAQ Potentiostat e-corder 466 potentiostat connected to a computer that had eDaq EChem software version v2.1.12, were utilized (see 2.16(a)-(b)).

2.2.2.2 Chronoamperometric Studies

Chronoamperometry is an electrochemical technique in which the working electrode produces a current as a result of applying a potential. This current is monitored as a function of time.

In the experimental work, chronoamperometry was one of most useful technique to examine both the stability, durability and reproducibility of the prepared films in PEC experiments, with and without light illumination (see, for example, Figure 2.16(c)). Using chronoamperometry, a comparison in current density could be readily made between different

films, tested as the working electrode. Figure 16(c) shows an example of a sample photocurrent with light illumination (depicted as starting at *) and without light illumination (starting at #).

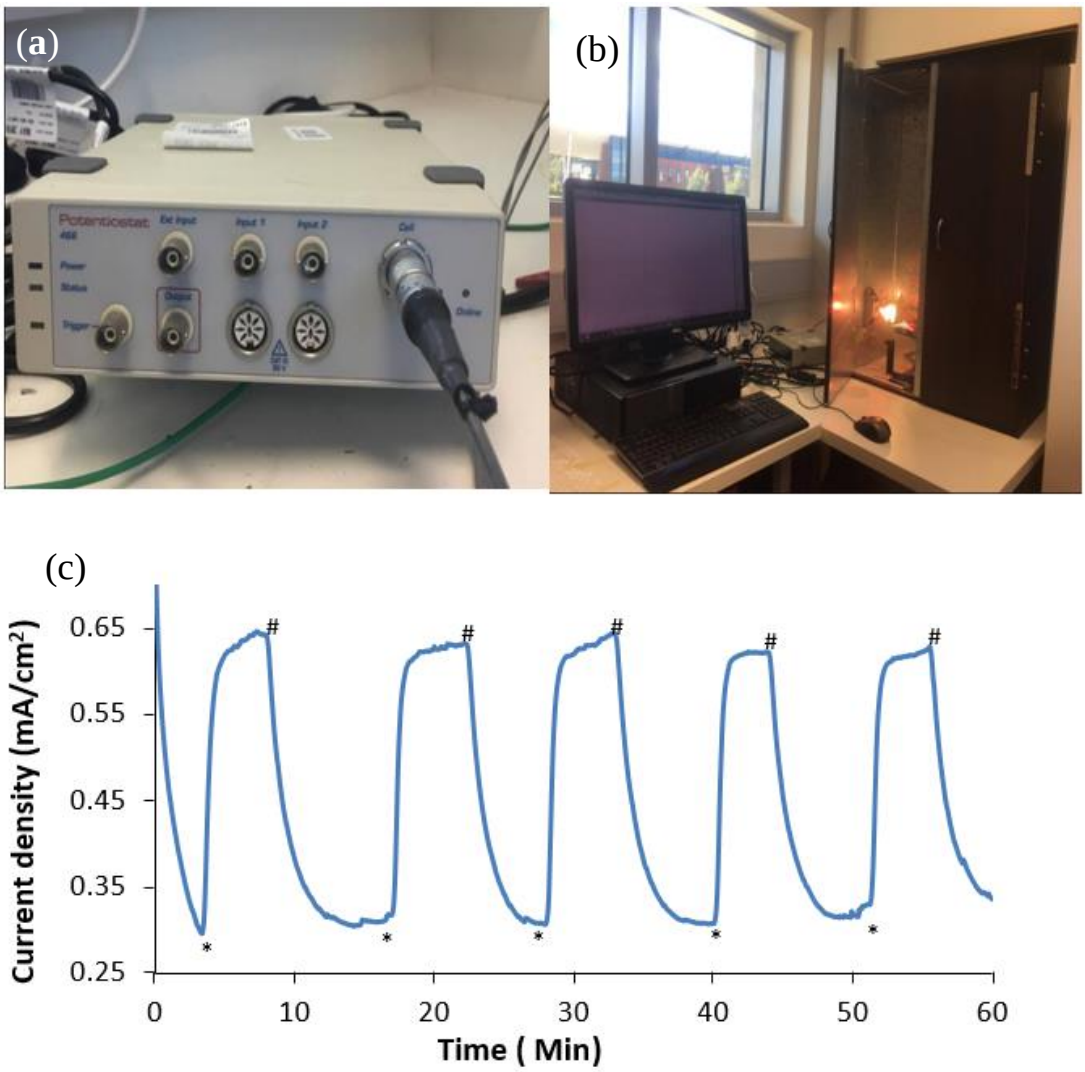

Figure 2.16: *(a) eDaq 466 Potentiostat e-corder 466; (b) eDaq equipped with faraday cage cabinet and computer with eDaq EChem software version v 2.1.12. (c) shows an example of a photocurrent where * signifies that the light was switched on and # signifies that the light was switched off.*

2.2.2.3 Electrochemical Impedance Spectroscopy (EIS)

EIS involves applying a small alternating current (AC) to probe the impedance characteristics of a photoelectrochemical cell. The AC signal is scanned through a wide range of frequencies, resulting in an EIS spectrum, that can be useful to study capacitive, resistive and diffusion processes that could be occurred in the photoelectrochemical cell.[11]

EIS is often measured *via* an excitation signal producing a pseudo-linear system when the current respond to sinusoidal potential at the same frequency but shifted in phase (Figure 2.17). The equations 2.1 and 2.2 describe the sinusoidal response of the system:

$$Z = Z_0 \frac{\cos(\omega t)}{\cos(\omega t - \varphi)} \quad \ldots (2.2)$$

$$Z = Z_0 \, (\cos \varphi + j \sin \varphi) \quad \ldots (2.3)$$

Z represents the resistance according to Ohm's law and it has a real part according to the equation ($Z = Z_0 \cos \varphi$) and an imaginary Z part according to ($Z = Z_0 \sin \varphi \, j$). When real and imaginary Z parts are plotted on the X-axis and Y-axis of a chart, one obtains a "Nyquist Plot". Each point on the Nyquist Plot represents the impedance frequency at a specific frequency. The left-hand side of a "Nyquist Plot" represent the high frequency area while the right-hand side of the plot attributed to the low frequency (Figure 2.18).

On a Nyquist Plot the vector (arrow) of the length |Z| represents the impedance as a vector (arrow) of length |Z| while the angle between |Z| and X-axis is commonly called "phase angle" is φ (=arg Z).[12]

Referring to Figure 2.18: the arc semicircle in a Nyquist Plot is characteristic of a single "time constant". This constant is a physical value that describes the interface of the electrochemical reaction (electrolye-catalyst-gas). The behaviour of this impedance interface can be fitted to an equivalent electric circuit (EEC) consisting of a resistance and a capacitor

as depicted in Figure 2.19. EIS plots often have several arc semicircles but only a portion of a semicircle can appear from each of these arcs. Thus, in order to obtain comprehensive EEC, for a complete impedance spectrum, several time constants required to be combined in series.

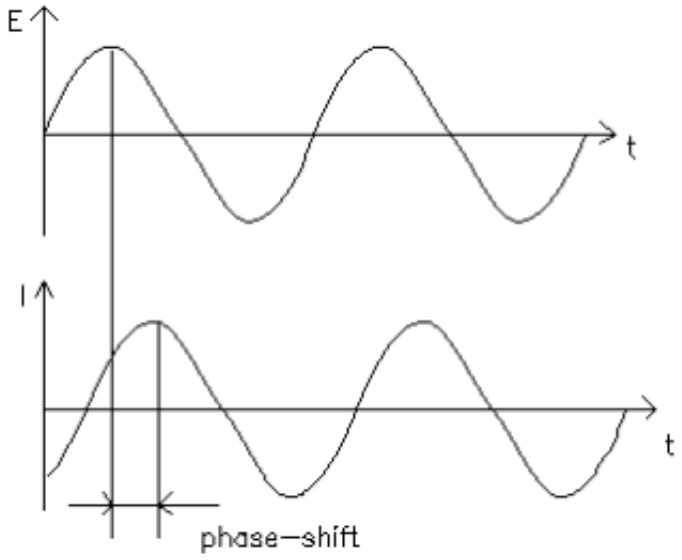

Figure 2.17: *The application of a sinusoidal voltage (top) generates a sinusoidal current response (bottom), showing a phase shift.*[12].

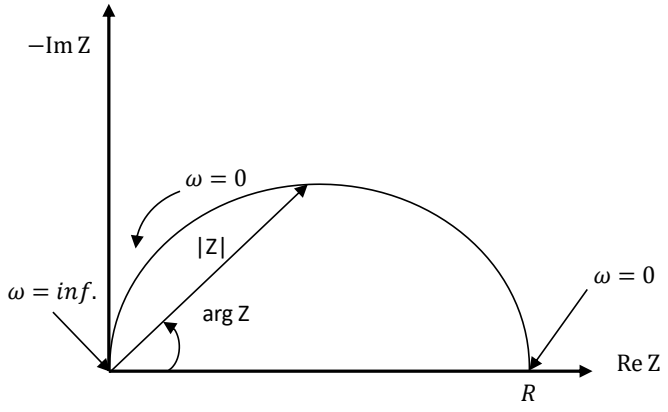

Figure 2.18: *Nyquist plot with impedance vector. Reproduced with permission from.*[12]

Nyquist plots do not provide any information about the frequency, so another popular presentation method is employed called “Bode plot” depicted in Figure 2.20. Here the impedance, represented by ($|Z| = Z_0$), is plotted against the log of the frequency on the X-axis. A Bode plot may provide both the absolute values of the impedance ($|Z| = Z_0$) and the phase-shift on the Y-axis.

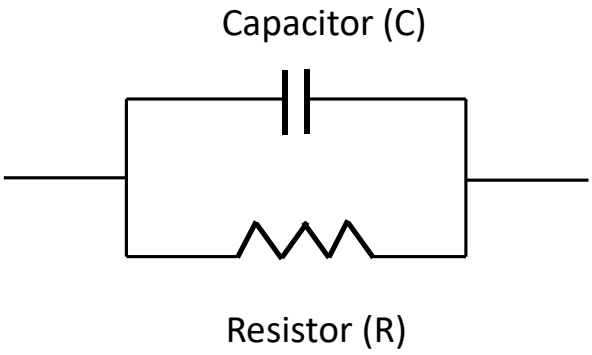

Figure 2.19: *Simple equivalent electric circuit with one time constant represented as a resistor (R) in parallel with a capacitor (C)* [12].

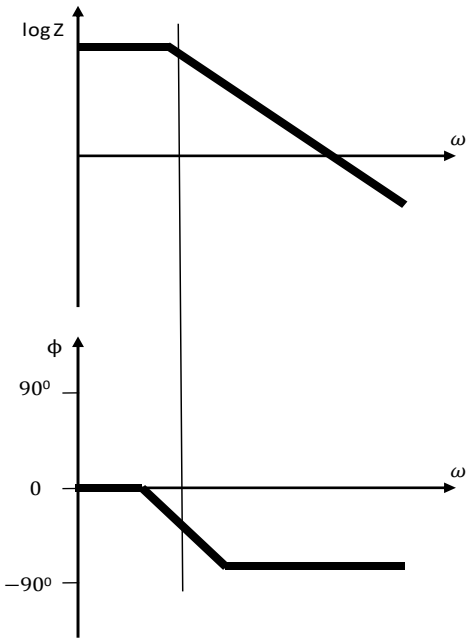

Figure 2.20: *Bode plot with one time constant.*[12]

Figure 2.20 represents the Bode plot of a single time constant like that shown in an EEC in Figure 2.19. As can be seen in Figure 2.20, impedance sits at a constant magnitude at low frequencies, with the current passing almost completely through the resistor, so that the phase angle sits at 0^o. In contrast, at higher frequencies, the current has to be divided in order to pass through the capacitor. In the resistor, the flow of current is proportional to the magnitude of voltage, while in the capacitor, the flow of current is proportional to the voltage gradient, introducing a phase shift between voltage and current, as can be seen in Figure 2.17. In a pure capacitor, the current is 90^o out of phase with the voltage thereby forcing the phase angle to shift towards -90^o in the Bode plot at lower frequencies.[12]

Typically in our experiments, EEC was also performed to include several combinations of ohmic resistances (R_Ω) and interfacial charge transfer (can be represented by both charge transfer resistance (R_{ct}) and capacitance that can be expressed as double layer capacitance (C_{ct}) and a constant phase element (CPE), including $Q_{CPE,ct}$, $n_{CPE,ct}$, and $C_{CPE,ct}$).[13] R_Ω can be determined by the total contributions from contact resistances and the ohmic resistance of the cell contents such as the electrolyte (related to electrolyte ionic resistivity) and/or electrodes. The R_{ct} parameter expresses the kinetics of the electrochemical reactions at the interfaces of three phase (electrolyte-catalyst-gas evolution). C_{ct} represents the capacitive nature of the interfaces of these three phases and charge separation between ions and electrons through the interface. However, in practical work, a CPE can be used. The CPE is generally believed to originate from a distribution in the current density along the electrode surface as a result of surface inhomogeneity.[14] This can be inferred from the analogy with the behaviour of porous electrodes (and other electrodes with intentional inhomogeneity).[14] A CPE can also be used instead of a pure C_{ct} in order to improve fitting of experimental data. CPE model behaviour can mainly be attributed to surface roughness, inhomogeneity, and porosity, reactivity, potential and current distributions that related to electrode geometry. Q_{CPE} represents CPE in which the constant Q has the dimensions $\Omega\ cm^2\ s^{-(1-\alpha)}$ (where the α parameter is attributed to $n_{CPE,ct}$ and has a value in the range ($0< n_{CPE,ct}\leq 1$) related to the rotation angle in Figure 2.18. $C_{CPE,Ct}$ represents capacitive nature of CPE.[14]

The data modelled with a CPE can be used to calculate the double layer capacitance (C_{ct}) via the Brug equation (equ. 2.4) for time constants normal distribution of electrode elements.[14]

$$Q^{-1} = C_0^{1-\alpha}\left[R_\Omega^{-1} + R_{ct}^{-1}\right]^{\alpha} \quad \ldots (2.4)$$

where, Q is attributed to $Q_{CPE,ct,}$, α attributed to $n_{CPE,ct}$ and its value in range ($0< n_{CPE,ct}\leq 1$), while C_0 attributed to $C_{CPE,ct}$ in this research.[13]

In this study (EIS) a SP-300 Biologic Science Instruments was used to perform EIS studies, which were conducted potentiostatically at the experiment conditions employed, with frequencies between 0.1 Hz and 150 KHz applied for OER experiments and frequencies between 10 Hz to 200 KHz for HER experiments. EC-Lab V10.44 and Z-View 3.5C software were used for EIS analysis, spectrum and fitting.

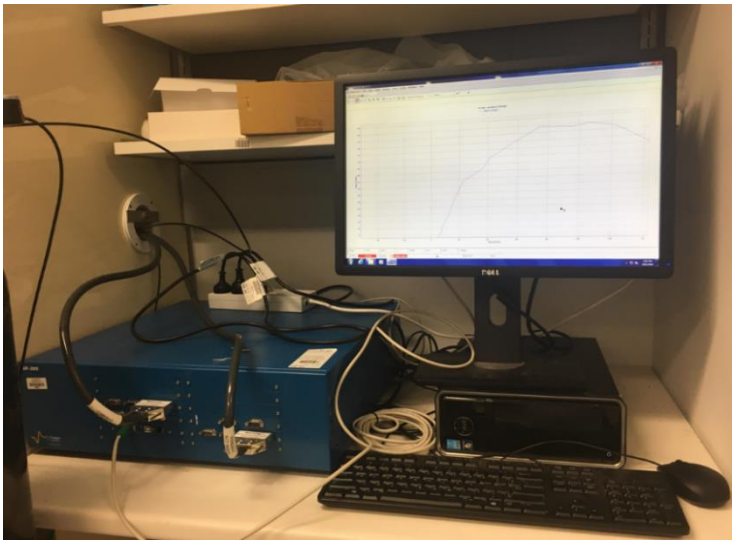

Figure 2.21: *EIS machine model SP-300 Biologic Science Instruments*

2.2.2.4 Tafel Plots and Exchange Current Densities

A Tafel plot compares the rate of an electrochemical reaction (plotted on a logarithmic or natural logarithmic axis) to the overpotential.[15] The Tafel equation is shown in equ. (2.5):

$$\eta = A\ ln\ (\frac{j}{j_0}) \qquad \ldots(2.5)$$

where η is the overpotential, A is the Tafel slope, and j and j_0 represent the current density and exchange current density (in A/m^2), respectively.

Theoretically, the Tafel slope can also be represented by equation (2.6) when the reaction mechanism involves the transfer of a single electron:[15]

$$A\ = \frac{kT}{e\alpha} \qquad \ldots (2.6)$$

where k is represents the Boltzmann constant, T is the absolute temperature (in K), e is the elementary charge and α is the "charge transfer coefficient", the value of which must be between 0 and 1. The exchange current density (i_o) is determined from the intercept of the plot with the y-axis (converted to a normal number).

In order to calculate the Tafel slope of the oxygen evolution reaction (OER) at pH 12, the theoretical minimum E at pH 12 has to be calculated *via* equation (1.3)

$$E = E^o - 0.0591(pH) \qquad \ldots (1.3)$$

$$E = 1.23 - 0.0591(pH)$$

where 1.23 V is the E^o for water oxidation at standard conditions of temperature and pressure (STP) according to equation (1.1). The theoretical minimum E for water oxidation at pH 12 is therefore 0.52 V vs SHE.

As the Ag/AgCl reference electrode has a potential of 0.23 V *vs* SHE, the theoretical minimum E *vs* Ag/AgCl for water oxidation is:

0.52 - 0.23 = 0.29 V *vs* Ag/AgCl

In experimental work on the OER, the working electrode was scanned slowly via LSV (0.2 mV/sec) in the range (0.29 - 0.80) V *vs* Ag/AgCl. The overpotential (η) was calculated by subtracting 0.29 V from the voltage obtained *via* the LSV scan. Thereafter, Tafel plots were constructed by plotting the overpotential (η) on the *y*-axis *vs* the natural logarithm (*ln*) of the current density on the *x*- axis. From such plots, the Tafel slope and exchange current density were determined, as shown in Figure 2.22.

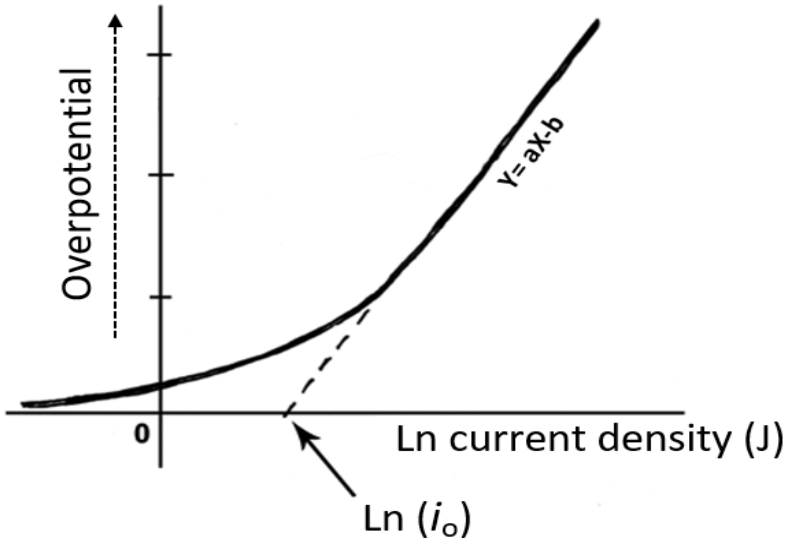

Figure 2.22: *Schematic of a Tafel plot showing how the Tafel slope and the exchange current density (i_o) are determined.*

In the case of studies involving the HER in acidic conditions, E° is equal to 0 V according to equation (1.6). Thus,

$$E = 0\text{-}0.0591\ pH$$

Since the electrolyte was adjusted to pH 1,

$$E = -0.0591\ vs\ SHE$$

Because the Ag/AgCl reference electrode has a potential of 0.23 V *vs* SHE, E vs Ag/AgCl will be

$$E = -0.0591\text{-}0.23$$

$$E = -0.2891\ V$$

The seclected film was made the working electrode in a PEC cell and scanned slowly *via* LSV as described above (in the range of -0.289 to -0.75 V *vs* Ag/AgCl). The Tafel slope and exchange current density were determined by a similar method to that described above.

2.3 Preparation Methods

2.3.1 GO Synthesis

In order to prepare fully oxidized graphite, dry graphite flakes were first thermally treated at 700 °C in a vertical tube furnace under N_2 atmosphere. The resulting expanded graphite (EG) was used as a precursor for GO synthesis, following previously described methods.[16-20] Briefly, 1 g of EG and 200 mL of concentrated H_2SO_4 were mixed and stirred in a flask for 24 h at room temperature. $KMnO_4$ (5 g) was then added slowly to the mixture. The reaction vessel was placed in an ice bath and 200 mL of DI water containing 50 mL of 30% H_2O_2 were poured slowly into the mixture. The suspension changed colour to light brown. After stirring for another 30 min, the resulting GO particles were washed and centrifuged with HCl solution (9:1 water: c.HCl by volume), then centrifuged again and washed with DI water until the pH of the solution became 3 - 4. The resultant GO sheets were dispersed in deionized water by gentle shaking. Then, a GO dispersion in ethanol was prepared by extracting the water from the parent aqueous GO dispersion by repeated centrifugation-washing steps (6 times, for 10 - 30 min each, at 11000 rpm).[21] The parent aqueous GO (15 mL) (~2.5 mg ml^{-1}) was poured into a 50 ml centrifuge tube (Nalgene), to which 20 ml ethanol was added, followed by vigorous mixing using a vortex shaker. After each centrifuging, 30 ml of the supernatant was poured off and replaced with 30 ml of ethanol and then mixed vigorously by vortex shaking. This process was repeated a further 5 times to replace the water with ethanol. Finally, the dispersion was sonicated in a bath sonicator for 1 h before being centrifuged again to make a high concentration dispersion (~30 mg/ml GO).

2.3.2 Preparation of Electrodes

2.3.2.1 Preparation of PEDOT, PEDOT/nano-Ni, PEDOT/nano-Ni/rGO on FTO-coated glass slides (Chapter 3, Chapter 4)

Uncoated glass and FTO-coated glass slides were immersed in acetone within a Thin Layer Chromatography Chamber (TLCC). The baths with the immersed slides were sonicated for 90 min, whereafter the slides were washed with water and dried by blowing air over them. The FTO and uncoated glass slides were then labelled. All slides were thereafter treated in a digital ozone-UV cleaner for 20 min. The slides were then cleaned in a plasma cleaner in order to obtain hydrophilic surfaces with which to fix the coated chemical solutions during spin-coating. The FTO and glass substrates were heated to dryness on an IKA® RCT basic hotplate at 60°C.

To prepare the PEDOT, PEDOT/nano-Ni, and PEDOT/nano-Ni/rGO films on FTO glass slides, the following procedure was used (nano-Ni = nanoparticulate Ni). Where applicable, a GO ethanol solution (e.g. 0.2 ml) was transferred to a small glass vial and the volume increased to 1.2 ml by adding absolute ethanol. The solution was sonicated for 10 min and then stirred with a magnetic stirrer for 7-8 min. Where applicable, nano-Ni (e.g. 125 mg) was added gradually with magnetic stirring continuing for 2.5 h thereafter. A solution of dissolved iron(III) p-toluenesulfonate hexahydrate [Fe(III)-*p*TS] (100 mg) in 0.15 ml ethanol was then added to the mixture(in this case the amount of effective Fe is equal to 10 mg). The resulting solution (100 µL) was dropcast onto the slide surface using a micropipette. The slides were then spun at 2000 revolutions per min (rpm) for 180 s. After spin-coating, the sample was quickly transferred to a hotplate, where it was dried at 60 ^{o}C for 15 min.

Vapour phase polymerisation was carried out in a separate conical flask (500 mL capacity), equipped with a rubber stopper containing a crocodile clip suspended above the bottom of the flask. EDOT (0.450 mL) was placed in the flask and the dried, spin-coated FTO or uncoated glass substrates were held above the EDOT solution by the crocodile clip, with

the stopper in place. The stoppered conical flask was then placed in an oven at 60 ^{o}C for 60 min, during which time the EDOT vapour polymerised into PEDOT polymer on the slide surface. After polymerisation was complete, the sample was removed, washed very thoroughly with ethanol, and then left to dry overnight.

The resulting dried FTO-coated samples were converted to usable electrodes by attaching a copper wire to the FTO surface with conductive silver paint and epoxy resin. When the silver paste was fully solidified, epoxy glue was used to cover the contact area of the wire as well as any exposed clean FTO glass surface.

Immediately prior to testing as a (photo) electrocatalyst, the GO present in all films was reduced electrochemically to rGO using cyclic voltammetry (performed in 0.2 M Na_2SO_4 (pH 12); 8-10 cycles between -1.2 V and 0.8 V, *vs.* Ag/AgCl, at 50 mV/s scan speed) for OER and in case of HER study

2.3.2.2 Preparation of PPy, PPy/nano-Ni, PPy/rGO PPy/nano-Ni/rGO, Ni/rGO, PEDOT/nano-Co_3O_4, PEDOT/nano-Co_3O_4 / rGO, Co_3O_4/rGO, PEDOT/ CNT, Co_3O_4 /CNT, PEDOT/nano-Co_3O_4/CNT, FTO-coated and microscopic glass slides (Chapter 5, Chapter 6)

The methodology of preparing these electrodes was the same as that in the experimental part section (2.3.2 preparation of Electrodes), including spin revolutions per min (rpm) speed and the time of vapour phase polymerization taking into considerations only the following points only

(1) The required amount of the catalyst that will be either Ni or Co_3O_4 ,

(2) The amount of GO or CNT in polymerisation solution,

More details will discussed in their chapters

2.3.3 Synthesis of Poly(acrylamide) Hydrogel (Chapter 7)

Acrylamide monomer (99.9%), N,N′-methylenebis(acrylamide), sodium chloride (≥99.9%) and lithium chloride (≥99.9%) and α-ketoglutaric acid were purchased from Sigma Aldrich, Australia. Poly(acrylamide) hydrogel-forming solution was synthesized by adding 20% (w/v) using Milli-Q water at room temperature (21 ^{o}C). Acrylamide monomer powder was added to yield a 2 M acrylamide concentration. Then, 470µl of 2% w/v of N,N-methylenbis(acrylamide) and 0.014 (w/v) of α-ketoglutaric acid were added as cross-linking co-polymer and photoinitiator, respectively. The gel solution was stirred and degassed in a vacuum desiccator for 20 min under 0.1 bar pressure, at room temperature. The acrylamide solution was poured into a U-shaped glass tube (diameter = 20 mm, length 130 mm). Solutions were cross-linked using a Dymax BlueWave 75 Rev 2.0 UV Light at 1.15 W/cm^2 intensity.

2.4 Poly(acrylamide) Hydrogel Characterizations

For mechanical tensile testing, solutions were poured into a 15 cm x 15 cm box, cured and cut into "dog-bone" shapes (conforming to JIS – K625060). Compression testing was carried out on gels which were cast and cured in a cylindrical mould (diameter = 18 mm, height = 10 mm). For electrical characterization, hydrogel samples (height = 6 mm, width = 5 mm) of varying length between 5 mm and 25 mm were cast in plastic moulds with reticulated vitreous carbon foam (RVC, ERG Aerospace, 20 pores per inch) at each end. The water loss percentage of the various polyacrylamide (PAAm) hydrogels was evaluated using equation 2.8. Masses were recorded using a digital lab balance.

$$\text{Water loss } \% = \frac{\text{Mass of hydrogel} - \text{Starting mass of hydrogel}}{\text{Starting mass of hydrogel}} \text{ x } 100 \qquad \ldots (2.8)$$

The hydrogel electrical conductivity has been characterized by recording the electrical impedance for frequencies between 1Hz and 100 kHz using a custom-designed setup, as described in previous studies.[22-23]

2.5 Experimental Work Protocol

Figure 2.22 illustrates how the research was carried out. The first step of each catalytic study was to systematically increase the performance of the composite film that applied as working electrode. CV and chronoamperometry was used to compare the different films. Having identified the optimum film, in second stage, we studied the performance of the optimum film. This included gas chromatography, as well as extensive characterisation involving EA, XRD, XPS, SEM, TEM (if needed), EIS spectroscopy and determination of the thickness and conductivity of the film, along with other controls film (to thereby highlight the interesting chemical and physical properties of the optimum thin film).

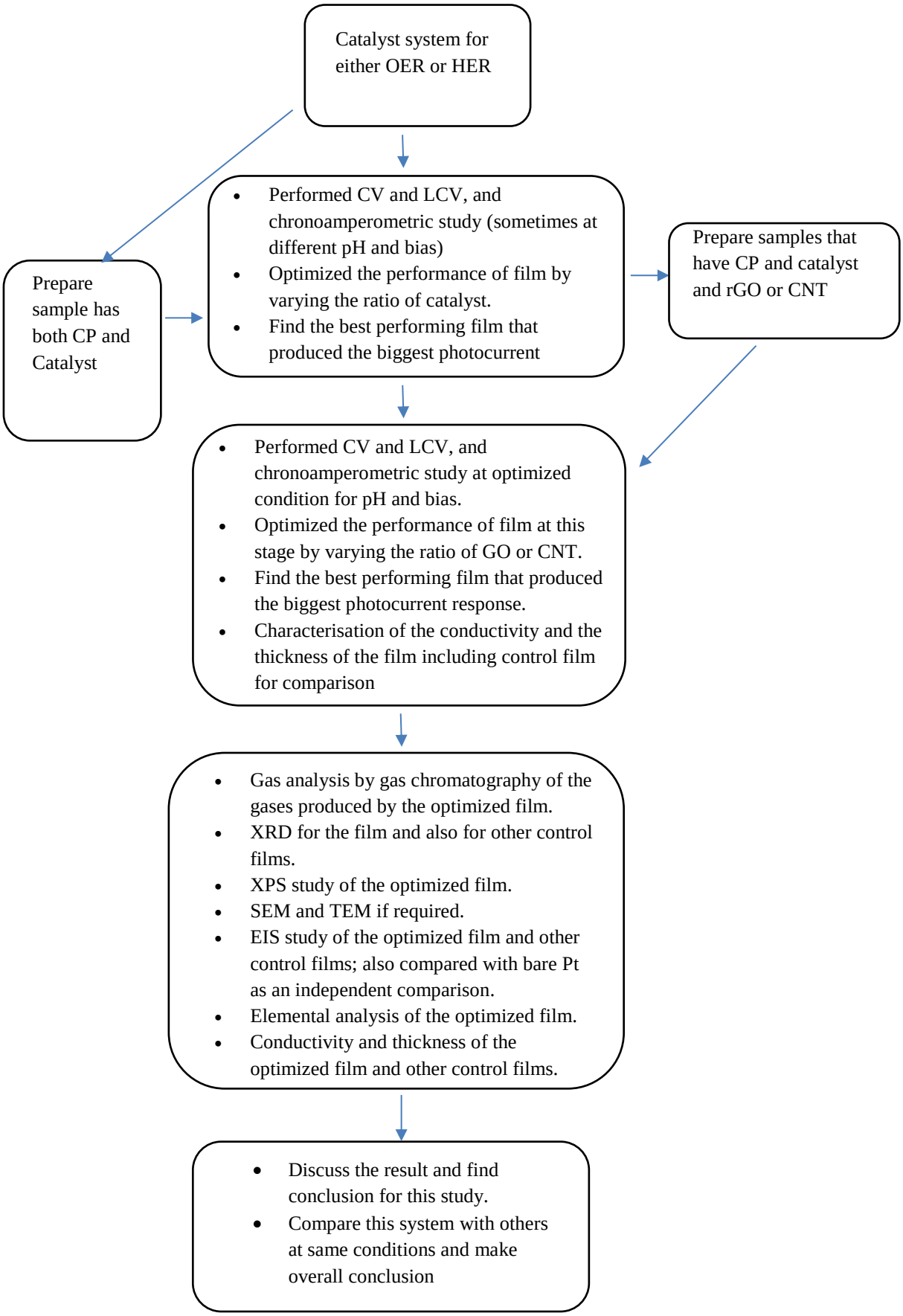

Figure 2.23: *Experimental protocol used in this study.*

2.6 References

1. Four Point Probe Resistivity Measurements. https://www.pveducation.org/pvcdrom/characterisation/four-point-probe-resistivity-measurements (accessed 20 Jun 2018).
2. Mishra, A.; Dwivedi, J.; Shukla, K.; Malviya, P. X-Ray Diffraction and Fourier Transformation Infrared Spectroscopy Studies of Copper (II) Thiourea Chloro and Sulphate Complexes. *J. Phys.: Confer. Series* **2014**, *534* (1), 1-4.
3. Heide, P. v. d. *X-Ray Photoelectron Spectroscopy : An Introduction to Principles and Practices*. John Wiley & Sons, Inc: Hoboken, New Jersey, **2016**; pp 35-97
4. Shelby, C. Scanning Electron Microscope. https://www.purdue.edu/ehps/rem/lab oratory/equipment%20safety/Research%20Equipment/sem.html (accessed 20 Jun 2018).
5. Swapp, S. Scanning Electron Microscopy (SEM). https://serc.carleton.edu/research_education/geochemsheets/techniques/SEM.html (accessed 25 June 2018).
6. Jensen, E. Example: Mechanism of Scanning electron microscopy. http://www.texample.net /tikz/examples/scanning-electron-microscopy/ (accessed 25 June 2018).
7. Carter, C. B.; Williams, D. B. *Transmission Electron Microscopy, Diffraction, Imaging, and Spectroscopy*. Springer International Publishing: Switzerland, **2016**; pp 439-466
8. Basic Plasma Cleaner http://harrickplasma.com/products/basic-plasma-cleaner (accessed 20 Jun 2018).
9. Cyclic voltammetry https://chem.libretexts.org/Core/Analytical_Chemistry/Instrumental_Analysis/Cyclic_Voltammetry (accessed 20 Jun 2018).
10. Linear sweep voltammetry. https://www.revolvy.com/topic/Linear-sweep-voltammetry (accessed 20 Jun 2018).
11. Cook, D. Overview of Electrochemical Impedance Spectroscopy. https://www.gamry.com/support/technical-support/getting-started-with-gamry-software/eis300-potentiostatic-electrochemical-impedance-spectroscopy/ (accessed 20 Jun 2018).
12. O'Hayre, R.; Cha, S.-W.; Colella, W.; Prinz, F. B. *Fuel Cell Fundamentals*. Third Edition ed.; *John Wiley & Sons*: New York, **2016**; pp 3-72
13. Basics of Electrochemical Impedance Spectroscopy. https://www.gamry.com/application-notes/EIS/basics-of-electrochemical-impedance-spectroscopy/ (accessed 20 Jun 2018).
14. Brug, G. J.; van den Eeden, A. L. G.; Sluyters-Rehbach, M.; Sluyters, J. H. The analysis of electrode impedances complicated by the presence of a constant phase element. *Journal of Electroanalytical Chemistry and Interfacial Electrochemistry* **1984**, *176* (1), 275-295.

15. Allen, J.; Bard, L. R. F. *Electrochemical methods : fundamentals and applications*. Second Edition; *John Wiley & Sons*: New York, **2001**; pp 25-26.
16. Esrafilzadeh, D.; Jalili, R.; Stewart Elise, M.; Aboutalebi Seyed, H.; Razal Joselito, M.; Moulton Simon, E.; Wallace Gordon, G. High-Performance Multifunctional Graphene-PLGA Fibers: Toward Biomimetic and Conducting 3D Scaffolds. *Adv. Funct. Mater.* **2016**, *26* (18), 3105-3117.
17. Jalili, R.; Aboutalebi Seyed, H.; Esrafilzadeh, D.; Shepherd Roderick, L.; Chen, J.; Aminorroaya-Yamini, S.; Konstantinov, K.; Minett Andrew, I.; Razal Joselito, M.; Wallace Gordon, G. Scalable One-Step Wet-Spinning of Graphene Fibers and Yarns From Liquid Crystalline Dispersions of Graphene Oxide: Towards Multifunctional Textiles. *Adv. Funct. Mater.***2013**, *23* (43), 5345-5354.
18. Jalili, R.; Aboutalebi, S. H.; Esrafilzadeh, D.; Konstantinov, K.; Razal, J. M.; Moulton, S. E.; Wallace, G. G. Formation and Processability of Liquid Crystalline Dispersions of Graphene Oxide. *Mater. Horiz.* **2014**, *1* (1), 87-91.
19. Naficy, S.; Jalili, R.; Aboutalebi, S. H.; Gorkin Iii, R. A.; Konstantinov, K.; Innis, P. C.; Spinks, G. M.; Poulin, P.; Wallace, G. G. Graphene oxide dispersions: tuning rheology to enable fabrication. *Mater. Horiz.* **2014**, *1* (3), 326-331.
20. Gambhir, S.; Jalili, R.; Officer, D. L.; Wallace, G. G. Chemically Converted Graphene: Scalable Chemistries to Enable Processing and Fabrication. *NPG Asia Mater.* **2015**, *7*, 186 (1-15).
21. J Jalili, R.; Aboutalebi, S. H.; Esrafilzadeh, D.; Konstantinov, K.; Moulton, S. E.; Razal, J. M.; Wallace, G. G. Organic Solvent-Based Graphene Oxide Liquid Crystals: A Facile Route Toward the Next Generation of Self-Assembled Layer-by-Layer Multifunctional 3D Architectures. *ACS Nano* **2013**, *7* (5), 3981-3990.
22. Bai, Y.; Chen, B.; Xiang, F.; Zhou, J.; Wang, H.; Suo, Z. Transparent hydrogel with Enhanced water Retention Capacity by Introducing Highly Hydratable Salt. *Appl. Phys. Lett.* **2014**, *105* (15), 151903-151908.
23. Warren, H.; Gately Reece, D.; O'Brien, P.; Gorkin, R.; in het Panhuis, M. Electrical Conductivity, Impedance, and Percolation Behavior of Carbon Nanofiber and Carbon Nanotube Containing Gellan Gum Hydrogels. *J. Polym.Sci. Part B: Polym. Phys.* **2014**, *52* (13), 864-871.

Chapter 3

Synergistic Amplification of Water Oxidation Catalysis on Pt by a Thin-Film Conducting Polymer Composite

Declaration: Portions of this chapter are drawn from a journal article entitled: "*Synergistic Amplification of Water Oxidation Catalysis on Pt by a Thin-Film Conducting Polymer Composite*", that has been published in *ACS Applied Energy Materials* **2018**, *1*, 4235-4246 (DOI: 10.1021/acsaem.8b00728), for which I, Mohammed Alsultan, was the first author, along with co-authors: Sivakumar Balakrishnan, Jaechol Choi, Rouhollah Jalili, Prerna Tiwari, Pawel Wagner, and Gerhard F. Swiegers. My contribution involved: (i) carrying out the laboratory research and measurements, (ii) constructing the plots and figures from the data obtained, and (iii) writing the first draft of the journal article.

3.1 Introduction

Conducting polymer (CP) thin films have recently gained attention as potentially useful substrates for immobilizing water oxidation catalysts, particularly solar-assisted or solar-driven catalysts.[1] For example, the conducting polymer poly(*ter*thiophene), incorporating Mn porphyrins, has been demonstrated to selectively split seawater into oxygen only, with no measurable chlorine formation detected.[2] In

common with several other systems involving thin-film conducting polymer substrates however, the catalytic activity was weak, achieving current densities in the low $\mu A/cm^2$ range. [1-2]

Water oxidation is an uphill chemical reaction that requires an electrochemical cell potential of at least 1.23 V *vs* NHE. In practice, higher potentials must be applied due to the overpotential of the oxygen evolution reaction (OER).[3] The activity of water oxidation electrocatalysts typically depends on the active area of the electrode involved,[4] the electrical resistance of the conduction pathways to the electrode surface,[5] and the external bias that is applied.[6] Sunlight may also be harnessed if the materials employed have wide visible light absorption bands. [7-9]

Conducting polymers have the potential – at least in theory – to mediate all of the above properties and thereby maximally assist the catalytic process. However, that potential has remained largely unrealised with conducting polymer substrates appearing to mostly restrain and not fully facilitate catalytic processes.[1] A key challenge in this respect is to understand how to fabricate conducting polymer supports in a form that promotes the highest possible catalytic activity. At present, only very general guidelines are available.[1]

A case in point is poly(3,4-ethylenedioxythiophene) (PEDOT), which is widely considered to be the best available conducting polymer in terms of its conductivity, transparency to visible light, stability, and capacity for fast electrochemical switching.[10] Several studies have examined PEDOT within oxygen-generating electrodes.[2,11] However, its performance in such systems has generally been poor, being apparently hampered by a relatively low intrinsic conductivity and catalytic capacity, even at its maximum bias of 0.8 V (vs Ag/AgCl) and pH at 12.[1-2] At higher voltages and pHs, PEDOT may be susceptible to degradative over-oxidation.

To fully understand what is needed in PEDOT thin-films, it was of interest to see whether such supports could be induced to produce *synergistic amplifications* of catalytic performance. That is, it was of interest to see whether a PEDOT support could

accelerate a catalytic effect beyond what may be expected from the catalyst alone? To test this concept, composites of PEDOT that incorporated known, active OER catalysts (to boost catalytic performance)[12] and suitable conducting materials (to augment conductivity) were fabricated and studied. The ratios of the components were also varied to see how this affected performance.

This chapter describes studies of uniformly deposited PEDOT composites containing nanoparticulate Ni ('nano-Ni') (av. diameter: 20 nm) as an active OER catalyst and reduced graphene oxide ('rGO') as a conductor. While graphene oxide is hydrophilic[13-14] and insulating,[15] it is more conducting in its reduced, rGO form.[16-18] Studies have, additionally, shown that rGO has potential in OER catalysis[19-39] (and other forms of catalysis).[40]

The chapter further reports that thin-film composites containing specific ratios of the above components display synergistically amplified[19,41] OER photoelectron- catalysis. Moreover, the catalytic performance of a thin film of PEDOT : nano-Ni : rGO having a molar ratio of 4.5 (C; PEDOT) : 1 (Ni) : 9.5 (C; other) significantly superseded that of other combinations. It also superseded the performance of Pt, the industry-standard, benchmark OER electrocatalyst. When poised at 0.80 V (vs Ag/AgCl) in pH 12 solution, a Pt electrode yielded 0.15 mA/cm^2. When then overcoated with the above PEDOT/nano-Ni/rGO composite, the Pt produced an order-of-magnitude greater current of 1.10-1.15 mA/cm^2 under the same conditions (including a photocurrent of 0.55 mA/cm^2 under 0.25 sun illumination). Studies suggested that the above composite contained an optimum ratio of catalyst density to conductivity and thickness in which the PEDOT electrically connected the largest number of catalytic sites (thereby maximizing the catalytically active area) by the shortest, most conductive pathway (thereby minimizing the Tafel slope). The resulting synergistic matching of the electrical connectivity and conductivity with the catalytic capacity induced the amplified catalytic performance. This approach potentially offers a means of maximizing the effectiveness of thin-film conducting polymers as catalyst supports.

3.2 Results and Discussion

3.2.1 Studies of PEDOT/nano-Ni on FTO

In the first stage of this study, uniformly deposited thin-films of vapour-phase polymerized PEDOT containing varying quantities of nano-Ni (av. 20 nm diameter) on FTO glass slides (4.2 cm^2) were examined. On the basis of previous work,[2] the films were tested as water oxidation electro- and/or photo-catalysts in 0.2 M Na_2SO_4 aqueous solution, with the pH adjusted to 12, while biased at 0.8 V (*vs* Ag/AgCl). These voltage and pH conditions provide the most favourable settings for OER catalysis under which PEDOT can be safely tested without risking oxidative damage.[2] The standard potential for water oxidation at pH 0 is 1.23 V *vs* SHE. However, at pH 12 the minimum theoretical potential is 0.52 V vs. SHE, which equates to 0.29 V *vs* Ag/AgCl (as it was mentioned in the introduction, a higher bias is required to force water-splitting reaction foreword). The testing was carried out with and without light illumination from a SoLux daylight MR16 halogen light bulb (ca. 0.25 sun intensity).

Figure 3.1 depicts representative data from this study. As can be seen, increases in the relative quantity of nano-Ni initially led to higher dark currents, as well as higher photocurrents. Thus, a control PEDOT film with no nano-Ni, exhibited tiny currents (Figure 3.1(a)), whereas films prepared from polymerisation mixtures containing 20 mg nano-Ni (Figure 3.1(b)), 100 mg nano-Ni (Figure 3.1(c)), or 125 mg nano-Ni (Figure 3.1(d)) produced ever higher dark currents (0.15-0.25 mA/cm^2 respectively) and photocurrents (0.20-0.40 mA/cm^2 respectively). However, the net current declined when more than 125 mg nano-Ni was incorporated into the films For example, PEDOT containing 135 mg nano-Ni (Figure 3.1(e)) produced an unchanged dark current of ca. 0.25 mA/cm^2 but a lower photocurrent of only ca. 0.30 mA/cm^2. The additional nano-Ni clearly decreased light absorption by the film.

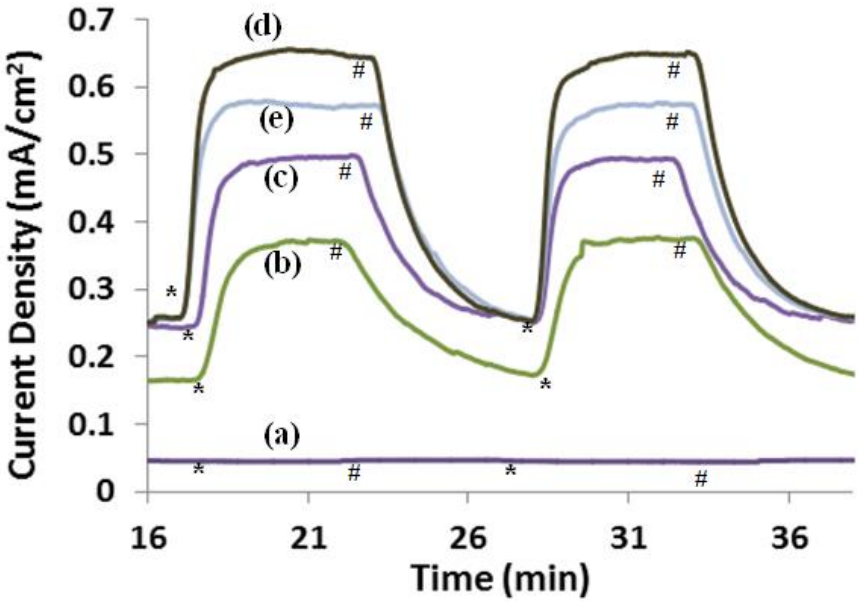

Figure 3.1: *Chronoamperograms at 0.8 V (vs. Ag/AgCl) in 0.2 M Na_2SO_4 (pH 12), with and without light illumination (0.25 sun), of FTO glass slides coated with: PEDOT/Nano-Ni, where the quantity of nano-Ni in the vapour phase polymerisation solution was: (a) 0 mg nano-Ni (PEDOT only; control), (b) 20 mg nano-Ni, (c) 100 mg nano-Ni, (d) 125 mg nano-Ni, and (e) 135 mg nano-Ni. (*='light on', #='light off").*

On this basis, PEDOT/nano-Ni films containing 125 mg of nano-Ni produced the greatest catalytic effect. Further studies examined the incorporation of rGO into this film. The rGO was prepared as described in the Experimental Section.

3.2.2 Studies of PEDOT/nano-Ni/rGO on FTO

In the second stage of the study, thin-films of PEDOT/nano-Ni/rGO on FTO glass were prepared and tested in which the polymerisation mixture contained 125 mg of nano-Ni and varying weights of rGO. The maximum amount of GO that could be incorporated in the films using the vapour phase polymerisation technique was 6 mg. Beyond this level, the polymerisation mixtures became too thick to spin-coat successfully. Immediately prior to

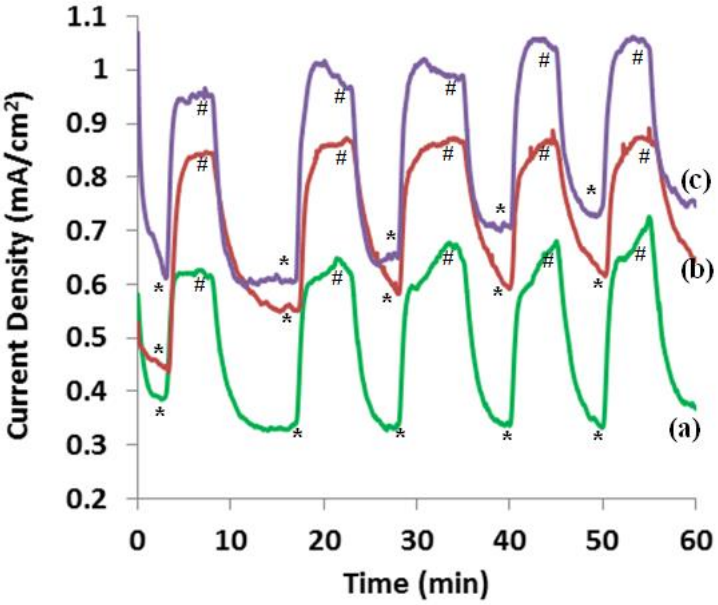

Figure 3.2: *Chronoamperograms at 0.80 V (vs Ag/AgCl) in 0.2 M Na_2SO_4 (pH 12) over 1 h of operation, with and without light illumination (0.25 sun), of FTO glass slides coated with thin films of PEDOT/nano-Ni/rGO, where the polymerisation mixtures contained 125 mg of nano-Ni and the following quantities of rGO: (a) 4.8 mg, (b) 5.4 mg, and (c) 6.0 mg. (*='light on', #='light off').*

testing as a (photo) electrocatalyst, the GO in the films was reduced electrochemically to rGO using cyclic voltammetry (performed in 0.2 M Na_2SO_4 (pH 12); 5 cycles between -1.2 V and 0.8 V, *vs.* Ag/AgCl, at 50 mV/s scan speed). The average charge transferred during the reduction process was 1.6 μC, consistent with a very mild partial reduction.

Figure 3.2 depicts chronoamperograms of the best performing of these films, on FTO glass, at 0.80 V (*vs* Ag/AgCl) in 0.2 M Na_2SO_4 (pH 12) over 1 h of operation, with and without light illumination (0.25 sun).

A systematic increase in the dark currents and photocurrents with increasing rGO loading was observed (Figure 3.2(a)-(c)). The largest dark current (0.6-0.7 mA/cm^2) and photocurrent (0.30-0.35 mA/cm^2) was produced by PEDOT/nano-Ni/rGO containing 125 mg nano-Ni and 6.0 mg rGO. This film was typically 0.62 μm thick and exhibited a conductivity of 8.56 S/cm (when prepared and tested on a glass slide).

3.2.3 Studies of Control Films on FTO; Catalytic Amplification due to the PEDOT

To assess the influence of the rGO component on the catalytic performance of the above film, control films were prepared and tested containing: (i) 6.0 mg of rGO alone (Figure 3.3(a)), (ii) PEDOT containing 6.0 mg rGO (Figure 3.3(b)), and (iii) 6.0 mg rGO and 125 mg nano-Ni only, with no PEDOT present (Figure 3.3(c)). As the nano-Ni would not adhere to the FTO without a binder, a control thin-film of nano-Ni only could not be prepared.

As can be seen in Figure 3.3, all of these control films produced notably smaller dark currents and photocurrents than the PEDOT/nano-Ni/rGO film containing 125 mg nano-Ni and 6.0 mg rGO (Figure 3.2(c)). For example, the best performing control film, which comprised of 6.0 mg rGO and 125 mg nano-Ni only, without any PEDOT present (Figure 3.3 (c)), yielded a dark current that was ca. 0.2 mA/cm^2 lower and a photocurrent that was ca. 0.15 mA/cm^2 lower than the above PEDOT/nano-Ni/rGO film.

These combined differences therefore represent a net catalytic amplification (of ca. 0.35 mA/cm^2) that was created by the presence of the PEDOT in the above PEDOT/nano-Ni/rGO film. This amplification is substantial, being at least 50% of the combined dark and photocurrent of the control film (Figure 3.3(c)).

It is also noteworthy that this amplification was finely dependent on the precise composition of the PEDOT/nano-Ni/rGO film, since, as demonstrated in Figures 3.1 and 3.2, even small changes in the quantities of nano-Ni or rGO present led to substantial declines in the dark and photocurrents. That is, the observed amplification was synergistically dependent on the exact proportions of the components in the PEDOT/nano-Ni/rGO composite.

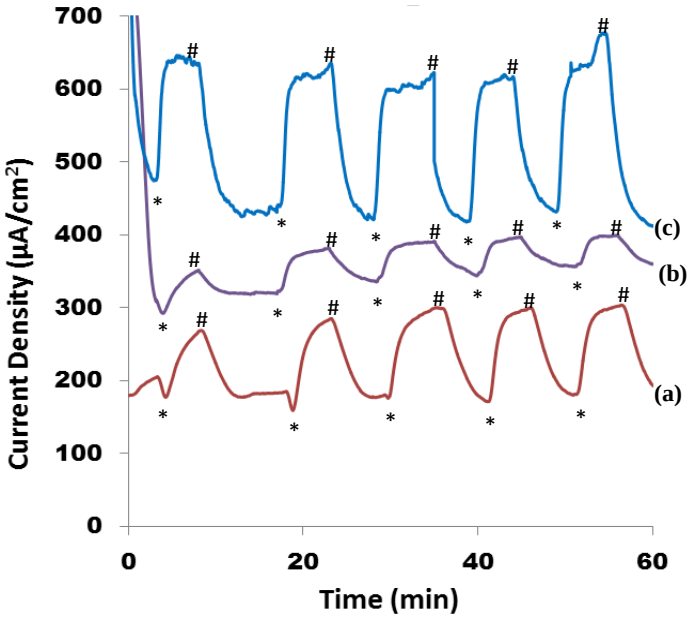

Figure 3.3: *Chronoamperograms at 0.80 V (vs Ag/AgCl) in 0.2 M Na_2SO_4 (pH 12) over 1 h of operation, with and without light illumination (0.25 sun), of FTO glass slides coated with thin films comprising of: (a) 6.0 mg rGO, (b) PEDOT containing 6.0 mg rGO, and (c) 6.0 mg rGO and 125 mg nano-Ni only (without any PEDOT). (*='light on', #='light off').*

3.2.4 Comparative Studies with Pt

While numerous OER catalysts have been examined at pHs above 13,[19-21] studies against which we could compare the above data, at pH 12, did not appear to be available. A comparison was therefore made with the standard industry OER catalyst, Pt. To that end, a FTO slide was sputter-coated with Pt (100 nm) and tested it under the same conditions. Figure 3.4(a) shows the result. As can be seen, the freshly-prepared bare Pt electrode generated a steady current over 1 h of ca. 150 μA/cm^2. This was substantially less than the best performing PEDOT/nano-Ni/rGO thin film.

To properly compare the two, a freshly-prepared Pt-coated FTO slide was prepared with a thin film of PEDOT/nano-Ni/rGO containing 125 mg of nano-Ni and 6 mg of rGO. The resulting PEDOT/nano-Ni/rGO on Pt/FTO produced dark currents

of 0.55-0.60 mA/cm^2 and photocurrents of 0.55 mA/cm^2 to give a total current of 1.10-1.15 mA/cm^2 (Figure 3.4(b)). This was far in excess of the currents generated by the bare Pt film. They were also larger than the equivalent currents of the PEDOT/nano-Ni/rGO on FTO alone (Figure 3.2(c)). This can be ascribed to the lower sheet resistance increased from the more conductive metallic Pt substrate on the FTO.

The PEDOT/nano-Ni/rGO on Pt/FTO had highest catalytic effect than other control films. It yielded a consistent 1.10-1.15 mA/cm^2 for over 40 h of constant light illumination (Figure 3.5). When the light was then turned off, the current fell to its earlier measured dark current. After the light was again turned on, the photocurrent recovered completely, at which level it continued up to the 50 h mark.

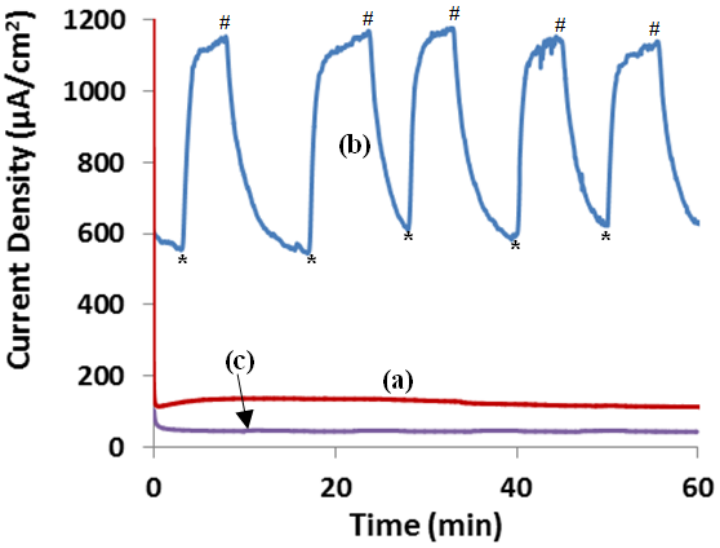

Figure 3.4: *Chronoamperograms at 0.80 V (vs Ag/AgCl) in 0.2 M Na_2SO_4 (pH 12) over 1 h of operation, with and without light illumination (0.25 sun), of FTO glass slides coated with thin films of: (a) bare Pt, (b) Pt overcoated with PEDOT/nano-Ni/rGO, where the polymerisation mixture contained 125 mg of nano-Ni and 6 mg of rGO, and (c) PEDOT only (control). (*='light on', #='light off').*

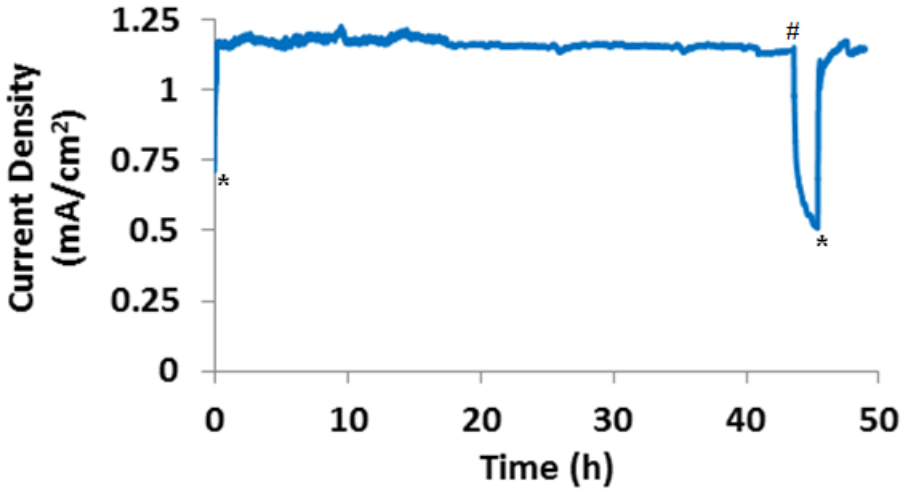

Figure 3.5: *Chronoamperogram at 0.80 V (vs Ag/AgCl) in 0.2 M Na_2SO_4 (pH 12) over 50 h of operation, with and without light illumination (ca. 0.25 sun), of an FTO glass slide coated with a thin film of Pt overcoated with PEDOT/nano-Ni/rGO containing 125 mg nano-Ni and 6 mg rGO (*='light on', #='light off).*

During the above work, gas bubbles could be seen to form and release on the PEDOT/nano-Ni/rGO film containing 125 mg nano-Ni and 6 mg rGO. To determine the identity of the gas being generated, it was collected and tested using a specialized, sealed cell (described in Chapter 2). The cell comprised of two sealed half-cells interfaced to each other *via* a proton conducting Nafion 117 membrane. The OER half-cell was constantly flushed with a steady stream of argon as a carrier gas; the gas outlet was connected to a dedicated gas chromatograph (described in Chapter 2). Periodic GC measurements indicated that the argon carrier gas passing through the OER half-cell was pure before operation but contained a large peak whose retention time corresponded to that of oxygen during operation (Figure 3.6). A small peak due to

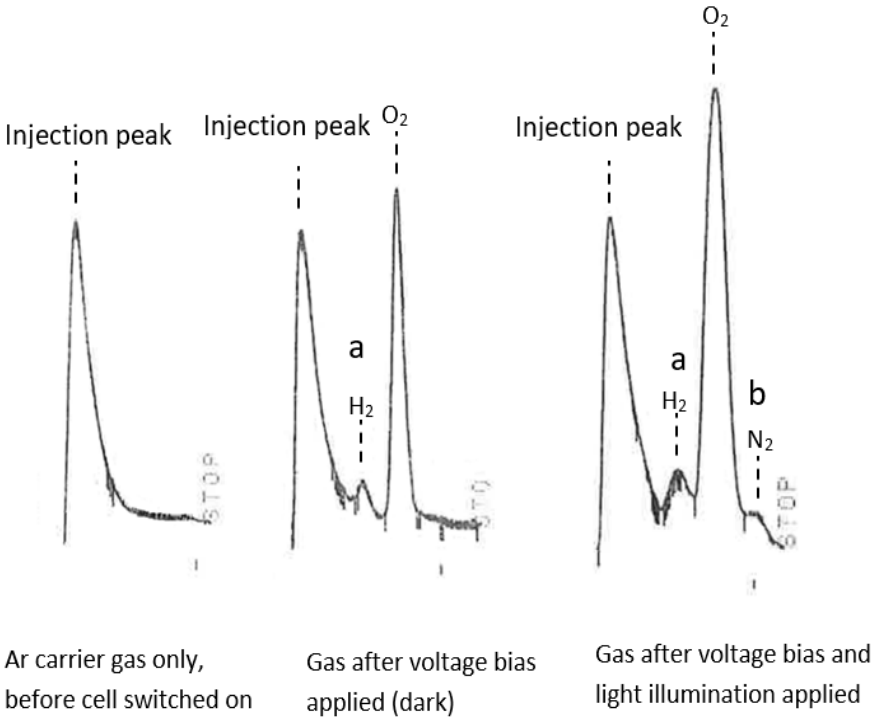

Figure 3.6: *GC traces of gases collected the main peaks related to O_2 and there were a trace of H_2 (a) and N_2 (b) gases.*

hydrogen, which presumably crossed-over the Nafion membrane from the other half-cell, was also observed. Tiny peaks corresponding to N_2 were also occasionally detected as a shoulder on the oxygen peak. Such peaks likely derived from very small amounts of air that got into the system.

The gas ratios were determined by integrating the peaks and found to be typically 96 O_2 : 4 H_2 without light illumination. With light illumination, representative gas ratios were 89 O_2 : 9 H_2 : 2 N_2. Neglecting H_2, which came from the other half-cell, and trace N_2, which came from the air, O_2 was the only gas detected, both with and without light illumination. Gas bubbles formed on the Pt mesh counter electrode were also (and separately) shown to be pure H_2 using the same equipment.

3.2.6 Changes in the Electrolyte

To ensure that the Nafion inter-electrode membrane and the volume of electrolyte employed successfully counteracted any substantial pH changes that could occur in the unbuffered 0.2 M Na_2SO_4 (pH 12) electrolyte within the O_2-generating half-cell, its pH was monitored. Figure 3.7 shows that the pH change during the first 20 h of operation was 0.35 pH units. A declining pH in the O_2-generating, anode, half-cell is fully consistent with and indicative of water oxidation under unbuffered, alkaline conditions.

To check whether the electrode had formed any peroxide, which is an alternative oxidation product, we tested the solution after 5 h of operation with Qantofix® peroxide test strips that were capable of detecting ≥180 μg of peroxide in the volume of electrolyte present. None was detected. As a total charge of 86.2 C had flowed through the cell during that time and peroxide generation involves 2 mol e^- per mol peroxide formed, it could be concluded that ≤0.000012% of the charge had been involved in peroxide formation.

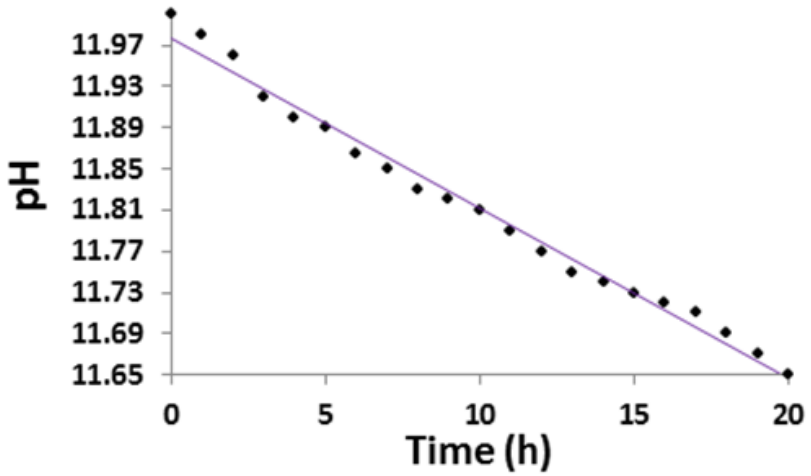

Figure 3.7: *pH change during the first 20 h of the experiment with (i-t) data displayed in Figure 3.5.*

3.2.7 Other Possible Oxidation Processes: the Faradaic Efficiency

In order to further assess the incidence of other oxidation processes (outside of water oxidation), we examined the current profile, without light illumination, during the first few minutes of catalytic testing of the control films comprising of 125 mg nano-Ni and 6.0 mg rGO only (without any PEDOT) (Figure 3.8(a)) and PEDOT containing 6.0 mg rGO (Figure 3.8(b)). The control film comprised of only 6 mg of rGO displayed a stable, unchanging current (Figure 3.8(c)).

As can be seen in Figure 3.8(a), the nano-Ni/rGO control film without any PEDOT exhibited a current spike of up to ca. 2,100 mA/cm^2 in the first few seconds. This stands in contrast to the flat current profile of the rGO control film in Figure 3.8(c) and is consistent with the expected oxidation of the Ni catalyst surface. The oxidation was fully complete after 3 min (charge consumed: 0.293 C), with an unchanging, stable current thereafter.

Figure 3.8(b) similarly shows a transient oxidation of the PEDOT/rGO control film that is indicative of further oxidation of the PEDOT, as seen previously.[2] That oxidation was complete after 4 min (charge consumed: 0.607 C), with a stable current thereafter. PEDOT is well-known to disintegrate/delaminate upon over-oxidation due to physical stresses arising from oxidatively-induced morphological changes in the coating and breaks in the polymer chains.[42] The robust integrity of the coating over 50 h of continuous operation (Figure 3.5) indicates that the polymer was not further oxidized.

The flat, unchanging current of the control film containing only 6.0 mg rGO (Figure 3.8(c)) was not surpincreased. As noted earlier, the GO used in the film was prepared with a large excess of the powerful oxidant $KMnO_4$, in sulfuric acid. As such, it was not subject to additional oxidation. This was further confirmed by the absence in the above GC studies of products that would result from such an oxidation, namely, CO or CO_2 gas (Figure 3.6). The only oxidation process that could have been expected

in this respect was a reversal of the mild partial reduction to rGO that was performed immediately prior to catalytic testing. The flat current profile suggested, however, that such a reversal either did not occur or occurred only very slowly.

The stable currents after 4 min in Figures 3.8(a)-(c) were well below that sustained by the most active PEDOT/nano-Ni/rGO thin film over 50 h under the same conditions, which consumed 861.8 C. This charge is sufficient to 1-electron oxidize every monomer in the PEDOT and every C in the GO >4-times over. The PEDOT coating would have delaminated long before every monomer was oxidized. Moreover, as noted earlier, small changes in the ratio of the components present in this most active film led to notable declines in current. These features are inconsistent with and could not have arisen if the observed currents were due to one of the components in that film being oxidatively consumed in any substantial proportion

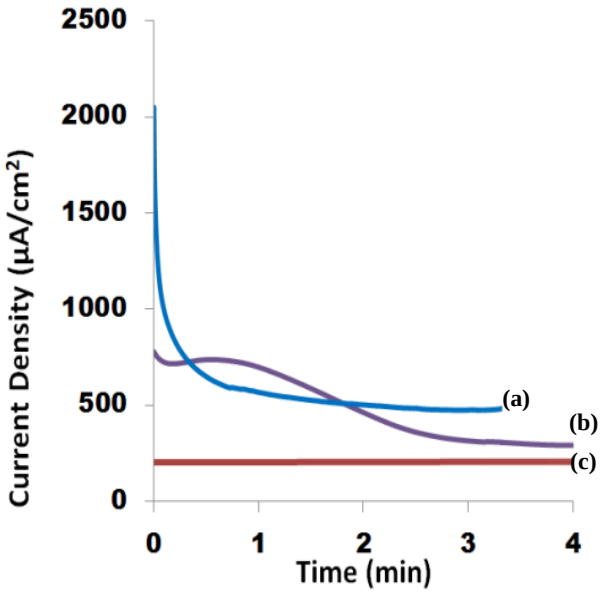

Figure 3.8: *Chronoamperograms over the first 4 min of operation, at 0.80 V (vs Ag/AgCl) in 0.2 M Na_2SO_4 (pH 12) without light illumination, of FTO glass slides coated with control thin films comprising of: (a) 125 mg nano-Ni and 6.0 mg rGO only (without any PEDOT), (b) PEDOT containing 6.0 mg rGO, and (c) 6.0 mg rGO.*

The minimum quantity of oxygen produced by the most active PEDOT/nano-Ni/rGO film could be determined by integration of the oxygen peak in the above GC studies (Figure 3.6) and comparison with a previously determined calibration curve. This indicated that at least 50.9% (dark) and 52.2% (under light illumination) of the volume of oxygen expected from the electrons passing through the electrode was injected through the GC column in these studies. These results were, however, an under-estimate because the cell used in those studies (as described in Chapter 2) could not be made gas-tight and had to be operated with a positive pressure of carrier gas to exclude air ingress. This resulted in leaking of an unquantifiable proportion of the product gas.

It can be concluded that the only possible oxidation process that could have occurred in the system beyond water oxidation, was the reversal of the partial reduction of GO performed immediately before catalytic testing. That represented <0.1% of the overall charge that passed through the electrode during 50 h of operation (Figure 3.5). Accordingly, the Faradaic efficiency for oxygen generation was likely toward quantitative, but unequivocally more than 50.9% (dark) or 52.9% (light). Even in if the latter percentages were the more accurate, they indicate a 4-fold faster generation of O_2 than the bare Pt electrode under the same conditions.

3.2.8 Characterisation of the PEDOT/Nano-Ni/rGO Electrode

To determine the molar composition of the most catalytically active PEDOT nano-Ni and 6 mg rGO, elemental analysis studies were undertaken. As the quantity of material in such a film was far below the minimum needed for an elemental analysis, multiple identical films were prepared on FTO glass, dried, carefully scraped off, and combined.

Analysis of the combined films indicated that they contained 21.00% Ni, 8.54% S, 60.10% C, and no Fe. As only PEDOT contains S, while rGO contains only C, O

(but not analysed) and nano-Ni only Ni, it was possible to calculate the molar ratio of PEDOT : Ni : rGO to be 4.5 (C; PEDOT) : 1 (Ni) : 9.5 (C; other).

The morphology of the PEDOT/Nano-Ni/rGO film was examined using Scanning Electron Microscopy (SEM). Samples for the SEM experiments were prepared by coating a PEDOT/Nano-Ni/rGO film on FTO glass with a 7 nm layer of Pt in order to provide a sufficient signal. Figure 3.9(a) depicts a representative SEM image of the deposited film, showing that it comprised a highly porous surface structure. EDX-mapping (Figure 3.9(b)-(e)) indicated uniform distributions of Ni (nano-Ni), C (PEDOT and rGO), O (PEDOT and rGO), and S (PEDOT) over the film.

Transmission electron microscopy (TEM) (Figure 3.10(a)) showed that the nano-Ni and the rGO plates were generally not in contact with each other, each being separately enveloped by the PEDOT. The nano-Ni particles were 20-50 nm in diameter (the dark structures in Figure 3.10(a)), while the rGO plates were ca. 200-300 nm wide and long (shown as the light-coloured background structures in Figure 3.10(a)). Figure 3.10(b) shows a TEM of the interface between the PEDOT and the nano-Ni. As can be

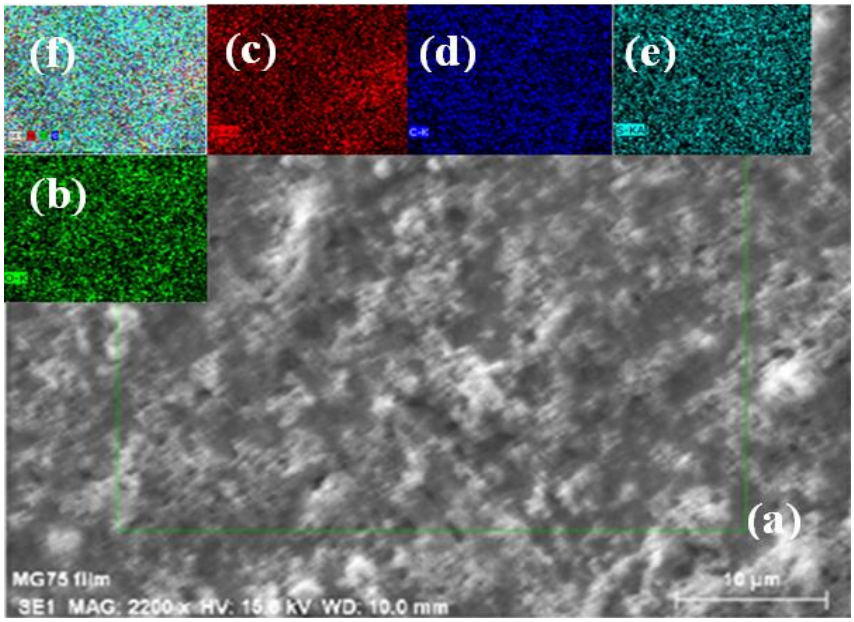

Figure 3.9: *(a) Scanning electron microscope image of PEDOT/Nano-Ni/rGO containing 125 mg nano-Ni and 6 mg rGO. The inset images show the elemental distributions, using EDX, of: (b) O, (c) Ni, (d) C, (e) S, and (f) O, Ni, C, S together.*

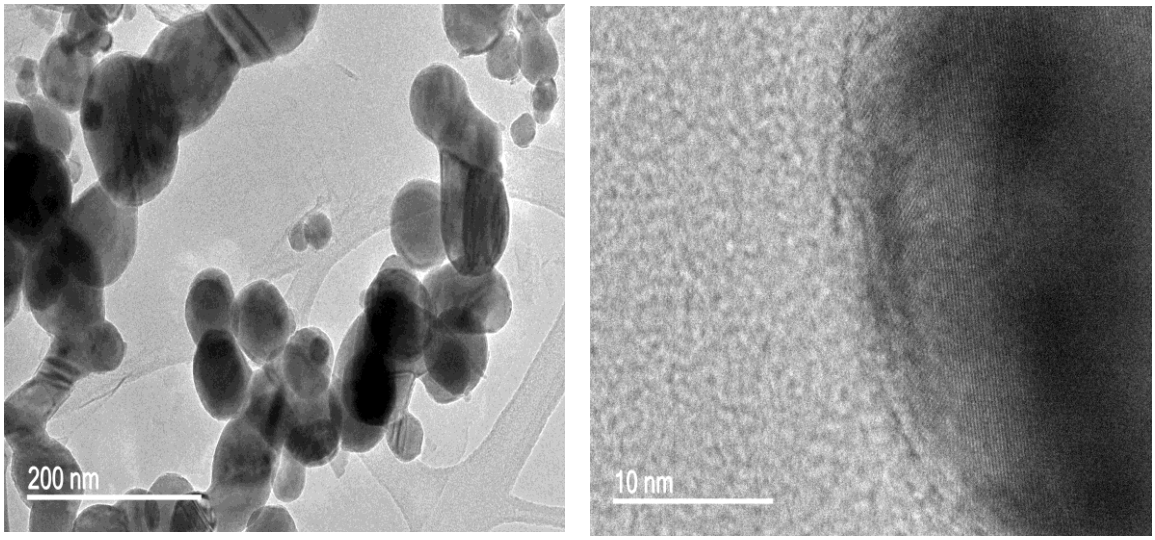

Figure 3.10: *(a) Transmission electron microscopy image of PEDOT/Nano-Ni/rGO, showing the rGO plates and the nano-Ni particles. (b) TEM of the nano-Ni/PEDOT interface.*

seen, the PEDOT generally made seamless contact with the Ni lattice. This was also true for the rGO.

To establish whether the water oxidation catalysis changed the elemental composition and chemical states of the above PEDOT/nano-Ni/rGO film, it was further analysed, after 6 h of continuous operation, with X-ray photoelectron spectroscopy (XPS). The resulting spectra, which are shown as the individual data points in Figure 3.11 closely matched modelled data for PEDOT/nano-Ni/rGO, indicating that there had been no substantive elemental or chemical changes to the film.

The survey spectrum indicated peaks corresponding to O 1s, C 1s, Ni 2p and S 2p. The O 1s and C 1s spectra were characteristic of PEDOT and rGO, while the S 2s spectra derived from PEDOT. The C 1s spectrum contained deconvolution peaks at 284.34, 285.2, 286.1, 286.90, 288 and 290.8 eV (Figure 3.11(b)). The peak at 284.34

eV represented a sp^2 carbon hybrid, characteristic of C=C bonds. The peak at 285.2 eV represented a sp^3 carbon hybrid arising from C-C and C-H bonds. The peak at 286.1 eV refers to the C-S bond. Finally, the peaks at 288.0 eV and 289.0 eV refer to C=O and O-C=O $\boldsymbol{\pi} - \boldsymbol{\pi}$ interactions respectively.[43-51] The S 2p spectrum displayed peaks at 163.5 eV and 165.5 eV, that corresponded to the S $2p_{3/2}$ and $2p_{1/2}$ binding energies. These derived from the C- S bond and S^+, arising from the S atoms of the PEDOT fragments. The other two small peaks refer to $2p_{3/2}$ and $2p_{1/2}$ arising from sulfonic groups in the PTS structure.[52-56]

The O 1s spectrum of the film had peaks at 529.8 eV, 531.9 eV and 533.43 eV. They relate to the binding energy of the Ni-O, C=O and C-O bonds respectively.[57-59] Finally, for the Ni spectrum, there were two main peaks due to Ni $2p_{1/2}$ and $2p_{3/2}$ transitions in the range 848–885 eV (Figure 3.11(d)). The main peak at ca. 845.85 eV had an intense satellite at 860.9 eV, which represents Ni $2p_{1/2,}$ while the peak at 873.6 eV with an intense satellite at 879.5 eV was due to the presence of Ni 2p 3/2, both of which are both characteristic of the Ni^{2+} ion.[60-61]

A number of conclusions could be drawn from the above characterization studies. Firstly, the observed amplification of the catalytic effect did not derive from an interaction between the nano-Ni and the rGO in the film. These components were generally separately enveloped by the PEDOT, which formed an apparently seamless interface with them. The amplification also did not arise from chemical or elemental changes in the film during catalysis. Nor was it due to a catalytic effect arising from residual Fe left over from the polymerisation step.

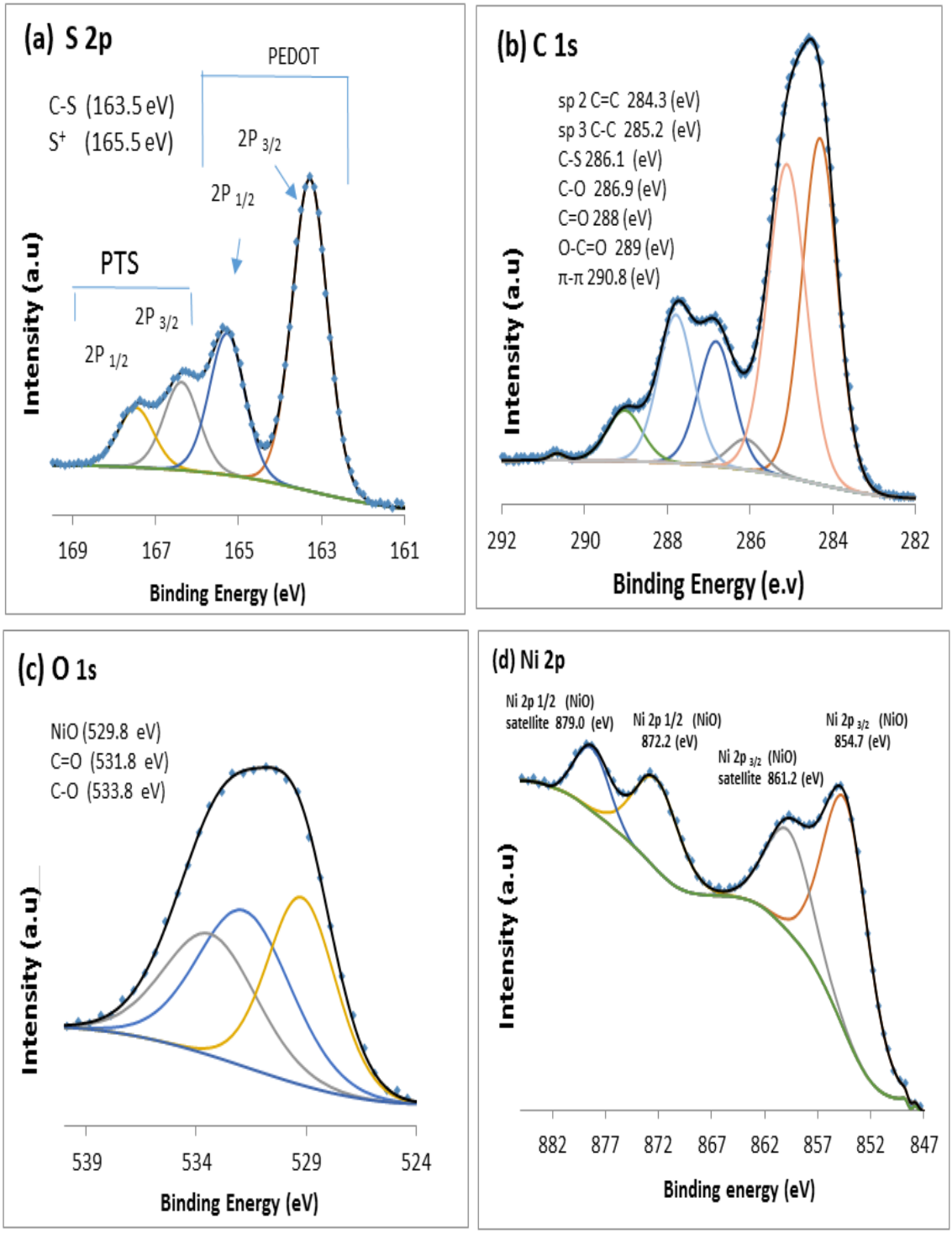

Figure 3.11: *XPS spectra using a monochromatic MgKα X-ray source of PEDOT/nano-Ni/rGO after 6 h at 0.8 V (vs. Ag/AgCl) in 0.2 M Na_2SO_4 (pH 12) showing measured data (individual data points) and modelled data (solid lines) for the: (a) S 2p, (b) C 1s, (c) O 1s, (d) Ni 2p spectra.*

3.2.9 EIS and Tafel Plot Studies

To further investigate the origin of the catalytic amplification, electrochemical impedance spectroscopy (EIS) and Tafel plot studies were undertaken. Figure 3.12(a)-(b) depict the Nyqist and Bode plots respectively, at 0.8 V *vs* Ag/AgCl and pH 12, of: (i)-(ii) the control PEDOT only electrode (with and without illumination), (iii) the control bare Pt electrode, and (iv)-(v) the Pt electrode overcoated with PEDOT/nano-Ni/rGO (with and without illumination). For each sample, two distinct processes can be distinguished in the Nyquist plot: (I) a large arc at intermediate to low frequencies (10-100 Hz), which is clearly visible in the main graph in Figure 3.12(a), and (II) a small arc at high frequencies (1,000-10,000 Hz) that is barely discernible at low Z values in the inset graph in Figure 3.12(a). The latter is characteristic of charge transfer during catalysis. The frequencies of the former are typical of interfacial and solution processes. Previous studies at pH 12 have assigned such low to intermediate frequency arcs to adsorption processes involving transfer of ions (charge carriers) from the diffuse layer to the catalyst.[62] Accordingly, the EIS data was modelled with the equivalent circuit shown in Figure 3.12(c).[63] The modelled results are depicted as the solid lines in Figure 3.12(a). As can be seen, an excellent match was achieved with the measured data (shown by the individual data points in Figure 3.12(a)). Table 3.1 lists key results of the modelling.

The capacitance C_{dl} provides a comparative measure of the electrochemically active area of the samples tested. As can be seen in Table 3.1, the control bare Pt exhibited a substantially lower capacitance (9.89 μF cm^{-2}) than the Pt/PEDOT/nano-Ni/rGO (34.0 μF cm^{-2} without light illumination, 38.9 μF cm^{-2} with light illumination). The Pt/PEDOT/nano-Ni/rGO clearly had an electroactive area that was substantially larger than the bare Pt. The catalytic performance of the Pt/PEDOT/nano-Ni/rGO electrode was therefore due, in part, to a large catalytically active area.

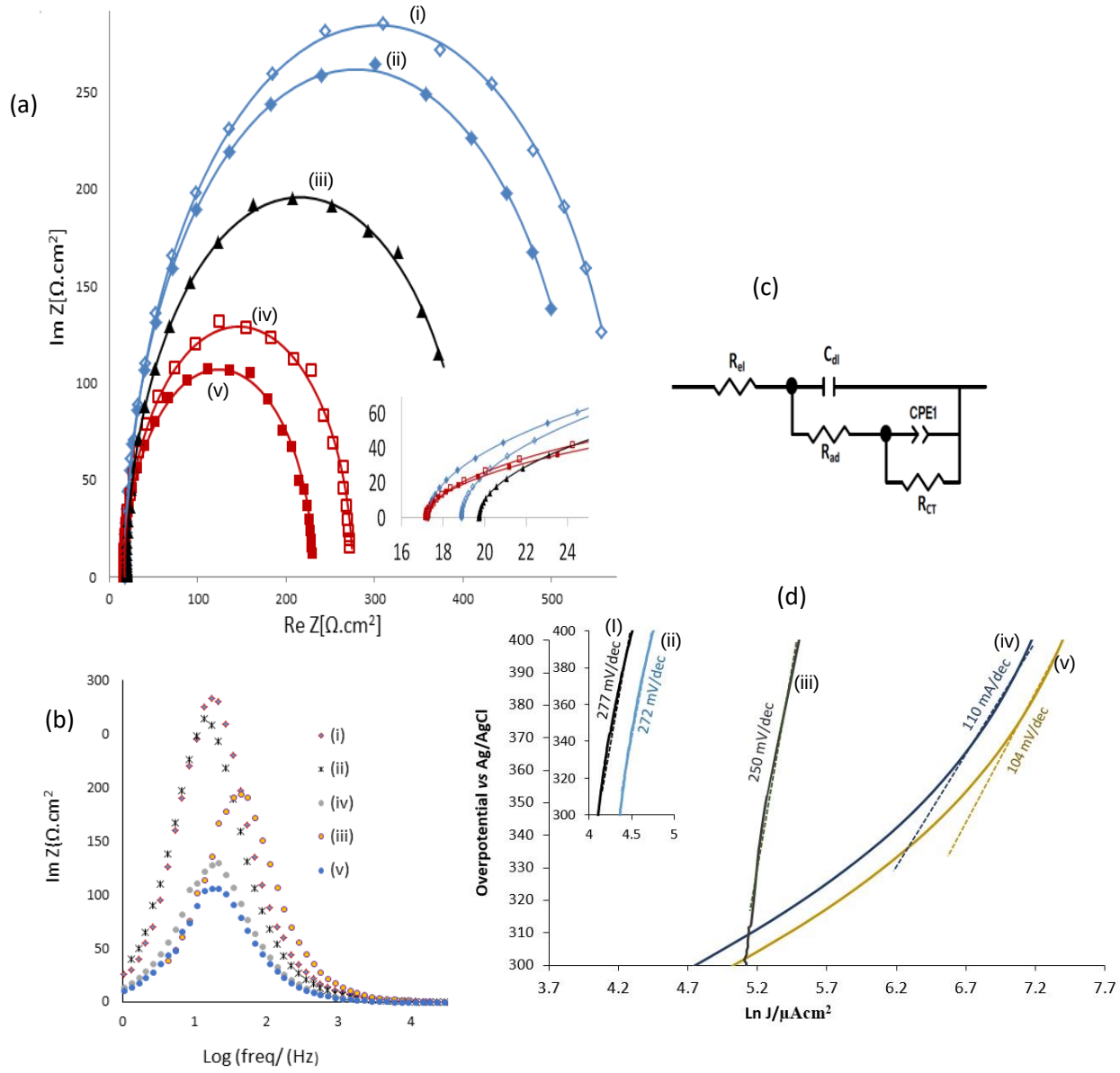

Figure 3.12: *(a) Nyquist and (b) Bode plots at 0.8 V vs Ag/AgCl (pH 12), showing measured data (individual data points) and modelled data (solid lines) using the equivalent circuit depicted in (c), as well as (d) Tafel plots of: (i) PEDOT only (dark; no light illumination), (ii) PEDOT only (with light illumination), (iii) Pt only, (iv) Pt overcoated with PEDOT/nano-Ni/rGO containing 125 mg nano-Ni and 6.0 mg rGO (dark; no light illumination), and (v) Pt overcoated with PEDOT/nano-Ni/rGO containing 125 mg nano-Ni and 6.0 mg rGO (with light illumination).*

The capacitance C_{dl} provides a comparative measure of the electrochemically active area of the samples tested. As can be seen in Table 3.1, the control bare Pt exhibited a substantially lower capacitance (9.89 μF cm^{-2}) than the Pt/PEDOT/nano-Ni/rGO (34.0 μF cm^{-2} without light illumination, 38.9 μF cm^{-2} with light illumination). The Pt/PEDOT/nano-Ni/rGO clearly had an electroactive area that was substantially larger than the bare Pt. The catalytic performance of the Pt/PEDOT/nano-Ni/rGO electrode was therefore due, in part, to a large catalytically active area.

The resistance associated with adsorption, R_{ad}, and the charge transfer resistance, R_{CT}, of the PEDOT/nano-Ni/rGO on Pt/FTO (R_{ad} 110.4 Ω cm^2 and R_{CT} 103.2 Ω cm^2 (R_{total} = 213.6 Ω cm^2) with light illumination; R_{ad} 132.4 Ω cm^2 and R_{CT} 125.3 Ω cm^2 (R_{total} = 257.7 Ω cm^2) without light illumination) were also lower than the bare Pt (R_{ad} 270.4 Ω cm^2 and R_{CT} 120.7 Ω cm^2 (R_{total} = 391.1 Ω cm^2)). The PEDOT/nano-Ni/rGO was therefore a more active catalyst than the bare Pt, per unit area, at least under the testing conditions. As can be seen in Table 3.1 the trend values of the resistances generally decresed from the top to the bottom to produce minimum Ohmic values on the PEDOT/nano-Ni/rGO on Pt/FTO (light). Thus, this optimized film exhibted higher current because, according to Ohm's law, the current produced is inversely proportioned to the resistance.

Accordingly, the PEDOT/nano-Ni/rGO on Pt/FTO achieved its high catalytic performance because it had a larger electroactive area that was also more active per unit area. By contrast, the PEDOT alone displayed a smaller area that was less active. The ohmic resistance, R_{el}, was of the same order for all samples (17.16-19.73 Ω cm^2), as would be expected (Table 3.1).

Figure 3.12(d) shows Tafel plots of the catalysts, with results listed in the last two columns of Table 3.1. It seems that the Tafel slopes are linear for the PEDOT/nano-Ni/rGO on Pt/FTO (with and without light) and PEDOT (without light (i) and with light

(ii)). However, the Tafel slope of the control Pt has a curve due to the observed decrease in its activity during the testing period.

The current density, i_o, provides a measure of the rate of catalysis at the reversible potential, when the overpotential is zero. As can be seen, the bare Pt displayed the highest i_o, indicating that it had the highest intrinsic catalytic capability at zero overpotential. Interestingly, the PEDOT control exhibited higher i_o values with and without light illumination than the PEDOT/nano-Ni/rGO. This indicates that PEDOT is itself capable of acting as an OER catalysis. However, the high Tafel slopes, A, of the PEDOT control indicates that such a catalytic contribution would have been small under the test conditions in Figure 3.5.

Sample	R_{el} Ω cm^2	R_{ad} Ω cm^2	C_{dl} μF cm^{-2}	R_{CT} Ω cm^2	Q_{CPE} $\mu\Omega^{-1}cm^{-2}s^n$	n_{CPE}	C_{CPE} μF cm^{-2}	A mV/dec	i_o μA cm^2
PEDOT (dark)	18.9 ± 1.6	420.3 ± 3.4	16.1± 0.2	148.3 ± 2.7	0.07± 0.03	0.88 ± 0.11	0.01± 0.009	277± 16	20.60 ±3.60
PEDOT (light)	17.3 ± 1.3	400.1 ± 2.6	20.9 ± 1.5	122.9 ± 3.3	0.14± 0.04	0.88 ± 0.12	0.02 ± 0.01	272 ± 15	25.88 ±4.34
Pt only	19.7± 1.2	270.4 ± 12.4	9.9± 0.5	120.7 ± 2.1	0.06± 0.01	0.92 ± 0.32	0.02± 0.01	250± 17	50.46 ±12.50
PEDOT/nano-Ni/rGO on Pt/FTO (dark)	17.3 ± 0.8	132.4 ± 0.7	34.0± 0.2	125.3 ± 1.2	0.25± 0.01	0.89 ± 0.21	0.05± 0.01	110± 13	15.20 ±2.76
PEDOT/nano-Ni/rGO on Pt/FTO (light)	17.2± 1.1	110.4± 0.3	38.9± 0.2	103.2± 1.6	0.40± 0.03	0.88± 0.14	0.08 ± 0.01	104± 10	17.97 ±2.15

Table 3.1: *Data from modelling of electrochemical impedance spectroscopy (ohmic resistance (R_{el}), adsorption resistance (R_{ad}), diffuse layer capacitance (C_{dl}), catalytic charge transfer resistance (R_{CT}), and capacitance expressed in terms of a constant phase element (Q_{CPE}, n_{CPE}, and C_{CPE})).*[64] *Data from Tafel plot studies (slope (A), exchange current density (i_o)). ('dark' = without light illumination; 'light' = with light illumination)*

By contrast, catalysis by the PEDOT/nano-Ni/rGO must have been very strongly activated by the application of the voltage bias. The extent of that activation is confirmed by the Tafel slope. As can be seen, the PEDOT/nano-Ni/rGO on Pt/FTO required only 104 mV (with light illumination) and 110 mV (without light illumination) to increase the reaction rate by a factor of 10 at pH 12. This was very much less than the bare Pt (250 mV)[65] and the control PEDOT (272-277 mV), explaining why the PEDOT/nano-Ni/rGO on Pt/FTO was so much more active at 0.8 V vs Ag/AgCl.

3.2.10 The Origin of the Catalytic Amplification

It therefore appears that the catalytic amplification in the PEDOT/nano-Ni/rGO film on Pt/FTO derived from a confluence of two effects: (i) a large catalytically active area that became (ii) highly active per unit area when a voltage bias was applied to it. The extreme sensitivity of the catalytic amplification to the precise composition of the PEDOT/nano-Ni/rGO film (as demonstrated in Figures 3.2 and 3.3) indicates that these two effects were intimately connected with the composition of the film. That is, the organisation of the PEDOT and the other components in the film must have been such as to create the above effects.

During OER catalysis in basic media, electrons are generated at a catalyst. At a bias of 0.8 V, PEDOT is in its conducting form. When interfaced with an OER catalyst like nano-Ni, that is generating electrons, a PEDOT support will transport those electrons to the external circuit of the cell. In so doing, it would, effectively, also transmit the applied bias to the catalyst. The PEDOT in the above PEDOT/nano-Ni/rGO film containing 125 mg nano-Ni and 6.0 mg rGO, was clearly unusually efficient at carrying out these tasks. That could only have been the case if the electrical pathways between the catalyst sites and the external circuit were short and high conductance.

The earlier-described characterisation studies showed that the PEDOT in the film was porous. The PEDOT also enveloped and seamlessly interfaced with the nano-Ni and rGO in the film. In so doing, it would certainly have electrically connected a large number of catalytically capable Ni atoms to the external circuit. If the electrical pathways were, additionally, short and highly conductive then that would explain the high catalytically active area. It would also explain the strong transmission of the applied bias to the catalytic sites.

In other words, it appears that the composition of the above film, relative to the other, less catalytically active films described above, was such as to uniquely connect the largest number of catalytic sites by the shortest, most conductive pathway. That pathway may have included rGO platelets.

That is, the amplification appears to have derived from a synergistic matching of the electrical connectivity, conductivity and catalytic capacity of the film.

The net result was the creation of a catalytic effect having an order of magnitude higher activity than bare Pt under the conditions of testing. To the best of our knowledge, the above amplification is the largest yet noted for PEDOT (as a proportion of the Pt catalytic activity).[1]

The application of the above approach provides a potential means to maximise the utility of thin-film conducting polymers as catalyst supports.

3.4 Conclusions

In this chapter, the conditions under which thin-film conducting polymer supports may be induced to synergistically amplify catalysis have been studied. Composite PEDOT films containing nano-Ni and rGO have been studied as (photo)electrocatalysts of water oxidation in 0.2 M Na_2SO_4 with the pH adjusted to 12. Films containing PEDOT : nano-Ni : rGO in the specific molar ratio of 4.5 (C; PEDOT) : 1 (Ni) : 9.5 (C; other) proved to be highly active, especially when overcoated on a Pt

electrode. Control films containing other combinations of the above components, produced notably lower currents. The above PEDOT/nano-Ni/rGO on Pt/FTO film generated a sustained current density of 1.10-1.15 mA/cm^2 at 0.80 V (*vs* Ag/AgCl) over >40 h of operation under constant light illumination of 0.25 sun. This was an order of magnitude greater than an equivalent bare Pt electrode, which produced <0.15 mA/cm^2 under the same conditions. Oxygen was the sole gas generated. SEM/EDX, TEM, XPS, EIS and Tafel plot studies showed that the catalytic amplification was created by the PEDOT in the above film. The source of this amplification is proposed to derive from a high catalytically active area coupled with a high activity per unit area under the applied voltage bias. It could be concluded that, in the above film, the PEDOT electrically connected the largest number of catalytic sites (thereby maximizing the catalytically active area) by the shortest, most conductive pathway (thereby minimizing the Tafel slope). That is, the amplification was created by matching the connectivity, conductivity, and catalytic capacity of the film.

3.5 References

1. Alsultan, M.; Ranjbar, A.; Swiegers, G. F.; Wallace, G. G.; Balakrishnan, S.; Huang, J. Application of Conducting Polymers in Solar Water-Splitting Catalysis. In *Industrial Applications for Intelligent Polymers and Coatings*, Hosseini, M.; Makhlouf, A. S. H., Eds. Springer International Publishing: Switzerland, **2016**; pp 223-251.
2. Chen, J.; Wagner, P.; Tong, L.; Wallace Gordon, G.; Officer David, L.; Swiegers Gerhard, F. A Porphyrin-Doped Polymer Catalyzes Selective, Light-Assisted Water Oxidation in Seawater. *Angew.Chem.* **2012**, *124* (8), 1943-1946.
3. Fabbri, E.; Habereder, A.; Waltar, K.; Kotz, R.; Schmidt, T. J. Developments and Perspectives of Oxide-Based Catalysts for the Oxygen Evolution Reaction. *Catal. Sci. Technol.* **2014**, *4* (11), 3800-3821.
4. Liao, C.-H.; Huang, C.-W.; Wu, J. C. S. Hydrogen Production From Semiconductor-Based Photocatalysis via Water Splitting. *Catal.* **2012**, *2* (4), 491-516
5. Kuo, D.-Y.; Kawasaki, J. K.; Nelson, J. N.; Kloppenburg, J.; Hautier, G.; Shen, K. M.; Schlom, D. G.; Suntivich, J. Influence of Surface Adsorption on the Oxygen Evolution Reaction on IrO_2(110). *J. Am. Chem. Soc.*. **2017**, *139* (9), 3473-3479.
6. Pijpers, J. J. H.; Winkler, M. T.; Surendranath, Y.; Buonassisi, T.; Nocera, D. G. Light-Induced Water Oxidation at Silicon Electrodes Functionalized with a Cobalt Oxygen-Evolving Catalyst. *Proc. Natl. Acad. Sci. USA* **2011**, *108* (25), 10056-10061.
7. Jafari, T.; Moharreri, E.; Amin, S. A.; Miao, R.; Song, W.; Suib, L. S. Photocatalytic Water Splitting—The Untamed Dream: A Review of Recent Advances. *Mol.* **2016**, *21* (7), 900 (1-29).
8. Li, X.; Yu, J.; Low, J.; Fang, Y.; Xiao, J.; Chen, X. Engineering Heterogeneous Semiconductors for Solar Water Splitting. *J. Mater. Chem. A* **2015**, *3* (6), 2485-2534.
9. Jing, T.; Dai, Y.; Ma, X.; Wei, W.; Huang, B. Electronic Structure and Photocatalytic Water-Splitting Properties of $Ag_2ZnSn(S_{1-x}Se_x)_4$. *J. Phys. Chem. C* **2015**, *119* (50), 27900-27908.
10. Peter, J. H.; Misra, D. Conducting Polymers and Their Applications. *Electrochem. Soc. Interface* **2012**, *12* (3-4), 61.
11. Gustafson, M. P.; Matsumoto, K.; MacFarlane, D. R.; Winther-Jensen, B. An Investigation of the Properties of Conducting Polymer Alloys for Water Oxidation. *Electrochim. Acta* **2014**, *122*, 166-172.
12. Chowdhury, A. D.; Agnihotri, N.; Sen, P.; De, A. Conducting $CoMn_2O_4$ - PEDOT Nanocomposites as Catalyst in Oxygen Reduction Reaction. *Electrochim. Acta* **2014**, *118*, 81-87.

13. Haubner, K.; Murawski, J.; Olk, P.; Eng Lukas, M.; Ziegler, C.; Adolphi, B.; Jaehne, E. The Route to Functional Graphene Oxide. *ChemPhysChem* **2010**, *11* (10), 2131-2139.
14. Wang, G.; Wang, B.; Park, J.; Yang, J.; Shen, X.; Yao, J. Synthesis of Enhanced Hydrophilic and Hydrophobic Graphene Gxide Nanosheets by a Solvothermal method. *Carbon* **2009**, *47* (1), 68-72.
15. Si, Y.; Samulski, E. T. Synthesis of Water Soluble Graphene. *Nano Lett.* **2008**, *8* (6), 1679-1682.
16. Sharma, D.; Kanchi, S.; Sabela, M. I.; Bisetty, K. Insight into the Biosensing of Graphene Oxide: Present and Future Prospects. *Arab. J. Chem.* **2016**, *9* (2), 238-261.
17. Mohan, V. B.; Brown, R.; Jayaraman, K.; Bhattacharyya, D. Characterisation of Reduced Graphene Oxide: Effects of Reduction Variables on Electrical Conductivity. *Mater. Sci. Eng.: B* **2015**, *193*, 49-60.
18. Gao, P.; Liu, J.; Lee, S.; Zhang, T.; Sun, D. D. High Quality Graphene Oxide–CdS–Pt Nanocomposites for Efficient Photocatalytic Hydrogen Evolution. *J. Mater. Chem.* **2012**, *22* (5), 2292-2298.
19. Liang, Y.; Li, Y.; Wang, H.; Zhou, J.; Wang, J.; Regier, T.; Dai, H. Co_3O_4 Nanocrystals on Graphene as a Synergistic Catalyst for Oxygen Reduction Reaction. *Nat. Mater.* **2011**, *10*, 780.
20. Liu, Q.; Jin, J.; Zhang, J. $NiCo_2S_4$@graphene as a Bifunctional Electrocatalyst for Oxygen Reduction and Evolution Reactions. *ACS Appl. Mater. Interfaces* **2013**, *5* (11), 5002-5008.
21. Long, X.; Li, J.; Xiao, S.; Yan, K.; Wang, Z.; Chen, H.; Yang, S. A Strongly Coupled Graphene and FeNi Double Hydroxide Hybrid as an Excellent Electrocatalyst for the Oxygen Evolution Reaction. *Angew.Chem. Int.Ed.* **2014**, *53* (29), 7584-7588.
22. Gao, M.-R.; Cao, X.; Gao, Q.; Xu, Y.-F.; Zheng, Y.-R.; Jiang, J.; Yu, S.-H. Nitrogen-Doped Graphene Supported $CoSe_2$ Nanobelt Composite Catalyst for Efficient Water Oxidation. *ACS Nano* **2014**, *8* (4), 3970-3978.
23. Ge, X.; Liu, Y.; Goh, F. W. T.; Hor, T. S. A.; Zong, Y.; Xiao, P.; Zhang, Z.; Lim, S. H.; Li, B.; Wang, X.; Liu, Z. Dual-Phase Spinel $MnCo_2O_4$ and Spinel $MnCo_2O_4$ /Nanocarbon Hybrids for Electrocatalytic Oxygen Reduction and Evolution. *ACS Appl. Mater.Interfaces* **2014**, *6* (15), 12684-12691.
24. Ma, W.; Ma, R.; Wang, C.; Liang, J.; Liu, X.; Zhou, K.; Sasaki, T. A Superlattice of Alternately Stacked Ni–Fe Hydroxide Nanosheets and Graphene for Efficient Splitting of Water. *ACS Nano* **2015**, *9* (2), 1977-1984.

25. Yu, X.; Zhang, M.; Yuan, W.; Shi, G. A High-Performance Three-Dimensional Ni-Fe Layered Double Hydroxide/Graphene Electrode for Water Oxidation. *J. Mater. Chem. A* **2015**, *3* (13), 6921-6928.
26. Jiao, L.; Zhou, Y.-X.; Jiang, H.-L. Metal-Organic Framework-Based CoP/Reduced Graphene Oxide: High-Performance Bifunctional Electrocatalyst for Overall Water Slitting. *Chem. Sci.* **2016**, *7* (3), 1690-1695.
27. Cui, X.; Ren, P.; Deng, D.; Deng, J.; Bao, X. Single Layer Graphene Encapsulating Non-Precious Metals as High-Performance Electrocatalysts for Water Oxidation. *Energy Environ. Sci.* **2016**, *9* (1), 123-129.
28. Liu, X.; Liu, W.; Ko, M.; Park, M.; Kim Min, G.; Oh, P.; Chae, S.; Park, S.; Casimir, A.; Wu, G.; Cho, J. Metal (Ni, Co)-Metal Oxides/Graphene Nanocomposites as Multifunctional Electrocatalysts. *Adv. Funct. Mater.* **2015**, *25* (36), 5799-5808.
29. Bikkarolla, S. K.; Papakonstantinou, P. $CuCo_2O_4$ Nanoparticles on Nitrogenated Graphene as Highly Efficient Oxygen Evolution Catalyst. *J. Power Sources* **2015**, *281*, 243-251.
30. Srivastava, M.; Elias Uddin, M.; Singh, J.; Kim, N. H.; Lee, J. H. Preparation and Characterization of Self-Assembled Layer by Layer $NiCo_2O_4$–Reduced Graphene Oxide Nanocomposite with Improved Electrocatalytic Properties. *J. Alloys Compd* **2014**, *590*, 266-276.
31. Zhan, Y.; Xu, C.; Lu, M.; Liu, Z.; Lee, J. Y. Mn and Co Co-substituted Fe_3O_4 Nanoparticles on Nitrogen-Doped Reduced Graphene Oxide for Oxygen Electrocatalysis in Alkaline Solution. *J. Mater. Chem. A* **2014**, *2* (38), 16217-16223.
32. Youn, D. H.; Park, Y. B.; Kim, J. Y.; Magesh, G.; Jang, Y. J.; Lee, J. S. One-Pot Synthesis of NiFe Layered Double Hydroxide/Reduced Graphene Oxide Composite as an Efficient Electrocatalyst for Electrochemical and Photoelectrochemical Water Oxidation. *J. Power Sources* **2015**, *294*, 437-443.
33. Ng, Y. H.; Iwase, A.; Kudo, A.; Amal, R. Reducing Graphene Oxide on a Visible-Light $BiVO_4$ Photocatalyst for an Enhanced Photoelectrochemical Water Splitting. *J. Phys. Chem. Lett.* **2010**, *1* (17), 2607-2612.
34. Guo, J.; Li, Y.; Zhu, S.; Chen, Z.; Liu, Q.; Zhang, D.; Moon, W.-J.; Song, D.-M. Synthesis of WO_3@Graphene Composite for Enhanced Photocatalytic Oxygen evolution From water. *RSC Adv.* **2012**, *2* (4), 1356-1363.
35. Quintana, M.; López, A. M.; Rapino, S.; Toma, F. M.; Iurlo, M.; Carraro, M.; Sartorel, A.; Maccato, C.; Ke, X.; Bittencourt, C.; Da Ros, T.; Van Tendeloo, G.; Marcaccio, M.; Paolucci, F.; Prato, M.; Bonchio, M. Knitting the Catalytic Pattern of Artificial Photosynthesis to a Hybrid Graphene Nanotexture. *ACS Nano* **2013**, *7* (1), 811-817.

36. Li, P.; Jin, Z.; Xiao, D. A One-Step Synthesis of Co-P-B/rGO at Room Temperature with Synergistically Enhanced Electrocatalytic Activity in Neutral Solution. *J. Mater. Chem. A* **2014**, *2* (43), 18420-18427.
37. Yuan, W.; Shen, P. K.; Jiang, S. P. Controllable Synthesis of Graphene Supported MnO_2 Nanowires via Self-Assembly for Enhanced Water Oxidation in Both Alkaline and Neutral Solutions. *J. Mater. Chem. A* **2014**, *2* (1), 123-129.
38. Najafpour, M. M.; Rahimi, F.; Fathollahzadeh, M.; Haghighi, B.; Holynska, M.; Tomo, T.; Allakhverdiev, S. I. Nanostructured Manganese Oxide/Carbon Nanotubes, Graphene and Graphene Oxide as Water-Oxidizing Composites in Artificial Photo synthesis. *Dalton Trans.* **2014**, *43* (28), 10866-10876.
39. Wang, D.; Watanabe, F.; Zhaoa, W. Reduced Graphene Oxide-NiO/Ni Nano membranes as Oxygen Evolution Reaction Electrocatalysts. *ECS J. Solid State Sci. Technol.* **2017**, *6* (6), M 3049-3054.
40. Agegnehu, A. K.; Pan, C.-J.; Rick, J.; Lee, J.-F.; Su, W.-N.; Hwang, B.-J. Enhanced Hydrogen Generation by Cocatalytic Ni and NiO Nanoparticles Loaded on Graphene Oxide Sheets. *J. Mater. Chem.* **2012**, *22* (27), 13849-13854.
41. Bin, D.; Ren, F.; Wang, Y.; Zhai, C.; Wang, C.; Guo, J.; Yang, P.; Du, Y. Pd-Nanoparticle-Supported, PDDA-Functionalized Graphene as a Promising Catalyst for Alcohol Oxidation. *Chem. Asian J.* **2015**, *10* (3), 667-673.
42. Láng Győzö, G.; Ujvári, M.; Vesztergom, S.; Kondratiev, V.; Gubicza, J.; Szekeres Krisztina, J. The Electrochemical Degradation of Poly(3,4-ethylenedioxythiophene) Films Electrodeposited From Aqueous Solutions. *Phys. Chem*. **2016**, *230*(9), 1281-1302.
43. Wei, Z.; Xia, T.; Ma, J.; Feng, W.; Dai, J.; Wang, Q.; Yan, P. Investigation of the Lattice Expansion for Ni Nanoparticles. *Mater. Charact.* **2007**, *58* (10), 1019-1024.
44. Dave, K.; Park, K. H.; Dhayal, M. Two-step Process for Programmable Removal of Oxygen Functionalities of Graphene Oxide: Functional, Structural and Electrical Characteristics. *RSC Adv.* **2015**, *5* (116), 95657-95665.
45. Mhamane, D.; Aravindan, V.; Kim, M.-S.; Kim, H.-K.; Roh, K. C.; Ruan, D.; Lee, S. H.; Srinivasan, M.; Kim, K.-B. Silica-Assisted Bottom-up Synthesis of Graphene-Like High Surface Area Carbon for Highly Efficient Ultracapacitor and Li-ion Hybrid Capacitor Applications. *J. Mater. Chem. A* **2016**, *4* (15), 5578-5591.
46. Yuan, K.; Xu, Y.; Uihlein, J.; Brunklaus, G.; Shi, L.; Heiderhoff, R.; Que, M.; Forster, M.; Chassé, T.; Pichler, T.; Riedl, T.; Chen, Y.; Scherf, U. Straightforward Generation of Pillared, Microporous Graphene Frameworks for Use in Supercapacitors. *Adv. Mater.* **2015**, *27* (42), 6714-6721.

47. Shaikh, A.; Parida, S.; Bohm, S. One Step Eco-Friendly Synthesis of Ag-Reduced Graphene Oxide Nanocomposite by Phytoreduction for Sensitive Nitrite Determination. *RSC Adv.* **2016**, *6* (102), 100383-100391.
48. Benjwal, P.; Kumar, M.; Chamoli, P.; Kar, K. K. Enhanced Photocatalytic Degradation of Methylene Blue and Adsorption of Arsenic(iii) by Reduced Graphene Oxide (rGO)-Metal Oxide (TiO_2/Fe_3O_4) based nanocomposites. *RSC Adv.* **2015**, *5* (89), 73249-73260.
49. Wang, L.; Li, Y.; Han, Z.; Chen, L.; Qian, B.; Jiang, X.; Pinto, J.; Yang, G. Composite Structure and Properties of Mn_3O_4/Graphene Oxide and Mn_3O_4/Graphene. *J. Mater. Chem. A* **2013**, *1* (29), 8385-8397.
50. Choe, J. E.; Ahmed, M. S.; Jeon, S. 3,4-Ethylenedioxythiophene Functionalized Graphene with Palladium Nanoparticles for Enhanced Electrocatalytic Oxygen Reduction Reaction. *J. Power Sources* **2015**, *281*, 211-218.
51. Park, H.; Lee, S. J.; Kim, S.; Ryu, H. W.; Lee, S. H.; Choi, H. H.; Cheong, I. W.; Kim, J.-H. Conducting Polymer Nanofiber Mats via Combination of Electrospinning and Oxidative Polymerization. *Polym.* **2013**, *54* (16), 4155-4160.
52. Wang, M.; Zhou, M.; Zhu, L.; Li, Q.; Jiang, C. Enhanced Polymer Solar Cells Efficiency by Surface Coating of the PEDOT: PSS with Polar Solvent. *Sol. Energy* **2016**, *129*, 175-183.
53. Ji, T.; Tan, L.; Hu, X.; Dai, Y.; Chen, Y. A Comprehensive Study of Sulfonated Carbon Materials as Conductive Composites for Polymer Solar Cells. *Phys. Chem. Chem. Phys.* **2015**, *17* (6), 4137-4145.
54. Kanwat, A.; Jang, J. Extremely Stable Organic Photovoltaic Incorporated with WO_x Doped PEDOT:PSS Anode Buffer Layer. *J. Mater. Chem.C* **2014**, *2* (5), 901-907.
55. Bagri, A.; Mattevi, C.; Acik, M.; Chabal, Y. J.; Chhowalla, M.; Shenoy, V. B. Structural Evolution During the Reduction of Chemically Derived Graphene Oxide. *Nat. Chem.* **2010**, *2*, 581-587.
56. Sridhar, V.; Lee, I.; Chun, H.-H.; Park, H. Hydroquinone as a Single Precursor for Concurrent Reduction and Growth of Carbon Nanotubes on Graphene Oxide. *RSC Adv.* **2015**, *5* (84), 68270-68275.
57. Xing, Z.; Ju, Z.; Zhao, Y.; Wan, J.; Zhu, Y.; Qiang, Y.; Qian, Y. One-Pot Hydrothermal Synthesis of Nitrogen-Doped Graphene as High-Performance Anode Materials for Lithium Ion Batteries. *Sci. Rep.* **2016**, *6*, 26146 (1-10).
58. Yu, H.; Zhang, B.; Bulin, C.; Li, R.; Xing, R. High-Efficient Synthesis of Graphene Oxide Based on Improved Hummers Method. *Sci. Rep.* **2016**, *6*, 36143 (1-7).

59. Zhang, J.; Zeng, D.; Zhao, S.; Wu, J.; Xu, K.; Zhu, Q.; Zhang, G.; Xie, C. Room Temperature NO_2 Sensing: What Advantage Does the rGO-NiO Nanocomposite Have Over Pristine NiO? *Phys. Chem. Chem. Phys.* **2015**, *17* (22), 14903-14911.
60. Kumar, D. R.; Manoj, D.; Santhanalakshmi, J. Electrostatic Fabrication of Oleylamine Capped Nickel Oxide Nanoparticles Anchored Multiwall Carbon Nanotube Nanocomposite: A Robust Electrochemical Determination of Riboflavin at Nanomolar Levels. *Anal. Methods* **2014**, *6* (4), 1011-1020.
61. George, G.; Anandhan, S. Synthesis and Characterisation of Nickel Oxide Nanofibre Webs with Alcohol Sensing Characteristics. *RSC Adv.* **2014**, *4* (107), 62009-62020.
62. Shimizu, K.; Lasia, A.; Boily, J.-F. Electrochemical Impedance Study of the Hematite/Water Interface. *Langmuir.* **2012**, *28* (20), 7914-7920.
63. Swierk, J. R.; Klaus, S.; Trotochaud, L.; Bell, A. T.; Tilley, T. D. Electrochemical Study of the Energetics of the Oxygen Evolution Reaction at Nickel Iron (Oxy)Hydroxide Catalysts. *J. Phys .Chem. C* **2015**, *119* (33), 19022-19029.
64. Brug, G. J.; van den Eeden, A. L. G.; Sluyters-Rehbach, M.; Sluyters, J. H. The Analysis of Electrode Impedances Complicated by the Presence of a Constant Phase Element. *J. Electroanal. Chem. Interfac. Electrochem.* **1984**, *176* (1), 275-295.
65. Pletcher, D.; Sotiropoulos, S. Hydrogen adsorption-Desorption and Oxide Formation-Reduction on Polycrystalline Platinum in Unbuffered Aqueous Solutions. *J. Chem. Soc. Faraday Trans.***1994**, *90* (24), 3663-3668.

Chapter 4

Synergistic Amplification of Catalytic Hydrogen Generation by a Thin-Film Conducting Polymer Composite

Declaration: Portion of this chapter are drawn from a journal article entitled: "*Synergistic Amplification of Catalytic Hydrogen Generation by a Thin-Film Conducting Polymer Composite*", that has been published in *Catalysis Science and Technology* **2018**, *8*, 4169-4179 (DOI: 10.1039/c8cy00780b), for which I, Mohammed Alsultan, was the first author, along with co-authors: Jaechol Choi, Rouhollah Jalili, Pawel Wagner, and Gerhard F. Swiegers. My contribution involved: (i) carrying out the laboratory research and measurements, (ii) constructing the plots and figures from the data obtained, and (iii) writing the first draft of the journal article.

4.1 Introduction

Hydrogen is widely considered to be the ideal fuel for a future clean, sustainable, and environmentally friendly energy technology.[1-2] Not only does hydrogen have a high energy density (122 kJ/g) compared to fossil fuels (e.g. gasoline, 40 kJ/g),[3-4] but it is also non-polluting, generating only water as a waste product. For these reasons, the production of hydrogen via water-splitting in electrochemical (EC) or photo-electrochemical (PEC) cells, has been of particular interest.

Inherently conducting polymers (ICPs) exhibit potentially useful properties as porous, conductive, and light-harvesting supports in catalytic hydrogen-generating ECs/PECs.[5-6] As noted previously, of the various, available ICPs, poly(3,4-ethylenedioxythiophene) (PEDOT) is most attractive.[7-10] As a catalyst of the hydrogen evolution reaction (HER) ($2H^+ + 2e^- \rightarrow H_2$) however, PEDOT generates only very small current densities that typically fall in the low $\mu A/cm^2$ range. For this reason, PEDOT is only of practical interest in combination with other materials and conductors, such as non-conducting polymers (e.g. polyethyleneglycol, PEG),[11-12] carbon materials (e.g. single wall carbon nanotubes),[13] metallic nanoparticles (e.g. Pd),[14] and light-activated semiconductors (e.g. Si).[15] While a number of studies have examined such thin-film PEDOT composites as HER catalysts, few have considered how PEDOT could be deployed to promote the highest possible catalytic activity. One study that considered this question involved a PEDOT-PEG composite that was deposited on a Au-coated Gore-Tex substrate.[12] That system yielded sustained current densities for HER catalysis of 2.2 mA/cm^2 at -0.35 V (vs SCE) in strong acid (1 M H_2SO_4), that were closely comparable to that produced by the industry benchmark HER catalyst, Pt, under the same conditions. The high activity of the PEDOT-PEG derived from the large surface area of the Gore-Tex substrate. The PEG also increased proton diffusion and overall conductivity.[12] To the best of my knowledge, this system appears to be the most active reported PEDOT-based HER electrocatalyst as a proportion of the comparable activity of Pt.

The previous chapter examined the conditions under which thin-film conducting polymer supports may be induced to synergistically amplify water oxidation catalysis beyond what may be expected from the catalyst alone.[16] The conclusion was that the conducting polymer should electrically connect the largest number of catalytic sites by the shortest, least-resistive pathways to thereby achieve: (1) the greatest active area that is also: (2) the most responsive to the applied bias (minimizing the Tafel slope).[11] That is, the connectivity, conductivity and catalytic

capacity of the film should be matched. This approach led to an optimized 0.62 μm thick film (4.2 cm^2) containing PEDOT, nano-Ni (125 mg) and rGO (6.0 mg) that catalyzed water oxidation at a rate that was an order of magnitude greater than an equivalent bare Pt electrode.

While the above approach led to significantly amplified water oxidation catalysis, the same rules should apply to other types of catalysis, like HER catalysis. That is, if the above deductions were valid and a particular ratio of catalyst density to film conductivity and thickness was needed, then the same or a similar ratio should also amplify other forms of catalysis, like HER catalysis. To study whether this was the case, this Chapter examines whether the above combination or a similar ratio thereof, will also amplify catalytic H_2 generation. Nano-Ni should be an H_2-generating (photo)catalyst, while graphene oxide, which is normally insulating and hydrophobic,[17-18] becomes conducting[19-21] and potentially catalytic when reduced to rGO.[22-39]

This chapter reports that an optimized 0.61 μm thick film (4.2 cm^2) containing PEDOT and the very specific ratio of 125 mg nano-Ni and 5.4 mg rGO yields a sustained current density for HER catalysis of 3.6 mA/cm^2 (including ca. 0.2 mA/cm^2 due to the light illumination) at -0.75 V (*vs* Ag/AgCl) in 0.2 M Na_2SO_4 adjusted to pH 1 (by adding 0.05 M H_2SO_4) after 3 h under 0.25 sun. These settings represent the most favourable conditions for HER catalysis under which the nano-Ni is not susceptible to dissolution. This current density was 64% higher than a benchmark, control bare Pt electrode, which produced 2.2 mA/cm^2 under identical conditions. It was also higher than a control film that contained only 125 mg nano-Ni and 5.6 mg rGO, without any PEDOT. Other ratios produced notably lower activities. While the PEDOT acted as a hole (h^+) conductor rather than an electron (e^-) conductor in this case, the remarkable similarity of the composition of the above film and that from the previous chapter strongly support the general proposition that thin-film conducting polymer supports may be induced to synergistically amplify catalysis by connecting the largest number of

catalytic sites by the shortest, most conductive pathways. The above thin-film appears to be the most active PEDOT-based HER catalyst yet reported, as a proportion of the catalytic activity of Pt under the same conditions.

4.2 Results and Discussion

4.2.1 CV studies of control films of nano-Ni/rGO on FTO glass

In the first stage of this study, the most favourable pH and voltage bias conditions were sought to determine the conditions under which HER catalysis by the proposed composite PEDOT/nano-Ni/rGO thin films could be studied without degradation of the films. As PEDOT is known to be stable under even strongly reducing conditions in 1 M H_2SO_4 (pH 0.3),[12] thin-film mixtures of nano-Ni and rGO only (without any PEDOT) that had been spin-coated onto FTO glass and dried, we studied. These films proved to bind robustly to the FTO glass. The nano-Ni had an average diameter of 20 nm; the rGO was prepared as described in the Experimental Section.

To assess the best conditions for HER catalysis by these thin-films, without degradation, their CVs were measured under reducing conditions (-0.25 V to -1.1 V *vs* Ag/AgCl) without light illumination, over a range of pHs (0-12). At a pH of 0, the nano-Ni/rGO films delaminated from the FTO glass, suggesting that one of the components degraded. However, the films were stable to delamination at pH's of 1 and above.

Films having a wide variety of weight ratios of nano-Ni: rGO were studied. All displayed characteristic HER catalytic currents (Figure 4.1). One film had the same weight ratio of 125 mg nano-Ni : 6 mg rGO that had been observed in Chapter 3, to be most active, when combined with PEDOT. The relative current densities of this film at -1.1 V (*vs* Ag/AgCl) during scanning increased from ca. 1.2 mA/cm^2 at pH 12 to ca. 3 mA/cm^2 at pH 1. By contrast, an equivalent, sputtered, bare Pt film on an FTO glass

slide yielded, at pH 1, an onset potential of 0.32 V and a current density of ca. 8 mA/cm^2 at -1.1 V (*vs* Ag/AgCl) (Figure 4.1). It therefore appeared advantageous to study the

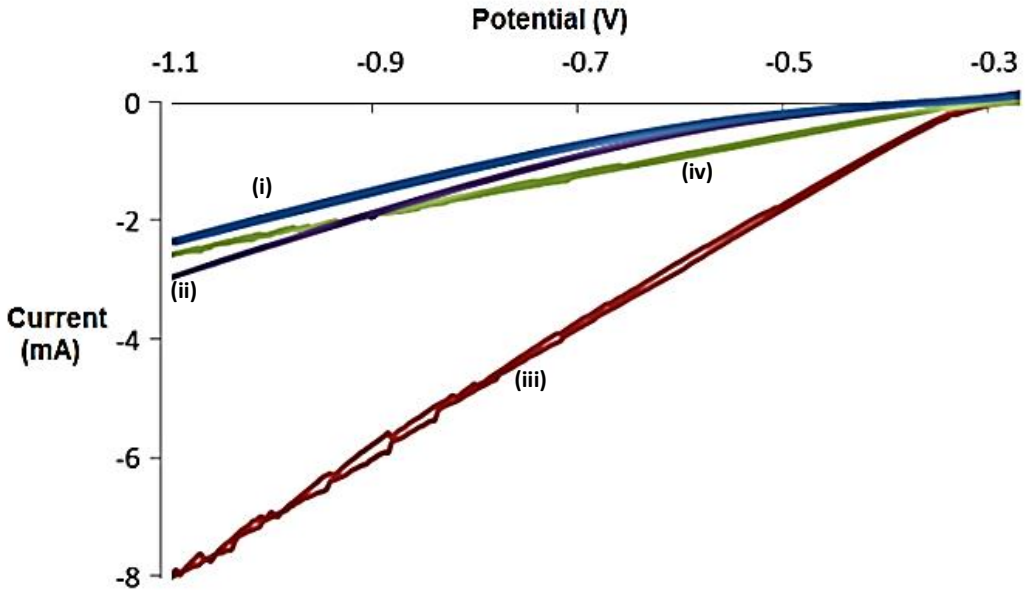

Figure 4.1: *Cyclic voltammograms (vs Ag/AgCl) in 0.05 M H_2SO_4/0.2 M Na_2SO_4 at pH 1 without light illumination, of FTO glass slides having 1 cm^2 active geometric area, coated with: (i)-(ii) nano-Ni/rGO (ratio 125 mg nano-Ni : 6 mg rGO), (i) immediately after preparation and (ii) after 15 scans; or: (iii)-(iv) 100 nm of sputter-coated Pt, (iii) immediately after preparation and (iv) after 15 scans. Scan rate: 5 mV/s.*

proposed PEDOT/Nano-Ni/rGO composite films at a pH of 1. However, the Pourbaix diagram for Ni (Figure 4.2)[40] indicated that at pH 1, Ni is susceptible to oxidation with subsequent formation of soluble Ni(II) at potentials more positive than -0.375 V vs NHE (-0.605 V *vs* Ag/AgCl). At potentials more negative than this, Ni is favored to remain in its metallic state. Accordingly, it was decided to study the proposed PEDOT/nano-Ni/rGO composite films on FTO glass slides in 0.05 M H_2SO_4 / 0.2 M Na_2SO_4 (pH 1) at potentials of -0.75 V vs Ag/AgCl, which was well clear of the -0.605

V threshold. In addition, the film was biased at -0.75 V before placed in electrolyte solution to prevent dissolution of nano-Ni particles.

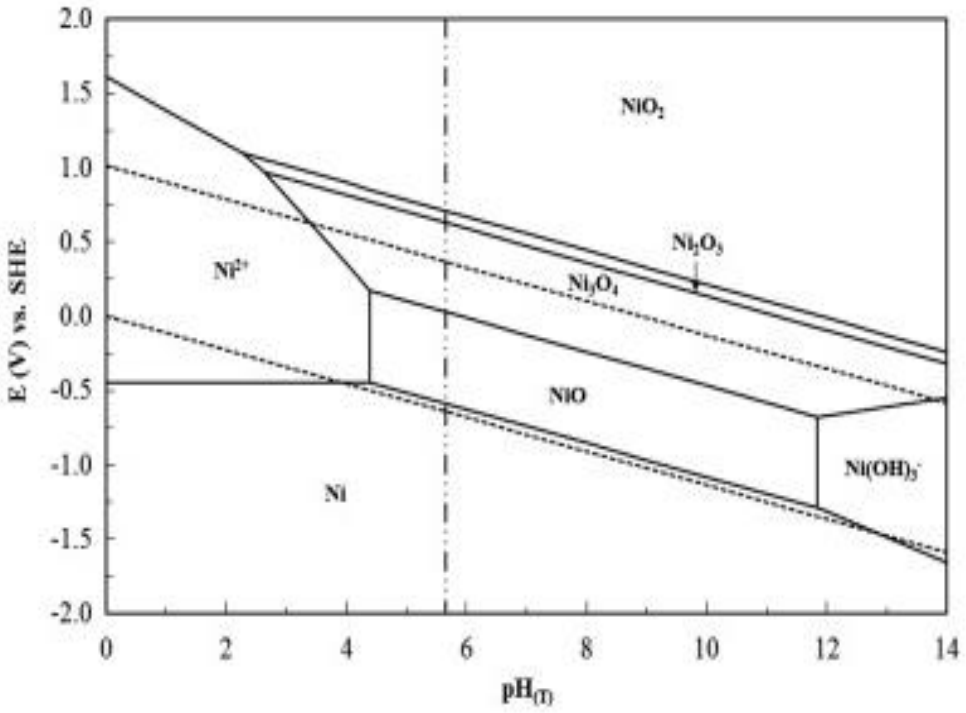

Figure 4.2: *Pourbaix diagram for Ni. Reproduced with permission from ref. 40 (licence number 4471280265777).*

4.2.2 Chronoamperometric Studies of Films of Nano-Ni, rGO, PEDOT, PEDOT/Nano-Ni, PEDOT/rGO, and PEDOT/Nano-Ni/rGO on FTO

In the second stage of this work, PEDOT thin-films were prepared incorporating nano-Ni and/or rGO on FTO glass, using vapor phase polymerization. This technique involved spin-coating a fixed, small volume of an ethanol solution of Fe(III)-*p*TS oxidant (100 mg) that may contain nano-Ni and/or rGO onto an FTO glass slide. The slide was then dried and suspended in a sealed flask above liquid 3,4-

ethylenedioxythiophene (EDOT), causing the formation via vapour phase polymerization (VPP) of a PEDOT film of 55-65 μm thickness. After polymerization, the film was thoroughly washed to remove excess of oxidant and then dried.

The following samples were prepared on FTO glass slides: (i) PEDOT (control), (ii) PEDOT containing nano-Ni (control), (iii) PEDOT containing rGO (control), and (iv) PEDOT containing various mixtures of nano-Ni and rGO. Each of the films were prepared by incorporating nano-Ni (0 mg - 250 mg) and/or rGO (0 mg - 6 mg) in the spin-coating solution for vapour-phase polymerisation, with a uniformly thin PEDOT layer then being formed containing various mixtures of nano-Ni and rGO.

Chronoamperograms were measured at -0.75 V *vs* Ag/AgCl for each sample, as a working electrode in 0.05 M H_2SO_4 / 0.2 M Na_2SO_4, with and without light illumination using a SoLux daylight MR16 halogen light bulb (0.25 sun intensity). The earlier prepared films of nano-Ni/rGO were also tested. A large (2 cm x 2 cm) Pt mesh served as the counter electrode. The control PEDOT film produced a low current density of ca. 46 μA/cm^2 (including a ca. 5 μA/cm^2 photoelectrically-induced photocurrent due to the light illumination) (Figure 4.3(a)(i)). A PEDOT/nano-Ni film yielded a higher, but still low current density of ca. 56 μA/cm^2 (including ca. 9 μA/cm^2 due to the light illumination) (Figure 4.3(a)(ii)). A PEDOT/rGO film generated ca. 70 μA/cm^2 (including ca. 6 μA/cm^2 due to the light illumination) (Figure 4.3(a)(iii)). The low currents suggested that the PEDOT in the control films was coating the additives, particularly the nano-Ni catalyst, and blocking their catalytic activity.

Remarkably however, this did not seem to be a problem with the PEDOT/nano-Ni/rGO films, the most active of which yielded a current density of around 3.6 mA/cm^2 (=3600 μA/cm^2; including ca. 200 μA/cm^2 due to the light illumination) (Figure 4.4(i)). This was about 60-times the current densities of the equivalent PEDOT-containing control films.

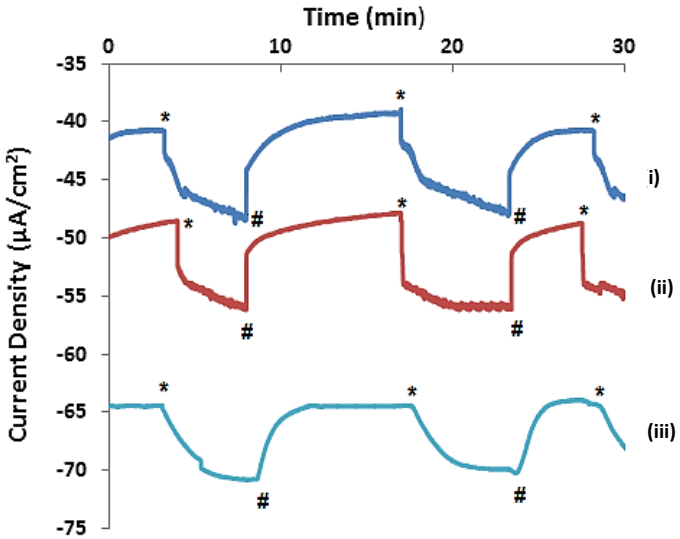

Figure 4.3: *Chronoamperograms at -0.75 V (vs Ag/AgCl) in 0.05 M H_2SO_4/0.2 M Na_2SO_4, after 3 h of operation, with and without light illumination (0.25 sun), of FTO glass slides coated with: (i) PEDOT alone, (ii) PEDOT/nano-Ni (125 mg nano-Ni), and (iii) PEDOT/rGO (5.4 mg rGO) (*='light on', #='light off). Note that the data in graph (b) is in mA/cm^2 and therefore substantially larger than the data in graph (a), which is in μA/cm^2.*

An interesting feature of the performance of the PEDOT/nano-Ni/rGO films was what can only be described as an extreme sensitivity to the proportion of rGO present. The maximum catalytic performance was obtained when the film was made using 5.4 mg rGO in the spin-coated polymerisation solution (Figure 4.4(i)). The presence of a mere 0.6 mg more rGO (6.0 mg; Figure 4.4(ii)) or 0.6 mg less rGO (4.8 mg; Figure 4.4(iii)) in the film led to significant declines in the catalytic activity; namely, to 3.2 mA/cm^2 and 2.8 mA/cm^2 respectively, after 3 h under light illumination. A lesser sensitivity was seen with the nano-Ni, for which 125 mg proved optimum, as described in Chapter 3.[16]

The relatively slow rise times of the photocurrents after the light illumination is switched on has been observed before, and is characteristic of PEDOT.[41]

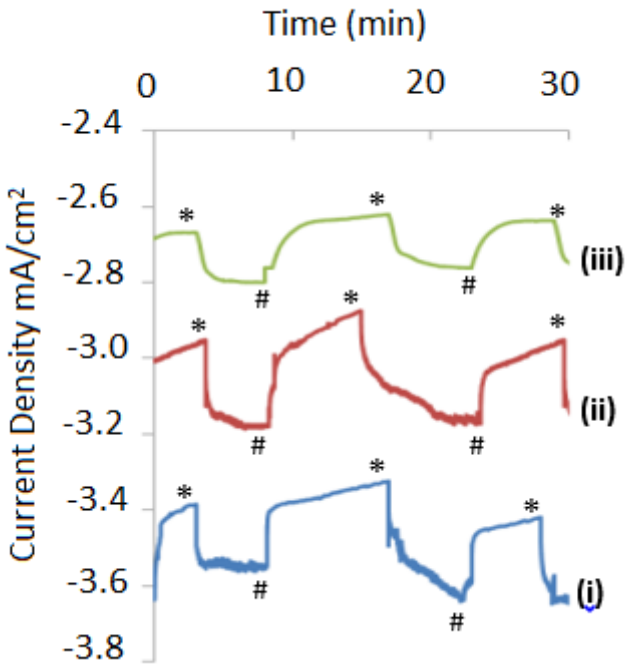

Figure 4.4: *Chronoamperograms at -0.75 V (vs Ag/AgCl) in 0.05 M H_2SO_4/0.2 M Na_2SO_4 (at pH 1) of FTO glass slides coated with: PEDOT/nano-Ni/rGO coatings after 3 h, with and without light illumination, where the coatings all contained 125 mg nano-Ni but with (b)(i) 5.4 mg rGO, (b)(ii) 6.0 mg rGO, or (b)(iii) 4.8 mg rGO (*='light on', #='light off).*

As shown in Figure 4.5, the current density after 3 h under light illumination of the PEDOT/nano-Ni/rGO film containing 125 mg nano-Ni and 5.4 mg rGO (3.6 mA/cm^2; Figure 4.5(i)) substantially exceeded that produced by an equivalent nano-Ni/rGO film, without PEDOT, containing the same ratio of nano-Ni : rGO of 125 mg : 5.4 mg (2.1 mA/cm^2; Figure 4.5 (ii)). The presence of the PEDOT therefore added at least 1.5 mA/cm^2 (or 70%) to the current density. Gas bubbles could be clearly seen to form and release on both films.

By contrast, the bare Pt control electrode generated only ca. 2.2 mA/cm^2 under the same conditions (Figure 5.4 (iii)), which was comparable to the nano-Ni/rGO film (Figure 5.4 (ii)).

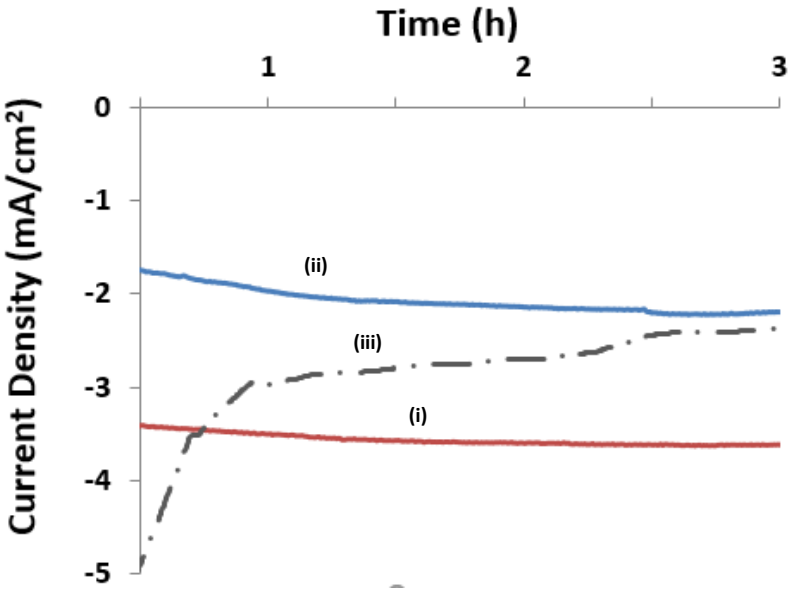

Figure 4.5: *Chronoamperograms at -0.75 V (vs Ag/AgCl) in 0.05 M H_2SO_4/0.2 M Na_2SO_4 of FTO glass slides coated with: (i) PEDOT/nano-Ni/rGO (125 mg nano-Ni/5.4 mg rGO; with light illumination), (ii) nano-Ni/rGO without PEDOT (control) (125 mg nano-Ni/5.4 mg rGO; with light illumination), and (iii) bare Pt (control) (without light illumination). declining sharply, especially over the first 1 h of operation.*[27] *As can be seen in Figure 4(iii), its current density stabilized at a level well below that of the PEDOT/nano-Ni/rGO thin-film composite (Figure 4.5(i)). The presence of the PEDOT was clearly critical to the superior performance.*

4.2.3 Gas Collection Studies of PEDOT/Nano-Ni/rGO on FTO

To determine the identity of the bubbles formed on the most active PEDOT/Nano-Ni/rGO thin film, we collected and tested the gas produced using a specialized, sealed cell (as described in Chapter 2) connected to a dedicated gas chromatograph (as also described in Chapter 2). The GC analysis showed only a single peak whose retention time corresponded to hydrogen (Figure 4.6). Peaks due to other gases, including air nitrogen and/or oxygen, were notably absent. Gas formed on the Pt mesh counter electrode shown to be pure oxygen.

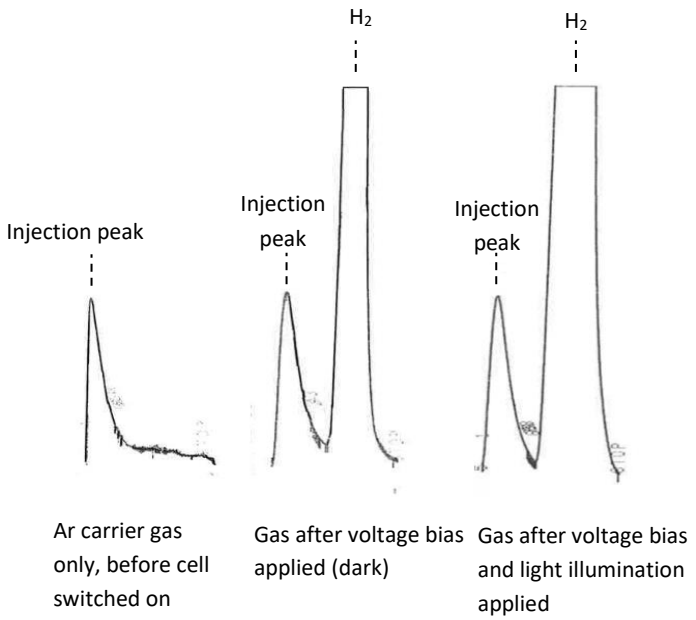

Figure 4.6: *Gas chromatography trace of the gas collected.*

The PEDOT/nano-Ni/rGO film clearly catalysed the HER, with the nano-Ni/rGO components likely producing about 60% of the electrocatalytic effect and a synergistic amplification arising from the PEDOT accounting for the rest. The light-induced current density comprised only about 5% of the total catalytic effect.

4.2.4 Characterisation of the PEDOT/Nano-Ni/rGO Electrode

To determine the composition of the most active PEDOT/Nano-Ni/rGO film on the working electrode, elemental analysis studies were undertaken. Given that the quantity of material in such films was far below the minimum needed for an elemental analysis, multiple identical films were prepared, dried, carefully scraped off the FTO glass, and combined.

Analysis of the combined films indicated that they contained 22.00% Ni, 11.30% S, 48.70% C and no Fe. As only the PEDOT contained the element S, while rGO contained only C and the nano-Ni only Ni, it was possible to calculate the molar ratio of PEDOT : Ni : rGO to be 5.6 (C; PEDOT) : 1 (Ni) : 5.2 (C; rGO). This ratio was

very similar to that previously observed in Chapter 3 to give the largest amplification in catalytic water oxidation.[16]

Scanning Electron Microscopy (SEM), Transmission Electron Microscopy (TEM), X-ray powder diffraction (XRD), and X-ray photoelectron spectroscopy (XPS) analyses were also performed on the PEDOT/nano-Ni/rGO films prior to and after catalytic testing in order to assess structural and chemical changes in the catalytic film.

Figure 4.7(a) depicts a representative SEM image of the most active PEDOT/nano-Ni/rGO film after 3 h of operation, showing that its surface had become more porous. EDX-mapping (Figure 4.7(a), insets) still indicated uniform distributions of Ni (nano-Ni), C (rGO and PEDOT), and S (PEDOT) elements.

Measurements also showed that the above PEDOT/nano-Ni/rGO film, which had been prepared as a layer that was 0.61-0.63 μm thick, had swelled to ca. 0.85 μm thickness upon immersion for 5 min in the 0.05 M H_2SO_4 / 0.2 M Na_2SO_4 electrolyte. After 3 h of operation, it was 0.98 μm thick. Clearly, the PEDOT/nano-Ni/rGO film swelled and became more porous during operation. As in the previous Chapter,[16] TEM showed the PEDOT to separately envelope each of the nano-Ni and the rGO platelets, with little contact between the nano-Ni and the rGO present. The PEDOT generally made seamless contact with the Ni lattice and with the rGO. There was no observable change to these interfaces after 3 h of operation.

Figure 4.8 depicts powder X-ray diffraction (XRD) data for the PEDOT/nano-Ni/rGO film, as compared to control PEDOT (undoped), rGO, and its parent GO. The data did not substantially change over 3 h of operation.

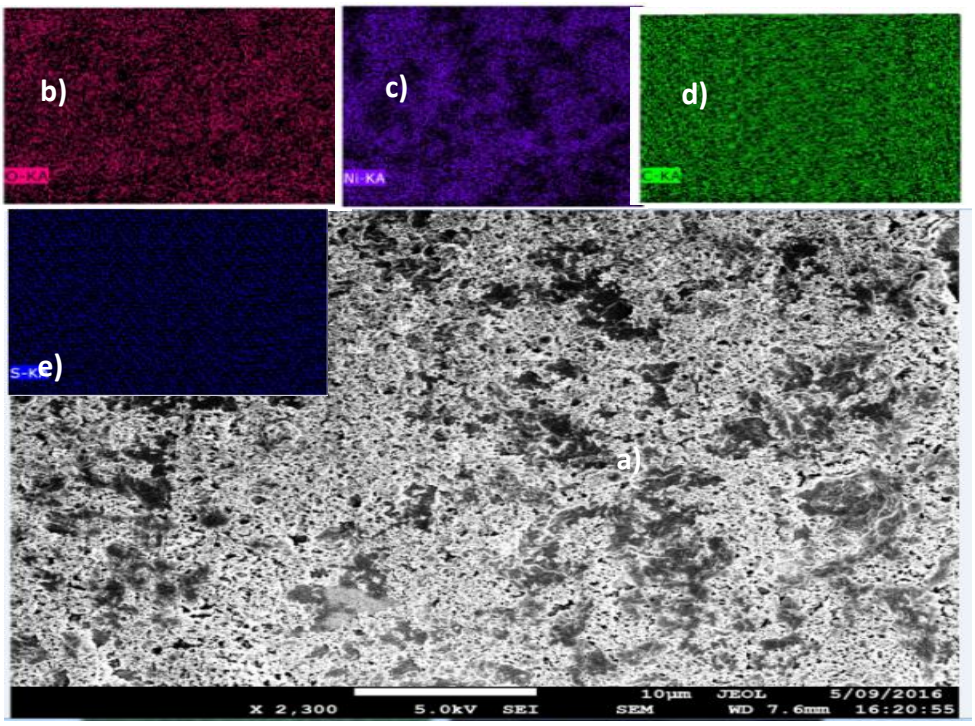

Figure 4.7: *(a) Scanning electron microscope image of PEDOT/Nano-Ni/rGO containing 125 mg nano-Ni and 5.4 mg rGO. The inset images show the elemental distributions, using EDX, of: (b) O, (c) Ni, (d) C, and (e) S.*

As can be seen, the XRD of the GO displayed a distinctive diffraction peak at $2\theta = 10.27°$ due to the (002) carbon crystalline plane, revealing the presence of oxygen functional groups on the graphite sheets.[42-47] The XRD scan of the rGO shows, however, that the sharp peak at 10.2° had disappeared and been replaced by a new broad peak centred at 22.90°, consistent with the oxygen functionalities being significantly reduced.[48-49] As well, a clear diffraction peak at 26.1°, due to the (002) plane in the short-range order of stacked graphene sheets, was visible.[50-51] The XRD of pure PEDOT exhibited a peak at $2\theta = 25.90°$ which could be attributed to the (020) reflection due to the intermolecular spacing of the polymer backbone.[52-53] The XRD of the PEDOT/nano-Ni/rGO film also displayed a broad peak at $2\theta = 17\text{-}25°$ due to the

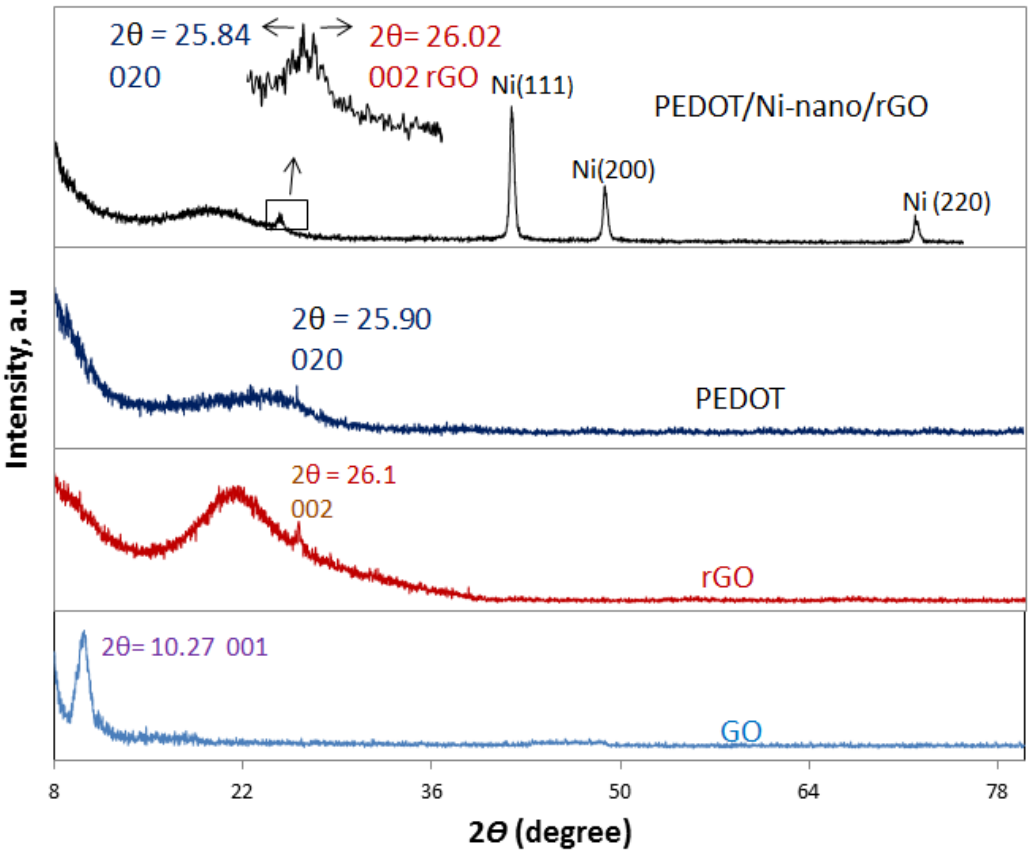

Figure 4.8: *Powder X-ray diffraction (XRD) of PEDOT/Nano-Ni/rGO containing 125 mg nano-Ni and 5.4 mg rGO, relative to control PEDOT, control rGO, and control GO.*

rGO, as well as two peaks at 2θ 25.84° and 26.02° due to the combination of the PEDOT and the rGO. A pattern of three peaks at 44.52°, 51.80° and 76.35° were due to the Ni(111), Ni(200) and Ni(220) planes, confirming the presence of the face centered cubic (fcc) structure of nickel in the nanoparticles.[54]

To determine whether the catalysis altered the chemical states and elemental composition of the PEDOT/nano-Ni/rGO film, it was analysed using XPS after 3 h of operation. The resulting spectra, which were substantially similar, are depicted by the individual data points in Figure 4.9. The modelled spectra, shown by the solid lines in Figure 4.9, closely matched the experimental data.

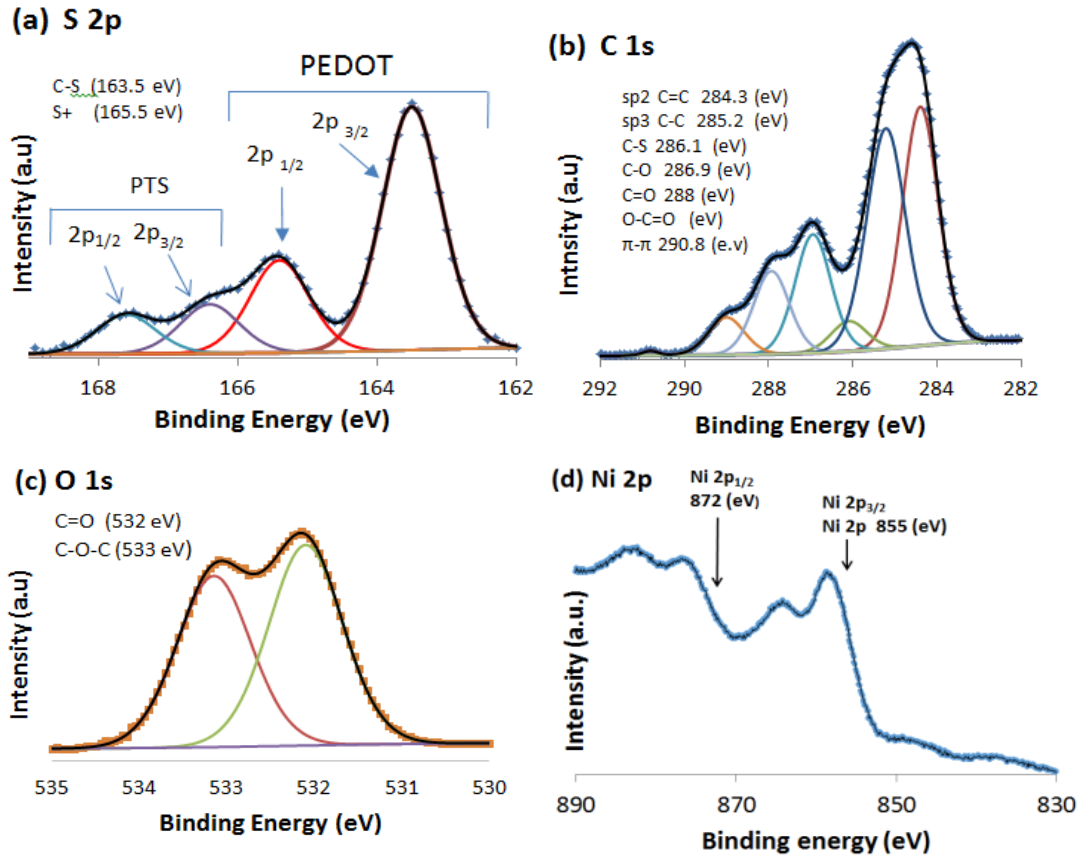

Figure 4.9: *X-ray photoelectron spectroscopy (XPS) of PEDOT/Nano-Ni/rGO containing 125 mg nano-Ni and 5.4 mg rGO, showing measured data (individual data points) and modelled data (solid lines) for the: (a) S 2p, (b) C 1s, (c) O 1s, (d) Ni 2p spectra.*

The main peaks corresponded to O 1s, C 1s, Ni 2p and S 2p. The O 1s and C 1s spectra were associated with both PEDOT and rGO, while the S 2s spectrum derived only from the PEDOT. The C 1s spectrum contained four deconvolution peaks at 284.5, 285.2, 286.90 and 289 eV (Figure 4.9(b)). The peak at 284.5 eV represented a sp^2 carbon hybrid, which related to the C=C binding energy. The peak at 285.2 eV represented a sp^3 carbon hybrid and related to C-S, C-C, and/or C-H binding energies. Finally, the peaks at 288.0 and 289.0 eV related to C=O and O-C=O binding energies, respectively.[55-64] The S 2p spectrum contained peaks at 163.5 and 165.5 eV, which related to the binding energy of the $2p_{3/2}$ and $2p_{½}$ that correspond to the C-S bond and S^+. These were assigned to the S atoms of the PEDOT fragments. The other two small peaks relate to the $2p_{3/2}$ and $2p_{½}$ of the sulfonic groups in the *p*TS structure.[65-68] The O

1s spectrum of the film displayed two peaks at 532 and 533.4 eV. These related to the binding energy of C=O and/or C-O bonds respectively.[69-71] Finally, the Ni 2p spectra exhibited two main peaks at 855 and 872 eV, relating to 1/2 and 3/2 spin respectively.

4.3.5 Electrochemical Impedance Spectroscopy (EIS) and Tafel Plot Studies of the PEDOT/Nano-Ni/rGO

To better understand the origin of the synergistic amplification, EIS and Tafel plot measurements were performed on the most active PEDOT/nano-Ni/rGO electrode and compared to the control films of nano-Ni/rGO containing 125 mg nano-Ni and 5.4 mg rGO (without PEDOT), control bare Pt, and control PEDOT alone, with and without light illumination. The individual data points in Figure 4.10(a) and Figure 4.10(c) depict the measured data from the EIS studies. The bare Pt control produced haphazard, irreproducible data due, most likely, to interference arising from gas bubble formation. For this reason it is not depicted. Figure 4.11 shows the Tafel plots.

As can be seen in the Nyqist and corresponding Bode plots (Figures 4.10 (a),(c)), the performance of the control PEDOT samples, with and without illumination, were governed by diffusion processes with frequencies about the $10^{0.5}$ Hz range. The nano-Ni/rGO and PEDOT/nano-Ni/rGO samples (with and without illumination) were, however, dominated by processes at intermediate frequencies ($10^{1-1.5}$ Hz), which are more typical of interfacial and solution charge transfer processes, like adsorption.[72] High frequency components at 10^{3-4} Hz were not observed (Figure 4.10(a) inset). It can be concluded that catalytic hydrogen generation by nano-Ni/rGO and PEDOT/nano-Ni/rGO (with and without light illumination) was kinetically controlled.

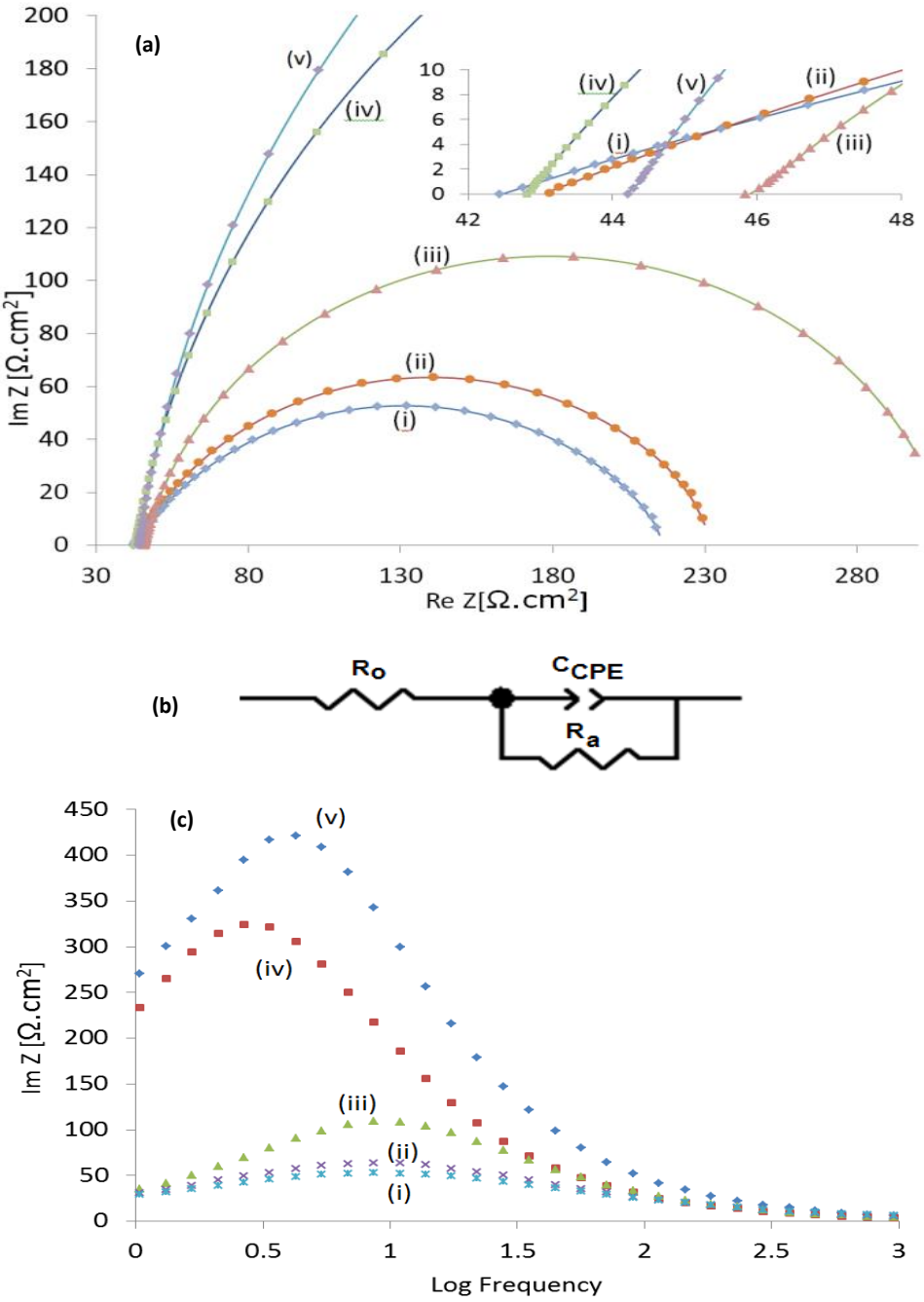

Figure 4.10: *(a) Nyquist plot, (b) equivalent circuit, and (c) Bode plot; at -0.75 V (vs Ag/AgCl); showing measured data (individual data points) and modelled data (solid lines) (modelled using the equivalent circuit depicted in (b)), of: (i) PEDOT/nano-Ni/rGO containing 125 mg nano-Ni and 5.4 mg rGO (with light illumination), (ii) PEDOT/nano-Ni/rGO containing 125 mg nano-Ni and 5.4 mg rGO (without light illumination), (iii) control nano-Ni/rGO (without PEDOT) containing 125 mg nano-Ni and 5.4 mg rGO (with light illumination), (iv) control PEDOT only (with light illumination), and (v) control PEDOT only (without light illumination).*

Accordingly, we modelled the EIS data using the equivalent circuit depicted in Figure 8(b), as used previously.[72-78] The modelled data is shown as the solid lines in Figure 4.10 (a). As can be seen, there is an excellent match between the measured data and the modelled data. Table 4.1 provides results deriving from the modelling, including the ohmic resistance, R_o, solution/interfacial/charge transfer resistance, R_{ct}, and capacitance, which was expressed in terms of a constant phase element (n_{CPE}, and C_{CPE}).[65] The constant phase element provided the best fit of the measured and modelled data.

The value of C_{CPE} showed a notable increase in going from control PEDOT to the nano-Ni/rGO film, to the PEDOT/nano-Ni/rGO film, without and, then, with light illumination. This indicates that the PEDOT/nano-Ni/rGO film had a slightly greater active area than the nano-Ni/rGO film, and a much greater active area than the control PEDOT alone. Illumination of the PEDOT/nano-Ni/rGO with light still further increased its active area.

The PEDOT/nano-Ni/rGO also exhibited more efficient catalysis at -0.75 V *vs* Ag/AgCl, as demonstrated by a lower R_{ct} (173.8 Ω cm^2 with light illumination, vs 189.5 Ω cm^2 without light illumination and 265.6 Ω cm^2 for the nano-Ni/rGO film). The control PEDOT was substantially less active as evidenced by very high R_{ct} values (1005 Ω cm^2 with light illumination, and 749.2 Ω cm^2 without light illumination). The ohmic resistance R_o was similar for each sample, falling in the range 42.43-45.84 Ω cm^2.

Figure 4.11 depicts Tafel plots for the catalysts, with results tabulated in the last two columns of Table 4.1. The exchange current density, i_o, indicates the (intrinsic) catalytic rate for each material at the reversible potential, with an overpotential of zero. As can be seen, the control PEDOT exhibited the highest i_o indicating it to be a good HER catalyst (14.80 mA/cm^2 without light illumination; 15.74 mA/cm^2 with light illumination).

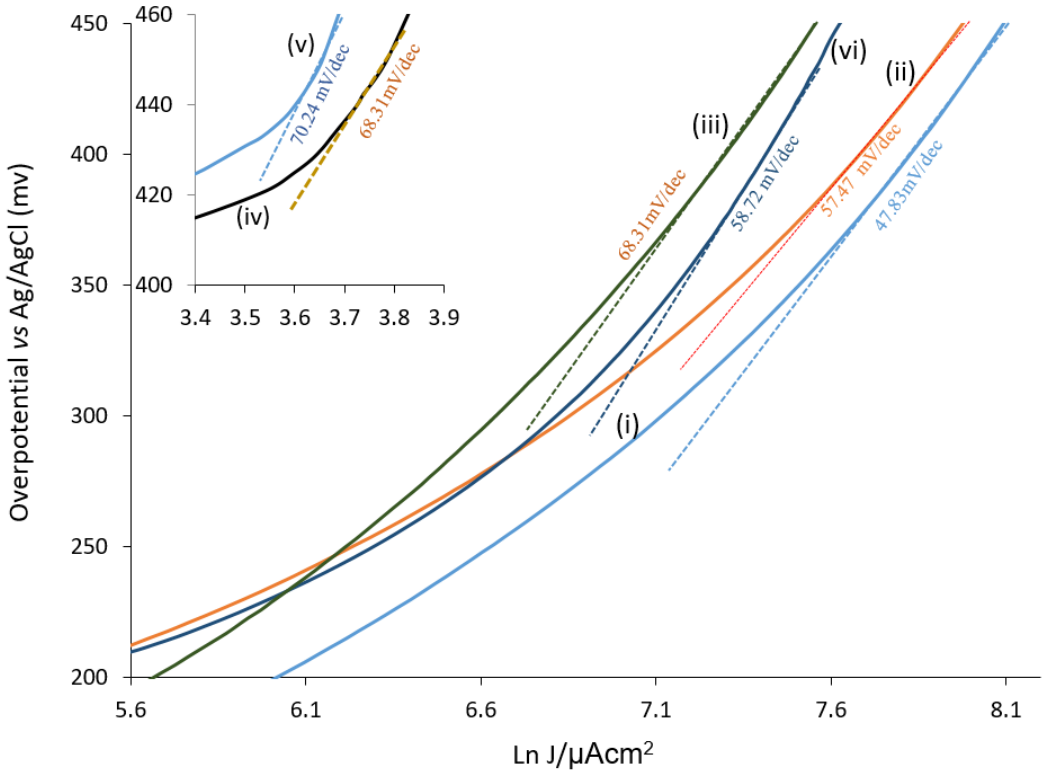

Figure 4.11: *Tafel plots for: (i) PEDOT/nano-Ni/rGO containing 125 mg nano-Ni and 5.4 mg rGO (with light illumination), (ii) PEDOT/nano-Ni/rGO containing 125 mg nano-Ni and 5.4 mg rGO (without light illumination), (iii) control nano-Ni/rGO (without PEDOT) containing 125 mg nano-Ni and 5.4 mg rGO (with light illumination), (iv) control PEDOT only (with light illumination), (v) control PEDOT only (without light illumination), and (vi) control bare Pt.*

The nano-Ni/rGO (without PEDOT) exhibited the highest i_o of the metal-containing catalysts (9.07 mA/cm^2), with the bare Pt control following behind (7.02 mA/cm^2). The PEDOT/nano-Ni/rGO samples with and without light illumination were, in fact, the least intrinsically active. However, their lower Tafel slopes (A), particularly that of PEDOT/nano-Ni/rGO under light illumination, meant that their catalytic activity was more strongly accelerated by the applied bias than the control nano-Ni/rGO and control Pt samples.

Their catalytic activity at -0.75 V (*vs* Ag/AgCl) was 3.6 mA/cm^2 for PEDOT/nano-Ni/rGO *vs*. 2.1 mA/cm^2 for the same quantities of nano-Ni/rGO without the PEDOT. That is, the presence of the PEDOT increased the catalytic rate by 1.5 mA/cm^2. The PEDOT/nano-Ni/rGO was also 64% more active than a benchmark, control bare Pt electrode under identical conditions, which produced 2.2 mA/cm^2. The above thin-film appears to be the most active PEDOT-based HER catalyst yet reported as a proportion of the catalytic activity of Pt under the same conditions.

Sample	**R_o (Ω cm^2)**	**R_{ct} (Ω cm^2)**	**Q_{CPE} ($\mu\Omega^{-1}$cm^{-2}s^n)**	**n_{CPE}**	**C_{CPE} (μFcm^{-2}x10^4)**	**A (mV/dec)**	**i_o (μA cm^2)**
PEDOT (dark)	43.57 ± 2.33	1005.0 ± 5.3	96.3 ± 2.1	0.80 ±0.23	2.43 ± 0.87	70.24 ±4.22	14.80 ±1.23
PEDOT (light)	42.81 ± 2.12	749.2 ± 4.2	105.0 ± 2.0	0.80 ±0.21	2.69 ± 0.77	68.31 ±2.85	15.74 ±2.23
Nano-Ni/rGO (light)	45.84 ± 2.39	265.6 ± 1.2	142.0 ± 2.6	0.81 ± 0.22	4.20 ± 0.72	58.72 ±4.30	9.07 ±1.55
PEDOT/nano-Ni/rGO (dark)	43.38 ± 2.24	189.5 ± 1.3	156.0 ± 2.5	0.80 ± 0.18	4.25 ± 0.62	57.74 ±3.96	6.45 ±1.11
PEDOT/nano-Ni/rGO (light)	42.43 ± 2.11	173.8 ± 1.3	165.0 ± 2.6	0.81 ± 0.16	4.71 ± 0.23	47.83 ±2.34	6.67 ±2.11
Pt	----	-----	-----	----	-----	58.35 ±4.56	7.02 ±3.44

Table 4.1: *Data from modelling of the EIS results in Figure 4.10 (ohmic resistance, Ro, charge transfer resistance, Rct, and charge transfer capacitance (Cct) expressed in terms of a constant phase element (nCPE, and CCPE));[79] and Tafel plots (slope A; exchange current density io). The equivalent circuit in Figure 4.10(b) was used to model the EIS data. ('dark' = without light illumination; 'light' = with light illumination).*

4.3.6 The Mechanism and Origin of the Catalytic Amplification

At -0.75 V, PEDOT is in its non-conducting form, meaning that it does not formally have a capacity to conduct electrons. However, in this state, PEDOT is an

excellent hole (h^+) transporting material, meaning that holes formed on the PEDOT backbone can migrate to the FTO surface.

The catalytic mechanism therefore likely involves protons (H^+) being converted to hydrogen (H_2) on a catalytic site in the thin film coating, with electrons being extracted from a nearby PEDOT chain to facilitate this process. The PEDOT chain is then left with holes (h^+), which migrate through the PEDOT to the surface of the FTO slide, where they are then quenched by electrons provided via the external circuit. The rate at which holes are formed and migrate through the PEDOT to the external circuit will be strongly affected by the applied bias. That is, unlike the previous chapter where the PEDOT acted as electron conductor, in this case the PEDOT acts as a semi-conductor, providing electrons and transporting the resulting holes to the external circuit.

While the mechanism of charge transport by the PEDOT is clearly different in this case, it can, nevertheless, be concluded that the catalytic amplification exhibited by the PEDOT/nano-Ni/rGO film relative to the nano-Ni/rGO control (without PEDOT) derived from a larger active area that was, additionally, more strongly activated by the voltage bias (yielding a lower Tafel slope). That is, also in this case, the presence of the PEDOT synergistically increased the electrochemically active area of the catalyst and made each catalytic site more responsive to the applied bias (i.e. it better transmitted the bias).

Despite the different mechanism of charge transport, the PEDOT therefore connected the largest number of catalytic sites (nano-Ni) by the shortest pathways, as was previously observed for water oxidation catalysis.[11] This is also consistent with a very particular ratio of catalyst density to film conductivity and thickness being needed to amplify the catalytic performance beyond what may have been expected from the catalyst alone. The weight ratio of PEDOT to nano-Ni (125 mg) to rGO (5.4 mg) was, moreover, very similar to that observed in the previous study on water oxidation

catalysis (for which the most active composite involved PEDOT with 125 mg nano-Ni and 6.0 mg rGO).

The above results therefore conform fully with the previously developed conclusions wherein a thin-film conducting polymer could be induced to amplify catalytic performance by synergistically matching the charge conductivity (e^- or h^+) with the catalytic capacity.

In the previous case of water oxidation catalysis,[11] the amplification was almost 10-fold over bare Pt, whereas it was only 1.64-fold higher than Pt in the present case. That can largely be explained by the higher i_o (7.02 μA/cm^2) and relatively lower Tafel slope (58.35 mV/dec) of the control Pt when compared to the most active PEDOT/nano-Ni/rGO thin film (i_o 6.67 μA/cm^2 and Tafel slope 47.83 mV/dec).

The control Pt was likely relatively more active as an HER catalyst than it was as a water oxidation catalyst, at least under the conditions employed. It is also possible that the PEDOT was a better electron conductor in the previous case of water oxidation catalysis than it was a hole conductor in the present case.

Another notable difference is that the control PEDOT alone (without nano-Ni or rGO) appears to have been a relatively better HER catalyst than it had been as a water oxidation catalyst.[11] Thus, it exhibited a higher i_o (14.80 μA/cm^2) coupled with a relatively low Tafel slope (68.31 mV/dec) under light illumination when compared to the most active PEDOT/nano-Ni/rGO thin film (i_o 6.67 μA/cm^2 and Tafel slope 47.83 mV/dec). The relative activity of the PEDOT appears to be borne out by the fact that the catalytic rate of the PEDOT control was limited by diffusion, presumably of protons, into the PEDOT matrix (as demonstrated the Bode plot in Figure 8(c)(iv)).

4. 3 Conclusions

Uniformly thin, vapour phase polymerized PEDOT films containing nano-Ni and rGO, on FTO glass, were examined as (photo)electrocatalysts of hydrogen generation. Composite thin-films incorporating PEDOT : nano-Ni : rGO having 5.6 (C; PEDOT) : 1 (Ni) : 5.2 (C; other) molar ratios yielded current densities of 3.6 mA/cm^2 (including ca. 200 $\mu A/cm^2$ due to light illumination) after 3 h at -0.75 V (vs Ag/AgCl) under 0.25 sun in 0.05 M H_2SO_4/0.2 M Na_2SO_4. The PEDOT substrate of the above film made a substantial contribution to this catalytic performance as demonstrated by the fact that, under identical conditions after 3 h, a nano-Ni/rGO film of equivalent composition, that did not contain PEDOT, generated only 2.1 mA/cm^2. Moreover, a comparable Pt thin film yielded only 2.2 mA/cm^2 after 3 h under identical conditions. Equivalent control PEDOT, PEDOT/nano-Ni, and PEDOT/rGO films were an order of magnitude less catalytically active. Studies confirmed that the PEDOT, likely acting as a hole transport medium, brought about the amplification by connecting the largest number of catalytic sites (nano-Ni) by the shortest, most conductive (for h^+ migration) pathways. Gas chromatography confirmed that hydrogen was the sole gas produced by the most active PEDOT/nano-Ni/rGO thin film. SEM/EDX indicated that the above film displayed a porous, swelled, open structure, in which the PEDOT largely bridges and binds the nano-Ni and rGO materials present. TEM indicated that the PEDOT formed an apparently seamless interface with the nano-Ni lattice and rGO platelets. XRD and XPS analyses confirmed the elemental composition and chemical structure of the composite. In demonstrating that a particular ratio of catalyst density to film conductivity and thickness was needed for the observed catalytic amplification, this work confirmed earlier findings to the same effect.[11]

4. 4 References

1. Züttel, A.; Remhof, A.; Borgschulte, A.; Friedrichs, O. Hydrogen: The Future Energy Carrier. *Philos. Trans. R. Soc. A-Math Phys. Eng. Sci.* **2010**, *368*, 3329-3371.
2. Ogden, J. M. Hydrogen: The Fuel of the Future? *Phys. Today* **2002**, *55* (4), 69-75.
3. Liao, C.-H.; Huang, C.-W.; Wu, J. C. S. Hydrogen Production From Semiconductor-Based Photocatalysis via Water Splitting. *Catal.* **2012**, *2* (4), 491-516.
4. Qi, J.; Zhang, W.; Cao, R. Solar-to-Hydrogen Energy Conversion Based on Water Splitting. *Adv. Energy Mater.* **2017**, *8* (5), 1-16
5. Alsultan, M.; Ranjbar, A.; Swiegers, G. F.; Wallace, G. G.; Balakrishnan, S.; Huang, J. Application of Conducting Polymers in Solar Water-Splitting Catalysis. In *Industrial Applications for Intelligent Polymers and Coatings*, Hosseini, M.; Makhlouf, A. S. H., Eds. Springer International Publishing: Switzerland, **2016**; pp 223-251.
6. Winther-Jensen, B.; MacFarlane, D. R. New Generation, Metal-Free Electrocatalysts for Fuel cells, Solar Cells and Water Splitting. *Energy Environ. Sci.* **2011**, *4* (8), 2790-2798.
7. Long, X.; Li, G.; Wang, Z.; Zhu, H.; Zhang, T.; Xiao, S.; Guo, W.; Yang, S. Metallic Iron–Nickel Sulfide Ultrathin Nanosheets As a Highly Active Electrocatalyst for Hydrogen Evolution Reaction in Acidic Media. *J. Am. Chem. Soc.* **2015**, *137* (37), 11900-11903.
8. Pyshkina, O.; Kubarkov, A.; Vladimir Sergeyev Poly(3,4-ethylenedioxythiophene): Synthesis and Properties. *Sci. J. Riga Techn. Univ.* **2010**, 51-54.
9. Kros, A.; Sommerdijk, N. A. J. M.; Nolte, R. J. M. Poly(pyrrole) Versus Poly(3,4-ethylenedioxythiophene): Implications for Biosensor Applications. *Sens. Actuators B: Chem.* **2005**, *106* (1), 289-295.
10. Carlberg, C.; Chen, X.; Inganäs, O. Ionic Transport and Electronic Structure in Poly(3,4ethylenedioxythiophene). *Solid State Ion.* **1996**, *85* (1), 73-78.
11. Gu, C.; Norris, B. C.; Fan, F.-R. F.; Bielawski, C. W.; Bard, A. J. Is Base-Inhibited Vapor Phase Polymerized PEDOT an Electrocatalyst for the Hydrogen Evolution Reaction? Exploring Substrate Effects, Including Pt Contaminated Au. *ACS Catal.* **2012**, *2* (5), 746-750.
12. Winther-Jensen, B.; Fraser, K.; Ong, C.; Forsyth, M.; MacFarlane Douglas, R. Conducting Polymer Composite Materials for Hydrogen Generation. *Adv. Mater.* **2010**, *22* (15), 1727-1730.

13. Xie, K.; Wu, H.; Meng, Y.; Lu, K.; Wei, Z.; Zhang, Z. Poly(3,4-dinitrothiophene) /SWCNT Composite as a Low Overpotential Hydrogen Evolution Metal-Free Catalyst. *J. Mater. Chem. A* **2015**, *3* (1), 78-82.
14. Pandey, R. K.; Lakshminarayanan, V. Enhanced Electrocatalytic Activity of Pd-Dispersed 3,4-Polyethylenedioxythiophene Film in Hydrogen Evolution and Ethanol Electro-oxidation Reactions. *J. Phys. Chem. C* **2010**, *114* (18), 8507-8514.
15. Li, X.; Lu, W.; Dong, W.; Chen, Q.; Wu, D.; Zhou, W.; Chen, L. Si/PEDOT Hybrid Core/Shell Nanowire Arrays as Photoelectrodes for Photoelectrochemical Water-Splitting. *Nanoscale* **2013**, *5* (12), 5257-5261.
16. Alsultan, M.; Balakrishnan, S.; Choi, a.; Jalili, R.; Tiwari, P.; Wagner, P.; Swiegers, G. F. Synergistic Amplification of Water Oxidation Catalysis on Pt by a Thin-Film Conducting Polymer Composite. *ACS Appl. Energy Mater.* **2018**, advance article (DOI: 10.1021/acsaem.8b00728).
17. Wang, G.; Wang, B.; Park, J.; Yang, J.; Shen, X.; Yao, J. Synthesis of Enhanced Hydrophilic and Hydrophobic Graphene Oxide Nanosheets by a Solvothermal Method. *Carbon* **2009**, *47* (1), 68-72.
18. Khalil, I.; Julkapli, M. N.; Yehye, A. W.; Basirun, J. W.; Bhargava, K. S. Graphene–Gold Nanoparticles Hybrid—Synthesis, Functionalization, and Application in a Electrochemical and Surface-Enhanced Raman Scattering Biosensor. *Mater.* **2016**, *9* (6), 1-38.
19. Sharma, D.; Kanchi, S.; Sabela, M. I.; Bisetty, K. Insight into the Biosensing of Graphene Oxide: Present and Future Prospects. *Arab. J. Chem.* **2016**, *9* (2), 238-261.
20. Devadas, B.; Rajkumar, M.; Chen1, S.-M.; Saraswathi, R. Electrochemically Reduced Graphene Oxide/Neodymium Hexacyanoferrate Modified Electrodes for the Electrochemical Detection of Paracetomol. *Int. J. Electrochem.Sci.* **2012**, *7*, 3339 - 3349.
21. Kim, K. H.; Yang, M.; Cho, K. M.; Jun, Y.-S.; Lee, S. B.; Jung, H.-T. High Quality Reduced Graphene Oxide Through Repairing with Multi-Layered Graphene Ball Nanostructures. *Sci. Rep.* **2013**, *3*, 3251 (1-8).
22. Meng, F.; Li, J.; Cushing, S. K.; Zhi, M.; Wu, N. Solar Hydrogen Generation by Nanoscale p–n Junction of p-Type Molybdenum Disulfide/n-type Nitrogen-Doped Reduced Graphene Oxide. *J. Am. Chem. Soc.* **2013**, *135* (28), 10286-10289.
23. Zheng, X.; Xu, J.; Yan, K.; Wang, H.; Wang, Z.; Yang, S. Space-Confined Growth of MoS_2 Nanosheets Within Graphite: The Layered Hybrid of MoS_2 and Graphene as an Active Catalyst for Hydrogen Evolution Reaction. *Chem. Mater.* **2014**, *26* (7), 2344-2353.

24. Ma, C.-B.; Qi, X.; Chen, B.; Bao, S.; Yin, Z.; Wu, X.-J.; Luo, Z.; Wei, J.; Zhang, H.-L.; Zhang, H. MoS_2 Nanoflower-Decorated Reduced Graphene Oxide Paper for High-Performance Hydrogen Evolution Reaction. *Nanoscale* **2014**, *6* (11), 5624-5629.
25. Peng, S.; Li, L.; Han, X.; Sun, W.; Srinivasan, M.; Mhaisalkar Subodh, G.; Cheng, F.; Yan, Q.; Chen, J.; Ramakrishna, S. Cobalt Sulfide Nanosheet/Graphene/Carbon Nanotube Nanocomposites as Flexible Electrodes for Hydrogen Evolution. *Angew. Chem.* **2014**, *126* (46), 12802-12807.
26. Tang, Y. J.; Gao, M. R.; Liu, C. H.; Li, S. L.; Jiang, H. L.; Lan, Y. Q.; Han, M.; Yu, S. H. Porous Molybdenum-Based Hybrid Catalysts for Highly Efficient Hydrogen Evolution. *Angew. Chem. Int. Ed.* **2015**, *54* (44), 12928-12932.
27. Li, Y.; Wang, H.; Peng, S. Tunable Photodeposition of MoS_2 Onto a Composite of Reduced Graphene Oxide and CdS for Synergic Photocatalytic Hydrogen Generation. *J. Phys. Chem. C* **2014**, *118* (34), 19842-19848.
28. Yan, H.; Tian, C.; Wang, L.; Wu, A.; Meng, M.; Zhao, L.; Fu, H. Phosphorus-Modified Tungsten Nitride/Reduced Graphene Oxide as a High-Performance, Non-Noble-Metal Electrocatalyst for the Hydrogen Evolution Reaction. *Angew. Chem.* **2015**, *127* (21), 6423-6427.
29. Jiao, L.; Zhou, Y.-X.; Jiang, H.-L. Metal-organic Framework-Based CoP/Reduced Graphene Oxide: High-Performance Bifunctional Electrocatalyst for Overall Water Splitting. *Chem. Sci.* **2016**, *7* (3), 1690-1695.
30. Ma, L.; Shen, X.; Zhou, H.; Zhu, G.; Ji, Z.; Chen, K. CoP Nanoparticles Deposited on Reduced Graphene Oxide Sheets as an Active Electrocatalyst for the Hydrogen Evolution Reaction. *J. Mater. Chem. A* **2015**, *3* (10), 5337-5343.
31. Pan, Y.; Yang, N.; Chen, Y.; Lin, Y.; Li, Y.; Liu, Y.; Liu, C. Nickel phosphide Nanoparticles-Nitrogen-Doped Graphene Hybrid as an Efficient Catalyst for Enhanced Hydrogen Evolution Activity. *J. Power Sources* **2015**, *297*, 45-52.
32. Chandrasekaran, S.; Choi, W. M.; Chung, J. S.; Hur, S. H.; Kim, E. J. 3D Crumpled RGO-Co_3O_4 Photocatalysts for UV-Induced Hydrogen Evolution Reaction. *Mater. Lett.* **2014**, *136*, 118-121.
33. Liu, X.; Liu, W.; Ko, M.; Park, M.; Kim Min, G.; Oh, P.; Chae, S.; Park, S.; Casimir, A.; Wu, G.; Cho, J. Metal (Ni, Co)-Metal Oxides/Graphene Nanocomposites as Multifunctional Electrocatalysts. *Adv. Funct. Mater.* **2015**, *25* (36), 5799-5808.
34. Zhang, J.; Wang, Q.; Wang, L.; Li, X. a.; Huang, W. Layer-controllable WS_2-Reduced Graphene Oxide Hybrid Nanosheets with High Electrocatalytic Activity for Hydrogen Evolution. *Nanoscale* **2015**, *7* (23), 10391-10397.
35. Chanda, D.; Hnat, J.; Dobrota, A. S.; Pasti, I. A.; Paidar, M.; Bouzek, K. The effect of Surface Modification by Reduced Graphene Oxide on the Electrocatalytic Activity

of Nickel Towards the Hydrogen Evolution Reaction. *Phys. Chem. Chem. Phys.* **2015**, *17* (40), 26864-26874.

36. Chen, R.; Song, Y.; Wang, Z.; Gao, Y.; Sheng, Y.; Shu, Z.; Zhang, J.; Li, X. a. Porous Nickel Disulfide/Reduced Graphene Oxide Nanohybrids with Improved Electro catalytic Performance for Hydrogen Evolution. *Catal.Commun.* **2016**, *85*, 26-29.
37. Rezaei, B.; Jahromi, A. R. T.; Ensafi, A. A. Ni-Co-Se Nanoparticles Modified Reduced Graphene Oxide Nanoflakes, an Advance Electrocatalyst for Highly Efficient Hydrogen Evolution Reaction. *Electrochim. Acta* **2016**, *213*, 423-431.
38. Tang, Y. J.; Wang, Y.; Wang, X. L.; Li, S. L.; Huang, W.; Dong, L. Z.; Liu, C. H.; Li, Y. F.; Lan, Y. Q. Molybdenum Disulfide/Nitrogen-Doped Reduced Graphene Oxide Nanocomposite with Enlarged Interlayer Spacing for Electrocatalytic Hydrogen Evolution. *Adv. Energy Mater.* **2016**, *6* (12), 1600116.
39. Chen, D.; Zou, L.; Li, S.; Zheng, F. Nanospherical like Reduced Graphene Oxide Decorated TiO_2 Nanoparticles: An Advanced Catalyst for the Hydrogen Evolution Reaction. *Sci. Rep.* **2016**, *6*, 20335 (1-8).
40. Cook, W. G.; Olive, R. P. Pourbaix diagrams for the nickel-water system extended to high-subcritical and low-supercritical conditions. *Corrosion Sci*.**2012**, *58*, 284-290.
41. Chen, J.; Wagner, P.; Tong, L.; Boskovic, D.; Zhang, W.; Officer, D.; Wallace, G. G.; Swiegers, G. F. ALight-Assisted, Polymeric Water Oxidation Catalyst That Selectively Oxidizes Seawater with a Low Onset Potential. *Chem. Sci.* **2013**, *4* (7), 2797-2803.
42. Hu, Z.-A.; Xie, Y.-L.; Wang, Y.-X.; Wu, H.-Y.; Yang, Y.-Y.; Zhang, Z.-Y. Synthesis and Electrochemical Characterization of Mesoporous Co_xNi_{1-x} Layered Double Hydroxides as Electrode Materials for Supercapacitors. *Electrochim. Acta* **2009**, *54* (10), 2737-2741.
43. Liu, X.; Huang, J.; Wei, X.; Yuan, C.; Liu, T.; Cao, D.; Yin, J.; Wang, G. Preparation and Electrochemical Performances of Nanostructured $CoxNi_{1-x}(OH)_2$ Composites for Supercapacitors. *J. Power Sources* **2013**, *240*, 338-343.
44. Zhao, Y.; He, S.; Wei, M.; Evans, D. G.; Duan, X. Hierarchical Films of Layered Double Hydroxides by Using a Sol-Gel Process and Their High Adaptability in Water Treatment. *Chem. Commun.* **2010**, *46* (17), 3031-3033.
45. Xu, J.; Gai, S.; He, F.; Niu, N.; Gao, P.; Chen, Y.; Yang, P. A Sandwich-Type Three-Dimensional Layered Double Hydroxide Nanosheet Array/Graphene Composite: Fabrication and High Supercapacitor Performance. *J. Mater. Chem. A* **2014**, *2* (4), 1022-1031.

46. Satheesh, K.; Jayavel, R. Synthesis and Electrochemical Properties of Reduced Graphene Oxide via Chemical Reduction Using Thiourea as a Reducing Agent. *Mater. Lett.* **2013**, *113*, 5-8.
47. Gupta, R. K.; Alahmed, Z. A.; Yakuphanoglu, F. Graphene Oxide Based Low Cost Battery. *Mater. Lett.* **2013**, *112*, 75-77.
48. Kavinkumar, T.; Manivannan, S. Uniform Decoration of Silver Nanoparticle on Exfoliated Graphene Oxide Sheets and its Ammonia Gas Detection. *Ceram. Int.* **2016**, *42* (1, Part B), 1769-1776.
49. K, M.; RG, B.; IB, A.; SM, S.; Lim HN, L. H.; NM, H.; Chia CH; S, M. Exceedingly Biocompatible and Thin-Layered Reduced Graphene Oxide Nanosheets Using an Eco-Friendly Mushroom Extract Strategy. *Ceram. Int.* **2014**, *10* (1), 1505-1519.
50. Zong, M.; Huang, Y.; Zhao, Y.; Sun, X.; Qu, C.; Luo, D.; Zheng, J. Facile Preparation, High Microwave Absorption and Microwave Absorbing Mechanism of RGO-Fe_3O_4 Composites. *RSC Adv.* **2013**, *3* (45), 23638-23648.
51. Si, Y.; Samulski, E. T. Exfoliated Graphene Separated by Platinum Nanoparticles. *Chem. Mater.* **2008**, *20* (21), 6792-6797.
52. Zhang, L.; Jamal, R.; Zhao, Q.; Wang, M.; Abdiryim, T. Preparation of PEDOT/GO, PEDOT/MnO_2, and PEDOT/GO/MnO_2 Nanocomposites and Their Application in Catalytic Degradation of Methylene Blue. *Nanoscale Res. Lett.* **2015**, *10* (1), 1-9.
53. Jo, S.-H.; Lee, Y.-K.; Yang, J.-W.; Jung, W.-G.; Kim, J.-Y. Carbon Nanotube-Based Flexible Transparent Electrode Ffilms Hybridized with Self-Assembling PEDOT. *Synth. Met.* **2012**, *162* (13), 1279-1284.
54. Jiang, Z.; Xie, J.; Jiang, D.; Wei, X.; Chen, M. Modifiers-Assisted Formation of Nickel Nanoparticles and Their Catalytic Application to p-Nitrophenol Reduction. *Cryst. Eng. Comm.* **2013**, *15* (3), 560-569.
55. Wei, Z.; Xia, T.; Ma, J.; Feng, W.; Dai, J.; Wang, Q.; Yan, P. Investigation of the Lattice Expansion for Ni Nanoparticles. *Mater. Characteriz.* **2007**, *58* (10), 1019-1024.
56. Dave, K.; Park, K. H.; Dhayal, M. Two-Step Process for Programmable Removal of Oxygen Functionalities of Graphene Oxide: Functional, Structural and Electrical Characteristics. *RSC Adv.* **2015**, *5* (116), 95657-95665.
57. Lu, J.; Li, Y.; Li, S.; Jiang, S. P. Self-Assembled Platinum Nanoparticles on Sulfonic Acid-Grafted Graphene as Effective Electrocatalysts for Methanol Oxidation in Direct Methanol Fuel Cells. *Sci. Rep.* **2016**, *6*, 21530 (1-12).
58. Mhamane, D.; Aravindan, V.; Kim, M.-S.; Kim, H.-K.; Roh, K. C.; Ruan, D.; Lee, S. H.; Srinivasan, M.; Kim, K.-B. Silica-Assisted Bottom-up Synthesis of Graphene-

Like High Surface Area Carbon for Highly Efficient Ultracapacitor and Li-ion Hybrid Capacitor Applications. *J. Mater. Chem. A* **2016**, *4* (15), 5578-5591.

59. Yuan, K.; Xu, Y.; Uihlein, J.; Brunklaus, G.; Shi, L.; Heiderhoff, R.; Que, M.; Forster, M.; Chassé, T.; Pichler, T.; Riedl, T.; Chen, Y.; Scherf, U. Straightforward Generation of Pillared, Microporous Graphene Frameworks for Use in Supercapacitors. *Adv. Mater.* **2015**, *27* (42), 6714-6721.
60. Shaikh, A.; Parida, S.; Bohm, S. One Step Eco-Friendly Synthesis of Ag-Reduced Graphene Oxide Nanocomposite by Phytoreduction for Sensitive Nitrite Determination. *RSC Adv.* **2016**, *6* (102), 100383-100391.
61. Benjwal, P.; Kumar, M.; Chamoli, P.; Kar, K. K. Enhanced Photocatalytic Degradation of Methylene Blue and Adsorption of Arsenic(iii) by Reduced Graphene Oxide (rGO)-Metal Oxide (TiO_2/Fe_3O_4) Based Nanocomposites. *RSC Adv.* **2015**, *5* (89), 73249-73260.
62. Wang, L.; Li, Y.; Han, Z.; Chen, L.; Qian, B.; Jiang, X.; Pinto, J.; Yang, G. Composite Structure and Properties of Mn_3O_4/Graphene Oxide and Mn_3O_4/Graphene. *J. Mater. Chem. A* **2013**, *1* (29), 8385-8397.
63. Choe, J. E.; Ahmed, M. S.; Jeon, S. 3,4-Ethylenedioxythiophene Functionalized Graphene with Palladium Nanoparticles for Enhanced Electrocatalytic Oxygen Reduction Reaction. *J. Power Sources* **2015**, *281*, 211-218.
64. Park, H.; Lee, S. J.; Kim, S.; Ryu, H. W.; Lee, S. H.; Choi, H. H.; Cheong, I. W.; Kim, J.-H. Conducting Polymer Nanofiber Mats via Combination of Electrospinning and Oxidative Polymerization. *Polym.* **2013**, *54* (16), 4155-4160.
65. Wang, M.; Zhou, M.; Zhu, L.; Li, Q.; Jiang, C. Enhanced Polymer Solar Cells Efficiency by Surface Coating of the PEDOT: PSS with Polar Solvent. *Sol. Energy* **2016**, *129*, 175-183.
66. Ji, T.; Tan, L.; Hu, X.; Dai, Y.; Chen, Y. A Comprehensive Study of Sulfonated Carbon Materials as Conductive Composites for Polymer Solar Cells. *Phys. Chem. Chem. Phys.* **2015**, *17* (6), 4137-4145.
67. Kanwat, A.; Jang, J. Extremely stable organic photovoltaic incorporated with WOx doped PEDOT:PSS anode buffer layer. *J. Mater. Chem. C* **2014**, *2* (5), 901-907.
68. Bagri, A.; Mattevi, C.; Acik, M.; Chabal, Y. J.; Chhowalla, M.; Shenoy, V. B. Structural Evolution During the Reduction of Chemically Derived Graphene Oxide. *Nat. Chem.* **2010**, *2*, 581.
69. Sridhar, V.; Lee, I.; Chun, H.-H.; Park, H. Hydroquinone as a Single Precursor for Concurrent Reduction and Growth of Carbon Nanotubes on Graphene Oxide. *RSC Adv.* **2015**, *5* (84), 68270-68275.

70. Xing, Z.; Ju, Z.; Zhao, Y.; Wan, J.; Zhu, Y.; Qiang, Y.; Qian, Y. One-Pot Hydrothermal Synthesis of Nitrogen-Doped Graphene as High-Performance Anode Materials for Lithium Ion Batteries. *Sci. Rep.* **2016**, *6*, 26146 (1-10).
71. Yu, H.; Zhang, B.; Bulin, C.; Li, R.; Xing, R. High-efficient Synthesis of Graphene Oxide Based on Improved Hummers Method. *Sci. Rep.* **2016**, *6*, 36143 (1-7).
72. Ensafi, A. A.; Heydari-Soureshjani, E.; Jafari-Asl, M.; Rezaei, B. Polyoxometalate-Decorated Graphene Nanosheets and Carbon Nanotubes, Powerful Electrocatalysts for Hydrogen Evolution Reaction. *Carbon* **2016**, *99*, 398-406.
73. Nady, H.; Negem, M. Ni-Cu Nano-Crystalline Alloys for Efficient Electrochemical Hydrogen Production in Acid Water. *RSC Adv.* **2016**, *6* (56), 51111-51119.
74. Qiang, Y.; Guo, L.; Zhang, S.; Li, W.; Yu, S.; Tan, J. Synergistic Effect of Tartaric Acid with 2,6-diaminopyridine on the Corrosion Inhibition of Mild Steel in 0.5 M HCl. *Sci. Rep.* **2016**, *6*, 33305 (1-13).
75. Fiegenbaum, F.; de Souza, M. O.; Becker, M. R.; Martini, E. M. A.; de Souza, R. F. Electrocatalytic Activities of Cathode Electrodes for Water Electrolysis Using Tetra-Alkyl-Ammonium-Sulfonic Acid Ionic Liquid as Electrolyte. *J. Power Sources* **2015**, *280*, 12-17.
76. Jafari, H.; Akbarzade, K.; Danaee, I. Corrosion Inhibition of Carbon Steel Immersed in a 1M HCl Solution Using Benzothiazole Derivatives. *Arab. J. Chem.* **2014**,1-8.
77. Ren, B.; Li, D.; Jin, Q.; Cui, H.; Wang, C. Novel Porous Tungsten Carbide Hybrid Nanowires on Carbon Cloth for High-Performance Hydrogen Evolution. *J. Mater. Chem.A* **2017**, *5* (25), 13196-13203.
78. Konkena, B.; junge Puring, K.; Sinev, I.; Piontek, S.; Khavryuchenko, O.; Dürholt, J. P.; Schmid, R.; Tüysüz, H.; Muhler, M.; Schuhmann, W.; Apfel, U.-P. Pentlandite Rocks as Sustainable and Stable Efficient Electrocatalysts for Hydrogen Generation. *Nat. Commun.* **2016**, *7*, 1-8.
79. Brug, G. J.; van den Eeden, A. L. G.; Sluyters-Rehbach, M.; Sluyters, J. H. The Analysis of Electrode Impedances Complicated by The Presence of a Constant Phase Element. *J. Electroanal. Chem. Interfac. Electrochem.***1984**, *176* (1), 275-295

Chapter 5

Synergistic Amplification of Catalytic Oxygen and Hydrogen Generation from Water by Thin-Film Polypyrrole Composites

Declaration: Portions of this chapter are drawn from a draft journal article entitled: "*Synergistic Amplification of (Photo)Catalytic Oxygen and Hydrogen Generation from Water by Thin-Film Polypyrrole Composites"*, for which I, Mohammed Alsultan, am the first author, along with co-authors: Jaechol Choi, Rouhollah Jalili, Pawel Wagner, and Gerhard F. Swiegers. My contribution involved: (i) carrying out the laboratory research and measurements, (ii) constructing the plots and figures from the data obtained, and (iii) writing the first draft of the journal article.

5.1 Introduction

Thin film conducting polymers (CP) have been widely used to immobilize electrocatalysts and photoelectrocatalysts, especially in applications, where oxygen (O_2) and/or hydrogen (H_2) are generated from water.[1] Polypyrrole (PPy) is an inexpensive conducting polymer that is thermodynamically stable and readily prepared by polymerization of its monomer.[1] Light-activated water-splitting semiconductors like CdS, TiO_2 and ZnO display enhanced performances when coated with a thin layer of PPy.[1] In these applications, the semiconductor typically extracts electrons from the low bandgap PPy, which excites electrons in response to visible light. The electrons are

sufficiently energetic to reduce water to hydrogen. The holes that remain on the PPy are then also able to oxidize water, generating oxygen gas.[1]

There are believed to be three important features of PPy that make it useful for catalytic water-splitting applications when combined with a semiconductor:[1] (1) PPy has a bandgap (2.6 eV) that enhances photoelectrochemical performance under visible light, (2) the conductivity of PPy accelerates electron transfer during hole creation, and (3) the stability of PPy suppresses photo-corrosion of the solid-state semiconductor, thereby enhancing the stability of the system to water oxidation. PPy is also stable in acidic and neutral solutions, helping to prevent electron–hole recombination reactions (backward reactions).[1-3]

The chemical structures and doping method play a significant role in determining the properties of the PPy in such fabricated photoelectrodes. However, practical guidelines as to how best to deploy thin-film PPy layers have been notably absent.

In previous chapters the conditions under which thin-film conducting polymer supports may be induced to synergistically amplify catalytic performance beyond what may be expected from the catalyst only, have been studied. These studies showed that uniformly deposited poly(3,4-ethylenedioxythiophene) (PEDOT) composites containing very specific ratios of catalysts (nanoparticulate Ni, 'nano-Ni') and conductors (reduced graphene oxide, rGO) yielded substantially larger (photo)currents than equivalent, control films, including films that contained the same quantities of catalysts and conductors without the PEDOT. They also significantly out-performed the industry-standard, benchmark catalyst for water-splitting, Pt.

In order to further understand this effect, it was of interest to examine it with another conducting polymer that had a dissimilar capacity for catalysing water-splitting. In this chapter, synergistic amplification of catalytic oxygen and hydrogen-generation by thin-film polypyrrole composites containing nano-Ni and rGO are discussed. Very similar component ratios to those previously observed with PEDOT,

also yielded the largest possible catalytic amplifications. The amplifications were, however, substantially smaller than those produced with PEDOT.

5.2 Results and Discussion

5.2.1 Studies of PPy/nano-Ni/rGO on FTO and Pt as Water Oxidation (Photo) Catalysts

5.2.1.1 Preparation and Optimization of the PPy/nano-Ni/rGO thin film for Catalytic Oxygen Generation

In the first stage of this study, uniformly deposited thin-films were prepared of vapour-phase polymerized PPy containing varying quantities of nano-Ni (av. 20 nm diameter) and rGO on FTO glass slides (4.2 cm^2). Their performance was then tested in water oxidation (photo) catalysis in 0.2 M Na_2SO_4 aqueous solution, with the pH adjusted to 12, while biased at 0.8 V (*vs* Ag/AgCl). These voltage and pH conditions were the same as those in employed in Chapter 3 involving thin-film PEDOT/nano-Ni/rGO water oxidation (photo)catalysis. As in the previous study, GO was initially incorporated into the PPy and then thereafter partially electrochemically reduced to rGO (with a charge exchanged, in this case, of 1.9 x 10^{-6} C).

The observed trends in respect of the composition of the most active thin-film were identical to those in Chapter 3, with the highest performing sample also containing 125 mg of nano-Ni and 6.0 mg of rGO. (Figure 5.1 and Figure 5.2). The dark currents (0.35-0.50 mA/cm^2) and full currents under light illumination (0.80-0.90 mA/cm^2, including photocurrents) of the most active PPy/nano-Ni/rGO were, however, generally lower than those of the equivalent PEDOT/nano-Ni/rGO thin film.

Table 5.1 provides a comparison of the dark currents and currents under light illumination for the most active of the PPy/nano-Ni/rGO films *vs* the most active

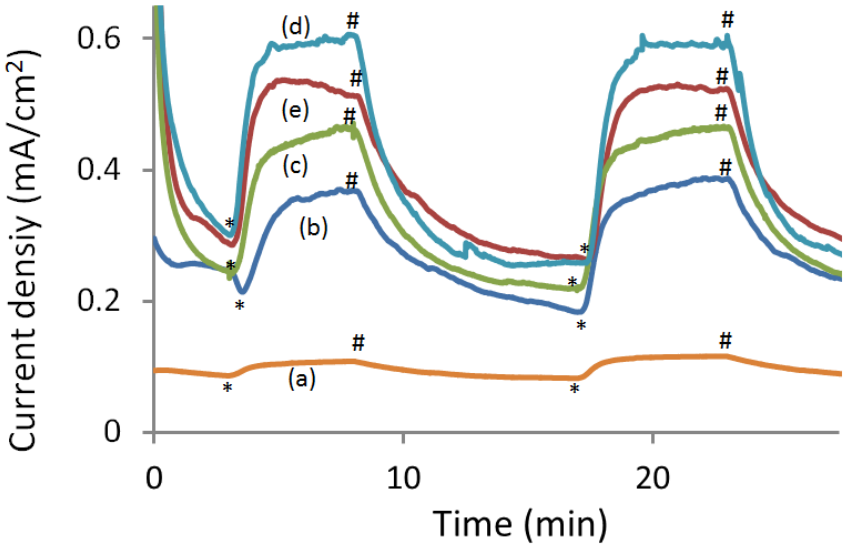

Figure 5.1: *Chronoamperograms at 0.8 V (vs. Ag/AgCl) in 0.2 M Na_2SO_4 (pH 12), with and without light illumination (0.25 sun), of FTO glass slides coated with: PPy/Nano-Ni, where the quantity of nano-Ni in the vapour phase polymerisation solution was: (a) 0 mg nano-Ni (PPy only; control), (b) 20 mg nano-Ni, (c) 100 mg nano-Ni, (d) 125 mg nano-Ni, and (e) 135 mg nano-Ni. (*='light on', #='light off').*

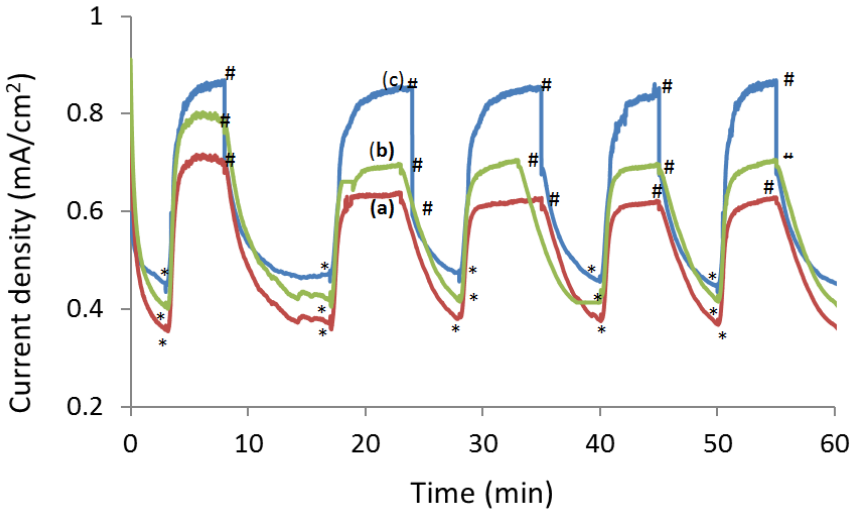

Figure 5.2: *Chronoamperograms at 0.80 V (vs Ag/AgCl) in 0.2 M Na_2SO_4 (pH 12) over 1 h of operation, with and without light illumination (0.25 sun), of FTO glass slides coated with thin films of PPy/nano-Ni/rGO, where the polymerisation mixtures contained 125 mg of nano-Ni and the following quantities of rGO: (a) 4.8 mg, (b) 5.4 mg, and (c) 6.0 mg. (*='light on', #='light off').*

Composition of thin film (CP=conducting polymer)	**Current density in dark (mA/cm^2)**		**Current density in light (mA/cm^2)**	
	PPy	**PEDOT**	**PPy**	**PEDOT**
CP : 100 mg nano-Ni	**0.21-0.24**	0.23-0.25	**0.45-0.46**	0.54-0.55
CP : 135 mg nano-Ni	**0.27-0.30**	0.28-0.29	**0.52-0.53**	0.57-0.58
CP : 125 mg nano-Ni	**0.25-0.26**	0.26-0.27	**0.58-0.59**	0.65-0.66
CP : 125 mg nano-Ni: 4.8 mg rGO	**0.36-0.37**	0.34-0.37	**0.61-0.62**	0.62-0.65
CP : 125 mg nano-Ni: 5.4 mg rGO	**0.41-0.43**	0.57-0.61	**0.68-0.69**	0.84-0.86
CP : 125 mg nano-Ni: 6.0 mg rGO	**0.43-0.47**	0.62-0.75	**0.84-0.86**	0.98-1.15

Table 5.1: *Comparison of results from chronoamperograms at 0.80 V (vs Ag/AgCl) in 0.2 M Na_2SO_4 (pH 12) over 1 h of operation, with and without light illumination (0.25 sun), of FTO glass slides coated with thin films of PPy/nano-Ni/rGO or PEDOT/nano-Ni/rGO.*

Composition of thin film (CP=conducting polymer)	**Thickness (µm)**		**Conductivity (S/cm^2)**	
	PPy	**PEDOT**	**PPy**	**PEDOT**
CP : 125 mg nano-Ni: 4.8 mg rGO	**0.63**	0.61	**6.06**	8.30
CP : 125 mg nano-Ni: 5.4 mg rGO	**0.65**	0.61	**6.90**	8.53
CP : 125 mg nano-Ni: 6.0 mg rGO	**0.66**	0.62	**7.78**	8.56
125 mg nano-Ni: 6.0 mg rGO	0.58		3.80	

Table 5.2 *Typical conductivities and thicknesses of PPy and PEDOT thin films.*

PEDOT/nano-Ni/rGO films under the same conditions. The results clearly show that the performance of the PEDOT-containing films was not significantly different to the PPy-containing films when only nano-Ni was present. However, the further addition of increasing amounts of rGO more strongly amplified the performance of the PEDOT-containing films relative to the PPy-containing films. That is, increasing conductivity had a stronger effect in the former than the latter thin films.

Table 5.2 provides a comparison of thickness and conductivity for the most active of the PPy/nano-Ni/rGO films *vs* the most active PEDOT/nano-Ni/rGO films under the same conditions of rGO ratios. Practically, it was observed that increases in the amounts of rGO

present resulted in enhancements of the conductivity of both PEDOT and PPy-containing films. Secondly, PEDOT-containing films had, in general, lower thicknesses and were more conductive compared to the same ratios of rGO in PPy-containing films.

5.2.1.2 Performance of Control Thin Films

Figure 5.3 depicts chronoamperograms of the control coatings, over 1 h (I) and over the first few minutes (II). As can be seen, they all yielded notably lower currents compared to PPy/nano-Ni/rGO containing 125 mg nano-Ni and 6.0 mg rGO (Figure 5.3(c)). For example, the control coating comprised of 6.0 mg rGO and 125 mg nano-Ni only (without any PPy) yielded a current density under light illumination of 0.65-0.70 mA/cm^2, which was around 25% lower than the current density of the PPy film containing 125 mg nano-Ni and 6.0 mg rGO. That is, the presence of the PPy in the most active thin film amplified the current density by 25%.

Figure 5.3(II) also shows that all of the alternative oxidation processes (involving oxidation or partial oxidation of the components of the film themselves) were complete within 3 min, with stable dark currents obtained thereafter. The charge involved in oxidation of the PPy itself (Figure 3(II)(b) was calculated to be 0.379 C, while the charge required to oxidize the nano-Ni surface to Ni oxide was 0.293 C.

5.2.1.3 Performance of the Most Active PPy/nano-Ni/rGO thin film on Pt

We further tested the most active PPy/nano-Ni/rGO thin film on a sputtered, bare Pt electrode. The film had a thickness of 0.66 μm, with a conductivity (measured on a non-conducting glass slide) of 7.78 S/cm. Figure 5.4(c) shows that, on Pt/FTO, the thin film produced dark currents of 0.40-0.50 mA/cm^2 and photocurrents of 0.47-0.50 mA/cm^2 to give a total current of 0.90-0.97 mA/cm^2 (Figure 5.4(c)), which was far in excess of the currents generated by the bare Pt film (0.15 mA/cm^2) (Figure 5.4(b)).

They were also larger than the equivalent currents of the control PPy alone (Figure 5.4(a)). The higher currents of the PPy/nano-Ni/rGO on Pt/FTO compared to FTO alone can be ascribed to the diminished sheet resistance arising from the presence of the more conductive metallic Pt layer on the Pt/FTO substrate.

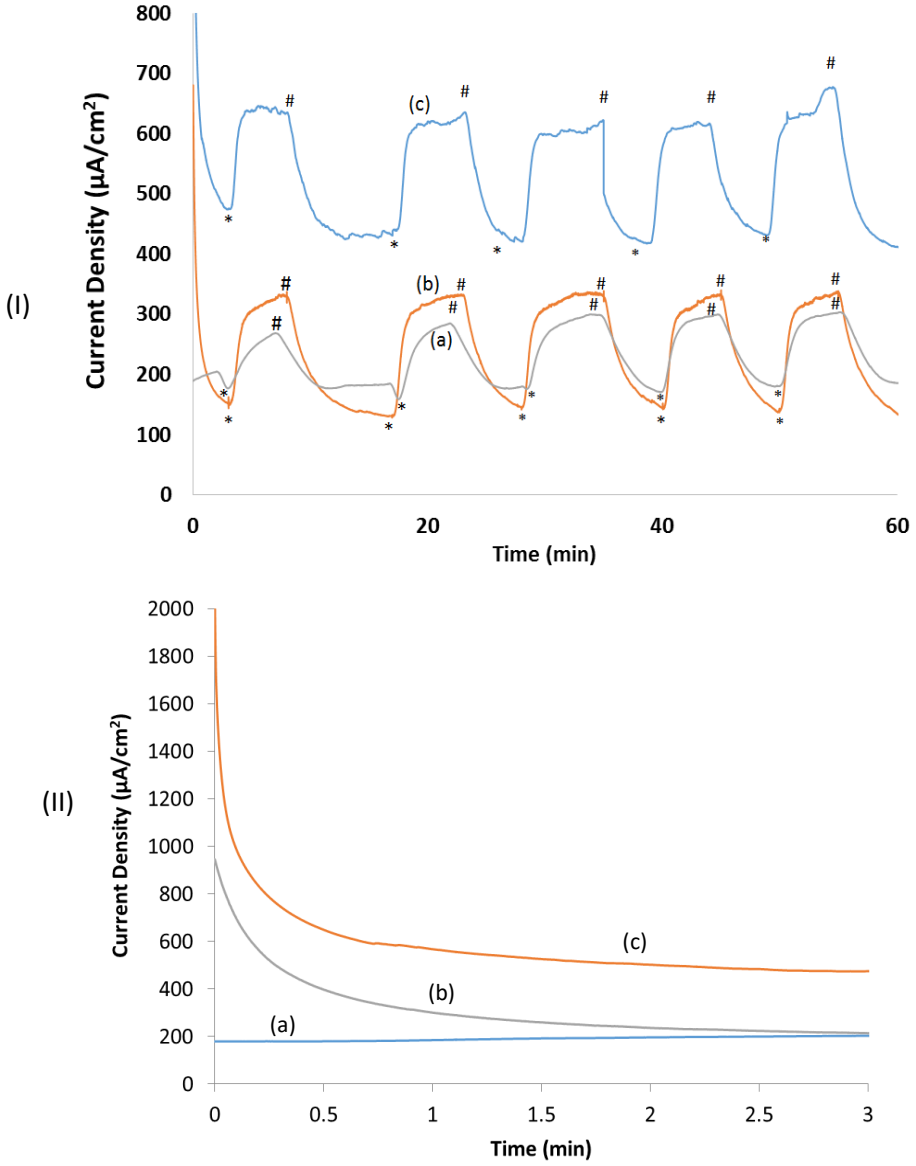

Figure 5.3: *Chronoamperograms over 1 h (I) and in the first few minutes (II) at 0.80 V (vs Ag/AgCl) in 0.2 M Na_2SO_4 (pH 12), with and without light illumination (0.25 sun), of FTO glass slides coated with control thin films comprising of: (a) 6.0 mg rGO only, (b) PPy containing 6.0 mg rGO, and (c) 6.0 mg rGO and 125 mg nano-Ni only (without any PPy). (*='light on', #='light off').*

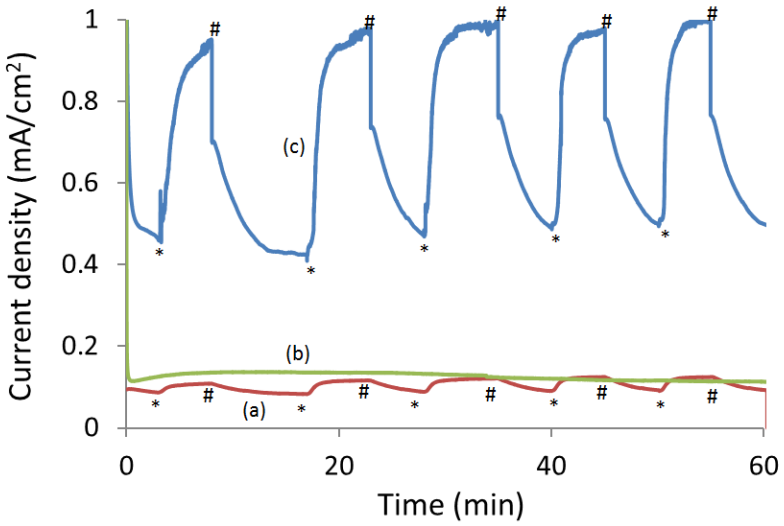

Figure 5.4: *Chronoamperograms at 0.80 V (vs Ag/AgCl) in 0.2 M Na_2SO_4 (pH 12) over 1 h of operation, with and without light illumination (0.25 sun), of FTO glass slides coated with thin films of: (a) bare Pt, (b) Pt overcoated with PPy/nano-Ni/rGO containing 125 mg nano-Ni and 6.0 mg rGO, and (c) PPy only (control). (*='light on', #='light off').*

Table 5.3 summarises the data and provides a comparison with the same data where PEDOT was the conducting polymer. As can be seen, the trends are very similar for PPy and PEDOT, with the PEDOT slightly outperforming the PPy.

Composition of thin film (CP=conducting polymer)	**Current density in dark (mA/cm²)**		**Current density in light (mA/cm²)**	
	PPy	**PEDOT**	**PPy**	**PEDOT**
CP : 125 mg nano-Ni: 6.0 mg rGO	**0.43-0.47**	0.62-0.75	**0.93-1.00**	1.10-1.15
CP only	0.07-0.08	0.06-0.07	0.10-0.11	0.08-0.09
Bare Pt	0.136-0.150		0.136-0.150	

Table 5.3: *Comparison of results from chronoamperograms at 0.80 V (vs Ag/AgCl) in 0.2 M Na_2SO_4 (pH 12) over 1 h of operation, with and without light illumination (0.25 sun), of FTO glass slides coated with thin films of PPy/nano-Ni/rGO or PEDOT/nano-Ni/rGO vs controls.*

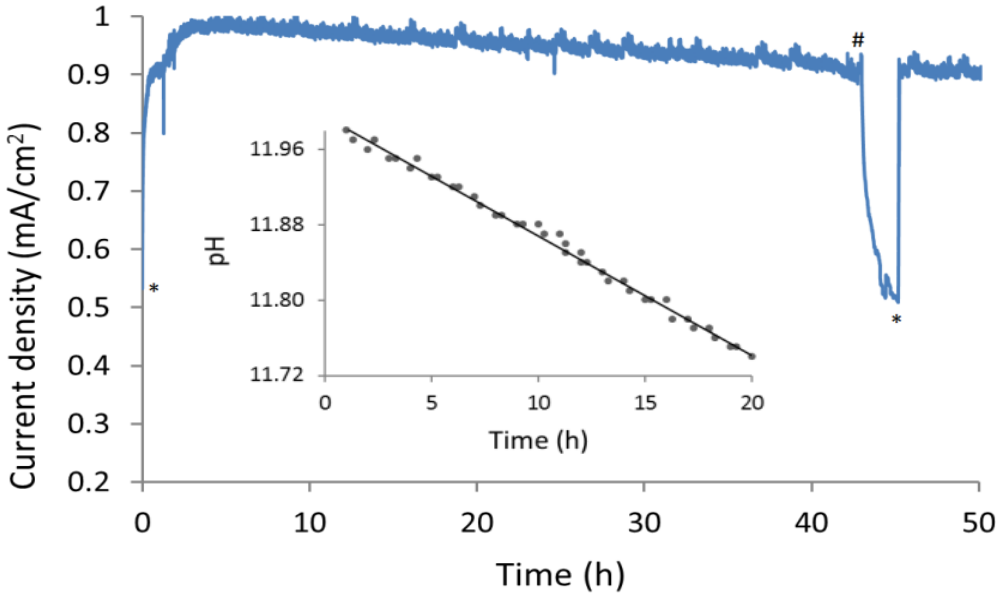

Figure 5.5: *Chronoamperogram at 0.80 V (vs Ag/AgCl) in 0.2 M Na_2SO_4 (pH 12) over 50 h of operation, with and without light illumination (ca. 0.25 sun), of an FTO glass slide coated with a thin film of Pt overcoated with PPy/nano-Ni/rGO, where the polymerisation mixture contained 125 mg of nano-Ni and 6 mg of rGO (*='light on', #='light off). The inset graph depicts the pH change during the first 20 h of the experiment.*

The PPy/nano-Ni/rGO on Pt/FTO was found to yield a consistent 0.92-1.00 mA/cm^2 for over 42 h of constant light illumination (Figure 5). When the light was thereafter turned off and on again, the current first fell to its earlier measured dark current and then went back up to its full current, including photocurrent, up to the 50 h mark.

The charge exchanged during the 50 h of operation was calculated to be 682.7 C, which is enough to 1-electron oxidize every pyrrole monomer and C-atom in the rGO within the thin film approximately 4-times over. That is, one quarter of the total charge passing through the electrode was more than sufficient to over-oxidize the PPy coating, causing it to delaminate and disintegrate, and to oxidatively destroy the rGO. The fact that this did not occur indicates, unambiguously, that only a small proportion of the observed currents could have been involved in side-reactions with the coatings.

The performance of the PPy thin film differed from that of the equivalent PEDOT thin film in that its current displayed a consistent, if small decline over the 50 h of testing. The highest current (1.00 mA/cm^2) was obtained after about 4 h. Thereafter, the current fell slowly to about 0.92 mA/cm^2 after 50 h (Figure 5.5).

A distinct pH change, consistent with water oxidation catalysis, was also observed (Figure 5 inset graph).

5.2.1.4 Studies on the Gas Produced; the Faradaic Efficiency

The gas in the gas bubbles produced by the most active PPy/nano-Ni/rGO thin-film was collected and tested by gas chromatography using the method and cell described in the experimental section (Chapter 2). This showed the generated gas to be oxygen (Figure 5.6). A trace of hydrogen was also observed. The hydrogen likely crossed over from the cathode, through the ion-permeable Nafion membrane that separated the two half-cells. Tiny N_2 peaks were also detected on occasion; these likely derived from small amounts of air that got into the system. The gas ratios were typically measured to be around 82%-85% O_2 and 11%-15% H_2, with or without light

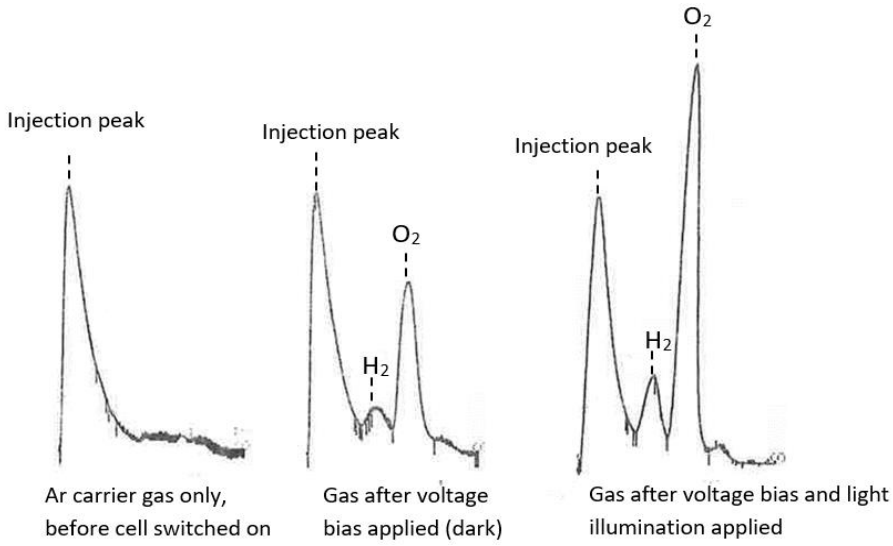

Figure 5.6: *GC traces of gases collected of OER system*

illumination. Up to 4% N_2 was detected. No CO_2 or CO was detected using GC, indicating that the rGO in the PPy/nano-Ni/rGO film was stable to oxidation during gas generation. Gas bubbles generated at the Pt mesh counter electrode were separately shown to be pure H_2 using the same equipment.

Integration of the oxygen peak in the GC (described in Chapter 2) indicated that the carrier gas that passed through the column contained 63.5% (dark) and 64.1% (with light illumination) of the expected volume of oxygen based on the electrons passing through the electrode. As noted earlier, these values are under-estimates because the cell used was not gas tight, meaning that an unquantified volume of oxygen leaked out. As such, they represent the minimum Faradaic efficiency of the process. The absence of other available oxidation pathways suggests that the actual faradaic efficiency was likely closer to 99.9% (since less than 0.1% of the charge over 50 h could have gone into oxidation to reverse the reduction that occurred during creation of the rGO from GO).

5.2.1.5 Characterisation of the Most Active PPy/nano-Ni/rGO Thin Film

Elemental analysis of the most active PPy/nano-Ni/rGO film was determined to be 26.00% Ni, 4.15% N, and 39.42% C with no Fe. As only the PPy contains the element N, while the rGO contains only C and the nano-Ni only Ni, it was possible to calculate the molar ratio of PPy : Ni : rGO to be 0.67 (N; PPy) : 1 (Ni) : 4.75 (C; other). This was low in PPy monomer relative to PEDOT monomer in the equivalent PEDOT film.

The morphology of the most active PPy/nano-Ni/rGO film was examined using scanning electron microscopy (Figure 5.7(a)). As can be seen, the structure is highly porous. EDX-mapping (Figure 5.7(a)(i)-(iv)) indicated uniform distributions of Ni (nano-Ni), C (PPy and rGO), O (rGO and pTS), and N (PPy) over the film.

.

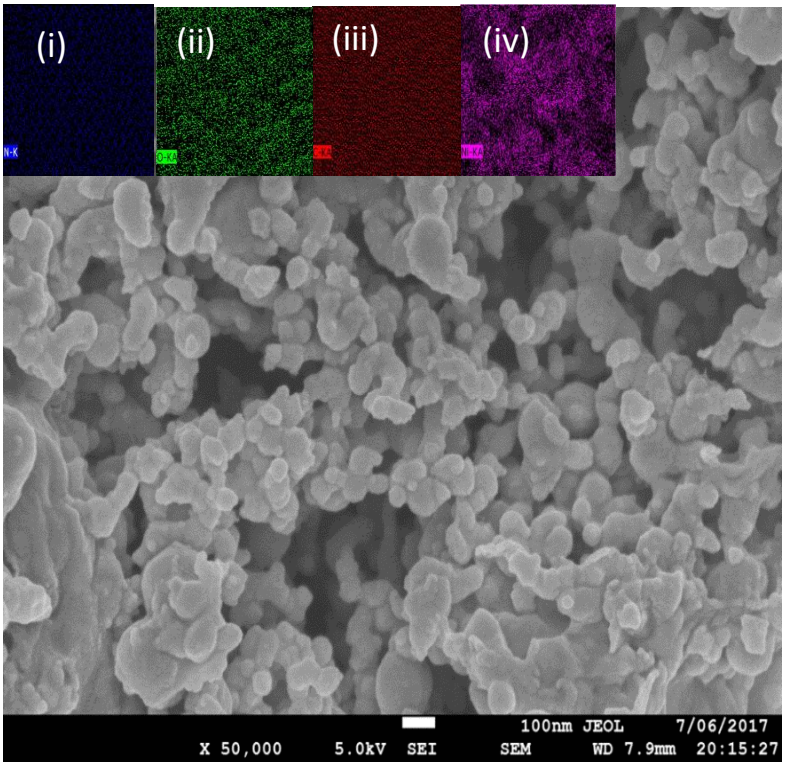

(a)

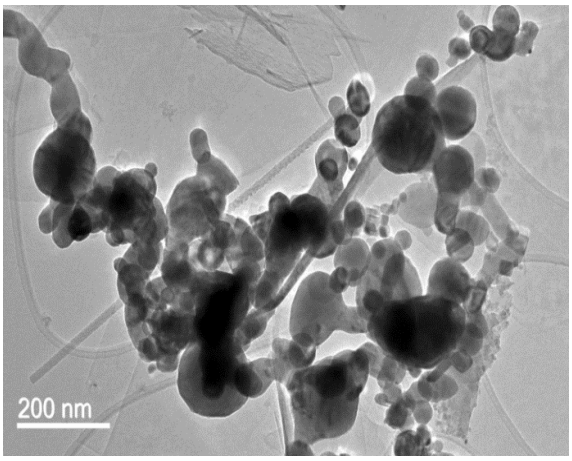

(b)

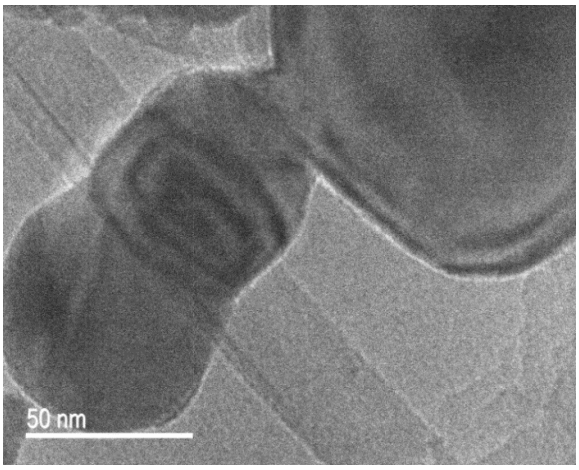

(c)

Figure 5.7: *(a) Scanning electron microscopy image of PPy/Nano-Ni/rGO containing 125 mg nano-Ni and 6.0 mg of rGO. The inset images show the elemental distributions, using EDX, of: (i) N, (ii) O, (iii) C, (iv) Ni. (b) Transmission electron microscopy image of PPy/Nano-Ni/rGO, showing the rGO plates and the nano-Ni particles. (c) TEM of the nano-Ni/PPy interface.*

Transmission electron microscopy (TEM) (Figure 5.7(b)) showed that the nano-Ni particles - rGO platelets were generally separately enveloped by the PPy and not in close contact with each other. The nano-Ni particles, which were 20-50 nm in diameter can be seen as the dark structures in Figure 5.7(b), while the rGO plates, which were ca. 200-300 nm wide and long, are shown as the light-coloured background structures in Figure 5.7(b). Figure 5.7(c) shows that the PPy made seamless contact with the Ni lattice. This was also true for the rGO. In respect of the TEM work, the PPy thin films were structurally very similar to the earlier studied PEDOT films.

X-ray photoelectron spectroscopy (XPS) model (XPS, PHI660) using a monochromatic Mg K as X-ray source was used to determine the elemental composition and chemical states of the PPy/nano-Ni/rGO film. Figure 5.8 depicts the measured data as the individual points shown. Modelling results are shown by the solid lines

The survey spectrum displays main peaks for O 1s, C 1s, Ni 2p and N 1s. The O 1s and spectra can refer to rGO while C 1s spectra can refer to either PPy or rGO while the N 1s spectrum can only derive from PPy. The C 1s spectra contain deconvolution peaks at 283.99, 284.5, 285.1, 286.8, 288.1, 288.9 and 291.2 eV (Figure 5.8(a)). The peak at 283.5 eV could represented a sp^2 carbon hybrid, which relates to the binding energy of C=C bonds, while the peak at 284.3 eV represent a sp^3 carbon hybrid and can refer to C-C or C-H. The peak at 285.1 eV refers to the binding energy of the C-N bond. Finally, 286.8, 288.1, 288.9 and 291.2 eV refer to C-O, C=O, O-C=O and $\pi - \pi$ interactions binding bonds respectively.[4-9] The O 1s spectra of the film has mainly three peaks at 529.8, 531.2, 532.5 and 532.5 eV that are due to the binding energy of Ni-O, C=O, C-O-H and C-O-C[10-12]bonds respectively. The N 1s spectra contained peaks at 499.97, 498.48, 401.88 eV, which refer to the binding energy of –NH-, =N- and N^+.[13-15] Finally, for the Ni atom spectrum, there are two main peaks referring to Ni $2p_{1/2}$ and $2p_{3/2}$ transitions in the range 854.7–861.2 eV, as can be seen in Figure 7(d). The main peak falls at ca. 854.7 eV with an intense satellite calculated at

861.2 eV representing Ni $2p_{1/2}$, while the peak at 872.2 eV with an intense satellite at 879.0 eV is due to the presence of Ni $2p_{3/2}$. These are both characteristic of the Ni^{2+} ion.[16]

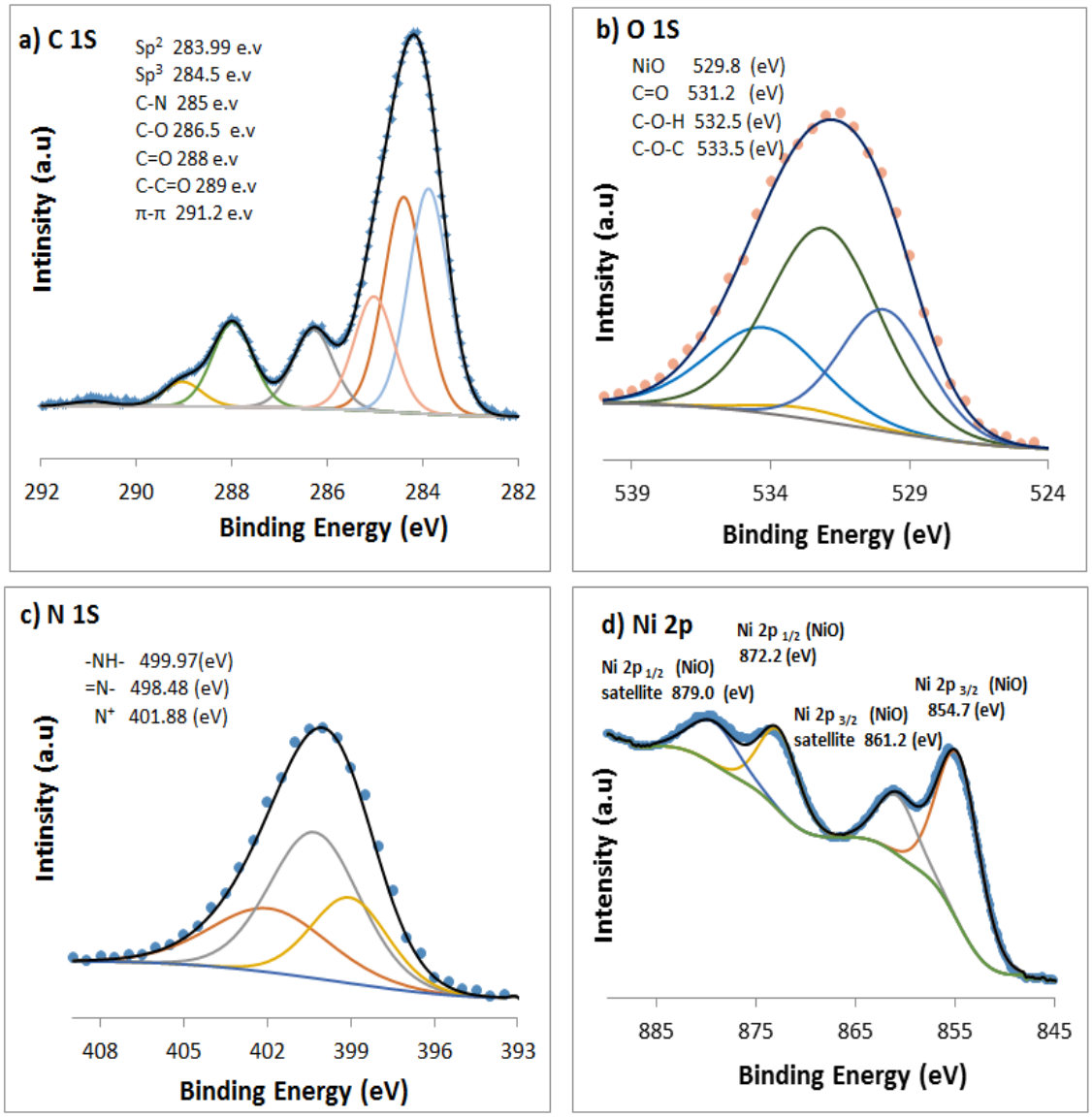

Figure 5.8: *XPS spectra of the PPy/nano-Ni/rGO film that contained 125 mg of nano Ni and 6.0 mg of rGO (where: (a), (b), (c) and (d) represent the spectra of N 1s, C 1s, O 1s and Ni 2p respectively. N 1s spectra derive from to the PPy while C 1s and O 1s can refer to either PPy or rGO. Ni 2p refers to nano-Ni).*

5.2.1.6 EIS and Tafel Plot Studies

Electrochemical impedance spectroscopy (EIS) and Tafel plot studies were undertaken at 0.80 V (*vs* Ag/AgCl) in 0.2 M Na_2SO_4 (pH 12). Figure 5.9(a)-(b) depict Nyquist and Bode plots respectively, of the Pt electrode overcoated with: PPy/nano-Ni/rGO containing 125 mg nano-Ni and 6.0 mg of rGO (with and without light illumination) (curves (iv)-(v) in Figure 5.9), the control, bare Pt (curve (iii) in Figure 5.9), and control PPy-only electrodes (with and without light illumination) (curves (i)-(ii) in Figure 5.9).

It was also observed that there were two distinct semicircles of impedance. The first sits in the range (10-100 Hz), which is clearly demonstrated in Figure 5.9(a)-(b), with a small semicircle at high frequencies (1,000-10,000 Hz) that is barely discernible at low Z values in the inset graph in Figure 5.9(a). The latter is characteristic of charge transfer that occurred during catalysis.

At pH 12, intermediate to low frequency processes can refer to adsorption, involving transfer of ions (charge carriers) from the diffuse layer to the catalyst.[17] The EIS data was therefore modelled with the equivalent circuit shown in Figure 5.9(c).[18] The modelled data provided an excellent match with the measured data.

The modelled data is provided in Table 5.4. For comparison purposes the equivalent data for PEDOT/nano-Ni/rGO on Pt is also listed in Table 5.4. As can be seen, the resistance associated with adsorption, R_{ad}, and the charge transfer resistance, R_{CT}, of the PPy/nano-Ni/rGO film was larger than that of the equivalent PEDOT/nano-Ni/rGO thin film (R_{ad} 165.8 Ω cm^2 *vs*. 110.4 Ω cm^2; and R_{CT} 111.6 Ω cm^2 *vs* 103.2 Ω cm^2, with light illumination; R_{ad} 179.2 Ω cm^2 *vs* 132.4 Ω cm^2; and R_{CT} 133.8 Ω cm^2 *vs*125.3 Ω cm^2, without light illumination). They were, however, still lower than the bare Pt (R_{ad} 270.4 Ω cm^2 and R_{CT} 120.7 Ω cm^2). This may be due to the presence of an oxide layer, which is known to form on Pt in basic solution.[19] In addition, the

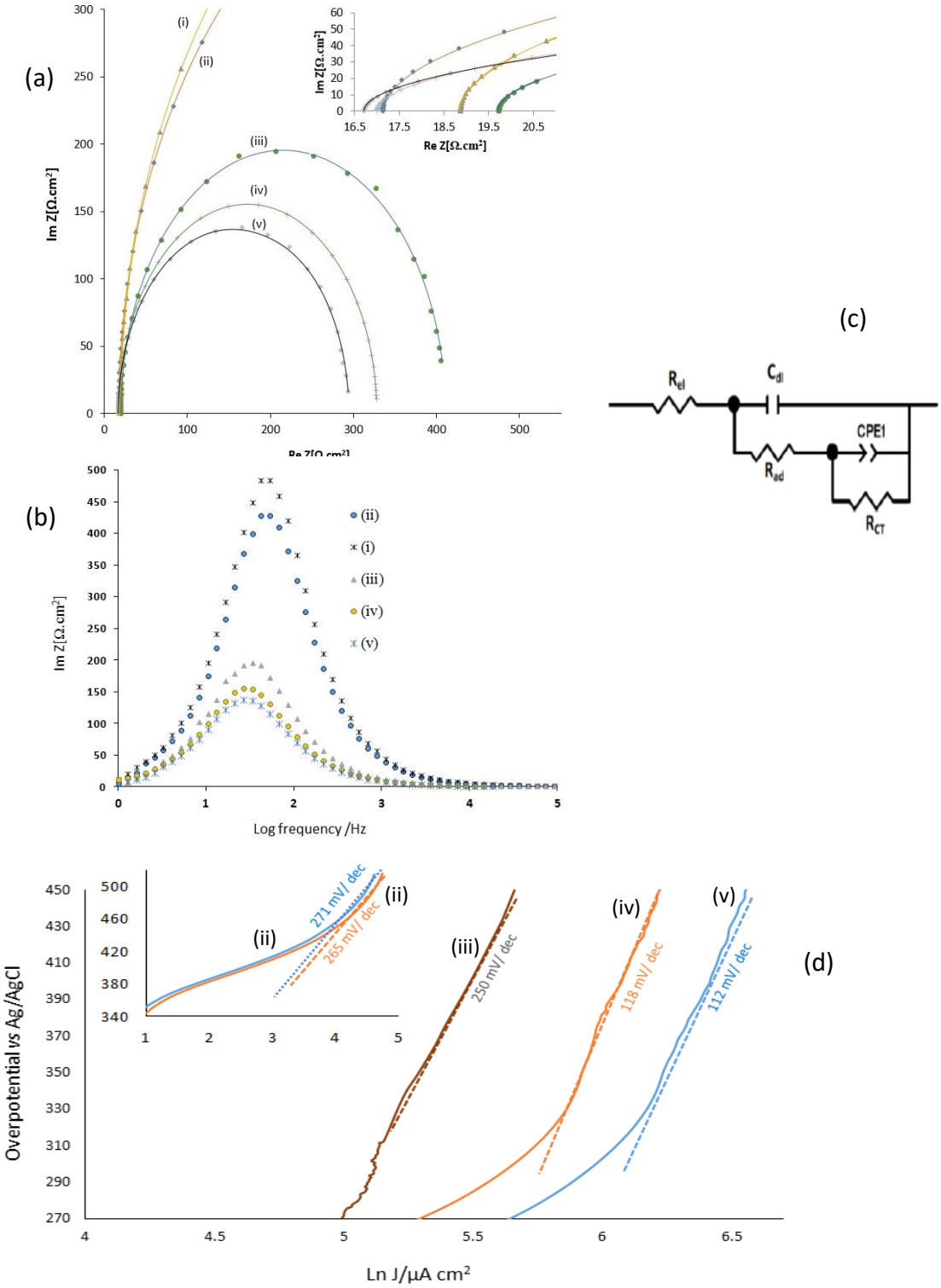

Figure 5.9: *(a) Nyquist and (b) Bode plots at 0.80 V (vs Ag/AgCl) in 0.2 M Na_2SO_4 (pH 12), showing measured data (individual data points) and modelled data (solid lines) using the equivalent circuit depicted in (c), as well as (d) Tafel plots of: (i) PPy only (dark; no light illumination), (ii) PPy only (with light illumination), (iii) Pt only, (iv) Pt overcoated with PPy/nano-Ni/rGO containing 125 mg nano-Ni and 6.0 mg rGO (dark; no light illumination), and (v) Pt overcoated with PPy/nano-Ni/rGO containing 125 mg nano-Ni and 6.0 mg rGO (with light illumination).*

corresponding semiconducting Ni oxide layer on the nano-Ni in the PPy/nano-Ni/rGO may be activated by the light illumination. NiO is well known as a semiconductor that can absorb light, generating more charge carriers, thereby enhancing the overall activity of water splitting.

Sample	**R_{el}** **Ω cm^2**	**R_{ad}** **Ω cm^2**	**C_{dl}** **μF cm^{-2}**	**R_{CT}** **Ω cm^2**	**Q_{CPE}** **μΩ^{-1} cm^{-2}s^n**	**n_{CPE}**	**C_{CPE}** **μF cm^{-2}**	**A mV/dec**	**i_o** **μA cm^2**
PEDOT (dark)	18.90 ± 1.60	420.3 ± 3.4	16.1 ± 0.2	148.3 ± 2.7	0.07 ±0.03	0.88 ±0.11	0.01± 0.01	277 ±14	20.60 ±3.74
PPy (dark)	**18.85** ± 1.40	**739.9** ± 2.6	**3.3** ± 1.6	**227.1** ± 2.9	**0.02** ± 0.03	**0.97** ± 0.10	**0.01**± 0.01	**271±** 14	**19.13** ±2.65
PEDOT (light)	17.26 ± 1.30	400.1 ± 2.6	20.9 ± 1.5	122.9 ±3.3	0.14 ±0.04	0.88 ± 0.12	0.02± 0.01	272± 13	25.88 ±3.55
PPy (light)	**17.14** ± 1.20	**672.1** ± 1.4	**3.7** ± 1.5	**186.2** ± 3.1	**0.03** ± 0.04	**0.96** ± 0.11	**0.02**± 0.01	**265±** 13	**22.69** ±2.44
Pt only	**19.73** ± 1.20	**270.4** ± 12.4	**9.9** ± 0.5	**120.7** ± 2.1	**0.06** ±0.01	**0.92** ± 0.32	**0.02±** 0.01	**250±** 14	**50.46** ±4.22
Pt/PEDOT/nano -Ni/rGO (dark)	17.26 ± 0.85	132.4 ± 0.8	34.0 ± 0.2	125.3 ±1.2	0.25 ±0.01	0.89 ± 0.21	0.05± 0.01	110± 6	15.20 ±2.11
Pt/PPy/nano-Ni/rGO (dark)	**16.89** ± 1.20	**179.2** ± 1.0	**1.7** ± 0.3	**133.8** ± 1.1	**0.06** ± 0.02	**0.96** ± 0.18	**0.04**± 0.001	**118±** 7	**12.90** ±2.22
Pt/PEDOT/nano -Ni/rGO (light)	17.16 ± 1.10	110.4 ± 0.3	38.9 ± 0.2	103.2 ±1.7	0.40 ±0.03	0.88 ± 0.14	0.08± 0.01	104± 4	17.97 ±2.33
Pt/PPy/nano-Ni/rGO (light)	**16.72** ± 1.30	**165.8** ± 0.5	**2.4** ± 0.12	**111.6** ± 1.7	**0.07** ± 0.05	**0.96** ± 0.12	**0.05**± 0.01	**112** ±3	**14.25** ±2.15

Table 5.4: *Data from modelling of electrochemical impedance spectroscopy (ohmic resistance (R_{el}), adsorption resistance (R_{ad}), diffuse layer capacitance (C_{dl}), catalytic charge transfer resistance (R_{CT}), and capacitance expressed in terms of a constant phase element (Q_{CPE}, n_{CPE}, and C_{CPE})).*[20] *Data from Tafel plot studies (slope (A), exchange current density (i_o)). ('dark' = without light illumination; 'light' = with light illumination)*

The Bode plots show that the major resistance in the PPy/nano-Ni/rGO film was adsorption, which shows up in the 10-100 Hz range. This was also observed in the equivalent PEDOT/nano-Ni/rGO thin film. By contrast, the major resistance for bare Pt was the charge transfer resistance, which appears in the 100-10,000 Hz range. In other words, the major impediment to reaction likely involved absorption of the water reactant to the PPy/nano-Ni/rGO catalyst. For bare Pt this was less of an impediment.

The Ohmic resistance (R_{el}) of PPy/nano-Ni/rGO on Pt was somewhat lower than for the equivalent PEDOT thin film. For this reason the film PPy/nano-Ni/rGO on Pt can exhibts higher current than PEDOT film according to Ohm's law.

The most surprising aspect of the PPy/nano-Ni/rGO data is its much lower electroactive area per unit area than the equivalent PEDOT/nano-Ni/rGO (as can be seen in Table 5.4, the C_{dl} of PPy/nano-Ni/rGO was 1.70 µF cm^{-2} in the dark, increasing to 2.40 µF cm^{-2} under light illumination. These values are more than 4 times smaller than the C_{dl} values for the equivalent PEDOT/Nano-Ni/rGO. It can be concluded that PPy has less activity than PEDOT which resulting in decreases C_{dl} of PPy/nano-Ni/rGO film if compaired to PEDOT/Nano-Ni/rGO film. The less conductivityof PPy results in lower synergitic effects through PPy/nano-Ni/rGO contents in both stated dark and light. Concequently, this effect reduces the catalyst behaviour in overall water – splitting reaction. Therefore, the electrochemical propteries of PPy has crucial rules in PPy/nano-Ni/rGO film performance.

This could be one of the reasons that the PPy/Nano-Ni/rGO exhibits current densities lower than the equivalent PEDOT/Nano-Ni/rGO film. Thus, for example, Figure 5.3 shows that the current density of Pt/PPy/Nano-Ni/rGO under illumination fell in the range 0.92-1.00 mA/cm^2, while the equivalent PEDOT/Nano-Ni/rGO exhibited 1.10-1.15 mA/cm^2, which is about a 20% difference. The electrochemically active area was 75% smaller but there was the increase in the catalytic activity was approximately 3-fold. That is, the catalytic activity per unit active area of the PPy/nano-

Ni/rGO thin film must have been around 3-times that of the equivalent PEDOT/nano-Ni/rGO film.

The Tafel plots of the catalysts (Figure 5.9(d), and Table 5.4, last two columns) describe their overall catalytic performance, not taking into account their differing electrochemically active area. As can be seen, the thin films involving PPy displayed, in all cases, higher Tafel slopes and smaller exchange current densities (i_o) than the equivalent PEDOT film (both with and without light illumination). Thus, the PPy thin films were intrinsically less active (lower i_o values) and were also less activated by the application of a voltage bias (higher Tafel slopes). For example, the PPy/nano-Ni/rGO film required 112 mV (with light illumination) and 118 mV (without light illumination) to increase the reaction rate by a factor of 10, while the PEDOT/Nano-Ni/rGO only required 104 mV (with light illumination) and 110 mV (without light illumination).

Interestingly, the i_o values of the control PPy thin films, containing only PPy, were notably larger than those of the most active PPy/nano-Ni/rGO film, but not as high as the equivalent PEDOT only control films. Given that the PPy film has an approximately 4-fold smaller active area, it can be concluded that pristine PPy is, intrinsically, around 4-time more active per unit area in water oxidation catalysis than pristine PEDOT.

5.2.1.7 Summary: Water Oxidation by the Most Active PPy/nano-Ni/rGO Thin Film

PPy-films containing nano-Ni and rGO have been studied as electrocatalysts and photoelectrocatalysts of the oxygen evolution reaction (OER) in 0.2 M Na_2SO_4 with the pH adjusted to 12. While the control PPy, PPy/nano-Ni, and PPy/rGO films were catalytically weaker, films containing PPy: nano-Ni: rGO in a molar ratio of 1.0 (N; PPy): 1.49 (Ni): 7.07 (C; other) proved to be highly active, particularly over long times (50 hours). The above PPy/nano-Ni/rGO on Pt/FTO film generated a sustained

current density of 0.93-1.00 mA/cm^2 at 0.80 V (*vs* Ag/AgCl) over >45 h of operation under constant light illumination of 0.25 sun. This was an order of magnitude greater than an equivalent bare Pt electrode, which produced <0.15 mA/cm^2 under the same conditions. GC confirmed that oxygen was the sole gas generated. SEM/EDX, TEM, XPS, EIS and Tafel plot studies showed that the catalytic amplification was created by the PPy in the above film.

5.2.2 Studies of PPy/nano-Ni/rGO as Hydrogen Reduction (Photo) Catalysts

5.2.2.1 Studies of the PPy/nano-Ni/rGO thin films in Catalytic Hydrogen Generation

In the first stage of this study, films of vapour-phase polymerized PPy containing varying quantities of nano-Ni (av. 20 nm diameter) and rGO on FTO glass slides (4.2 cm^2) were prepared and tested in (photo) catalysis of the hydrogen evolution reaction (HER) (2 H^+ + 2 e^- -> H_2) in 0.05 M H_2SO_4 / 0.2 M Na_2SO_4 at –0.75 V *vs* Ag/AgCl (Figure 5.10). These voltage and pH conditions were the same as those in employed in the Chapter 4 studies involving PEDOT/nano-Ni/rGO thin-films. As in Chapter 4, GO was initially incorporated into the PPy and then thereafter partially reduced to rGO (with a net charge exchanged of ~1.9 x 10^{-6} C).

The observed trends in respect of the composition of the most active thin-film were essentially identical to those in the earlier PEDOT studies, with the highest performing sample also containing 125 mg of nano-Ni and 5.4 mg of rGO. Figure 5.10 depicts the optimization chronoamperograms showing that, for the PPy, the greatest catalytic effect was also obtained with 125 mg of nano-Ni and with 5.4 mg of rGO. The dark current (1.95-2.25 mA/cm^2) and full current under light illumination (2.35-2.40 mA/cm^2, including photocurrent) of the most active PPy/nano-Ni/rGO were, however, generally lower than those of the equivalent

PEDOT/nano-Ni/rGO thin film (Table 5.5). The most active film was 0.65 μm thick with a conductivity of 6.90 S/cm.

Table 5.5 provides a comparison of the dark and light current densities for the most active of the PPy/nano-Ni/rGO films *vs* the most active PEDOT/nano-Ni/rGO films under the same conditions. The table clearly shows that the performance of the PEDOT-containing films was not significantly different to the PPy-containing films when only nano-Ni was present.

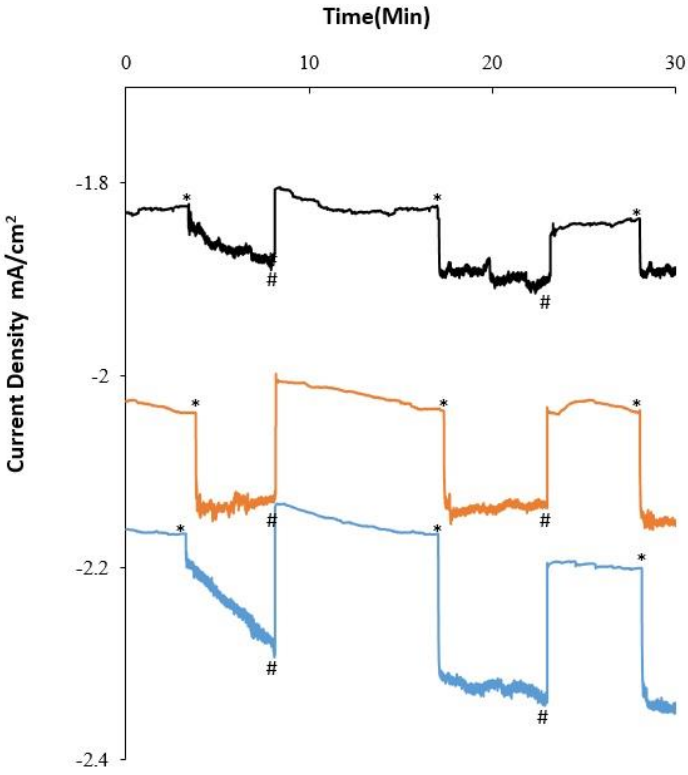

Figure 5.10: *Chronoamperograms at –0.75 V (vs Ag/AgCl) in 0.05 M H_2SO_4/0.2 M Na_2SO_4 of FTO glass slides coated with PPy/nano-Ni/rGO after 3 h of operation, with and without light illumination, where the coatings all contained 125 mg nano-Ni but where the rGO present varied as follows: (i) 5.4 mg rGO, (ii) 6.0 mg rGO, or (iii) 4.8 mg rGO. (*='light on', #='light off).*

Composition of thin film (CP=conducting polymer)	**Current density in dark (mA/cm^2)**		**Current density in light (mA/cm^2)**	
	PPy	**PEDOT**	**PPy**	**PEDOT**
CP only	**0.046-0.047**	0.040-0.041	**0.055-0.054**	0.047-0.048
CP : 125 mg nano-Ni	**0.055-0.056**	0.050-0.049	**0.063-0.064**	0.056-0.057
CP : 5.4 mg rGO	**0.065-0.066**	0.063-0.064	**0.077-0.078**	0.073-0.074
CP : 125 mg nano-Ni: 4.8 mg rGO	**1.81-1.82**	2.60-2.61	**1.90-1.91**	2.78-2.80
CP : 125 mg nano-Ni: 5.4 mg rGO	**2.18-2.20**	3.34-3.37	**2.38-2.60**	3.58-3.60
CP : 125 mg nano-Ni: 6.0 mg rGO	**2.00-2.15**	2.90-3.10	**2.12-2.15**	3.16-3.18

Table 5.5: *Comparison of results from chronoamperograms at -0.75 V (vs Ag/AgCl) in 0.05 M H_2SO_4/0.2 M Na_2SO_4 of FTO glass slides coated with thin films of PPy/nano-Ni/rGO or PEDOT/nano-Ni/rGO.*

However, the further addition of increasing amounts of rGO more strongly amplified the performance of the PEDOT-containing films relative to the PPy-containing films. That is, increasing conductivity had a stronger effect in the former than the latter thin films. This was also observed for water oxidation catalysis.

Figure 5.11 depicts chronoamperograms for the control films. Figure 5.12 shows the performance of the most active PPy/nano-Ni/rGo film over 3 h as a comparison with control bare Pt and the control film containing only 125 mg nano-Ni and 5.4 mg rGO only (without any PPy). As can be seen, the PPy-free film yielded a current density, after 3 h of operation under light illumination, of 2.10 mA/cm^2 (Figure 5.11(i)), which was around 24% lower than the 2.60 mA/cm^2 current density of the PPy film containing 125 mg nano-Ni and 5.4 mg rGO (Figure 5.11(ii)). That is, the presence of the PPy in the most active thin film amplified the current density by 24%.

The PPy film containing 125 mg nano-Ni and 5.4 mg rGO also outperformed the bare Pt control after 3 h, which yielded 2.2 mA/cm^2 after 3 h (Figure 5.11(iii)).

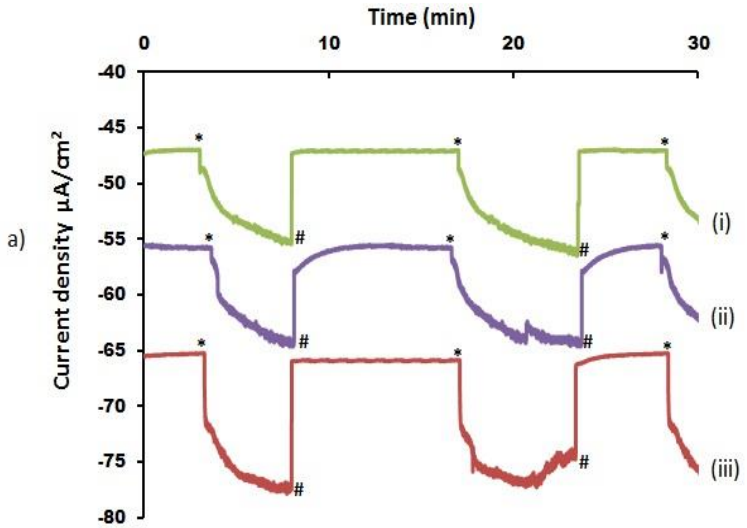

Figure 5.11: *Chronoamperograms at –0.75 V (vs Ag/AgCl) in 0.05 M H_2SO_4/0.2 M Na_2SO_4, after 3 h of operation, with and without light illumination (0.25 sun), of FTO glass slides coated with: (a) (i) PPy alone, (ii) PPy/nano-Ni, (iii) PPy/rGO; and (b) PPy/nano-Ni/rGO. (*='light on', #='light off). Note that the data in graph (b) is in mA/cm^2 whereas the data in graphs (a) are in µA/cm^2.*

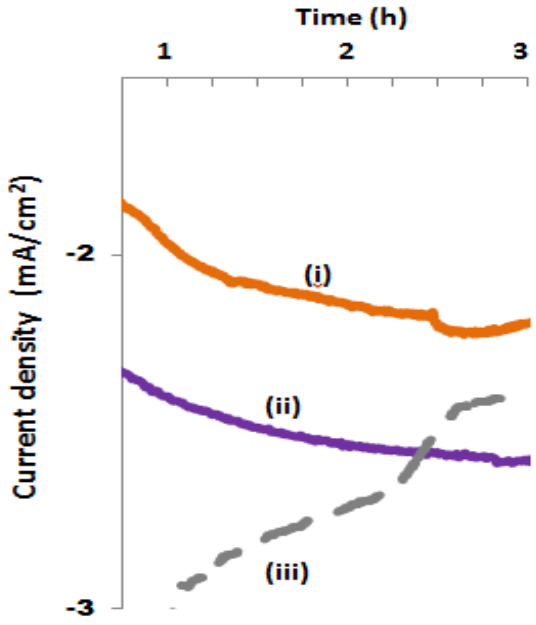

Figure 5.12 *Chronoamperograms at –0.75 V (vs Ag/AgCl) in 0.05 M H_2SO_4/0.2 M Na_2SO_4 of FTO glass slides coated with: (i) nano-Ni/rGO (125 mg nano-Ni/5.4 mg rGO; without light illumination), (ii) PPy/nano-Ni/rGO (with light illumination; 0.25 sun), and (iii) bare Pt (without light illumination).*

Composition of thin film (CP=conducting polymer)	Current density in dark (mA/cm^2)		Current density in light (mA/cm^2)	
	PPy	**PEDOT**	**PPy**	**PEDOT**
CP : 125 mg nano-Ni: 6.0 mg rGO	**2.18-2.20**	3.34-3.37	**2.38-2.60**	3.58-3.60
125 mg nano-Ni: 6.0 mg rGO	1.87		2.10	
Bare Pt	2.20		2.20	

Table 5.6: *Comparison of results after 3 hours operation, from chronoamperograms at -0.75 V (vs Ag/AgCl) in 0.05 M H_2SO_4/0.2 M Na_2SO_4 of FTO glass slides coated with thin films of PPy/nano-Ni/rGO or PEDOT/nano-Ni/rGO vs controls.*

In summary; it is clear that, for hydrogen generation catalysis, like PEDOT, the most active PPy thin-film:

- contained 125 mg Nano-Ni and 5.4 mg of rGO;
- outperformed control bare Pt; and
- outperformed a control thin-film comprising only 125 mg nano-Ni and 5.4 mg rGO.

Moreover, as for water oxidation, the performance of that most active PPy film was generally lower than the equivalent PEDOT film.

The nano-Ni/rGO components of the most active PPy/nano-Ni/rGO film produced about 75% of the electrocatalytic effect, with the PPy producing the rest. Given that the light-induced current density comprised only about 5% of the total, it seems that the PPy may have largely acted to amplify the simple electrocatalysis (not photoelectrocatalysis) in this case. At –0.75 V (*vs* Ag/AgCl), PPy is in its reduced, non-conducting form.

5.2.2.2 Gas Collection Studies of PEDOT/Nano-Ni/rGO on FTO

Gas chromatography was used to determine and identify the gas in the bubbles formed on the most active PPy/nano-Ni/rGO thin film on the FTO working electrode. A custom built cell and dedicated gas chromatograph (as described in Chapter 2) was used to collected and

characterize the gas produced at –0.75 V *vs* Ag/AgCl. In addition to the Ar carrier gas, the GC trace over 30 min of elution time contained only a single peak whose retention time corresponded to hydrogen (Figure 5.13). Peaks due to other possible gases, including air nitrogen and/or oxygen, were notably absent. Gas bubbles formed on the Pt mesh counter electrode were also (and separately) shown to be pure oxygen using the same equipment.

5.2.2.3 Characterization of the Most Active PPy/Nano-Ni/rGO Electrode

To establish the composition of the most active PPy/nano-Ni/rGO film on the working electrode, elemental analysis studies were undertaken. These indicated that they contained 28.0% Ni, 3.42% N and 37.04% C with no Fe. As only the PPy contains the element N, while the rGO contains only C and the nano-Ni only Ni, it was possible to calculate their molar ratio

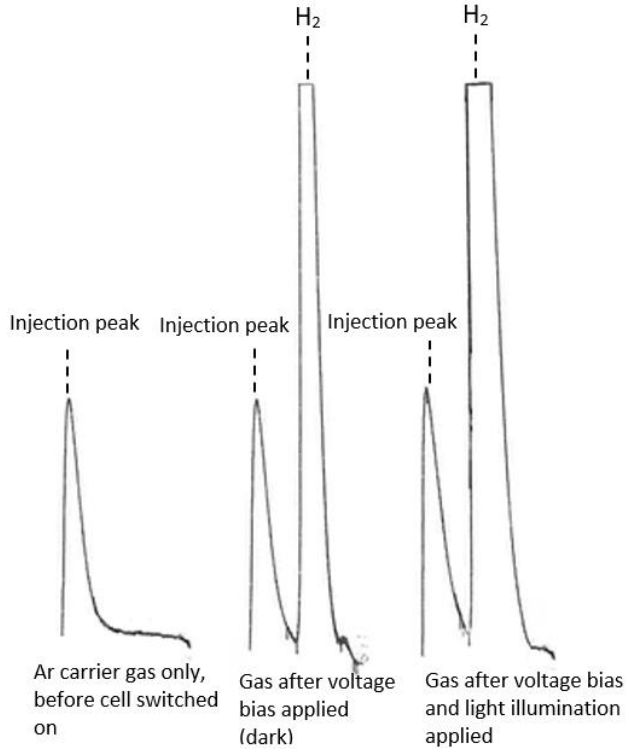

Figure 5.13: *GC traces of gases collected of HER system*

to be 0.51 (PPy monomer) : 1.00 (Ni) : 4.43 (C; other). By comparison the equivalent PEDOT film had a molar ratio of 0.93 (PEDOT monomer): 1.00 Ni: 5.20 (C; other). That is, there was less PPy monomer present in the film than there had been PEDOT monomer in that film.

The morphology of the PPy/Nano-Ni/rGO film after 3 h of operation was examined using Scanning Electron Microscopy (SEM). Figure 5.14 depicts an SEM image of the deposited film, showing that the surface had changed to the highly porous structure shown. EDX-mapping (Figure 5.14, insets) indicated uniform distributions of Ni (nano-Ni), C (rGO and PPy), and N (PPy).

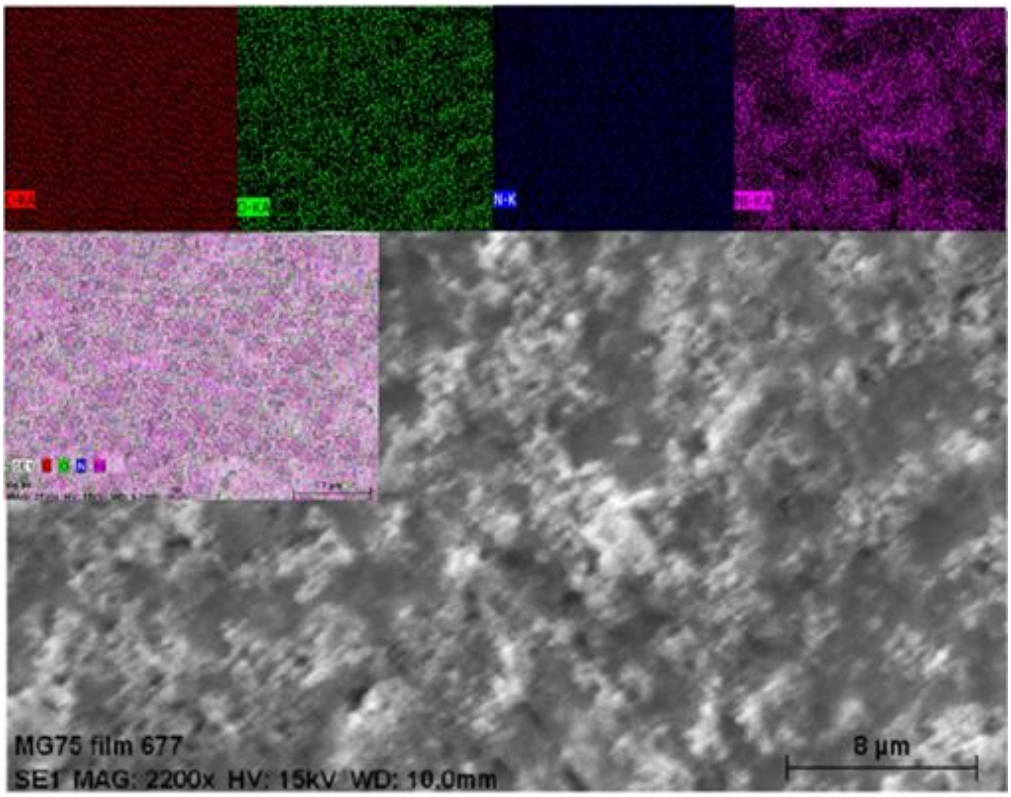

Figure 5.14: *Scanning electron microscope image of PPy/Nano-Ni/rGO (main picture) after 3 h of operation. The insets depict the distribution of the following elements according to EDX mapping (top from left to right): C, O, N and Ni, while the depiction at bottom left represents all of these elements in the film.*

Powder X-ray diffraction (XRD) patterns of GO, rGO, PPy and PPy/nano-Ni/rGO were recorded (Figure 5.15). XRD patterns of GO displayed a diffraction peak at 2θ = 10.2° due to the (002) carbon crystalline plane, revealing the introduction of oxygen functional groups on the graphite sheets.[21-26] The XRD scan of rGO confirmed that the sharp peak at 10.2° completely disappeared and a new broad peak, centered at 22.90°, formed, which clearly suggests that the oxygen rich functionalities were significantly reduced and thereby rGO was formed.[27-28]Also, a clear diffraction peak displayed at 26.2°, due to the (002) short-range order in the stacked graphene sheets.[29-30]

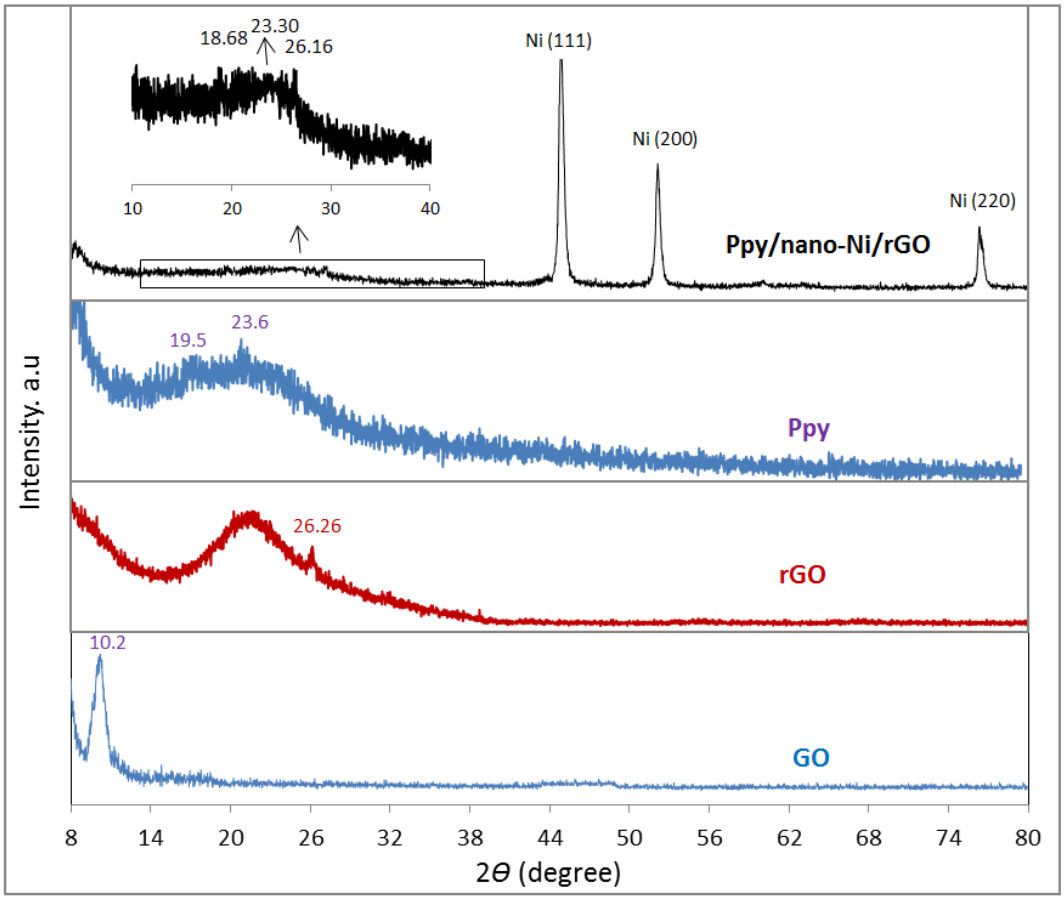

Figure 5.15: *Powder X-ray diffraction (XRD) of PPy/Nano-Ni/rGO and control: PEDOT, rGO, and GO.*

PPy displays peaks at 19.5° and 23° due to the π–π interactions along the polypyrrole chain, similar to that of aromatic groups, revealing the regular array of polypyrrole molecules.

PPy is semicrystalline in nature and the crystallinity exists due to the folding of polymer chain into single or double helix formation.[31-34] The XRD of the most active PPy/nano-Ni/rGO film also showed pattern peaks at 2θ 18.68°, 23.30° and 26.16°, confirming the contribution of PPy and rGO that shifted due to their combination together in the PPy/nano- Ni/rGO film. A pattern of three peaks appeared at 44.45°, 51.76° and 76.41° due to Ni(111), Ni(200) and Ni(220), clearly confirming the presence of the face centered cubic (fcc) structure of bulk nickel nanoparticles plane respectively.[35-36]

SEM, TEM, and XRD analyses were performed on samples after catalytic testing in order to assess the structural stability of the catalytic film. No significant change could be observed other than a relative increase in porosity. This suggested that the structure and composition of the film was set during the polymerization process and did not significantly change thereafter.

X-ray photoelectron spectroscopy (XPS) model (XPS, PHI660) using a monochromatic Mg K as X-ray source was used to establish the elemental composition and chemical states of PPy/nano-Ni/rGO film (Figure 5.16). The survey spectrum demonstrated main peaks for O 1s, C 1s, Ni 2p and N 1s. The O 1s spectra can refer to rGO while C 1s spectra can refer to PPy and rGO, while the N 1s spectrum can only refer to PPy. The C 1s spectra was modelled with deconvolution peaks at 283.96, 284.4, 285, 286.5, 288, 289 and 291.2 eV (Figure 5.16(b)). The peak at 283.96 eV could represent sp^2 carbon hybrid which related to C=C binding energy, while the peak at 284.4 eV represented sp3 carbon hybrid and

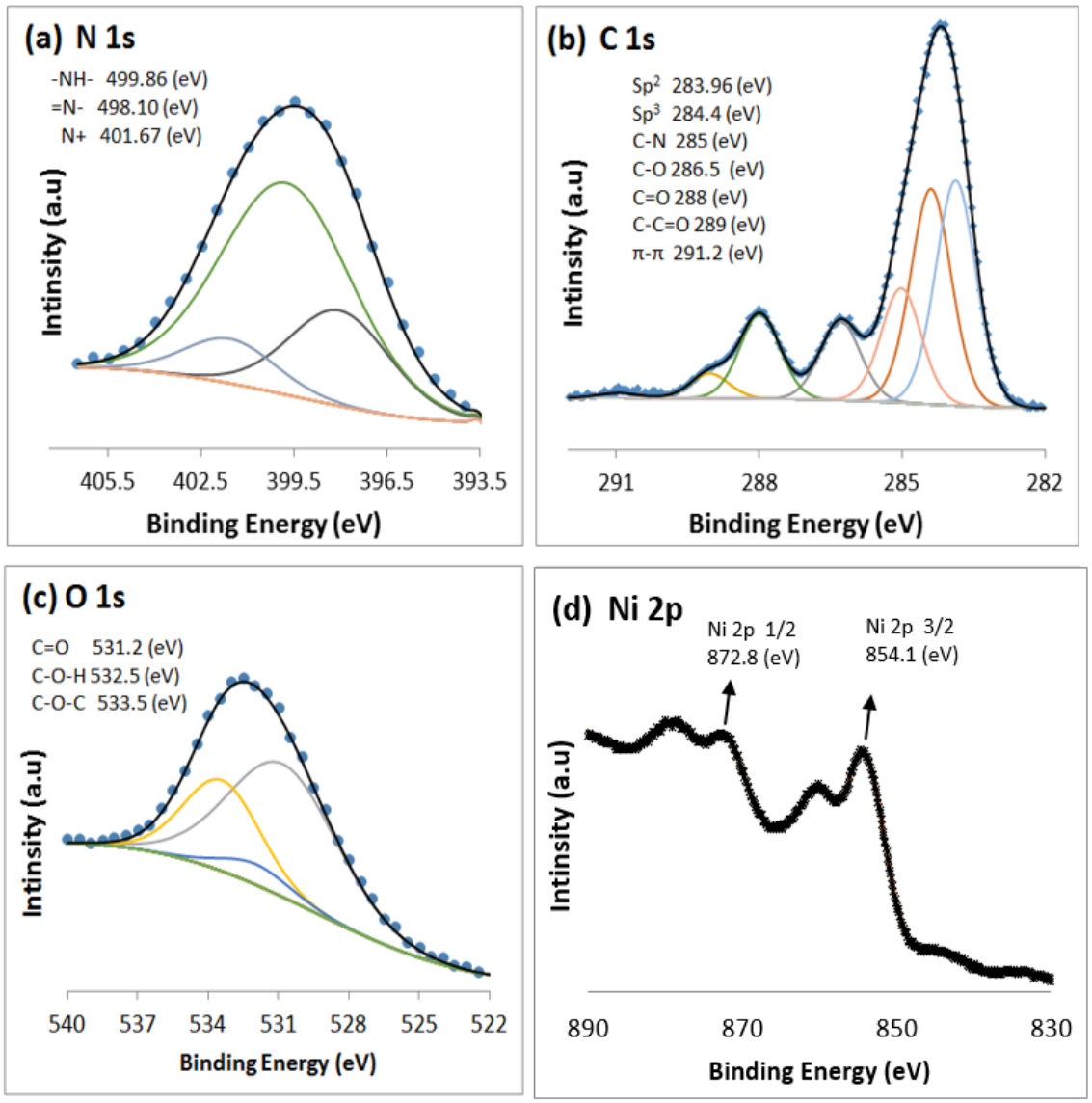

Figure 5.16: *X-ray photoelectron spectroscopy (XPS) of PPy/Nano-Ni/rGO after 3 h operation.*

can refer to C-C, C-H. The peak at 285 eV refers to C-N binding energy bond. Finally, 286.5, 288, 288 and 291.2 eV refer to C-O, C=O, O-C=O and π – π interactions binding bonds respectively.[4, 6-9, 37-39] The N 1s XPS spectra contained peaks at 499.97, 498.48, 401.88 eV and refer to binding energy bonds of –NH-, =N- and N^+.[13-15] The O 1s XPS spectra of the film has three peaks at 531.2, 532.5 and 533.5 eV due to the binding energy of C=O, C-O-H and C-O-C bonds respectively.[40-43] Finally, the Ni 2p spectra exhibited two main peaks at 854.1 and 872.8 eV, relating to 1/2 and 3/2 spin respectively.[44]

5.2.2.4 Electrochemical Impedance Spectroscopy (EIS) and Tafel Plot Studies of the PEDOT/Nano-Ni/rGO

As for the study of the PEDOT/nano-Ni/rGO electrode system in H_2 generation, EIS and Tafel plot studies were done for PPy/nano-Ni/rGO electrodes and compared with control films of nano-Ni/rGO, Pt, and PPy alone (with and without light illumination) (Figure 5.17). Similar EIS results were obtained with the control PPy samples (with and without illumination) being controlled by mass transport (diffusion) processes at low frequencies (about the 100.5 Hz) while the most active PPy/nano-Ni/rGO film (with and without illumination) was controlled by interfacial and charge transfer processes at intermediate frequencies (101-1.5 Hz).

Figure 5.17(b) shows the equivalent circuit used to model that data. The modelling is depicted by the solid lines in Figure 5.17(a), while the dots show the experimentally measured data. As can be seen, there is an excellent match between the measured data and the modelled data. Table 5.7 provides results deriving from the modelling, including the ohmic resistance, R_{el}, solution/interfacial/charge transfer resistance, R_{ct}, and capacitance, which was expressed in terms of a constant phase element (n_{CPE}, and C_{CPE}). The constant phase element provided the best fit of the measured and modelled data.

As can be seen in Table 5.7, C_{CPE} values of PPy, PPy/nano-Ni and PPy/nano-Ni/rGO films (with and without light illumination) produced significantly higher values than their equivalent PEDOT, PEDOT/nano-Ni and PEDOT/nano-Ni/rGO films. They were also increased, in going from control PPy to the nano-Ni/rGO film, to the PPy/nano-Ni/rGO film. This indicates that the PPy/nano-Ni/rGO and other control films for Ppy system had notably higher active areas and that illumination with light still further increased the active area. This is consistent with the highly porous structure observed in characterization. Thus, while there was relatively speaking less PPy monomer present than there had been PEDOT monomer, the PPy became notably more porous after operation, thereby producing the observed high electrochemically active areas.

The equivalent circuit in Figure 5.17(b) was used to model the EIS data. ('dark' = without light illumination; 'light' = with light illumination). Where nano-Ni and rGO are indicated to be present, the quantities were 125 mg nano-Ni, and 5.4 mg rGO.

The ohmic resistance (R_{el}) values were similar in going from PEDOT to PPy for all of the films, as would be expected given the constant inter-electrode separation used. However, the R_{ct} values of PPy, PPy/nano-nickel and PPy/nano-Ni/rGO were higher than their equivalent films PEDOT, PEDOT/nano-Ni, and PEDOT/Nano-Ni/rGO respectively. For example, Rct values of PPy/nano-Ni/rGO were 218.2 Ω cm^2 and 205.4 Ω cm^2 without and with light illumination respectively (*vs* 189.5 Ω cm^2 and 173 Ω cm^2 without and with light illumination respectively for the PEDOT/nano-Ni/rGO film). It is for this reason that the PPy/nano-Ni/rGO film exhibits less activity than PEDOT/nano-Ni/rGO.

In the Bode plots (Figure 15(c)), at the low frequency region, the Im Z values (in Ω.cm^2) of PPy and the most active PPy/nano-Ni/rGO (with and without light illumination) were shifted to higher values than their PEDOT equivalents. This confirmed that FTO coated with PEDOT and/or PEDOT with others materials had a better catalytic effect than PPy under the same condition. This means that in PEDOT system, the charges (ions) transferred faster from the diffusion layer to the catalyst. Similar trend was observed at high frequency regions confirming better catalysis for PEDOT system than PPy If the Bode plots (Figure 5.17(c)) for PPy in H_2 generation are compared with the Bode plots of the same catalyst but for O_2 generation (Figure 5.9(b)), then it can be concluded that the catalytic behaviour of PPy in acidic media was better than in alkaline media.

In addition, Figure 5.18 depicts Tafel plots of the catalysts, with results tabulated in the last two columns of Table 5.7. As can be seen in the Table, the Tafel slopes of the PPy, PPy/nano-Ni and PPy/nano-Ni films have higher values than their equivalent PEDOT films. This indicates that the catalytic activity of the PPy/nano-Ni/rGO system was generally lower than PEDOT/nano-Ni/rGO system. Furthermore, the exchange current densities (i_o) of PPy, PPy/nano-Ni and PPy/nano-Ni/rGO films were lower than their equivalent PEDOT films, which further resulted in lower activity.

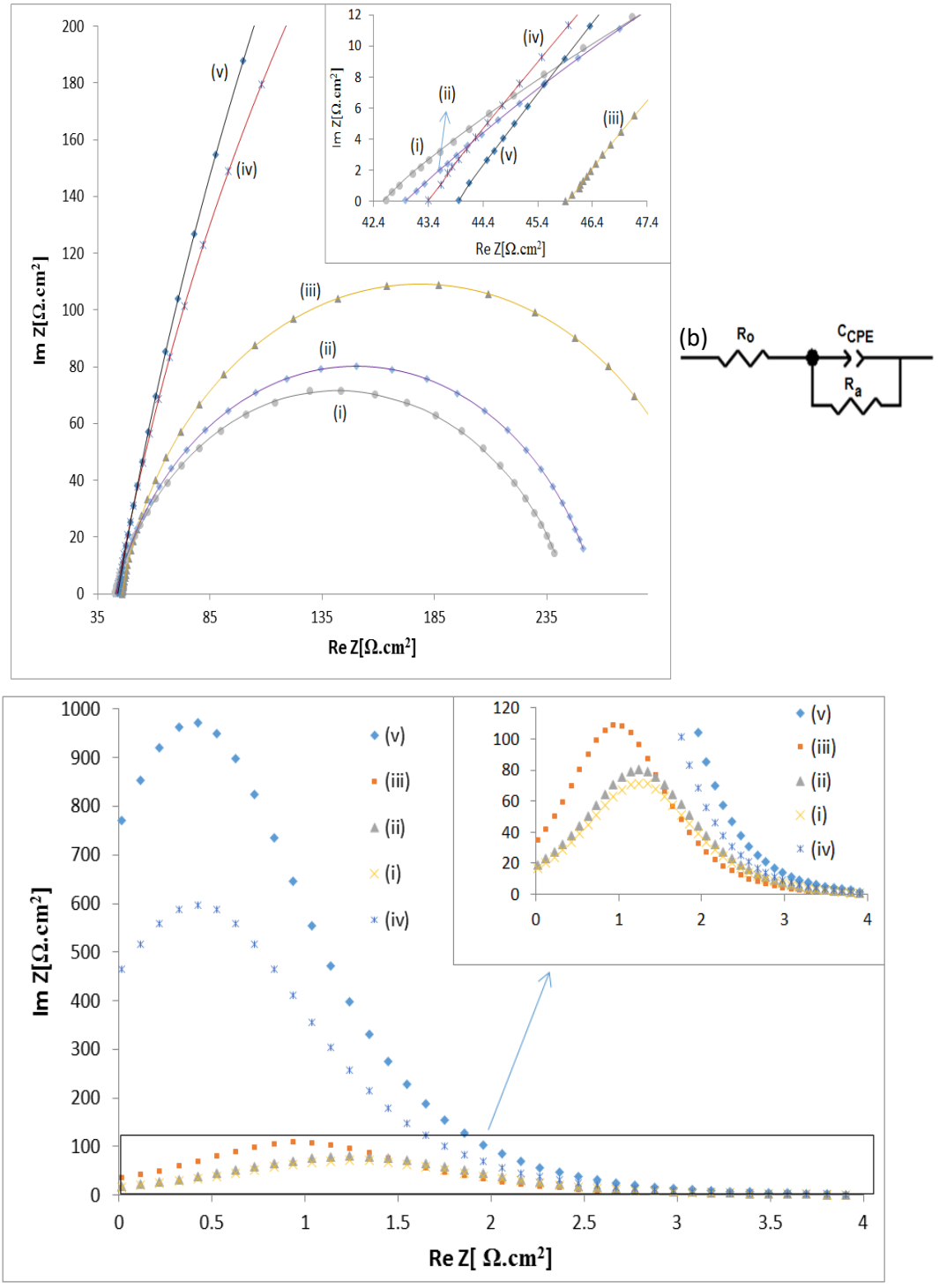

Figure 5.17: *(a) Nyquist plot, (b) equivalent circuit, and (c) Bode plot; at –0.75 V (vs Ag/AgCl); showing measured data (individual data points) and modelled data (solid lines) (modelled using the equivalent circuit depicted in (b)), for: (i) PPy/nano-Ni/rGO (with light illumination), (ii) PPy/nano-Ni/rGO (dark; without light illumination), (iii) nano-Ni/rGO, (iv) PEDOT only (with light illumination), and (v) PPy only (dark). Where nano-Ni and rGO are indicated to be present, the quantities were 125 mg nano-Ni, and 5.4 mg rGO.*

Sample	R_{el} Ω cm^2	R_{CT} Ω cm^2	Q_{CPE} μΩ^{-1}cm^{-2}	n_{cpe}	C_{CPE} μFcm^{-2}	A mV/dec	i_o μA cm^2
PEDOT (dark)	43.57 ± 2.33	1005 ±5	96.32 ±2.11	0.80 ±0.23	2.43 ±0.87	70.24 ± 4.22	14.80 ±1.23
PPy (dark)	**43.35** ± 2.29	**2450** ±8	**30.78** ±0.96	**0.87** ±0.22	**11.02** ±0.91	**83.39** ±3.44	**4.770** ±1.72
PEDOT (light)	42.81 ±2.12	749 ±4	105.0 ±2.0	0.80 ±0.21	2.69 ±0.77	68.31 ±2.85	15.74 ±2.23
PPy (light)	**43.31** ±2.11	**1492** ±4	**39.7** ±1.9	**0.86** ±0.21	**13.88** ±1.16	**69.04** ±3.44	**5.30** ±1.21
Nano-Ni/rGO	45.84 ±2.39	265.6 ±1.2	142.0 ±2.6	0.81 ±0.22	4.20 ±0.72	58.72 ±4.30	9.07 ±1.55
PEDOT/nano-Ni/rGO (dark)	43.38 ±2.24	189.5 ±1.3	156.0 ±2.5	0.80 ±0.18	4.25 ±0.62	57.74 ±3.96	6.45 ±1.11
PPy/nano-Ni/rGO (dark)	**42.97** ±2.18	**218.2** ±2.3	**99.5** ±2.5	**0.81** ±0.14	**28.00** ±0.46	**59.84** ±4.02	**2.56** ±0.78
PEDOT/nano-Ni/rGO (light)	42.43 ±2.11	173.8 ±1.3	165.0 ±2.7	0.81 ±0.16	4.71 ±0.23	47.83 ±4.33	6.67 ±2.11
PPy/nano-Ni/rGO (light)	**42.36** ±2.09	**205.4** ±2.23	**110.9** ±2.6	**0.81** ±0.14	**30.13** ±0.21	**50.07** ±5.23	**2.82** ±0.67
Pt	----	-----	-----	----	-----	58.35 ±4.56	7.02 ±3.44

Table 5.7: *Data from EIS modelling (ohmic resistance, Ro, charge transfer resistance, R_{ct}, and charge transfer capacitance (C_{ct}) expressed in terms of a constant phase element (n_{CPE} and C_{CPE}) and Tafel plots (slope A; exchange current density i_o).*

However, the catalytic activity of the most active PPy/nano-Ni/rGO film was still higher than that of Pt and, like the equivalent PEDOT/nano-Ni/rGO film, more strongly activated by the applied voltage bias. The PPy film synergistically enhanced the electrocatalysis in much the same way that the PEDOT did with the nano-Ni and the rGO.

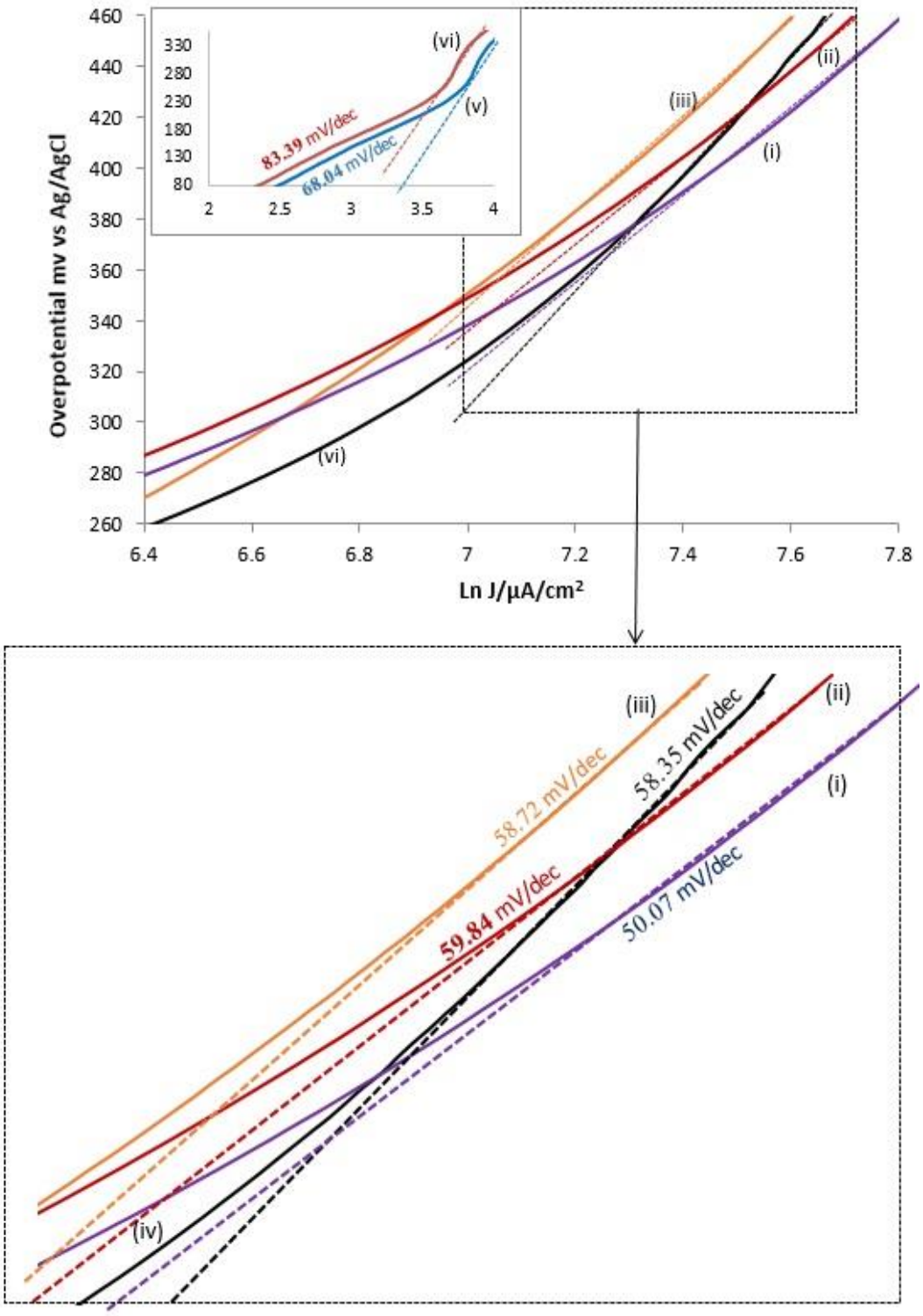

Figure 5.18: *Tafel plots for: (i) PPy/nano-Ni/rGO (with light illumination), (ii) PPy/nano-Ni/rGO (dark; without light illumination), (iii) Nano-Ni/rGO, (iv) Pt only, (v) PPy only (with light illumination), (vi) PPy only (dark; no light illumination).*

5.2.2.5 Summary: Hydrogen Generation Catalysis by the Most Active PPy/nano-Ni/rGO Thin Film

Tri-component PPy films containing nano-Ni and rGO have been studied as electrocatalysts and photoelectrocatalysts of hydrogen reduction in 0.05 M H_2SO_4/0.2 M Na_2SO_4 at -0.75 V *vs* Ag/AgCl. While the control PPy, PPy/nano-Ni, and PPy/rGO films were only weakly catalytic, films containing PPy: nano-Ni : rGO in a molar ratio of 0.51 (PPy monomer) : 1.00 (Ni) : 4.43 (C; other) proved to be highly active, particularly with time. After 3 h of operation under constant light illumination of 0.25 sun, they generated sustained current densities at –0.75 V (*vs* Ag/AgCl) of 2.6 mA/cm^2 (which included ca. 200 μA/cm^2 due to the light illumination). This was 25% greater than an equivalent nano-Ni/rGO film that did not contain PPy, which achieved 2.1 mA/cm^2, and a sputter-coated Pt film, which yielded 2.2 mA/cm^2, under the same conditions. Gas analysis demonstrated that hydrogen was the sole gas produced. SEM/EDX showed that the film comprised a porous structure in which the elemental constituents were evenly distributed.

5.3 Conclusions

In water oxidation catalysis, a 0.66 μm thick PPy film (7.78 S/cm) containing the specific ratio of 125 mg of nano-Ni and 6.0 mg of rGO on a Pt electrode, produced a significantly larger current (0.97-1.00 mA/cm^2; including a 0.48 mA/cm^2 photocurrent under light illumination of 0.25 sun) than the equivalent bare Pt control electrode (0.15 mA/cm^2) under the same conditions, over 50 h of operation.

The greatest amplification for hydrogen generation catalysis was produced by a 0.65 μm thick film (6.90 S/cm^2) containing 125 mg of nano-Ni and 5.4 mg of rGO that yielded a 18% higher current (2.6 mA/cm^2, including a 0.2 mA/cm^2 photocurrent under 0.25 sun) than the control bare Pt electrode (2.2 mA/cm^2) after 3 h of operation.

Its performance was also superior to an equivalent control film containing the same quantities of nano-Ni and rGO without any PEDOT (2.1 mA/cm^2). As in the case of PEDOT, minor variations in the above composition produced notably lower currents.

It can be concluded, firstly, that the above specific ratio of catalyst density to conductivity and thickness applies to thin-film conducting polymers in general and is not unique to PEDOT. That is, it also applies to other conducting polymer supports, like PPy. This is consistent with the conducting polymer connecting the largest number of catalytic sites by the shortest, least-resistive pathways. The effect of the lower conductivity of PPy relative to PEDOT is only to increase the resistance of those shortest pathways, thereby decreasing the extent of the amplification

5.4 References

1. Alsultan, M.; Ranjbar, A.; Swiegers, G. F.; Wallace, G. G.; Balakrishnan, S.; Huang, J. Application of Conducting Polymers in Solar Water-Splitting Catalysis. In *Industrial Applications for Intelligent Polymers and Coatings*, Hosseini, M.; Makhlouf, A. S. H., Eds. Springer International Publishing: Switzerland, **2016**; pp 223-251.
2. Mohan Kumar, G.; Raman, V.; Kawakita, J.; Ilanchezhiyan, P.; Jayavel, R. Fabrication of Polypyrrole/ZnCoO Nanohybrid Systems for Solar Cell Applications. *Dalton Trans.* **2010**, *39* (35), 8325-8330.
3. Wang, Z.; Xiao, P.; Qiao, L.; Meng, X.; Zhang, Y.; Li, X.; Yang, F. Polypyrrole Sensitized ZnO Nanorod Arrays for Efficient Photo-Electrochemical Splitting of Water. *Phys. B: Condens. Matt.* **2013**, *419*, 51-56.
4. Kellici, S.; Acord, J.; Ball, J.; Reehal, H. S.; Morgan, D.; Saha, B. A Single Rapid Route for the Synthesis of Reduced Graphene Oxide with Antibacterial Activities. *RSC Adv.* **2014**, *4* (29), 14858-14861.
5. Ok-Kyung, P.; Yong-Mun, C.; Jun Yeon, H.; Cheol-Min, Y.; Tea-Wook, K.; Nam-Ho, Y.; Hye Young, K.; Joong Hee, L.; Bon-Cheol, K.; Munju, G. Defect Healing of Reduced Graphene Oxide via Intramolecular Cross-Dehydrogenative Coupling. *Nanotechnol.* **2013**, *24* (18), 1-7.
6. Jimenez-Cervantes Amieva, E.; Fuentes-Ramirez, R.; Martinez-Hernandez, A. L.; Millan-Chiu, B.; Lopez-Marin, L. M.; Castaño, V. M.; Velasco-Santos, C. Graphene Oxide and Reduced Graphene Oxide Modification with Polypeptide Chains From Chicken Feather Keratin. *J. Alloys Compd.* **2015**, *643*, S137-S143.
7. Ossonon, B. D.; Belanger, D. Synthesis and Characterization of Sulfophenyl-Functionalized Reduced Graphene Oxide Sheets. *RSC Adv.* **2017**, *7* (44), 27224-27234.
8. Yang, Y.; Luo, L.; Xiao, M.; Li, H.; Pan, X.; Jiang, F. One-Step Hydrothermal Synthesis of Surface Fluorinated TiO_2/Reduced Graphene Oxide Nanocomposites for Photocatalytic Degradation of Estrogens. *Mater. Sci. Semicond. Process.* **2015**, *40*, 183-193.
9. Dave, K.; Park, K. H.; Dhayal, M. Two-Step Process for Programmable Removal of Oxygen Functionalities of Graphene Oxide: Functional, Structural and Electrical Characteristics. *RSC Adv.* **2015**, *5* (116), 95657-95665.

10. Zhou, X.; Chen, F.; Yang, J. Core@Shell Sulfur@Polypyrrole Nanoparticles Sandwiched in Graphene Sheets as Cathode for Lithium–Sulfur Batteries. *J. Energy Chem.* **2015**, *24* (4), 448-455.
11. Gui, J.; Zhang, J.; Liu, T.; Peng, Y.; Chang, J. Two-Step Controllable Preparation of NiO Nanocrystal Anchored Reduced Graphene Oxide Sheets and Their Electrochemical Performance as Supercapacitors. *New J. Chem.* **2017**, *41* (19), 10695-10702.
12. Wang, J.-G.; Yang, Y.; Huang, Z.-H.; Kang, F. Rational synthesis of MnO_2/conducting Polypyrrole@Carbon Nanofiber Triaxial Nano-Cables for High-Performance Supercapacitors. *J. Mater. Chem.* **2012**, *22* (33), 16943-16949.
13. Nam, D.-H.; Lim, S.-J.; Kim, M.-J.; Kwon, H.-S. One-Step Synthesis of a Si/CNT-Polypyrrole Composite Film by Electrochemical Deposition. *RSC Adv.* **2014**, *4* (20), 10212-10215.
14. Galan, T.; Lagunas, A.; Martinez, E.; Samitier, J. Fabrication of Bioactive Polypyrrole Microelectrodes on Insulating Surfaces by Surface-Guided Biocatalytical Polymerization. *RSC Adv.* **2015**, *5* (82), 67082-67088.
15. Cao, J.; Wang, Y.; Chen, J.; Li, X.; Walsh, F. C.; Ouyang, J.-H.; Jia, D.; Zhou, Y. Three-Dimensional Graphene Oxide/Polypyrrole Composite Electrodes Fabricated by One-Step Electrodeposition for High Performance Supercapacitors. *J. Mater. Chem. A* **2015**, *3* (27), 14445-14457.
16. George, G.; Anandhan, S. Synthesis and Characterisation of Nickel Oxide Nanofibre Webs with Alcohol Sensing Characteristics. *RSC Adv.* **2014**, *4* (107), 62009-62020.
17. Shimizu, K.; Lasia, A.; Boily, J.-F. Electrochemical Impedance Study of the Hematite/Water Interface. *Langmuir.* **2012**, *28* (20), 7914-7920.
18. Swierk, J. R.; Klaus, S.; Trotochaud, L.; Bell, A. T.; Tilley, T. D. Electrochemical Study of the Energetics of the Oxygen Evolution Reaction at Nickel Iron (Oxy)Hydroxide Catalysts. *J. Phys. Chem. C* **2015**, *119* (33), 19022-19029.
19. Pletcher, D.; Sotiropoulos, S. Hydrogen Adsorption-Desorption and Oxide Formation -Reduction on Polycrystalline Platinum in Unbuffered Aqueous Solutions. *J. Chem. Soc. Faraday Trans.* **1994**, *90* (24), 3663-3668.
20. Brug, G. J.; van den Eeden, A. L. G.; Sluyters-Rehbach, M.; Sluyters, J. H. The Analysis of electrode Impedances Complicated by the Presence of a Constant Phase Element. *J. Electroanal. Chem. Interfac. Electrochem.* **1984**, *176* (1), 275-295.
21. Hu, Z.-A.; Xie, Y.-L.; Wang, Y.-X.; Wu, H.-Y.; Yang, Y.-Y.; Zhang, Z.-Y. Synthesis and Electrochemical Characterization of Mesoporous Co_xNi_{1-x} Layered Double Hydroxides asElectrode Materials for Supercapacitors. *Electrochim. Acta* **2009**, *54* (10), 2737-2741.

22. Liu, X.; Huang, J.; Wei, X.; Yuan, C.; Liu, T.; Cao, D.; Yin, J.; Wang, G. Preparation and Electrochemical Performances of Nanostructured $Co_xNi_{1-x}(OH)_2$ Composites for Supercapacitors. *J. Power Sources* **2013**, *240*, 338-343.
23. Zhao, Y.; He, S.; Wei, M.; Evans, D. G.; Duan, X. Hierarchical Films of Layered Double Hydroxides by Using a Sol-Gel Process and Their High Adaptability in Water Treatment. *Chem. Commun.* **2010**, *46* (17), 3031-3033.
24. Xu, J.; Gai, S.; He, F.; Niu, N.; Gao, P.; Chen, Y.; Yang, P. A Sandwich-Type Three-Dimensional Layered Double Hydroxide Nanosheet Array/Graphene Composite: Fabrication and High Supercapacitor Performance. *J. Mater. Chem. A* **2014**, *2* (4), 1022-1031.
25. Satheesh, K.; Jayavel, R. Synthesis and Electrochemical Properties of Reduced Graphene Oxide via Chemical Reduction Using Thiourea as a Reducing Agent. *Mater. Lett.* **2013**, *113*, 5-8.
26. Gupta, R. K.; Alahmed, Z. A.; Yakuphanoglu, F. Graphene Oxide Based Low Cost battery. *Mater. Lett.* **2013**, *112*, 75-77.
27. Kavinkumar, T.; Manivannan, S. Uniform Decoration of Silver Nanoparticle on Exfoliated Graphene Oxide Sheets and its Ammonia Gas Detection. *Ceram. Int.* **2016**, *42* (1, Part B), 1769-1776.
28. K, M.; RG, B.; IB, A.; SM, S.; Lim HN, L. H.; NM, H.; Chia CH; S, M. Exceedingly Biocompatible and Thin-Layered Reduced Graphene Oxide Nanosheets Using an Eco-Friendly Mushroom Extract Strategy. *Ceram. Int.* **2014**, *10* (1), 1505-1519.
29. Zong, M.; Huang, Y.; Zhao, Y.; Sun, X.; Qu, C.; Luo, D.; Zheng, J. Facile Preparation, High Microwave Absorption and Microwave Absorbing Mechanism of RGO-Fe_3O_4 Composites. *RSC Adv.* **2013**, *3* (45), 23638-23648.
30. Si, Y.; Samulski, E. T. Exfoliated Graphene Separated by Platinum Nanoparticles. *Chem. Mater.* **2008**, *20* (21), 6792-6797.
31. Upadhyay, S.; Bagheri, S.; Abd Hamid, S. B. Enhanced Photoelectrochemical Response of Reduced-Graphene Oxide/$Zn_{1-x}Ag_xO$ Nanocomposite in Vvisible-Light Region. *Int. J. Hydrogen Energy* **2014**, *39* (21), 11027-11034.
32. Chitte, H. K.; Bhat, N. V.; Gore, M. A. V.; Shind, G. N. Synthesis of Polypyrrole Using Ammonium Peroxy Disulfate (APS) as Oxidant Together with Some Dopants for Use in Gas Sensors. *Mater. Sci. Applicat.* **2011**, *2* (10), 1491-1498.
33. Ma, Y.; Jiang, S.; Jian, G.; Tao, H.; Yu, L.; Wang, X.; Wang, X.; Zhu, J.; Hu, Z.; Chen, Y. CN_x Nanofibers Converted From Polypyrrole Nanowires as Platinum Support for Methanol Oxidation. *Energy Environ. Sci.* **2009**, *2* (2), 224-229.
34. Zhang, X.; Zhang, J.; Song, W.; Liu, Z. Controllable Synthesis of Conducting Polypyrrole Nanostructures. *J. Phys. Chem. B* **2006**, *110* (3), 1158-1165.

35. Jiang, Z.; Xie, J.; Jiang, D.; Wei, X.; Chen, M. Modifiers-Assisted Formation of Nickel Nanoparticles and Their Catalytic Application to p-nitrophenol Reduction. *Cryst. Eng. Comm.* **2013**, *15* (3), 560-569.
36. Tientong, J.; Garcia, S.; Thurber, C. R.; Golden, T. D. Synthesis of Nickel and Nickel Hydroxide Nanopowders by Simplified Chemical Reduction. *J. Nanotechnol.* **2014**, *2014*, 193162 (1-6).
37. Khanam, P. N.; Popelka, A.; Alejji, M.; AlMaadeed, M. A. Biotechnological Production Process and Life Cycle Assessment of Graphene. *J. Nanomater.* **2017**, *2017*, 5671584 (1-10).
38. Lim, C. S.; Chua, C. K.; Pumera, M. Detection of Biomarkers with Graphene Nanoplatelets and Nanoribbons. *Analyst* **2014**, *139* (5), 1072-1080.
39. Wenjing, H.; Qingli, H.; Wu, L.; Lihua, W.; Xifeng, X. Polypyrrole-Hemin-Reduce Graphene Oxide: Rapid Synthesis and Enhanced Electrocatalytic Activity Towards the Reduction of Hydrogen Peroxide. *Mater. Res. Express* **2014**, *1* (4), 1-17.
40. Xing, Z.; Ju, Z.; Zhao, Y.; Wan, J.; Zhu, Y.; Qiang, Y.; Qian, Y. One-Pot Hydro thermal Synthesis of Nitrogen-Doped Graphene as High-Performance Anode Materials for Lithium Ion Batteries. *Sci. Rep.* **2016**, *6*, 26146 (1-10).
41. Ou, J.; Zhang, Y.; Chen, L.; Zhao, Q.; Meng, Y.; Guo, Y.; Xiao, D. Nitrogen-Rich Porous Carbon Derived From Biomass as a High Performance Anode Material for Lithium Ion Batteries. *J. Mater. Chem. A* **2015**, *3* (12), 6534-6541.
42. Singh, A.; Salmi, Z.; Joshi, N.; Jha, P.; Kumar, A.; Lecoq, H.; Lau, S.; Chehimi, M. M.; Aswal, D. K.; Gupta, S. K. Photo-Induced Synthesis of Polypyrrole-Silver Nanocomposite Films on N-(3-trimethoxysilylpropyl)Pyrrole-Modified Biaxially Oriented Polyethylene Terephthalate Flexible Substrates. *RSC Adv.* **2013**, *3* (16), 5506-5523.
43. Kumar, R.; Oves, M.; Almeelbi, T.; Al-Makishah, N. H.; Barakat, M. A. Hybrid Chitosan/Polyaniline-Polypyrrole Biomaterial for Enhanced Adsorption and Antimicrobial Activity. *J. Colloid Interface Sci.* **2017**, *490*, 488-496.
44. Ji, Z.; Wang, Y.; Shen, X.; Ma, H.; Yang, J.; Yuan, A.; Zhou, H. Facile Synthesis and Enhanced Catalytic Performance of Reduced Graphene Oxide Decorated with Hexagonal Structure Ni Nanoparticles. *J. Colloid Interface Sci.* **2017**, *487*, 223-230.

Chapter 6

PEDOT/Nano-Co_3O_4/CNT Composite for Oxygen Generation in Photo-Catalytic Water Splitting

Declaration: Portions of this chapter are drawn from a draft journal article entitled: "*Remarkable Synergistic Amplification of Oxygen Generation in (Photo)Catalytic Water Splitting by a PEDOT/Nano-Co_3O_4/MWCNT Thin Film Composite"*, for which I, Mohammed Alsultan, am the first author, along with co-authors: Ruhollah Jalili, Pawel Wagner, and Gerhard F. Swiegers. My contribution involved: (i) carrying out the laboratory research and measurements, (ii) constructing the plots and figures from the data obtained, and (iii) writing the first draft of the journal article.

6.1 Introduction

Cobalt (Co) and its oxides, alloys and spinels, including $Co(OH)_2$,[1] Co_3O_4,[2] CoO,[3] NiCo,[4] CuCo,[5] and $LiCoO_2$,[6] have been widely investigated as photo- and electrocatalysts of the oxygen evolution reaction (OER) as they are abundant and cheap with high corrosion resistivity. Co_3O_4 is particularly renowned as a highly active catalyst of the OER.[2] However, this and the other species above have several disadvantages, including poor dispersibility, low conductivity, and poor charge carrier mobility[7]. Some studies have, however, previously reported that when cobalt oxides are combined with other organic materials such as reduced graphene oxide (rGO),[8]

graphene[9] or carbon nanotubes (CNTs)[10-12] in alkaline media, the resulting materials exhibited enhanced OER performance due to an increase in both the conductivity and the number of active catalytic sites on the surface of the resulting composite. This is appealing for investigation given the findings in the previous chapters that the key to fully utilizing conducting polymers as thin-film catalysts is to apply them in a form that maximizes the catalytically active area and the electrically connection (conductance) with each catalytic site.

Carbon nanotubes (CNTs) have some remarkable features that make them attractive in water splitting applications, including the following: (i) they provide high surface areas when interfaced with catalytic materials, (ii) they facilitate charge carrier (e^-, h^+) mobility, and (iii) they mobilize the catalyst on the CNT surface, which results in better OER activity.[13-34] The combination of Co_3O_4 and CNT have been the subject of several studies, such as: (i) Co_3O_4/ single-walled carbon nanotubes (SWNTs)-loaded on Indium Tin Oxide (ITO),[9] (ii) Co_3O_4/ Nitrogen-doped carbon nanotubes (NCNT),[10] and (iii) Co_3O_4/ carbon nanotubes (CNT),[11] The resulting hybrid species exhibit superior catalytic activity that has been attributed to the synergistic effects of CNT with the catalysts.

This chapter continues the theme of studying the optimum deployment of conducting polymers as catalyst supports in thin-film form, when combined with catalysts and conductors. However, in this chapter a different set of catalysts and conductors have been employed. Studies are reported of PEDOT films containing nanoparticulate Co_3O_4 ('nano-Co_3O_4') (av. diameter: 25 nm) as an active OER catalyst and multiwall carbon nanotubes (MWCNTs) as a conductor on FTO glass. The aim of changing the components in this way was to see whether the relationship between catalytic area and connectivity that was discovered and studied in the previous chapters also holds with very different catalysts (non-conductive metal oxide OER catalysts) and carbon-based conductors (MWCNTs).

As in Chapters 3 and 5, the films have been studied as electrodes in photocatalytic water oxidation in 0.2 M Na_2SO_4, adjusted to pH 12 as an electrolyte. It was found that films containing PEDOT: nano-Co_3O_4: CNT in a molar ratio of 6.92 (C; PEDOT): 1 (Co): 5.13 (C; other) exhibited excellent OER activity that exceeded anything yet observed in this thesis.

On FTO glass alone, this film produced a dark current density of 390-400 $\mu A/cm^2$ at 0.80 V (*vs* Ag/AgCl) with a total current density of 880-900 $\mu A/cm^2$ under light illumination (including 490-500 $\mu A/cm^2$ of photocurrents). This superseded the performance of the industry-standard OER catalyst, Pt, which only yielded 150 $\mu A/cm^2$ as same conditions. However, when the above PEDOT/nano-Co_3O_4/CNT composite film was overcoated on a Pt electrode, the resulting film produced an order-of-magnitude greater current of 2.62-2.74 mA/cm^2 including a photocurrent of 0.50-0.64 mA/cm^2 under 0.25 sun illumination at the same experimental conditions (0.2 M Na_2SO_4, adjusted to pH 12 as an electrolyte biased at 0.8 v *vs* Ag/AgCl). The study confirmed that the amplified catalytic performance of the tested film arose from an optimum catalytic density to conductivity and thickness in which the PEDOT electrically connected the largest number of active catalytic sites by the most conductive pathway. That is, the composite PEDOT thin-film, with very different catalyst and conductor components operated in complete accord with the principles developed in the earlier chapters of this thesis.

6.2 Results and Discussion

6.2.1 Studies of PEDOT/nano-Co_3O_4 on FTO

As in chapter 3, in first stage of this study, uniformly prepared thin-films of vapour-phase polymerized PEDOT containing varying quantities of nano-Co_3O_4 (av. 25 nm diameter) on FTO glass slides (4.2 cm^2), were examined as water oxidation

electro- and/or photo-catalysts in 0.2 M Na_2SO_4 aqueous solution, with the pH adjusted to 12, while biased at 0.8 V (*vs* Ag/AgCl).

Figure 6.1 depicts data from this study. As can be seen, when the relative quantity of nano-Co_3O_4 was increased, the dark current, as well as photocurrent increased. Thus, the control PEDOT film with no nano-Co_3O_4 showed a small current

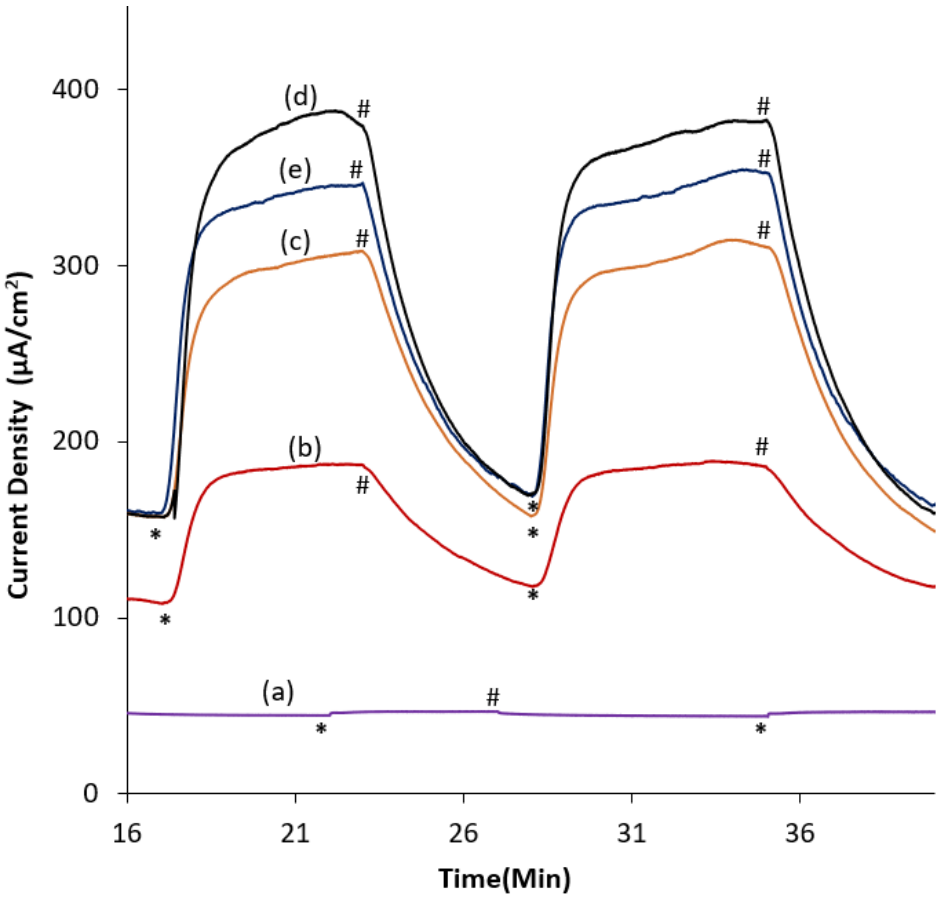

Figure 6.1 *Chronoamperograms at 0.8 V (vs. Ag/AgCl) in 0.2 M Na_2SO_4 (pH 12), with and without light illumination (0.25 sun), of FTO glass slides coated with: PEDOT/nano-Co_3O_4, where the quantity of nano-Co_3O_4 in the vapour phase polymerisation solution was: (a) 0 mg nano-Co_3O_4 (PEDOT only; control), (b) 40 mg nano-Co_3O_4, (c) 90 mg nano-Co_3O_4, (d) 110 mg nano-Co_3O_4, and (e) 120 mg nano-Co_3O_4. (*='light on', #='light off').*

density (Figure 6.1(a)). Whereas, the films that were prepared from polymerisation mixtures containing 40 mg nano-Co_3O_4 (Figure 6.1(b)), 90 mg nano-Co_3O_4 (Figure 6.1(c)), and 110 mg nano-Co_3O_4 (Figure 6.1(d) produced higher dark currents densities of (110-158 μA/cm^2) and photocurrents of (78.5-207μA/cm^2). When more than 110 mg of nano-Co_3O_4 was incorporated into the films, the net current started to decline. For example, the PEDOT film containing 120 mg of nano-Co_3O_4, produced an unchanged dark current of ca. 158 μ/cm^2 but a lower photocurrent of only ca. 172 μA/cm^2 (Figure 6.1 (e)). Consequently, any additional of nano-Co_3O_4 that was incorporated into the film resulted in a decrease of photocurrent. This effect was previously assigned to a decrease in the light absorption by the film caused by shadowing arising from the high density of Co_3O_4, which is non-transparent and also not activated by light. In conclusion, the film PEDOT/ Nano-Co_3O_4 that was prepared from a polymerisation mixture containing 110 mg of nano-Co_3O_4 exhibited the highest photocatalytic activity.

6.2.2 Studies of PEDOT/nano-Co_3O_4/CNT on FTO

The next step was to prepare and test the incorporation of varying weights of CNT in the PEDOT/nano-Co_3O_4 film containing 110 mg of nano-Co_3O_4. The maximum weight of CNT that could be incorporated in the films using the vapour phase polymerisation technique was 3.0 mg. Beyond this amount, the polymerisation mixtures became too thick to spin-coat successfully.

Figure 6.2 shows chronoamperograms of the best performing of these films on FTO glass under the same conditions (0.80 V *vs* Ag/AgCl in 0.2 M Na_2SO_4 adjusted to pH 12 over 1 h of operation, with and without light illumination of 0.25 sun).

As can be seen in Figure 6.2, the dark current and photocurrent increased with increasing CNT loading up to 2.0 mg ((Figure 6.2(a)-(b)). Thus, the largest dark current (380-450 μA/cm^2) and photocurrent (460-470 μA/cm^2) was produced by PEDOT/nano-Co_3O_4 /CNT containing 110 mg nano-Co_3O_4 and 2.0 mg CNT. This film had a thickness

of 0.98 µm and a conductivity of 5.98 S/cm. The net current declined dramatically when more than 2 mg of CNT was incorporated into the film; for example, PEDOT containing 110 mg nano-Co_3O_4 and 3.0 mg of CNT (Figure 6.2(c)) produced a significantly lower dark current of ca. 150 µA/cm^2 as well as a lower photocurrent of ca. 180 µA/cm^2. The additional CNT may also result in a decrease in light absorption by the film.

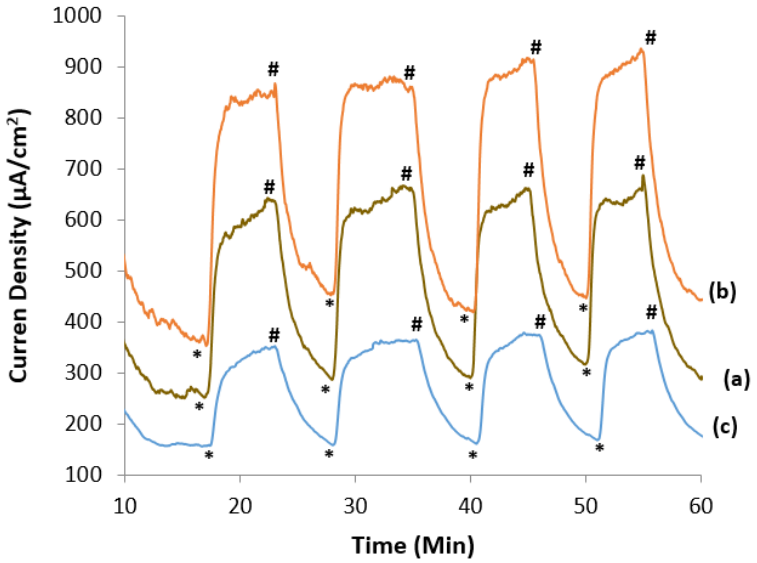

Figure 6.2: *Chronoamperograms at 0.80 V (vs Ag/AgCl) in 0.2 M Na_2SO_4 (pH 12) over 1 h of operation, with and without light illumination (0.25 sun), of FTO glass slides coated with thin films of PEDOT/nano-Co_3O_4/CNT, where the polymerisation mixtures contained 110 mg of nano-Co_3O_4 and the following quantities of CNT: (a) 1.0 mg, (b) 2.0 mg and (c) 3.0 mg (*='light on', #='light off').*

6.2.3 Studies of Control Films on FTO; Catalytic Amplification due to the PEDOT

Figure 6.3 shows the chronoamperogram data of the control films, over 1 h (Figure 6.3 (I)) and over the first few minutes (Figure 6.3(II)).

As can be seen in Figure 6.3(I), all the control films exhibited notably lower currents compared to PEDOT/nano-nanoCo_3O_4/CNT containing 110 mg nano-Co_3O_4 and 2.0 mg CNT (that can be seen in Figure 6.2(b)). Thus, the control coating comprising of 2.0 mg CNT and 110 mg nano-Co_3O_4 only (without any PEDOT),produced a photocurrent density of 430-440 µA/cm^2 (Figure 6.3(c)), which

(I)

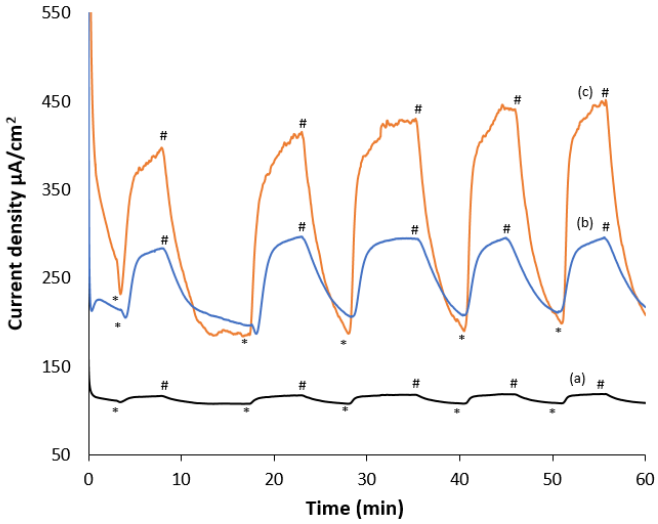

(II)

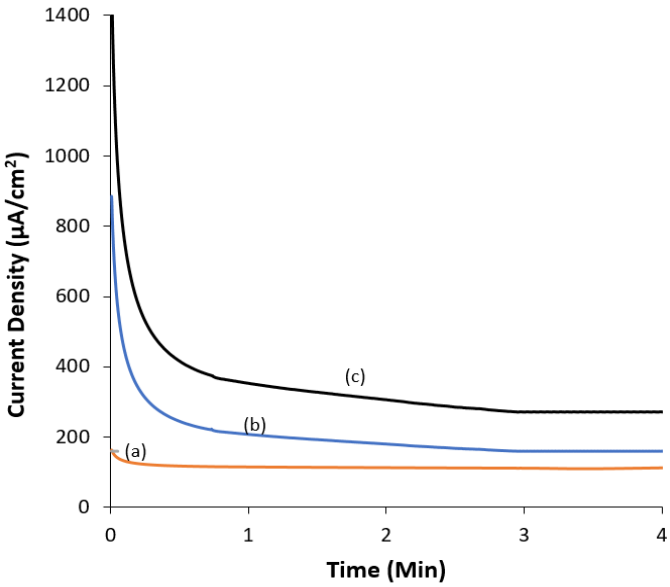

Figure 6.3: *Chronoamperograms over 1 h (I) and in the first few minutes (II) at 0.80 V (vs Ag/AgCl) in 0.2 M Na_2SO_4 (pH 12), with and without light illumination (0.25 sun), of FTO glass slides coated with control thin films comprising of: (a) 2.0 mg CNT only, (b) PEDOT containing 2.0 mg CNT, and (c) 2.0 mg CNT and 110 mg nano-Co_3O_4 only (without any PEDOT). (*='light on', #='light off').*

was around 50% lower than the current density of the PEDOT film containing 110 mg nano-Co_3O_4 and 2.0 mg CNT (Figure 6.2(b)). Thus, the presence of the PEDOT in the most active thin film (PEDOT/nano-nano-Co_3O_4/CNT) amplified the current density by about 50%.

As can be seen in Figure 6.3(II), the alternative water oxidation processes (involving oxidation or partial oxidation of the components of the film themselves) were complete within 4 min, with stable dark currents gained thereafter. The charge involved in the oxidation of the PEDOT itself (Figure 6.3(II)(b)) was calculated to be 0.162 C, while the charge required to partially oxidise the Co^{+2} to Co^{+3} in nano-Co_3O_4 film containing 2 mg CNT was calculated to be 0.434 C (Figure 6.3(II)(c)). In contrast, the current profile of the CNT control film in Figure 6.3(a) was approximately flat and is consistent with the expected absence of further oxidation at the catalyst surface.

6.2.4 Performance of the most active PEDOT/ nano-Co_3O_4/CNT thin film on Pt

As in Chapter 3, the most active PEDOT/nano-Co_3O_4/CNT thin film was examined on a sputtered Pt electrode in order to eliminate the effect of sheet resistance from the FTO. Figure 6.4(a) shows that the PEDOT/nano-Co_3O_4/CNT composite containing 110 mg nano-Co_3O_4 and 2.0 mg CNT on Pt/FTO, produced a dark current of 2.0-1.86 mA/cm^2 and a photocurrent of 0.50-0.64 mA/cm^2, giving a total current of 2.62-2.74 mA/cm^2. These current values were far higher than the currents generated by the control bare Pt film (Figure 6.4(III)-c), PEDOT/FTO (Figure 6.4(III)-d) and PEDOT/nano-Co_3O_4/CNT alone on FTO without Pt (Figure 6.2(b)). In addition, as can be seen in Figure 6.4 (II), PEDOT/nano-Co_3O_4/CNT film on Pt/FTO containing 110 mg nano-Co_3O_4 and 2.0 mg CNT on Pt/FTO (without PEDOT) produced a dark curent of 1.162-1.166 mA/cm^2 and limitted photocurrent of 0.076-0.098, giving a total current of 1.24 0-1.262 mA/cm^2. Thus, the presence of the PEDOT in the most active

thin film (PEDOT/nano-nano-Co_3O_4/CNT) on Pt/FTO amplified the current density by about 50%. The higher current density PEDOT/nano-Co_3O_4/CNT film on Pt/FTO attributed to the presence of the more conductive metallic Pt substrate on the FTO, with accompanying lower sheet resistance achieved with the presence of PEDOT.

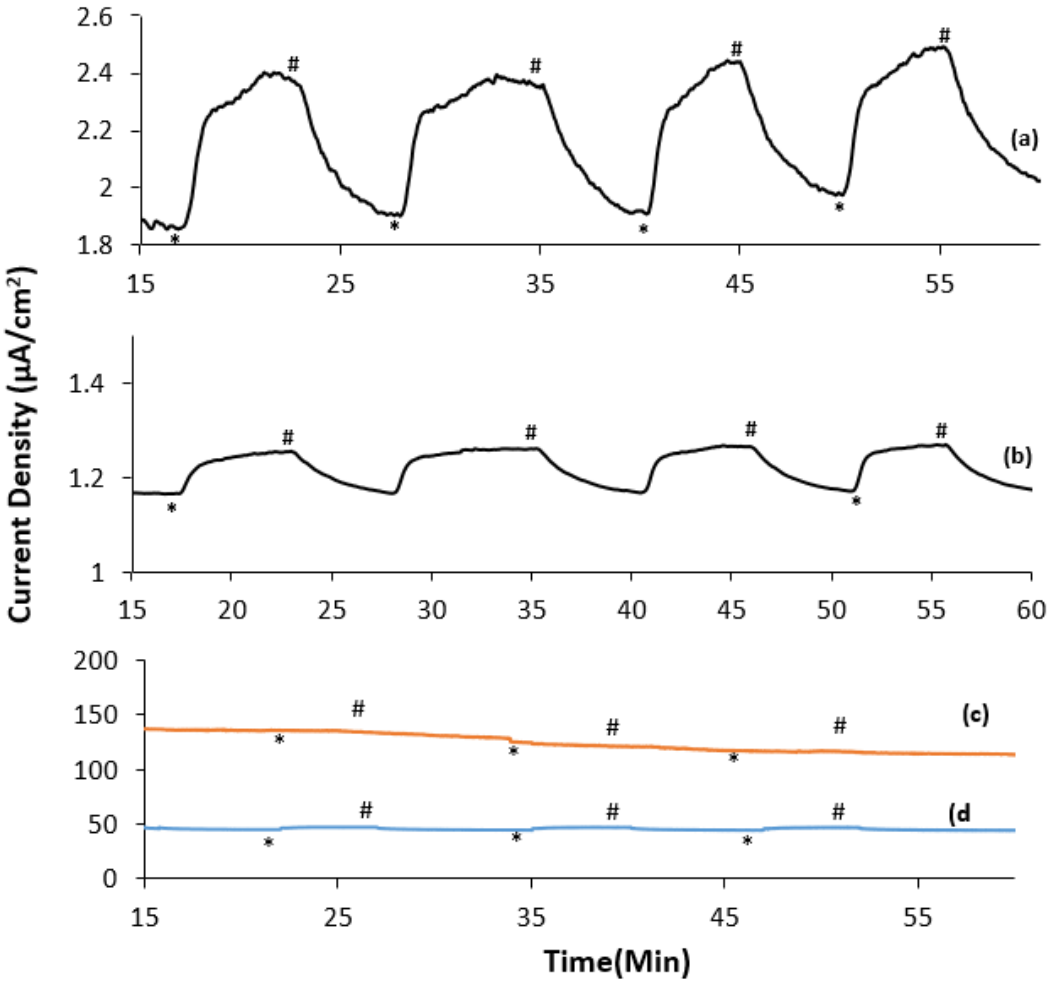

Figure 6.4: *Chronoamperograms at 0.80 V (vs Ag/AgCl) in 0.2 M Na_2SO_4 (pH 12) over 1 h of operation, with and without light illumination (0.25 sun), of FTO glass slides coated with thin films of: (I) Pt overcoated with PEDOT/nano-Co_3O_4/CNT, where the polymerisation mixture contained 110 mg of nano-Co_3O_4 and 2.0 mg of CNT, (II) Pt overcoated with nano-Co_3O_4/CNT, where the polymerisation mixture contained 110 mg of nano-Co_3O_4 and 2.0 mg of CNT(without PEDOT),(II) bare Pt (c)and (c) PEDOT only (control). (*='light on', #='light off').*

The charge exchanged during the 35 hours of operation was calculated to be 1253.9 C. It was more than sufficient to 1-electron oxidize every PEDOT monomer and C-atom in the CNT within the thin film, which would have caused it to delaminate and disintegrate. In additions, the oxidation features are inconsistent with and could not have arisen if the observed currents were due to one of the components in that film being oxidatively consumed in any substantial proportion.

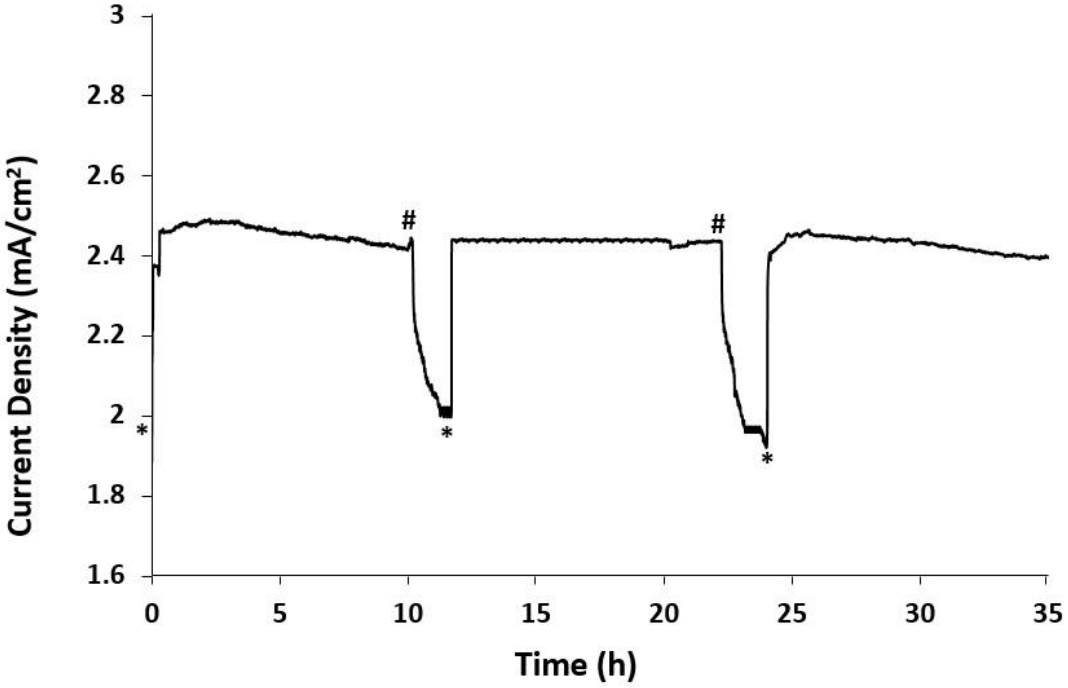

Figure 6.5: *Chronoamperograms at 0.80 V (vs Ag/AgCl) in 0.2 M Na_2SO_4 (pH 12) over 35 h of operation, with and without light illumination (ca. 0.25 sun), of an FTO glass slide coated with a thin film of Pt over-coated with PEDOT/nano-Co_3O_4/CNT/Pt/FTO, where the polymerisation mixture contained 110 mg of nano-Co_3O_4 and 2.0 mg of CNT (*='light on', #='light off).*

Figure 6.6 shows the change in the anode electrolyte pH versus time throughout the water oxidation process. As can be seen, the pH dropped during first 20 h by 0.37, which is consistent with, and can only occur if water oxidation catalysis is taking place.

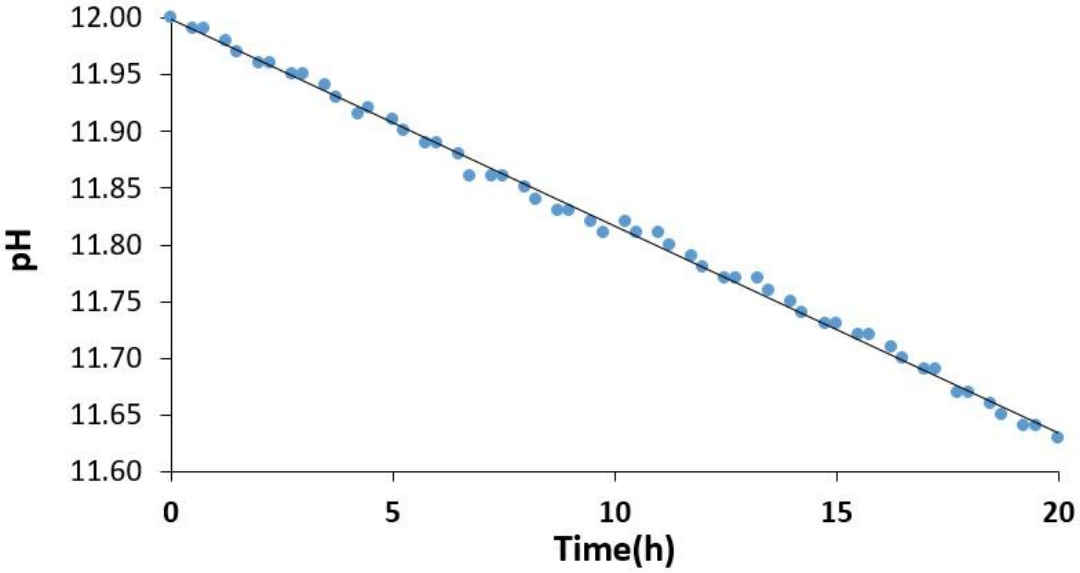

Figure 6.6: *pH change in the anode electrolyte during the first 20 h of the experiment with data displayed in Figure 6.5.*

6.2.5 Studies on the gas produced by the PEDOT/ Nano-Co_3O_4/CNT on Pt/FTO; the Faradaic Efficiency

The gases that were generated from the most active PEDOT/nano-Co_3O_4/CNT thin-film, were collected and characterised *via* gas chromatography (as described in Chapter 2). Figure 6.7 shows that oxygen (O_2) was the sole gas generated during the process, although traces of hydrogen (H_2), which came from the other half-cell *via* the ion-permeable Nafion membrane that separated the two half-cells, and atmospheric nitrogen (N_2) that came from leaks, were also detected on occasion. The gas ratios were determined by integrating the CG peaks, and found to be typically 95 O_2: 5 N_2 (tiny trace of N_2) without light illumination while in experiments with light illumination, representative gas ratios were 88.4 O_2: 9.3 H_2: 2.3 N_2. No peaks were observed for CO_2 and CO gases indicating there was no process involving complete oxidation of PEDOT

or CNT in the PEDOT/nano-Co_3O_4/CNT films. Thus, the film was resistive to oxidation during gas generation. Pure H_2 was generated at counter electrode (Pt mesh).

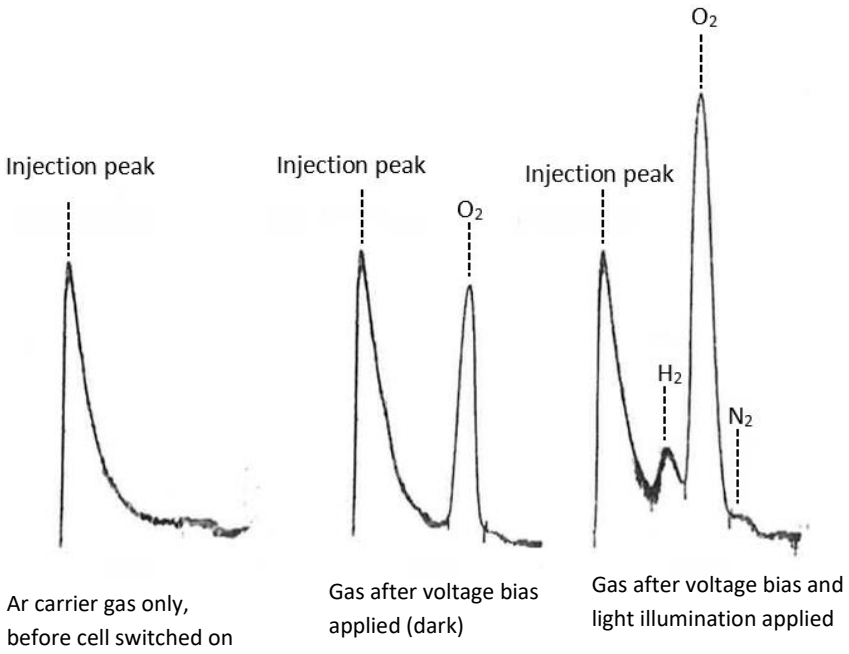

Figure 6.7: *GC traces of gases collected from the PEDOT/nano-Co_3O_4/CNT electrode*

The integration of oxygen peaks in GC chromatogram revealed that carrier gas that passed through the column contained 60.5% (dark) and 61.7% (with light illumination) of oxygen gas. This suggested that the Faradaic efficiency was more than or equal to 60.5-61.7% (but likely much higher given the fact that the apparatus was not gas tight and an unquantified amount of oxygen leaked from the cell during the experiment).

6.2.6 Characterization of the PEDOT/ Nano-Co_3O_4/CNT electrode

The composition of the most active PEDOT/ nano-Co_3O_4/CNT film on the working electrode was subjected to elemental analysis, giving the ratios of 17.0% Co, 11.40 % S, and 44.46 % C. As only the PEDOT contains the element S, while the CNT

contains only C and the nano-Co only Co, the molar ratio of PEDOT: Co : CNT was 6.92 (C; PEDOT) : 1 (Co) : 5.13 (C; others).

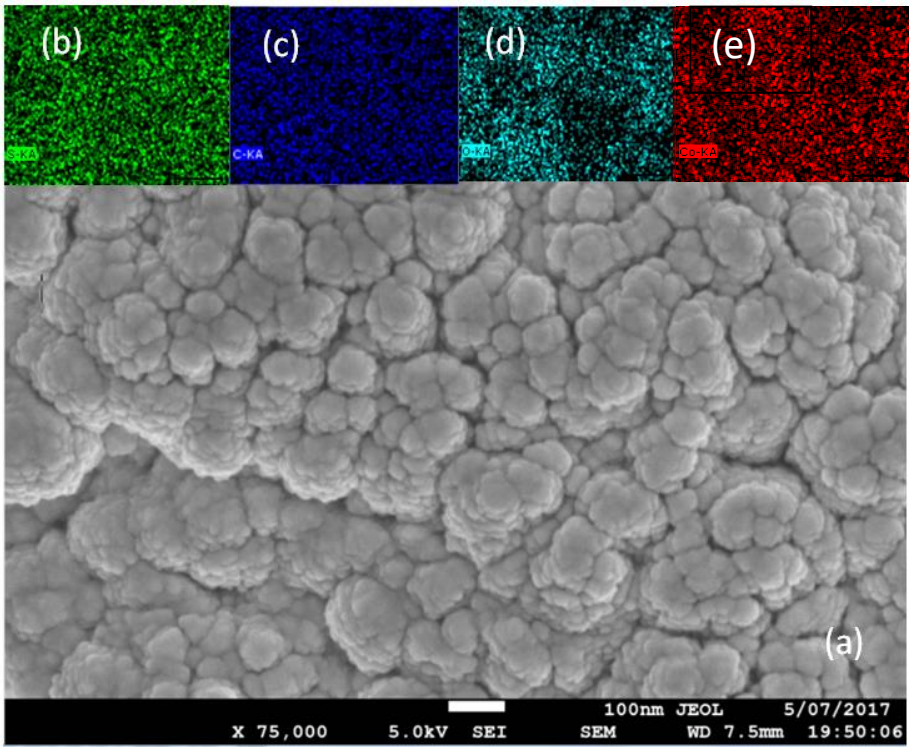

Figure 6.8: *The main image (a) represents the scanning electron microscope image of PEDOT/nano-Co_3O_4/CNT. The other images show the elemental distributions, using EDX, of (b) S, (c) C, (d) O, and (e) Co.*

The PEDOT/nano-Co_3O_4/CNT film morphology was examined after 3 h of water oxidation *via* Scanning Electron Microscopy (SEM). Figure 6.8 depicts a representative SEM image of the deposited film, showing a highly porous surface structure. EDX-mapping (Figure 6.8(b)-(e)) indicated uniform distributions of Co (nano-Co), C (PEDOT and CNT), O (PEDOT and Co_3O_4), and S (PEDOT) elements. Figure 6.9 shows the X-ray powder diffraction (XRD) pattern of PEDOT, CNT, and PEDOT/nano-Co_3O_4/CNT. XRD patterns of pure PEDOT produced a diffraction peak at 2θ 25.96° that can attribute to the (020) reflection due to the intermolecular spacing of polymer backbone.[35-36] The XRD scan of the CNT sample displayed diffraction peaks at 25.5° and

43.0°, attributed to the CNT (002) and (100) reflections respectively.[37-39] The XRD of the most active PEDOT/nano-Co_3O_4 /CNT film also showed two peaks at 25.56° and 25.94° (each marked *) that can be attributed to CNT and PEDOT in the PEDOT/nano-Co_3O_4/CNT film. Patterns of peaks at 18.9°, 31.26°, 36.9°, 38.52°, 44.82°, 55.46°, 59,48° and 65.34° corresponded to patterns from the nano-Co_3O_4 that exhibits cubic phase type space group *Fd3m* contribution (Figure 6.9).[37, 40-41]

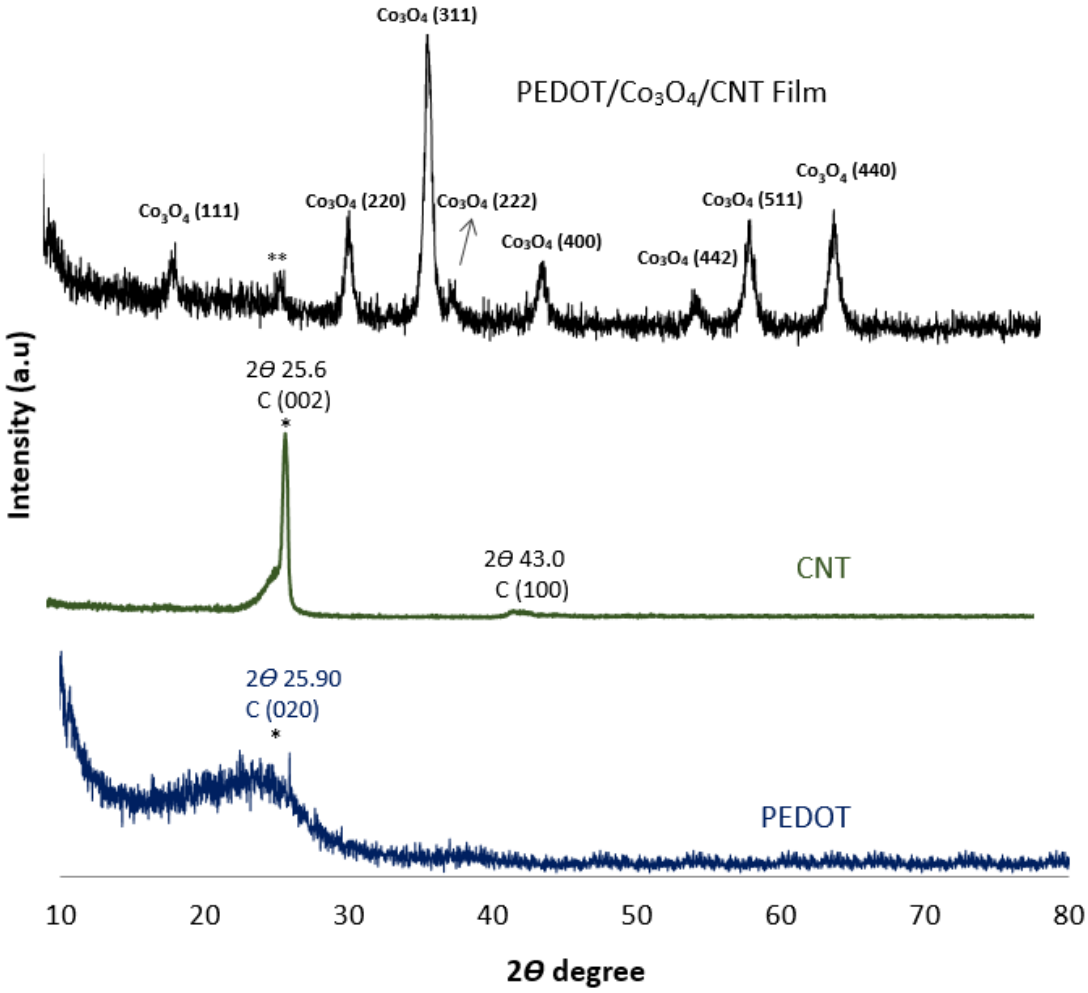

Figure 6.9: *Powder X-ray diffraction (XRD) of PEDOT/nano-Co_3O_4/CNT and control PEDOT and CNT.*

The elemental composition and chemical states of the PEDOT/nano-Co_3O_4/CNT film were further analysed with X-ray photoelectron spectroscopy (XPS) (Figure 6.10). The main peaks in the film data corresponded to S 2p, O 1s, C 1s, Co 2p and O 1s. The O 1s and C 1s

spectra were associated with both PEDOT and CNT while the S 2s spectrum derived only from the PEDOT. The C 1s spectrum contained six peaks at 284.4, 285.2, 286, 286.6, 288 and 289 eV (Figure 6.10(b)). The peak at 284.4 eV represented a sp^2 carbon hybrid that related to the C=C binding energy.[42-44]

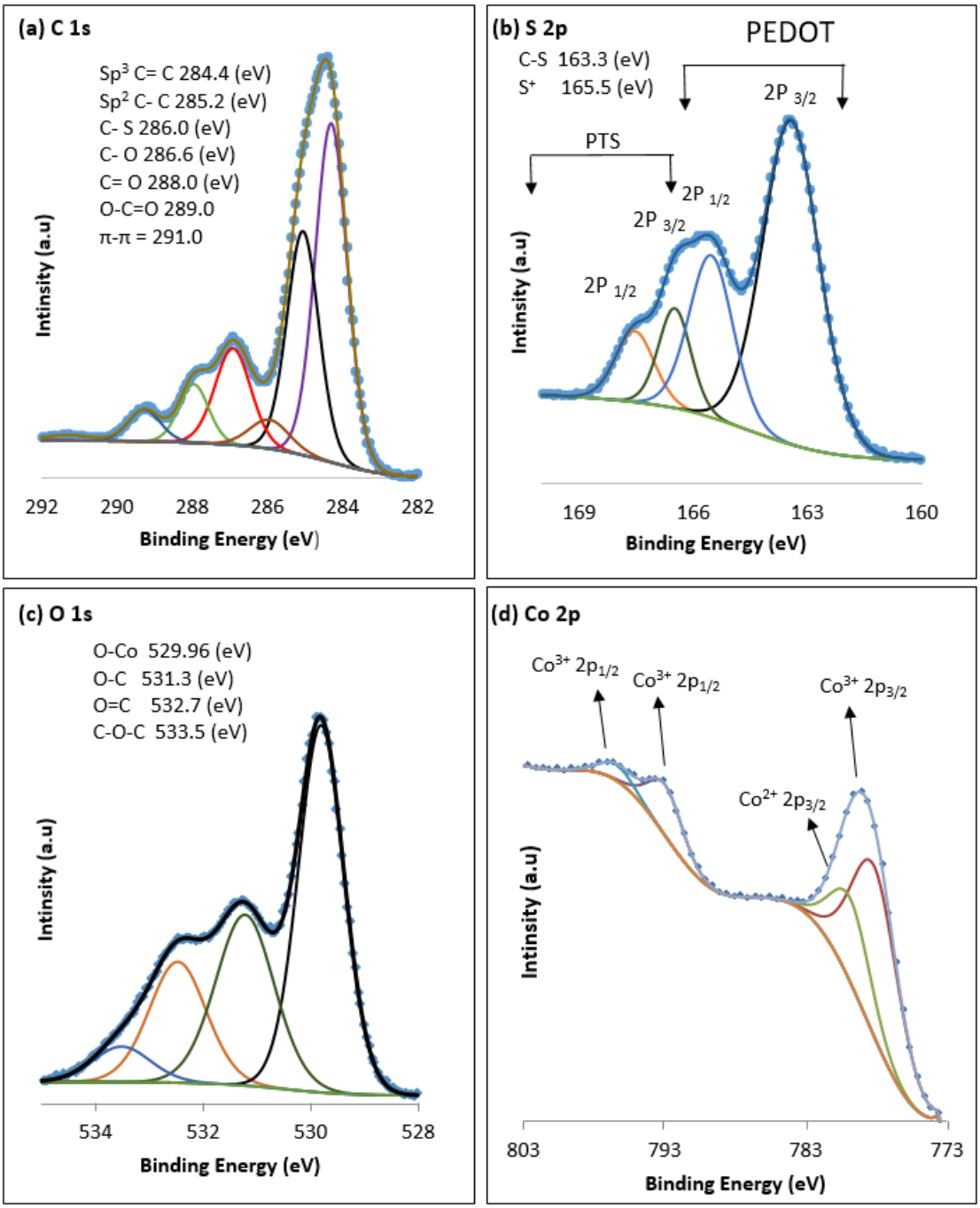

Figure 6.10*: XPS spectra of PEDOT/nano-Co_3O4/CNT film (a, b, c and d represent the spectra of C 1s, S 2p and O 1s and Co 2p respectively. C 1s spectra and O 1s can refer to both PEDOT and CNT while S 2p refers to PEDOT finally Co 2p refers to nano-Co_3O_4 particles.*

The peak at 285.2 eV represented an sp^3 carbon hybrid and related to C-C and C-H bonds, while the peaks at 286, 286.60, 288 289, 291 eV corresponded to C-S, C-O, C=O, O-C=O and π-π bonding respectively.[42-44,45-47] The S 2p XPS spectrum of the film contained peaks at 163.5 and 165.5 eV, which derived from the binding energy of the $2p^{3/2}$ and $2p^{½}$ that correspond to the C-S bond and S^+ of the PEDOT fragments.[48-49] The other two small peaks relate to the $2p^{3/2}$ and $2p^{½}$ of the sulfonic groups in the PTS structure. The O 1s XPS spectra of the film displayed four peaks at 529.96, 531.3, 532.7 and 535 eV deriving from O-Co, O-C, O=C and C-O-C or O-H bonds respectively.[50-51] Finally, for the Co 2p spectra, there were four main binding energies observed at 778.4, 780.6, 793.3, and 797.0 eV. These were attributed to Co^{3+} $2p^{3/2}$, Co^{2+} $2p^{3/2}$, Co^{3+} $2p^{1/2}$ and Co^{2+} $2p^{1/2}$, respectively.[52]

6.2.7 EIS and Tafel plot studies of the mechanism of the catalysis

Impedance spectroscopy (EIS) and Tafel plot investigation were undertaken at 0.80 V (*vs* Ag/AgCl) in 0.2 M Na_2SO_4 (pH 12). Figure 6.11(a)-(d) depicts Nyquist plots (a), the equivalent circuit (b), Bode plots (b), and Tafel plots (d) of: (i) Pt overcoated with PEDOT/nano-Co_3O_4/CNT containing 110 mg of nano-Co_3O_4 and 2.0 mg of CNT (with light illumination), (ii) Pt overcoated with PEDOT/nano-Co_3O_4/CNT (no light illumination), (iii) Pt only, (v) PEDOT only (with light illumination), and (iv) PEDOT only (no light illumination).

As noted previously, at pH 12, the EIS at low to intermediate frequencies is related to an adsorption process, involving the transfer of ions (charge carriers) from the diffuse layer to the catalyst.[53] At high frequencies, the EIS shows the charge transfer that occurred during catalysis.

As can be seen in Figure 6.11(a), an excellent match of EIS data was obtained, when the measured data was modelled using the equivalent circuit shown in Figure 6.6(b).[54] Two distinct semicircles of impedance were observed in the Nyquist plots: a semicircle at low

frequency (10-100 Hz) (shown in Figure 6.11(a)) and another partial semicircle at high frequencies in the range (1,000-10,000 Hz) (shown in the inset of Figure 6.11(a)).

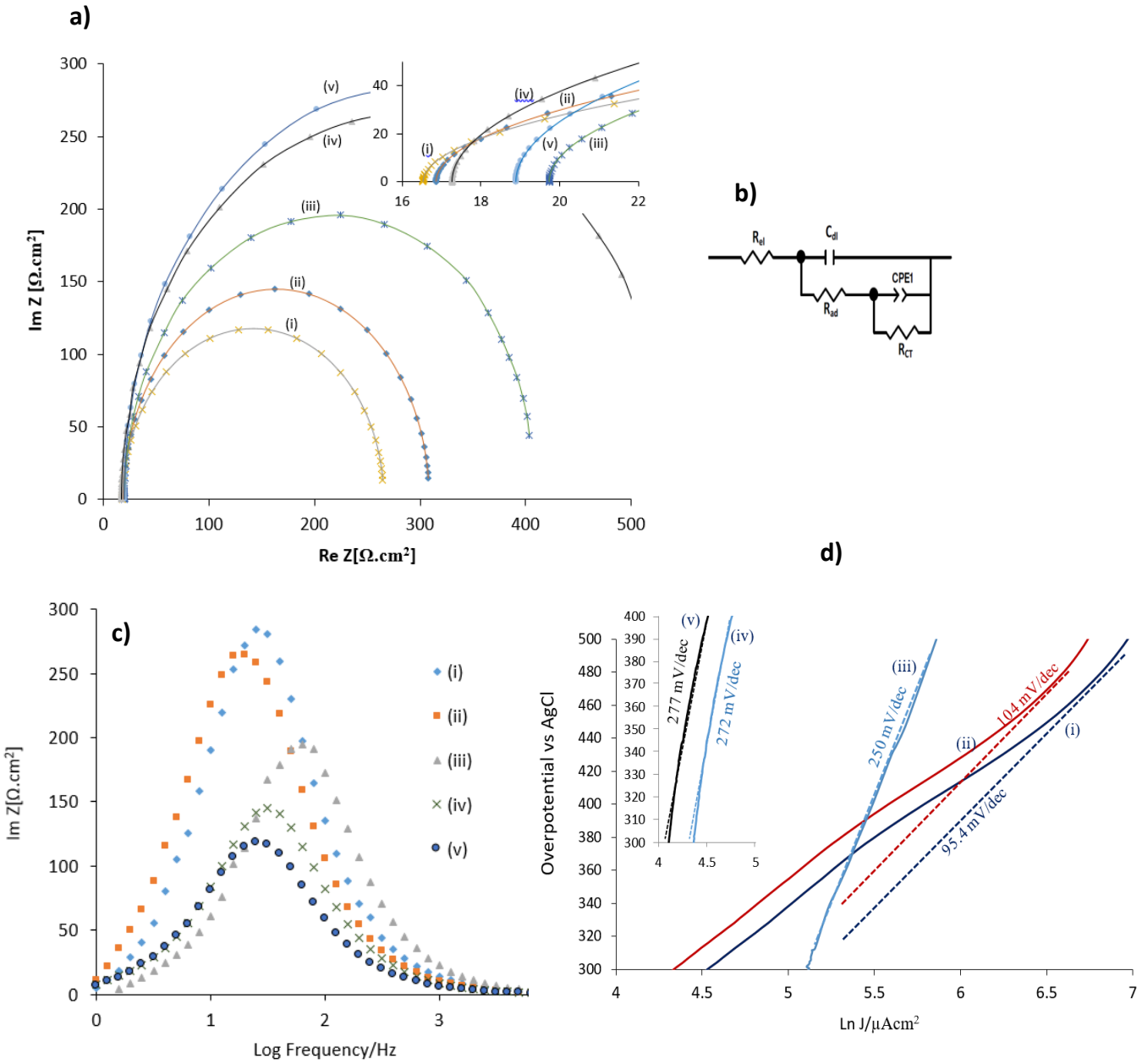

Figure 6.11: *(a) Nyquist plots showing measured data (individual data points) and modelled data (solid lines) using the equivalent circuit depicted in (b), and (c) Bode polts, as well as (d) Tafel plots of: (i) Pt overcoated with PEDOT/nano-Co_3O_4/CNT (with light illumination),(ii) Pt overcoated with PEDOT/nano-Co_3O_4/CNT (dark; no light illumination), (iii) Pt only, (iv) PEDOT only (with light illumination), and (v) PEDOT only (dark; no light illumination).*

Sample	R_{el} Ω cm^2	R_{ad} Ω cm^2	C_{dl} µF cm^{-2}	R_{CT} Ω cm^2	Q_{CPE} $\mu\Omega^1$ $cm^{-2}s^n$	n_{CPE}	C_{CPE} µF cm^{-2}	A mV/dec	i_o µA cm^2
PEDOT (dark)	18.89 ±1.60	420.3 ±3.4	16.1 ±0.2	148.3 ±2.7	0.07 ±0.03	0.88 ±0.11	0.01± 0.01	277± 14	20.60 ±3.74
PEDOT (light)	17.26 ±1.30	400.1 ±2.6	20.9 ±1.5	122.9 ±3.2	0.14 ±0.04	0.88 ±0.12	0.02± 0.01	272± 13	25.88 ±3.55
Pt only	19.73 ±1.20	270.4 ±12.4	9.89 ±0.54	120.7 ±2.1	0.06 ±0.01	0.92± 0.22	0.02± 0.01	250 ±14	50.46 ±4.22
Pt/PEDOT/Co_3O_4/CNT (dark)	16.86 ±2.44	233.7 ±17.8	41.55 ±3.44	64.68 ±4.66	3.28 ±0.11	0.86± 0.10	0.65± 0.12	104 ±4	5.56 ±0.65
Pt/PEDOT/Co_3O_4/C NT (light)	16.52 ±2.77	197.7 ±7.9	50.40 ±4.66	46.15 ±5.44	4.23 ±0.11	0.86± 0.09	0.88± 0.11	95.4± 3.8	3.46 ±0.35

Table 6.1: *Data from electrochemical impedance spectroscopy (ohmic resistance (Rel), adsorption resistance (R_{ad}), diffuse layer capacitance (C_{dl}), catalytic charge transfer resistance (R_{CT}), and capacitance expressed in terms of a constant phase element (Q_{CPE}, n_{CPE}, and C_{CPE}))*[55]*. Data from Tafel plot studies (slope (A), exchange current density (i_o)). ('dark' = without light illumination; 'light' = with light illumination).*

Table 6.1 shows the outcomes of modelling the measured data with the equivalent circuit (Figure 6.11(b)). As can be seen, The capacitance C_{dl} (which refers to electrochemically active area of the film) of Pt/PEDOT/nano-Co_3O_4/CNT film was 41.55 µF cm^{-2} without light illumination and 50.40 µF cm^{-2} with light illumination which exceeded the C_{dl} of the bare Pt /FTO control film by at least 4.2-times without light, or 5-times with light illumination.

Also, the total resistance R_P of the adsorption process (R_{ad}) and the charge transfer resistance (R_{CT}) of the most active film Pt/PEDOT/nano-Co_3O_4/CNT were calculated to be 243.85 Ω cm^2 ($R_P = R_{ad} + R_{CT}$) with light illumination and 298.38 Ω cm^2 without light illumination, which was lower the R_P resistance of bare Pt (391.1 Ω cm^2). These results were further evidence that proved the PEDOT/nano-Co_3O_4/CNT to be a better catalyst than the bare Pt per unit area under the testing conditions.

Interestingly the ohmic resistance (R_{el}) of the most active PEDOT/nano-Co_3O_4/CNT was 16.86 Ω cm^2 without light illumination and under reduced under light illumination to be 16.52 Ω cm^2. Both of these ohmic resistances were slightly lower than the ohmic resistance of control Pt/FTO film that was at 19.73 Ω cm^2

Figure 6.11(d) shows Tafel plots of the PEDOT/nano-Co_3O_4/CNT catalyst with other control films. The Tafel plot data are tabulated in the last two columns of Table 6.1. The control PEDOT film exhibited higher i_o values with and without light illumination than the active PEDOT/nano-Co_3O_4/CNT containing 110 mg Co_3O_4 and 2 mg CNT samples which indicated that the catalytic mechanism of PEDOT/nano-Co_3O_4/CNT was strongly dependent on the applied external bias. For example, the Pt/PEDOT/nano-Co_3O_4/CNT film required only 104 mV without light illumination and 95.4 mV with light illumination to increase the reaction rate by 10-times at pH 12 while the control bare Pt/FTO required 250 mV. Thus the PEDOT/nano-CO_3O_4/CNT film was more active than bare Pt/FTO under the experimental conditions.[56]

Through the amperometric, EIS and Tafel plots studied, it seems that PEDOT was accelerating the water-splitting reaction with assited of external bias. PEDOT also absorbs light, produces photogenerated charge carriers. The amazing synergestic effects of PEDOT, Co_3O_4 and CNT results in enhancement of overall water splitting system. Since Co_3O_4 nanoparticles can enhances OER ctatayst at high pH while MWCNT stabilis the catalyst on the FTO surface, increased the active service area and accelerates charge moblitity with PEDOT.

6.3 Conclusions

The film PEDOT/ Nano-Co_3O_4/CNT containing 110 mg nano-Co_3O_4 and 2 mg CNTs was prepared *via* a facile synthetic route including dispersion of the raw materials with a magnetic stirrer and spin coating them in FTO glass, followed by vapour phase polymerisation

to convert EDOT to PEDOT. The films have a high electrocatalytic and photoelectrocatalytic capacity for the OER in 0.2 M Na_2SO_4 solution at pH 12. While control PEDOT films were weakly catalytic, the film containing PEDOT: nano-Co_3O_4: CNT in a molar ratio of 6.92 (S; PEDOT): 1 (Co):5.13 (C; CNT) exhibited a high OER activity. The activity of the PEDOT/nano-Co_3O_4/CNT toward OER was further enhanced when it was overcoated on an FTO slide previously sputter-coated with a 100 nm thick coating of Pt. The PEDOT/nano-Co_3O_4/CNT on Pt/FTO film generated a sustained current density of 2.44-2.38 mA/cm^2 at 0.80 V (*vs* Ag/AgCl) over > 35 h of operation under constant light illumination of 0.25 sun. This included a photocurrent of ca. 0.44-0.50 mA/cm^2 due to the light illumination. These current densities were substantially larger than an equivalent sputter-coated Pt film, and other control films under the same conditions. Gas analysis demonstrated that oxygen was the only gas generated with high efficiency. SEM/EDX, TEM, XPS, EIS and Tafel plot studies showed the most active film PEDOT/nano-Co_3O_4/CNT containing 110 mg of Co_3O_4 and 2.0 mg in polymerisation solution has an amplification performance due to a synergistic co-operation between PEDOT and Co_3O_4 and CNT, which reduced the resistivity of the film and increased the catalytic performance of the film under light illumination.

6.4 References

1. Sidhureddy, B.; Thiruppathi, A. R.; Chen, A. Au Nanoparticle Incorporated $Co(OH)_2$ Hybrid Thin Film with High Electrocatalytic Activity and Stability for Overall Water Splitting. *J. Electroanal. Chem.* **2017**, *794*, 28-35.
2. Doyle, R. L.; Lyons, M. E. G. The Oxygen Evolution Reaction: Mechanistic Concepts and Catalyst Design. In *Photoelectrochemical Solar Fuel Production: From Basic Principles to Advanced Devices*, Giménez, S.; Bisquert, J., Eds. Springer International Publishing: Switzerland, **2016**; pp 41-104.
3. Kim, H.; Kim, Y.; Noh, Y.; Lee, S.; Sung, J.; Kim Won, B. Thermally Converted CoO Nanoparticles Embedded into N-Doped Carbon Layers as Highly Efficient Bifunctional Electrocatalysts for Oxygen Reduction and Oxygen Evolution Reactions. *ChemCatChem* **2017**, *9* (8), 1503-1510.
4. Yu, J.; Zhong, Y.; Zhou, W.; Shao, Z. Facile Synthesis of Nitrogen-Doped Carbon Nanotubes Encapsulating Nickel Cobalt Alloys 3D Networks for Oxygen Evolution Reaction in an Alkaline Solution. *J. Power Sources* **2017**, *338*, 26-33.
5. Kuang, M.; Han, P.; Wang, Q.; Li, J.; Zheng, G. CuCo Hybrid Oxides as Bifunctional Electrocatalyst for Efficient Water Splitting. *Adv. Funct. Mater.* **2016**, *26* (46), 8555-8561.
6. Zhao, S.; Rasimick, B.; Mustain, W.; Xu, H. Highly durable and active Co_3O_4 Nanocrystals Supported on Carbon Nanotubes as Bifunctional Electrocatalysts in Alkaline Media. *Appl. Catal. B: Environ.* **2017**, *203*, 138-145.
7. Wang, J.; Li, L.; Tian, H.; Zhang, Y.; Che, X.; Li, G. Ultrathin $LiCoO_2$ Nanosheets: An Efficient Water-Oxidation Catal. *ACS Appl. Mater. Interfaces* **2017**, *9* (8), 7100-7107.
8. Liang, Y.; Li, Y.; Wang, H.; Zhou, J.; Wang, J.; Regier, T.; Dai, H. Co_3O_4 Nanocrystals on Graphene as a Synergistic Catalyst for Oxygen Reduction Reaction. *Nat. Mater.* **2011**, *10*, 780-786.
9. Suryanto, B. H. R.; Lu, X.; Zhao, C. Layer-by-Layer Assembly of Transparent Amorphous Co_3O_4 Nanoparticles/Graphene Composite Electrodes for Sustained Oxygen Evolution Reaction. *J. Mater. Chem. A* **2013**, *1* (41), 12726-12731.
10. Wu, J.; Xue, Y.; Yan, X.; Yan, W.; Cheng, Q.; Xie, Y. Co_3O_4 Nanocrystals on Single-Walled Carbon Nanotubes as a Highly Efficient Oxygen-Evolving Catalyst. *Nano Res.* **2012**, *5* (8), 521-530.
11. Ahmed, M. S.; Choi, B.; Kim, Y.-B. Development of Highly Active Bifunctional Electrocatalyst Using Co_3O_4 on Carbon Nanotubes for Oxygen Reduction and Oxygen Evolution. *Sci. Rep.* **2018**, *8* (1), 2543 (1-10).

12. Zhao, X.; Li, F.; Wang, R.; Seo, J. M.; Choi, H. J.; Jung, S. M.; Mahmood, J.; Jeon, I. Y.; Baek, J. B. Controlled Fabrication of Hierarchically Structured Nitrogen-Doped Carbon Nanotubes as a Highly Active Bifunctional Oxygen Electrocatalyst. *Adv. Funct. Mater.* **2017**, *27* (9), 1605717 (1-9).
13. Hu, C.; Yi, Z.; She, W.; Wang, J.; Xiao, J.; Wang, S. Urchin-Like Non-Precious-Metal Bifunctional Oxygen Electrocatalysts: Boosting the Catalytic Activity via the In-situ Growth of Heteroatom (N, S)-Doped Carbon Nanotube on Mesoporous Cobalt Sulfide/Carbon Spheres. *J. Colloid Interface Sci.* **2018**, *524*, 465-474.
14. Li, X.; Fang, Y.; Zhao, S.; Wu, J.; Li, F.; Tian, M.; Long, X.; Jin, J.; Ma, J. Nitrogen-Doped Mesoporous Carbon Nanosheet/Carbon Nanotube Hybrids as Metal-Free Bi-functional Electrocatalysts for Water Oxidation and Oxygen Reduction. *J. Materials Chem. A* **2016**, *4* (34), 13133-13141.
15. Cheng, H.; Su, C.-Y.; Tan, Z.-Y.; Tai, S.-Z.; Liu, Z.-Q. Interacting $ZnCo_2O_4$ and Au Nanodots on Carbon Nanotubes as Highly Efficient Water Oxidation Electrocatalyst. *J. Power Sources* **2017**, *357*, 1-10.
16. Cheng, Y.; Liu, C.; Cheng, H.-M.; Jiang, S. P. One-Pot Synthesis of Metal–Carbon Nanotubes Network Hybrids as Highly Efficient Catalysts for Oxygen Evolution Reaction of Water Splitting. *ACS Appl. Mater. Interfaces* **2014**, *6* (13), 10089-10098.
17. Tian, G. L.; Zhao, M. Q.; Yu, D.; Kong, X. Y.; Huang, J. Q.; Zhang, Q.; Wei, F. Nitrogen-Doped Graphene/Carbon Nanotube Hybrids: In Situ Formation on Bifunctional Catalysts and Their Superior Electrocatalytic Activity for Oxygen Evolution/Reduction Reaction. *Small* **2014**, *10* (11), 2251-2259.
18. Chen, S.; Duan, J.; Jaroniec, M.; Qiao, S. Z. Nitrogen and Oxygen Dual-Doped Carbon Hydrogel Film as a Substrate-Free Electrode for Highly Efficient Oxygen Evolution Reaction. *Adv. Mater.* **2014**, *26* (18), 2925-2930.
19. Yu, X.; Hua, T.; Liu, X.; Yan, Z.; Xu, P.; Du, P. Nickel-Based Thin Film on Multiwalled Carbon Nanotubes as an Efficient Bifunctional Electrocatalyst for Water Splitting. *ACS Appl. Mater. Interfaces* **2014**, *6* (17), 15395-15402.
20. Cheng, Y.; Shen, P. K.; Jiang, S. P. NiO_x Nanoparticles Supported on Polyethylenimine Functionalized CNTs as Efficient Electrocatalysts for Supercapacitor and Oxygen Evolution Reaction. *Int. J. Hydrogen Energy* **2014**, *39* (35), 20662-20670.
21. Tian, G. L.; Zhang, Q.; Zhang, B.; Jin, Y. G.; Huang, J. Q.; Su Dang, S.; Wei, F. Toward Full Exposure of "Active Sites": Nanocarbon Electrocatalyst with Surface Enriched Nitrogen for Superior Oxygen Reduction and Evolution Reactivity. *Adv. Funct. Mater.* **2014**, *24* (38), 5956-5961.

22. Zhou, X.; Xia, Z.; Zhang, Z.; Ma, Y.; Qu, Y. One-Step Synthesis of Multi-Walled Carbon Nanotubes/Ultra-thin $Ni(OH)_2$ Nanoplate Composite as Efficient Catalysts for Water Oxidation. *J. Mater. Chem. A* **2014**, *2* (30), 11799-11806.
23. Lu, X.; Yim, W.-L.; Suryanto, B. H. R.; Zhao, C. Electrocatalytic Oxygen Evolution at Surface-Oxidized Multiwall Carbon Nanotubes. *J. Am. Chem. Soc.* **2015**, *137* (8), 2901-2907.
24. Li, X.; Fang, Y.; Lin, X.; Tian, M.; An, X.; Fu, Y.; Li, R.; Jin, J.; Ma, J. MOF Derived Co_3O_4 Nanoparticles Embedded in N-doped Mesoporous Carbon Layer/MWCNT Hybrids: Extraordinary Bi-functional Electrocatalysts for OER and ORR. *J. Mater. Chem. A* **2015**, *3* (33), 17392-17402.
25. Zhu, X.; Tang, C.; Wang, H.-F.; Zhang, Q.; Yang, C.; Wei, F. Dual-Sized NiFe Layered Double Hydroxides in Situ Grown on Oxygen-Decorated Self-Dispersal Nanocarbon as Enhanced Water Oxidation Catalysts. *J. Mater. Chem. A* **2015**, *3* (48), 24540-24546.
26. Fang, Y.; Li, X.; Hu, Y.; Li, F.; Lin, X.; Tian, M.; An, X.; Fu, Y.; Jin, J.; Ma, J. Ultrasonication-Assisted Ultrafast Preparation of Multiwalled Carbon Nanotubes /Au/Co_3O_4 Tubular Hybrids as Superior Anode Materials for Oxygen Evolution Reaction. *J. Power Sources* **2015**, *300*, 285-293.
27. Wang, Z.; Zhang, F.; Jin, C.; Luo, Y.; Sui, J.; Gong, H.; Yang, R. La_2O_3-NCNTs Hybrids in-Situ Derived From $LaNi_{0.9}Fe_{0.1}O_3$-C Composites as Novel Robust Bifunctional Oxygen Electrocatalysts. *Carbon* **2017**, *115*, 261-270.
28. Li, Y.; Jia, B.; Fan, Y.; Zhu, K.; Li, G.; Su, C. Y. Bimetallic Zeolitic Imidazolite Framework Derived Carbon Nanotubes Embedded with Co Nanoparticles for Efficient Bifunctional Oxygen Electrocatalyst. *Adva. Energy Mater.* **2017**, *8* (9), 1-9.
29. Tiwari Anand, P.; Kim, D.; Kim, Y.; Lee, H. Bifunctional Oxygen Electrocatalysis through Chemical Bonding of Transition Metal Chalcogenides on Conductive Carbons. *Adv. Energy Mater.***2017**, *7* (14), 1-9.
30. Das, D.; Das, A.; Reghunath, M.; Nanda, K. K. Phosphine-free avenue to Co_2P Nanoparticle Encapsulated N,P Co-doped CNTs: A Novel Non-Enzymatic Glucose Sensor and an Efficient Electrocatalyst for Oxygen Evolution Reaction. *Green Chem.* **2017**, *19* (5), 1327-1335.
31. Han, X.; Wu, X.; Zhong, C.; Deng, Y.; Zhao, N.; Hu, W. $NiCo_2S_4$ Nanocrystals Anchored on Nitrogen-Doped Carbon Nanotubes as a Highly Efficient Bifunctional Electrocatalyst for Rechargeable Zinc-Air Batteries. *Nano Energy* **2017**, *31*, 541-550.
32. Qu, K.; Zheng, Y.; Jiao, Y.; Zhang, X.; Dai, S.; Qiao, S. Z. Polydopamine-Inspired, Dual Heteroatom-Doped Carbon Nanotubes for Highly Efficient Overall Water Splitting. *Adv. Energy Mater.* **2016**, *7* (9), 1602068 (1-8).

33. Chaudhary, D.; Singh, S.; Vankar, V. D.; Khare, N. A ternary Ag/TiO_2/CNT Photoanode for Efficient Photoelectrochemical Water Splitting Under Visible Light Irradiation. *Int. J. Hydrogen Energy* **2017**, *42* (12), 7826-7835.
34. Yousefzadeh, S.; Reyhani, A.; Naseri, N.; Moshfegh, A. Z. MWCNT/WO_3 Nanocomposite Photoanode for Visible Light Induced Water Splitting. *J. Solid State Chem.* **2013**, *204*, 341-347.
35. Zhang, L.; Jamal, R.; Zhao, Q.; Wang, M.; Abdiryim, T. Preparation of PEDOT/GO, PEDOT/MnO_2, and PEDOT/GO/MnO_2 Nanocomposites and Their Application in Catalytic Degradation of Methylene Blue. *Nanoscale Res. Lett.* **2015**, *10* (1), 148 (1-9).
36. Jo, S.-H.; Lee, Y.-K.; Yang, J.-W.; Jung, W.-G.; Kim, J.-Y. Carbon Nanotube-Based Flexible Transparent Electrode Films Hybridized with Self-Assembling PEDOT. *Synth. Met.* **2012**, *162* (13), 1279-1284.
37. Yoon, T. H.; Park, Y. J. Carbon nanotube/Co_3O_4 Composite for Air Electrode of Lithium-Air Battery. *Nanoscale Res. Lett.* **2012**, *7* (1), 28 (1-4).
38. Al Khabouri, S.; Al Harthi, S.; Maekawa, T.; Nagaoka, Y.; Elzain, M. E.; Al Hinai, A.; Al-Rawas, A. D.; Gismelseed, A. M.; Yousif, A. A. Composition, Electronic and Magnetic Investigation of the Encapsulated $ZnFe_2O_4$ Nanoparticles in Multiwall Carbon Nanotubes Containing Ni Residuals. *Nanoscale Res. Lett.* **2015**, *10* (1), 262 (1-10).
39. Saleh, T. A. The Role of Carbon Nanotubes in Enhancement of Photocatalysis. In *Syntheses and Applications of Carbon Nanotubes and their Composites*, Suzuki, S., Ed. Springer International Publishing: **2013**; pp 479–493.
40. Reddy, M. V.; Beichen, Z.; Jia'en Nicholette, L.; Zhang, K.; V. R. Chowdari, B. Molten Salt Synthesis and Its Electrochemical Characterization of Co_3O_4 for Lithium Batteries. Electrochem. *Solid-State Lett.* **2011**, 14(5), A79-A82.
41. Yue, W.; Hill, A. H.; Harrison, A.; Zhou, W. Mesoporous Single-Crystal Co_3O_4 Templated by Cage-Containing Mesoporous Silica. *Chem. Commun.* **2007**, (24), 2518-2520.
42. Vilian, A. T. E.; Veeramani, V.; Chen, S.-M.; Madhu, R.; Kwak, C. H.; Huh, Y. S.; Han, Y.-K. Immobilization of myoglobin on Au Nanoparticle-Decorated Carbon Nanotube/Polytyramine Composite as a Mediator-Free H_2O_2 and Nitrite Biosensor. *Sci. Rep.* **2015**, *5*, 18390 (1-6)
43. Singh, B.; Murad, L.; Laffir, F.; Dickinson, C.; Dempsey, E. Pt based nanocomposites (mono/bi/tri-metallic) decorated using different carbon supports for methanol electro-oxidation in acidic and basic media. *Nanoscale* **2011**, *3* (8), 3334-3349.

44. Hanelt, S.; Friedrich, F. J.; Meyer-Plath, A. UV Spectrometric Indirect Analysis of Brominated MWCNTs with UV Active Thiols and an Alkene—Reaction Kinetics, Quantification and Differentiation of Adsorbed Bromine and Oxygen. *Materials* **2013**, *6* (8), 3036-3063

45. Lindfors, T.; Boeva, Z. A.; Latonen, R.-M. Electrochemical Synthesis of Poly(3,4-ethylenedioxythiophene) in Aqueous Dispersion of High Porosity Reduced Graphene Oxide. *RSC Adv.* **2014**, *4* (48), 25279-25286.

46. Konnola, R.; Joseph, K. Effect of Side-Wall Functionalisation of Multi-Walled Carbon Nanotubes on the Thermo-Mechanical Properties of Epoxy Composites. *RSC Adv.* **2016**, *6* (28), 23887-23899.

47. Zhang, X.; Huang, Y.; Liu, P. Enhanced Electromagnetic Wave Absorption Properties of Poly(3,4-ethylenedioxythiophene) Nanofiber-Decorated Graphene Sheets by Non-covalent Interactions. *Nano-Micro Lett.* **2016**, *8* (2), 131-136.

48. Ji, T.; Tan, L.; Hu, X.; Dai, Y.; Chen, Y. A Comprehensive Study of Sulfonated Carbon Materials as Conductive Composites for Polymer Solar Cells. *Phys. Chem. Chem. Phys.* **2015**, *17* (6), 4137-4145.

49. Zhang, W.; Zhao, B.; He, Z.; Zhao, X.; Wang, H.; Yang, S.; Wu, H.; Cao, Y. High-efficiency ITO-Free Polymer Solar Cells Using Highly Conductive PEDOT:PSS/ Surfactant Bilayer Transparent Anodes. *Energy Environ. Sci.* **2013**, *6* (6), 1956-1964.

50. Qiu, S.; Gu, H.; Lu, G.; Liu, J.; Li, X.; Fu, Y.; Yan, X.; Hu, C.; Guo, Z. Rechargeable Co_3O_4 Porous Nanoflake Carbon Nanotube Nanocomposite Lithium-Ion Battery Anodes with Enhanced Energy Performances. *RSC Adv.* **2015**, *5* (58), 46509-46516.

51. Zhang, Z.; Chen, Y.; Bao, J.; Xie, Z.; Wei, J.; Zhou, Z. Co_3O_4 Hollow Nanoparticles and Co Organic Complexes Highly Dispersed on N-Doped Graphene: An Efficient Cathode Catalyst for Li-O_2 Batteries. *Part. Part. Syst..Characteriz.* **2015**, *32* (6), 680-685.

52. Li, S.; Peng, S.; Huang, L.; Cui, X.; Al-Enizi, A. M.; Zheng, G. Carbon-Coated Co^{3+}-Rich Cobalt Selenide Derived From ZIF-67 for Efficient Electrochemical Water Oxidation. *ACS Appl. Mater. Interfaces* **2016**, *8* (32), 20534-20539.

53. Shimizu, K.; Lasia, A.; Boily, J.-F. Electrochemical Impedance Study of the Hematite/Water Interface. *Langmuir* **2012**, *28* (20), 7914-7920.

54. Swierk, J. R.; Klaus, S.; Trotochaud, L.; Bell, A. T.; Tilley, T. D. Electrochemical Study of the Energetics of the Oxygen Evolution Reaction at Nickel Iron (Oxy)Hydroxide Catalysts. *J. Phys. Chem.C* **2015**, *119* (33), 19022-19029.

55. Brug, G. J.; van den Eeden, A. L. G.; Sluyters-Rehbach, M.; Sluyters, J. H. The Analysis of Electrode Impedances Complicated by the Presence of a Constant Phase Element. *J. Electroanal. Chem. Interfac. Electrochem.* **1984**, *176* (1), 275-295.

56. Pletcher, D.; Sotiropoulos, S. Hydrogen Adsorption-Desorption and Oxide Formation-Reduction on Polycrystalline Platinum in Unbuffered Aqueous Solutions. *J. Chem. Soc., Faraday Trans.* **1994**, *90* (24), 3663-3668.

Chapter 7

Novel Hydrogel Separator for Spontaneous Bifunctional Oxygen and Hydrogen Evolution by Composite PEDOT/nano-Ni/rGO Films

Declaration: Portions of this chapter are drawn from a draft journal article entitled: "*A Novel Hydrogel Ion-Bridge Capable of Facilitating Sustained, Chemically-Driven Oxygen and Hydrogen Evolution from Water"*, for which I, Mohammed Alsultan, am the first author, along with co-authors: Khalid Zainulabdeen, Pawel Wagner, and Gerhard F. Swiegers, My contribution involved: (i) carrying out the laboratory research and measurements (except for the hydrogel properties tests), (ii) constructing the plots and figures from the data obtained, and (iii) writing the first draft of the journal article.

7.1 Introduction

Hydrogen (H_2) and oxygen (O_2) production from water in direct conversion under light illumination in a photoelectrochemical cell (PEC) is the ultimate aim for renewable, sustainable, and clean future energy. Great efforts have been devoted to developing and characterising new types of photocatalysts for direct water splitting[1-3] In a PEC system, an external voltage bias is often required. However, a chemical bias can be also applied to enhance PEC performance. Such a chemical bias ($\Delta E_{(V)}$) can be created by using two separated electrolytes in two half cells with different pHs. For

example, an electrolyte that has a high pH can be used in the anode half-cell of a PEC while an electrolyte with a low pH can be used in the cathode half-cell. The two halfs-cells can then be connected with a suitably conductive membrane or separator (Figure 7.1). The resulting chemical bias ($\Delta E_{(V)}$) can be calculated, at room temperature, with equation 7.1:[4-5]

$$\Delta E_{(V)} = 0.059\ \Delta pH. \qquad \ldots (7.1)$$

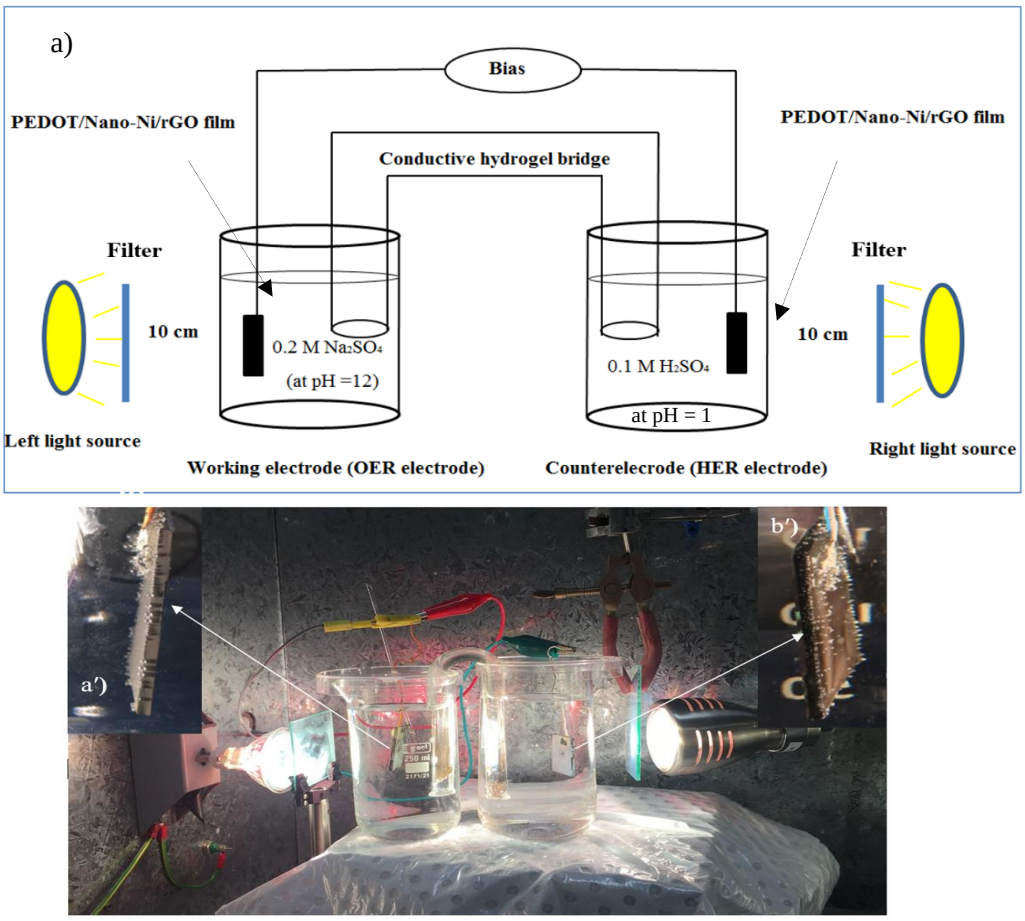

Figure 7.1: (*a) Schematic illustration of a photoelectrochemical cell utilizing PEDOT/nano-Ni/rGO films for water-splitting with no voltage bias applied. In the left half-cell, a light-assisted anode for OER catalysis is combined, on the right, with a light-assisted cathode half-cell for HER catalysis. A hydrogel bridge is provided between the two half-cells. (b) Photograph of the PEC cell setup used.*

where $\Delta E_{(V)}$ represents the chemical bias while ΔpH is the difference in pH values between the two halfs-cells. According to equ. (7.1), the chemical bias is around 0.55 V. This chemical bias ΔE(V) assists with the reaction in addition to the external bias, to thereby facilitate cataytic effects for both OER (at the working electrode) and HER (at the counter electrode).

In previous studies, Nafion and other ion-exchange membranes have been used to interface two half-cells. The results showed that maintaining the pH in both basic and acidic media is difficult due to the neutralisation processes related to OH^- and H^+ consumption in both the anolyte and catholyte during the electrocatalytic reaction.[5-9] In contrast, the performance of a hydrogel separator should exhibit advantages in this respect, like: (i) low preparation cost, (ii) ability to operate over a wide range of pH, and (iii) a potential capacity for relative long term stability in water splitting applications.[5]

In this chapter, we have developed a novel, mechanically durable, highly electrically conductive, and flexible polyacrylamide CsCl hydrogel and applied it as a separator for two water splitting half cells (cathode and anode). The cells split water upon being connected with the hydrogel, for up to 14 h of continuous testing. The feasibility of (and properties of) a chemical rather than an electrical potential to drive water splitting was thereby demonstrated, at least for a period of 14 h.

The separator comprised of a polyacrylamide–CsCl hydrogel. It was fixed in a U-tube to connect the two half-cells. One half- cell contained an electrolyte of 0.2 M Na_2SO_4 adjusted to pH 12 and a film electrode comprising of PEDOT/Nano-Ni/rGO containing 125 mg of nano-Ni and 6 mg of rGO (as decribed in Chapter 3 as having the highest performance). This half cell facilitated the OER. The second half-cell was for the HER. It contained 0.1 M H_2SO_4 and an electrode comprising of a film of PEDOT/Nano-Ni/rGO containing 125 mg of nano-Ni and 5.4 mg of rGO applied (as found to be highest performing in Chapter 4 at pH 1). The two half-cells was baised either at 1.23 V or 1.5 V for comparison.

7.2 Results and Discussion

7.2.1 Electrocatalytic and Photoelectrocatalytic Measurements

Figure 7.1(a)-(b) illustrates the PEC cell that was used in this study. The first step was to perform linear swept voltammetry (LSV) in the range 1.1-1.5 V (2-electrode cell voltage). Figure 7.2 represents LSV of the two half-cell after 10 scans in both states with and without light illumination. As can be seen in Figure 7.2, the current density of PEDOT/nano-Ni/rGO films increased from 368 µA/cm^2 without illumination to 415 µA/cm^2 with light at 1.5 V (where both films were exposed to light illumination). In addition, it was suggested that the nano-Ni particles in the PEDOT/nano-Ni/rGO films became partially covered with NiO when the potential in the LSV scan reached the range of 1.38-143 V[10] and above. With a NiO coating, the catalyst could better respond to light due as NiO is well known to be a semiconductor that absorbs light and co-operates with PEDOT and rGO through a synergistic effect (as discussed in Chapters 3 and 4).[11-12]

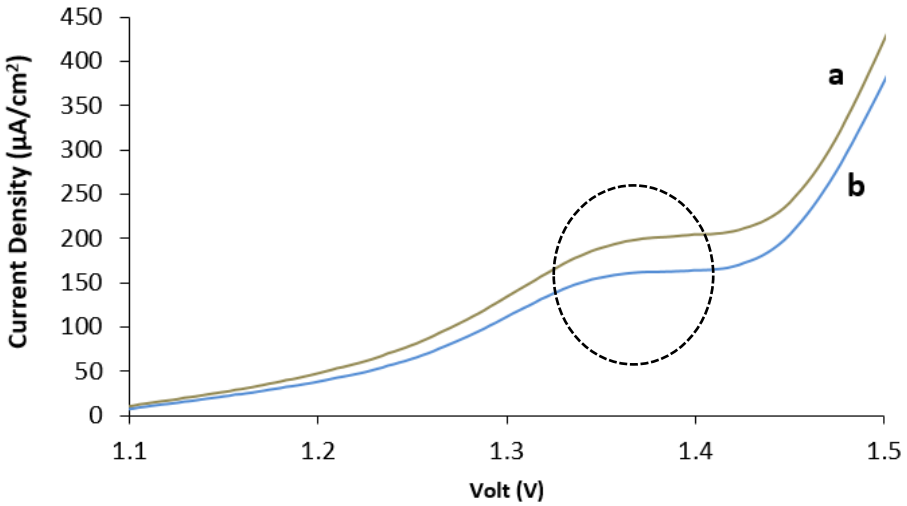

Figure 7.2: *Linear Sweep Voltammogram (LSV) of PEDOT/nano-Ni/rGO films, on FTO glass, in range (1.1-1.5 V; 2-electrode cell voltage). The anode was PEDOT/nano-Ni$_{(125\ mg)}$/rGO$_{(6\ mg)}$ film in 0.2 M Na_2SO_4 with pH 12 while the cathode was 0.1 PEDOT/nano-Ni$_{(125\ mg)}$/rGO$_{(5.4\ mg)}$ film (0.1 M H_2SO_4). Scan rate: 5 mv/s.*

The second step was to examine the chronoamperometric effects at cell voltages of 1.23 V and 1.5 V respectively. The former, of course, is the theoretical minimum voltage (E^o) needed to create water splitting. The latter is just above the so-called "thermoneutral voltage" (E^{TN}), which equates to the voltage at which water electrolysis is said to be 100% energy efficient.

As can be seen in Figure 7.3(a), when 1.23 V was applied, the dark current was 140 - 142 µA/ cm^2, and when the light was switched on, it has increased to 154 - 156 µA/cm^2, meaning that 14 µA/cm^2 was a photocurrent arising from light illumination (IP(i) in Figure 7.3(a)). When a bias of 1.5 V was applied, the dark current was 366 - 373 µA/cm^2, while, with light, it was raised to 386-391 µA/cm^2, producing 18-20 µA/cm^2 photocurrent (IP(ii) in Figure 7.3(b)).

In theory it is not possible to perform water-splitting at 1.23 V, however the chemical potential provided by the differing conditions at the cathode and anode, along with the influence of the light illumination, allowed the cell to readily split water at 1.23 V (albeit at a low overall current density).

The third step of this study was to perform chronoamperometry at 1.23 V and 1.5 V. The processing time was set for 14 h. As can be seen in Figure 7.3, when the light was turned on, the currents increased steadily at both 1.23 and 1.5 V. They stabilised after 3 h of operation to exhibit current densities of 484 and 192 µA/cm^2 at 1.23 and 1.5 V respectively. The current at 1.5 V started to degrade gradually to 59% of its stabilised current after 14 h of PEC operation. However, the current density was still better than that exhibited at 1.23 V, which also exhibited a high initial photocurrent density of 225 µA/cm^2. In contrast, the current density at bias of 1.23 V was more stable over 14 h of operation and dropped to only 88.2 % of its stabilised current of 55 µA/cm^2.

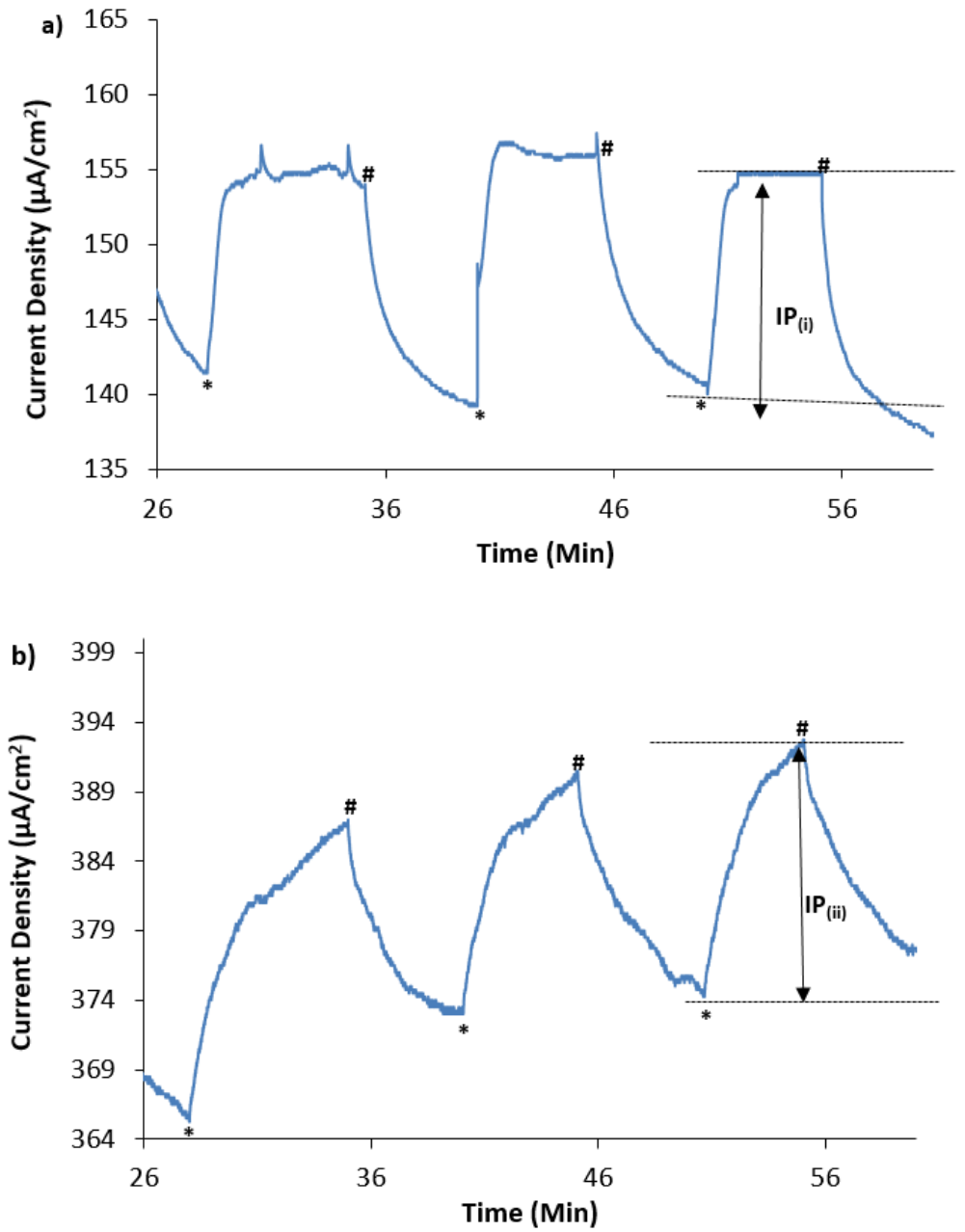

Figure 7.3: *Chronoamperogram of catalytic water-splitting with and without light illumination (ca. 0.25 sun), of FTO glass slides coated with PEDOT/nano-Ni-nano/rGO as illustrated in Fig 7.1 at a 2-electrode cell voltage of: (a) 1.23 V and (b) 1.5 V, respectively for 1 h of operation*

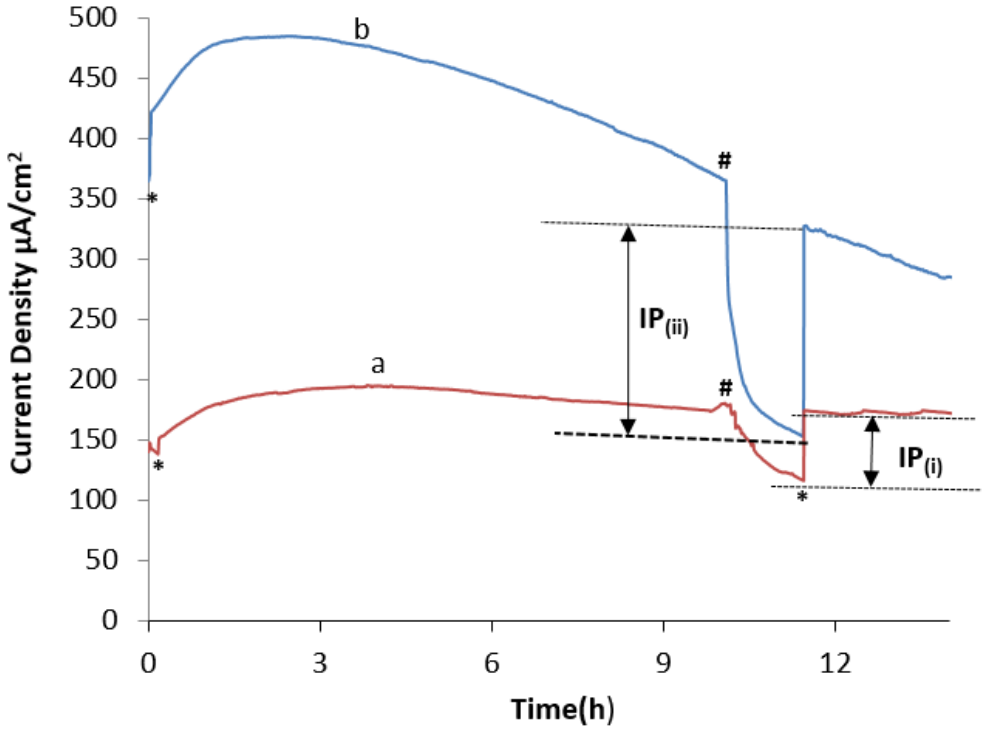

Figure 7.4: *Chronoamperogram of catalytic water-splitting with and without light illumination (ca. 0.25 sun), of FTO glass slide electrodes coated with a PEDOT/nano-Ni-nano/rGO as illustrated in Fig 7.1 at a 2-electrode cell voltage of: (a) 1.23 V and (b) 1.5 V, respectively for 14 h of operation. (*='light on', #='light off).*

7.2.3 Electrical and Mechanical Properties of Conductive Polyacrylamide Hydrogel- Cs-Cl

The hydrogel separator was found to have high conductivity (up to 310±31 mS/cm; Figure 7.5). The conductivity was higher than previously reported for polyacrylamide hydrogels, which was 0.22 mS/cm.[13] The significant value of this conductivity was probably related to the presence of Cs^+ and Cl^- ions in the gel. Cs^+ ions has a greater mobility through the polymer matrix due to it being less a polarising cation because of the shielding effect of the two additional electron shells compared with Li^+ ions, which would interact more with the polymer chains.

Moreover, the water content (%) in the hydrogel increased from 65% to 95% when the hydrogel was immersed in both electrolytes providing more carriers of water molecules to enhance the hydrogel conductivity as shown in Table 7.1. The pH of the hydrogel increased slightly over 14 h of PEC operation (Table 7.1).

The mechanical properties of hydrogel bridge polyacrylamide–CsCl (PAAm-CsCl) hydrogel have been examined before using it in water splitting systems to assess its mechanical durability.[14-17]

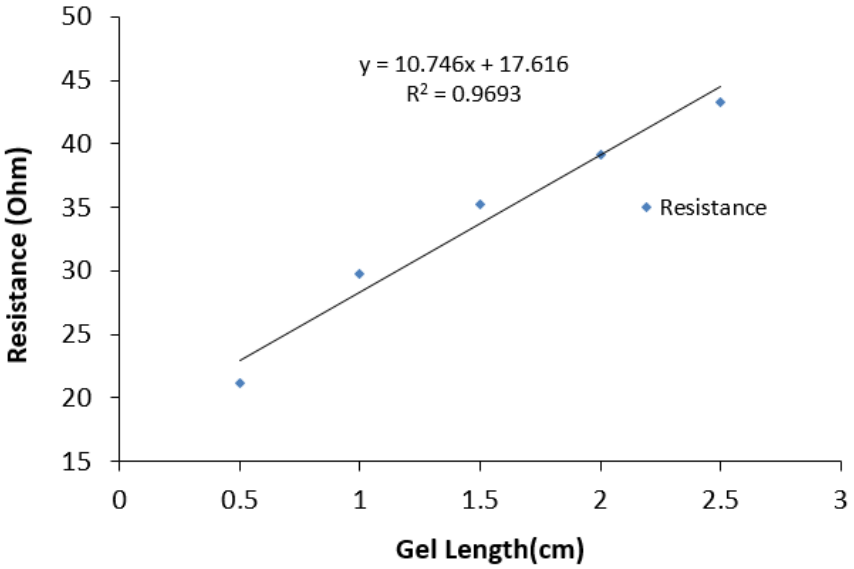

Figure 7.5: *Resistance as a function of length of the hydrogel separator used in this study.*

Parameter	Gel before experiment	Gel after experiment
Conductivity (mS/cm)	265±21	310±31
Water Content (%)	65	95
pH	2.5	3.1

Table 7.1: *Conductivity, pH and water content of hydrogel bridge (PAAm+CsCl)*

Figure 7.6 shows tensile and compression test analyses. The hydrogel displayed a tensile strength of 26±7 kPa with an ability to stretch to approximately 3-times its original length, providing reliable applicability as a stretchable conductive gel bridge.

The hydrogel exhibited a tensile modulus of 18±3 (kPa) with a significant ability to stretch of 298±19 % (Table 7.2).

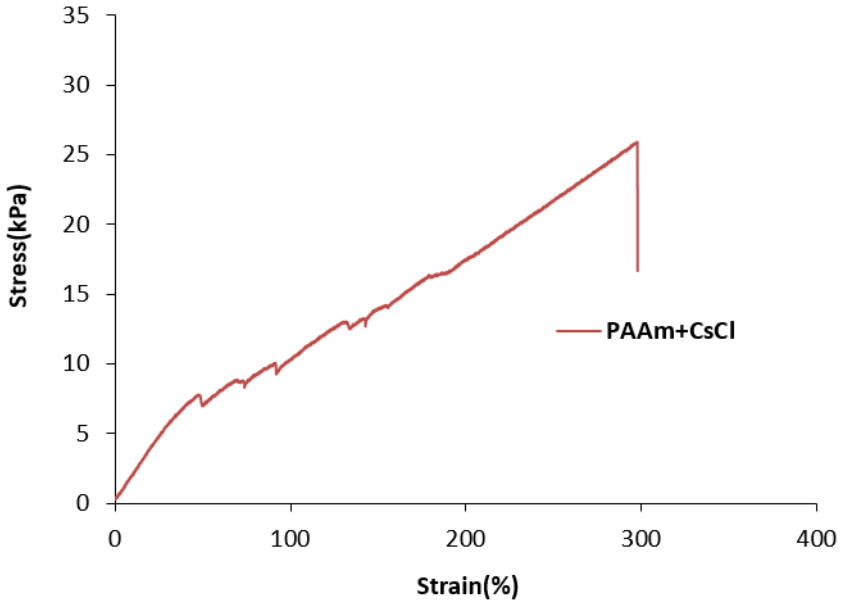

Figure 7.6: *Stress-strain curves for the ionic PAAm-CsCl hydrogel used in this study.*

Parameters	Values
Tensile Modulus (kPa)	18±3
Tensile strength (kPa)	26±7
Extension to Failure (%)	298±19

Table 7.2: *Tensile test parameters for PAAm - CsCl hydrogel used in this study.*

Furthermore, the compression test analysis was examined on the prepared hydrogel to assess its mechanical properties after applying compression action on it. Figure 7.7 displays the mechanical parameters of the hydrogel, such as compression secant modulus, ultimate compression stress and strain to the failure. Examining these mechanical properties was necessary to understand the mechanical durability of the gel.

As can be seen in Table 7.3 and Figure 7.7, the data for compression modulus, ultimate compression and strain to failure (%) revealed that the hydrogel had reliable mechanical properties.

Parameters	Values
Compression Modulus (kPa)	24±2
Ultimate compression (kPa)	824±31
Strain to failure (%)	91±8

Table 7.3: *Compression test parameters for PAAm - CsCl hydrogel*

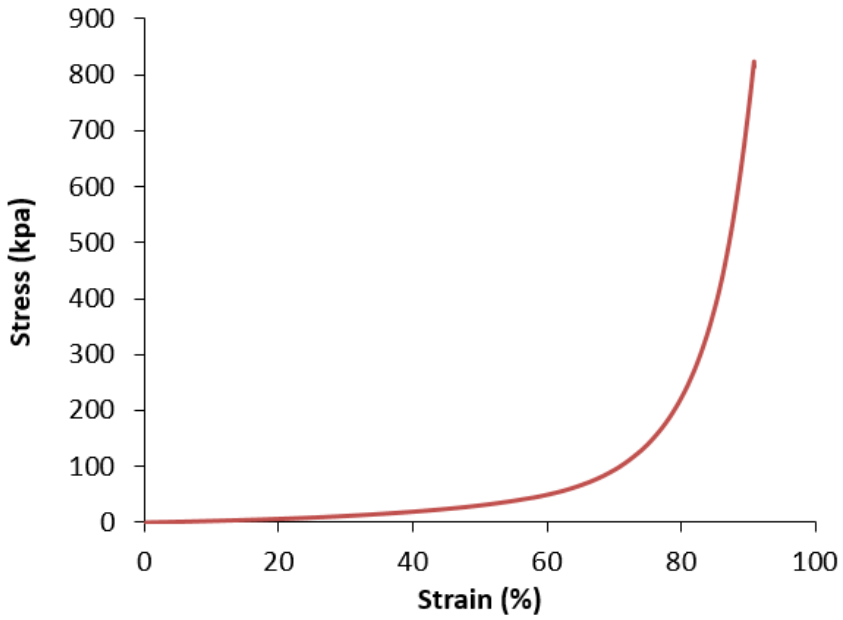

Figure 7.7: *Compression test analysis of PAAm-CsCl hydrogel.*

Finally, the hydrogel sample was stored at room temperature (21°C) and a relative humidity (RH) of 50% to test the water retention capacity of the hydrogel for 15 d. Hydrogel samples exhibited gradual shrinking as shown in Figure 7.8. The water loss of the hydrogel was approximately steady at 11% after storing it for 15 d. The main reason for the slow water loss during this period is the fact that the hydrogen was

embedded with CsCl salt that is considered to be a hygroscopic agent. It absorbs moisture from the air to balance the water content and substitute the water loss in the hydrogel. Based on that, the hydrogel substrate remained rich in water, enhancing it's mechanical and electrical durability when compared to other gels.[14, 16, 18]

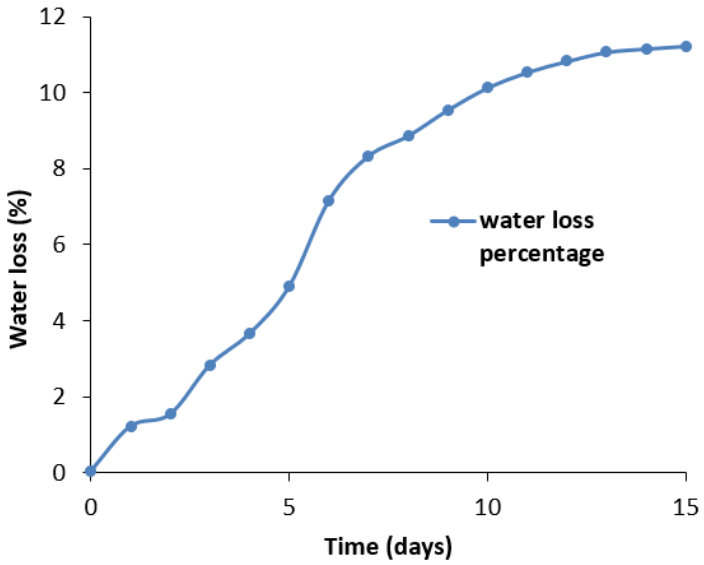

Figure 7.8: *A typical plot between water loss percentage and time in days for the PAAm+ CsCl hydrogel*

Since the left half-cell represents PEDOT/Nano-Ni/rGO containing 125 mg of nano-Ni and 6 mg of rGO (as decribed in Chapter 3 as having the highest performance). While the right half-cell represents PEDOT/Nano-Ni/rGO containing 125 mg of nano-Ni and 5.4 mg of rGO applied (as found to be highest performing in Chapter 4 at pH 1. Thus, the mechanism absorbing light and synergstic effect of these films have been discussed thoroughly in those chapters. Additionally, the hydrogel participated in both mechanism by playing a crucial role as ion-exchange membranes facilitating water-splitting performance.

7.3 Conclusions

Two thin film electrodes of PEDOT containing nano-Ni and rGO (as described in Chapters 3 and 4) have been applied in a PEC as working and counter electrode. The electrode for OER catalysis was immersed in aqueous alkaline 0.2 M Na_2SO_4 adjusted to pH 12. The counter electrode for HER catalysis was immersed in 0.1 M H_2SO_4.The half-cell electrolytes were connected *via* a novel, durable, conductive hydrogel bridge. The hydrogel exhibited excellent charge transfer mobility between the two half-cell electrolytes for periods of 14 h of testing. To the best of our knowledge, no other separator has been demonstrated to be capable of facilitating 14 h of continuous operation. The cell exhibits higher current at 1.5 V than at 1.23 V. However, the current at 1.23 V was sustained and relatively constant over 14 h of PEC operation; it declined only 11.8% from its stabilized current. In contrast, the current at 1.5 V degraded to 59 % of its stabilised current after 14 h of operation. The electrochemical properties of hydrogel were investigated before and after the operation.

This study demonstrated that ionic poly(acrylamide) hydrogels can be an effective salt bridge device for water splitting application for periods of at least 14 h of operation. The electrical and the mechanical features have been investigated.

This research contributes to the development of conducting, flexible and durable hydrogel materials for water-splitting.

7.4 References

1. Kassim, A.; Basar, Z. B.; Mahmud, H. N. M. E. Effects of Preparation Temperature on the Conductivity of Polypyrrole Conducting Polymer. *J. Chem. Sci.* **2002**, *114* (2), 155-162.
2. Bak, T.; Nowotny, J.; Rekas, M.; Sorrell, C. C. Photo-Electrochemical Hydrogen Generation from Water Using Solar Energy Materials-related aspects. *Int. J. Hydrogen Energy* **2002**, *27* (10), 991-1022.
3. Doyle, R. L.; Lyons, M. E. G. The Oxygen Evolution Reaction: Mechanistic Concepts and Catalyst Design. In *Photoelectrochemical Solar Fuel Production: From Basic Principles to Advanced Devices*, Giménez, S.; Bisquert, J., Eds. Springer International Publishing: Switzerland, **2016**; pp 41-104.
4. Selli, E.; Chiarello, G. L.; Quartarone, E.; Mustarelli, P.; Rossetti, I.; Forni, L. A Photocatalytic Water Splitting Device for Separate Hydrogen and Oxygen Evolution. *Chem. Commun.* **2007**, (47), 5022-5024.
5. Kaplan, A.; Korin, E.; Halevy, S.; Bettelheim, A. Chemical Bias of Electrochemical and Photoelectrochemical Water Splitting Using a Hydrogel Separator. *Electrochem. Commun.* **2015**, *60*, 97-99.
6. Antoniadou, M.; Bouras, P.; Strataki, N.; Lianos, P. Hydrogen and Electricity Generation by Photoelectrochemical Decomposition of Ethanol over Nanocrystalline Titania. *Int. J. Hydrogen Energy* **2008**, *33* (19), 5045-5051.
7. Hernandez-Pagan, E. A.; Vargas-Barbosa, N. M.; Wang, T.; Zhao, Y.; Smotkin, E. S.; Mallouk, T. E. Resistance and Polarization Losses in Aqueous Buffer-Membrane Electrolytes for Water-Splitting Photoelectrochemical Cells. *Energy Environ. Sci.* **2012**, *5* (6), 7582-7589.
8. Berger, A.; Segalman, R. A.; Newman, J. Material Requirements for Membrane Separators in a Water-Splitting Photoelectrochemical Cell. *Energy Environ. Sci.* **2014**, *7* (4), 1468-1476.
9. Walczak, K.; Chen, Y.; Karp, C.; Beeman Jeffrey, W.; Shaner, M.; Spurgeon, J.; Sharp Ian, D.; Amashukeli, X.; West, W.; Jin, J.; Lewis Nathan, S.; Xiang, C. Modeling, Simulation, and Fabrication of a Fully Integrated, Acid-stable, Scalable Solar-Driven Water-Splitting System. *ChemSusChem* **2015**, *8* (3), 544-551.
10. Menezes, P. W.; Indra, A.; Levy, O.; Kailasam, K.; Gutkin, V.; Pfrommer, J.; Driess, M. Using nickel manganese oxide catalysts for efficient water oxidation. *Chem.Commun.* **2015**, *51* (24), 5005-5008.
11. Gong, M.; Zhou, W.; Tsai, M.-C.; Zhou, J.; Guan, M.; Lin, M.-C.; Zhang, B.; Hu, Y.; Wang, D.-Y.; Yang, J.; Pennycook, S. J.; Hwang, B.-J.; Dai, H. Nanoscale nickel

oxide/nickel heterostructures for active hydrogen evolution electrocatalysis. *Nature Communications* **2014**, *5*, 4695.

12. Gennero de Chialvo, M. R.; Chialvo, A. C. Oxygen evolution reaction on thick hydrous nickel oxide electrodes. *Electrochimica Acta* **1988**, *33* (6), 825-830.
13. Chen, B.; Lu, J. J.; Yang, C. H.; Yang, J. H.; Zhou, J.; Chen, Y. M.; Suo, Z. Highly Stretchable and Transparent Ionogels as Nonvolatile Conductors for Dielectric Elastomer Transducers. *ACS Appl. Mater. Interfaces* **2014**, *6* (10), 7840-7845.
14. Bhadani, R.; Mitra Uttam, K. Synthesis and Studies on Water Swelling Behaviour of Polyacrylamide Hydrogels. *Macromolecular Symposia* **2016**, *369* (1), 30-34.
15. Gupta, N. V.; Shivakumar, H. G. Investigation of Swelling Behavior and Mechanical Properties of a pH-Sensitive Superporous Hydrogel Composite. *Iran. J. Pharm. Res. : IJPR* **2012**, *11* (2), 481-493.
16. Ahmed, E. M. Hydrogel: Preparation, characterization, and applications: A review. *Journal of Advanced Research* **2015**, *6* (2), 105-121.
17. Ullah, F.; Othman, M. B. H.; Javed, F.; Ahmad, Z.; Akil, H. M. Classification, processing and application of hydrogels: A review. *Materials Science and Engineering: C* **2015**, *57*, 414-433.
18. Sun, J. Y.; Keplinger, C.; Whitesides George, M.; Suo, Z. Ionic Skin. *Adv. Mater.* **2014**, *26* (45), 7608-7614.

Chapter 8

Conclusions and Perspectives

8.1 General Conclusion

Water splitting is the general term for a chemical reaction in which water is separated into its constituent materials, O_2 and H_2. In the last few decades, a lot of research on H_2 and O_2 production by water splitting has been carried out as a potential solution to an ideal future energy scenario and reduce the present dependence on fossil oil that increases greenhouse effects. Conductive polymers, modified graphene oxide, carbon nanotubes have been considered as organic materials, recently, within new classes of (photo)electrocatalysts for water splitting. As a result, water electrolysis or photo-electrolysis reactions have been rapidly enhanced due to the remarkable synergistic effects that can be gained, when they interface with other catalysts (such as transition metals or their oxides).[1-4]

8. 2 Conductive Polymers

Conducting polymers are attractive materials for a new water splitting technology because they may combine several desirable properties, including electronic conduction,[5] ionic conduction,[6] sensor functionality,[7] and electrochromism[8] (as well as other properties that were mentioned in Chapter 1, Section 1.6). They are also considered to offer potentially interesting photocatalytic properties under visible light. In our research, SEM/EDX, TEM, XPS, EIS and Tafel plot studies proved that when the PEDOT or PPy are incorporated with nanoparticles and carbon based materials, amplified catalytic effects due to amazing synergetic properties may be realized. For example, the resulting synergistic effect can provide

large numbers of active sites with the shortest, most conductive pathway for generated charge carriesr (h^+ and e^-), which result in further enhancement of the OER or HER process.

8.3 Carbon Based Materials (Modified Graphene Oxide and Carbon Nanotubes)

As noted previously, the electronic and chemical structure of modified graphene oxide allow it to enhance the performance of photocatalytic materials and photocatalyst supports. In the last decades many researchers have highlighted the roles and potential roles of GO in catalytic system. GO and rGO may act as: a catalyst in its own right, a redox mediator that accepts and transfers electrons, within dye-sensitized solar cells (DSSC), and as a co-catalyst. In our study, we found that rGO is also of interest when incorporated with CPs and catalytic nanoparticles within the film electrodes.

Multiwall carbon nanotubes (MCNT) may prospectively also be a stand-alone electrocatalyst for important reactions like the OER and HER, and even as a photoelectrocatalyst for the HER. MCNTs can providing high active areas and prevent the corrosion of the electrode during catalytic performance. In our study, we found that CNT played as important a role as rGO by accepting and transfer electrons within thin-film electrodes.

8. 4 Earth-Abundant Transition Metal Catalysts for Water Splitting

As is well-known, transition metals and their alloys, oxides and sulphate have been widely highlighted as alternative electrocatalysts to precious metals in water splitting applications. In addition, numerous examples of transition metal composites generate electrocatalytic results that are better than the noble metal itself.

The composite systems studied in this work, for both OER and HER catalysis, produced not only better catalytic behaviour than Pt itself under the same conditions but were

also highly stable and durable. For the OER, the best thin films were (at pH 12, 0.2 M Na_2SO_4 and 0.8 vs Ag/AgCl): PEDOT/nano-Co_3O_4/CNT > PEDOT/nano-Ni/rGO > PPy/nano-Ni/rGO > Pt > Ni-nano/rGO > PEDOT or PPy/rGO > PEDOT or PPy/nano-Ni > PEDOT or PPy. While for HER (0.05 H_2SO_4, -0.7 vs Ag/AgCl), the best thin films were: PEDOT/nano-Ni/rGO > PPy/nano-Ni/rGO > Pt > Ni-nano/rGO > PEDOT or PPy/rGO > PEDOT or PPy/nano-Ni > PEDOT or PPy. Co_3O_4 was not tested in HER catalysis because it dissolved in acidic media.

8. 5 Future Work: A Route to a New Class of Water-Splitting Semiconductors

Further work is required to investigate the prepared thin films on semiconductors that have already proved to be interesting photolytic water splitting applications. Examples of semiconductors that could be expected to be improved by the thin films studied here include: TiO_2, CdS, ZnO, $BiVO_4$, ZnS, Cu_2O, WO_3, Fe_2O_3, V_2O_5, Ta_2O_5, MoS_2, Ag_3PO_4, CdSe, $FeSe_2$, CoP_2, $NiFe_2O_4$, and so forth. While numerous studies have examined the above semiconductors with either CNTs, or CPs or rGO, to the best of our knowledge very few have utilized thin film CPs that have been optimized for maximum performance by inclusion of rGO, CNTs, and Ni nanoparticles. Thus, it seems there are large gaps that are worth exploring in the future in this field. The aim of such studies will be to investigate a variety of semiconductors coated with the prepared films in order to try to develop a new class of catalysts or photocatalysts that can be applied in future water splitting applications, or even can be industry-applied for future fuel resources.

Ultimately, as mentioned in the introduction of this thesis, the catalytic effects is more sensitive to the size of nanoparticles applied for water splitting. Future work is needed to study the water-splitting performance of the perepared films based using a variety of nanoparticles sizes for both Ni and Co_3O_4 nanoparticles.

8.6 References

1. Alsultan, M.; Ranjbar, A.; Swiegers, G. F.; Wallace, G. G.; Balakrishnan, S.; Huang, J. Application of Conducting Polymers in Solar Water-Splitting Catalysis. In *Industrial Applications for Intelligent Polymers and Coatings*, Hosseini, M.; Makhlouf, A. S. H., Eds. Springer International Publishing: Switzerland, **2016**; pp 223-251.
2. Yeh, T.-F.; Cihlář, J.; Chang, C.-Y.; Cheng, C.; Teng, H. Roles of Graphene Oxide in Photocatalytic Water Splitting. *Mater. Today* **2013**, *16* (3), 78-84.
3. Cozzarini, L.; Bertolini, G.; Šuran-Brunelli, S. T.; Radivo, A.; Bracamonte, M. V.; Tavagnacco, C.; Goldoni, A. Metal Decorated Carbon Nanotubes for Electrocatalytic Water Splitting. *Int. J. Hydrogen Energy* **2017**, *42* (30), 18763-18773.
4. Guo, D.-Z.; Zhang, G.-M.; Zhang, Z.-X.; Xue, Z.-Q.; Gu, Z.-N. Visible-Light-Induced Water-Splitting in Channels of Carbon Nanotubes. *J. Phys. Chem. B* **2006**, *110* (4), 1571-1575.
5. Le, T.-H.; Kim, Y.; Yoon, H. Electrical and Electrochemical Properties of Conducting Polymers. *Polym.* **2017**, *9* (4).
6. Armand, M. Polymers with Ionic Conductivity. *Adv. Mater.* **1990**, *2* (6-7), 278-286.
7. Persaud, K. C. Polymers for chemical sensing. *Mater. Today* **2005**, *8* (4), 38-44.
8. Brooke, R.; Mitraka, E.; Sardar, S.; Sandberg, M.; Sawatdee, A.; Berggren, M.; Crispin, X.; Jonsson, M. P. Infrared Electrochromic Conducting Polymer Devices. *J. Mater. Chem. C* **2017**, *5* (23), 5824-5830.

Appendices

Abbreviations:

RE reference electrode**, WE** working electrode and **CE** counter electrode

Table A. *Examples of recent applications of conducting polymers in water splitting.*

Examples of Composite have CP for OER, ORR or HER and reference No.	**A brief description of working conditions**	**Highlighted performance as reported with adding conductive polymer.**
PEDOT: PEG: PDTT ratios (1:2:2). [1]	LCD lamp equivalent to ~3–4 suns applied as light source. The composite loaded on Au Mylar and acted as working electrode, Pt and Ag/AgCl acted as counter and reference respectively. Mixture of Na_2HPO_4 and NaOH at pH 10.92 acted as electrolyte.	⇒ Interface of PEDOT with other materials harvesting light species producing bulk heterojunction can improve photocatalytic ability therefore PEDOT: PEG: PDTT has higher photocurrent density (50 µA/cm^2) than PEDOT (alone achieved only 20 µA/cm^2). ⇒ The presence of PEG reduce the VB energy because its assist the transition of electrons.
AgNPs/PEDOT/SiNW Arrays. [2]	Light intensity of 100 mW/cm^2 was applied as light source. The composite performed as working electrode while SCE and Pt mesh were applied as reference and counter electrodes respectively. The electrolyte was water/ meth. (1:1) at pH 1 adjusted via H_2SO_4.	⇒ Adding PEDOT to the system rising current density from less than 1 to 6.6 mA/cm^2 at SCE. ⇒ Solar-to-chemical energy conversion efficiency of 2.86 %. ⇒ Photocatalyst works for HER and H_2 rate evolution 36.05µmol cm^{-2}/h with no external potential ⇒ IPCE of ~35−42 % at visible region from 360 to 870 nm.
Nanocomposites PEDOT-$CoMn_2O_4$. [3]	The composite loaded on GCE and performed as working electrode while Pt and Ag/AgCl as counter and reference respectively. a solution of KOH was degassed by Ar and acted as electrolyte. The range from -0.7 V to 0.1 V and 0.6 to 1.0 V vs Ag/AgCl for ORR and OER study respectively. No light applied.	⇒ Adding PEDOT to the system rising current density from 1.5 to 5 mA/cm^2 at -0.8 V vs Ag/AgCl ⇒ Surprisingly exhibits high ORR. ⇒ In comparison with commercial Pt/C, the catalyst shows very similar behavior in range -0.6V to -0.4V with lower Tafel slope of 70 mV/ dec. ⇒ Very small reduction in stability after 500 CV cycles in rage -1V to 1V.
Pt/TiO_2/CdS/CdSe/PEDOT Photocatalytic electrode. [4]	Solar light simulator was used as source of light. The composite performed as working electrode while Pt and Ag/AgCl as counter and reference respectively. Mixture Na_2S and $N_{a2}SO_3$ acting were as sacrificial electrolyte (pH 12).	⇒ Adding PEDOT to the system raised to 13 mA/cm^2 at -0.2V vs Ag/AgCl ⇒ Adding PEDOT shifting the visible absorbance to longer wavelength. ⇒ Adding PEDOT rising the IPCE value to ~17.5% and the quantum efficiency was 6.9% at 700 nm. ⇒ Photocatalytic stability was tested under illumination with >420 nm light for 9 h .It was observed that adding PEDOT increases the stability because PEDOT reduced electrode's photocorrosion. TON reached about 2200. ⇒ H_2 evolution rate was 1.1 mmol/cm^2 in 6 h

TiO_2/dye/PEDOT:PSS. [5]	The composite loaded on FTO and applied as working electrode while Pt and SCE acted as counter and reference electrode respectively. Pitaya peel dye in distilled water acted as electrolyte.	⇒ Adding PEDOT to the system rising current density from 0.6 to 1.4 µA/cm^2 at 1.5 v *vs* SCE. ⇒ PEC for water splitting with low cost. ⇒ The presence of pitaya dye enhanced PEC performance. ⇒ The system was work for production hydrogen (HER)
MnTPPS/PEDOT:PSS. [6]	Halogen light bulb 50 watt was used, the composite was loaded in FTO glass and acted as working electrode while Ag/AgCl and Pt was reference and counter electrodes respectively. 0.1 M Na_2SO_4 acted as electrolyte.	⇒ PEDOT enhances the system performance due to it can accept or donate electrons in suitable conditions. ⇒ The current density increased from 37 to 48 µA/cm^2 at 0.65 V *vs* Ag /AgCl when PEDOT was added.
PEDOT: PSS as a part of seven layer of (BHJ) for (PSCs). [7]	Xenon lamp equivalent to 1 sun was applied as light source. Pt and Ni foam was used as cathode and anode while 1 M of NaOH as an electrolyte with 1.8 V of external bias. The PSCs set out of electrolyte but connected with Nickel foam via wire and PSCs itself was exposed to light.	⇒ Maximum current density reached 19 mA/cm^2. ⇒ The system has wide visible absorption in range 400-650 nm. ⇒ The system works for HER via Pt and OER via Ni foam. ⇒ Solar to fuel conversion efficiency reached 6 %.
NPG/PEDOT/WS_2. [8]	The composite supported tungsten sulphide acted as working electrode while graphene rode and SCE acted as counter and reference respectively. 0.5 H_2SO_4 was used as an electrolyte. No light was applied.	⇒ The system works for HER with current density of 0.04 mA/cm^2 with low Tafel slope of 53 mV/ dec and displayed onset potential of -164 mV. ⇒ PEDOT observed enhancing HER activity compared to planar Au-electrode.
$Pt_{0.5}Pd_{0.5}$NPs/PEDOT-SG/GCE. [9]	The composite was loaded on GCE and applied as working electrode while Pt acted as counter electrode. 0.5 mo/ L^1 H_2SO_4 was used as an electrolyte .No light was applied	⇒ Cheap HER and the system stable for more than 500 the scan of LSV ⇒ PEDOT facilitated H^+ diffusion due to its porosity and supported homogeneous dispersion of graphene nanosheets. ⇒ Current reached 0.301 µA at low potential of 0.1726 V vs Ag/AgCl with Tafel of 57 mV/ dec ⇒ In LSV study, the current reach more than 7 mA at -0.7 V vs Ag/AgCl.
CoNiMn-LDH/PPy/ rGO. [10]	The composite loaded on GCE and acted as working electrode. While Pt and SCE acted as reference and WE respectively. For ORR study, 0.1 M KOH was used as electrolyte and LSV range 0.95 V to 0.15 V at 5 mV/s. In OER study 1.0 M KOH was used and LSV range 1.25 to 1.70 V at 5 mV/s^1. No light was applied.	⇒ The system exhibited good bifunctional electrocatalysis for both OER and ORR. ⇒ In ORR study, the LSV reported that the presence of Ppy in the composite enhances the current density from -3 to - 5 mA/cm^2 at 0.2 V *vs* RHE. ⇒ In OER study, the LSV reported earlier onset potential at 369 mV to obtained 10 mA/cm^2 and current reached 29 mA/cm^2 at 1.7 V *vs* RHE and was stable after 1500 LSV scan.
Nanomaterials **Co_9S_8@ NOSC** containing poly pyrrole solid precursors. [11]	The composite was loaded on GCE. While Pt and Ag/AgCl electrode and a graphitic carbon rod were used as the working electrode, reference and counter electrodes, respectively. 1 M KOH was acted as electrolyte. No light was applied.	⇒ Noble metal-free system works bifunctionally for both OER and HER ⇒ In LSV current density increased from 10 at 1.6 to 20 mA/cm^2 at 1.74 V *vs* RHE. ⇒ Chronoamperometric responses showed at bias 1.57 *vs* RHE, a current density of 10 mA/cm^{2}over 6 h was obtained and then gradually started to decrease to reach 9 mA/cm^2 at the end of 10 h of the performance while at bias 1.85 V reached 50 mA/cm^2 and was stable over 8 h.

PPy 5-TNTs. 5 refers to elecropolymerization time for 5 minutes.[12]	A simulated solar illumination was applied.. The catalyst was loaded on Ti foil substrate and acted as working electrode while Pt and Ag/AgCl performed as counter and reference electrode respectively. 1 M KOH was used as electrolyte.	⇒ Photoelectrocatalyst composite working for water splitting for OER and HER. ⇒ Higher photocurrent density at 0.23 V (vs. Ag/AgCl) reached 3.5 mA/cm^2 while TNTs alone was less than 1.5 mA/cm^2. ⇒ Wide visible absorption n range 400-700 nm. ⇒ IPCE reached 92.5 % at 300 nm and was lower at visible region.
Mo_2C@NPC/NPrGO). N and C refers to Ppy as a source of N and C atoms.[13]	The catalyst was loaded on GCE and applied as working electrode while Pt and Ag/AgCl were used as counter and reference respectively. 0.5 M H_2SO_4 was used as electrolyte. No light was applied.	⇒ The composite works for HER electrocatalyst. ⇒ The catalyst was stable for more 1000 of CV cycles. ⇒ The current density exhibits 60 mA/cm^2 at -0.1 V vs RHE. ⇒ PPy was used as a source of N and C as well as reducing GO agent (the composite was burned at 900 ˚C for 2 h)
(PBTh) on glassy carbon.[14]	KL 2500 LCD halogen lamp used as a source of light .GC measurements carried on three references. The film on GCE acted as WE. While Ag/AgCl electrode used as reference. The cell was also has counter electrode. A 0.1 M phosphate buffer of pH 6.9 was used as the electrolyte.	⇒ Efficient photoelecrodes composite works for HER. ⇒ Early onset potential under visible light at -00.3 V vs SCE and photocurrent density of -45 µA/cm^2 at -1.2 V vs SCE were observed. ⇒ The chronoamperometric study exhibits a current density of 35 µA/cm^2 at 0.52 V vs SCE. ⇒ Interesting absorption in range 500-800 nm.
NC–CoO/C. N and C refers to Ppy as a source of N and C atoms.[15]	The catalyst was loaded on GCE and acted as WE while Pt and Hg/ HgO in 1m NaOH acted as CE and RE electrode respectively. 0.1M KOH used as electrolyte. No light was applied.	⇒ The composite works as bifunctional electrocatalyst for both ORR and OER. ⇒ In ORR exhibits similar behaviour of commercial Pt/C. ⇒ In OER was higher than Pt/C and exhibits earlier onset potential. ⇒ PPy suggested to wrap CoO nanoparticles prevent its aggregation during the catalytic reaction.
Ppy-Ru(2,2′-bipyridine)$_3^{2+}$/MoS_x.[16]	Solar light simulator was used as source of light. The composite was loaded on GCE and Ag/AgCl used as reference. Aqueous H_2SO_4 was used as electrolyte.	⇒ Efficient photoelecrodes composite works for HER. ⇒ At pH 0.3 and with external bias of -0.3 V vs Ag/AgCl, the photocurrent reached -40 µA/cm^2 while at pH 3, the photocurrent reached – 5 µA/cm^2. ⇒ The H_2 evolution rate at pH 3 reached 0.33 µmol while at pH 0.3 reached 0.53 µmol.
PTh-C (C refers to oxidation polymerization for 0◦C for 4 h and 50◦C for 1 h.[17]	PTh-C was dispersed in aqueous solution of Ascorbic Acid and exposed to 300-xenon lamp.	⇒ The system works for HER with rate reached 2.8-mmol/ h^1 g^1. ⇒ The system worked for 20 h with little reduction of its HER activity. ⇒ Good light absorption in range 300-600 nm. ⇒ PTh was working alone for HER and the temperature of oxidation polymerization was the control to optimized HER effect.

TiO_2/Au/ PTh. [18]	50 mW/cm^2 a solar simulator used as light. The composite was loaded on FTO and performed as WE while Ag/AgCl and Pt used as RE and CE respectively. 0.5 M $NaSO_4$ used as electrolyte.	⇒ The system works for HER with evolution rate reached 2.929 mmol/ h m^2. ⇒ The photocurrent density reached 0.2 mA/cm^2 at bias of 0.5 *vs* Ag/AgCl. ⇒ Two distinctive board absorption peaks the first from 200-400 nm and the second from 500-700 nm. The first due to all composite contents and the second related to plasmatic absorbance of metallic Au nanoparticles.
PTh-rGO-TiO_2 nanocomposite.[19]	The catalyst mixed with methylene blue and exposed to 250 W tungsten-halogen lamp.	⇒ The system works as a photoelectrocatalyst for HER . ⇒ The quantum efficiency reached 14.2% at 400 nm. ⇒ Wide board absorption from 200-350 nm. ⇒ Adding PTh to the system raised hydrogen evolution rate from 160 to 214.08 µmol/h.
CdS/PTh nano composites.[20]	An amount of photocatalyst dispersed in methyl viologen and exposed to 250-watt 250-halogen lamp.	⇒ The photocatalyst works for HER activity with evolution rate ⇒ Wide range absorption increased steadily from 400-800 nm.
Ppy/FeTCPP/Co.[21]	The composite loaded on GCE electrode and acted as WE. While a graphite rod and SCE were performed as CE and RE respectively. 0.1 M KOH was used as electrolyte. No light was applied.	⇒ Cheap, efficient and durable electrocatalysts for ORR, OER and HER. ⇒ The ORR study showed similar behaviour to Pt/C. For OER study the current density exhibits similar to RuO_2 nanoparticles. ⇒ The HER study showed higher current density of -10 mA/cm^2 at -2.4 V vs RHE.

Table B: *Examples of water electrolysis and PEC water splitting based on modified graphene oxide*

Examples of Composite have CP for OER, ORR or HER and reference No.	A brief description of working conditions	Highlighted performance as reported with adding rGO or CNT
CdS/MoS_2/graphene hybrids. [22]	The hybrid was dispersed in aqueous solution of lactic acid, suspension was purged with argon to remove dissolved air. Then the system exposed to 300W xenon lamp with a 400 nm cut-off filter.	⇒ H_2 production rate of 1913 mol/ (h.g), EIS spectra showed that presence of graphene increases the charge carrier transfer significantly. ⇒ 2D graphene layer offers high specific surface area, which is critical for high-efficiency photocatalysis. ⇒ Graphene acted as both electron acceptor and charge transporter resulting in superior activity of the synergic system. Charge carriers recombination was inhibited due to the existence of graphene with high conductivity and the intermediate energy levels of graphene in composites

Hybrid CNS:S-Se-Gr (CNS = Gr-C_3N_4 , Gr = graphene) through a thermal exfoliation method.[23]	The catalyst was dispersed in deionized water, with sodium sulphite and lactic acid as holes scavengers. Then the system was exposed to 500 W Xe lamp. Bias potential of 0.2 V *vs* Ag/AgCl was applied. Prior to the experiment, the cell was purged with N_2 gas to exclude O_2. Pt wire and Ag/AgCl were used as counter and reference electrodes respectively.	⇒ Hydrogen evolution rate was 2.59 mmol/ (g.h). ⇒ Graphene acted as electron-conducting channels. ⇒ Presence of graphene increases significantly the visible absorbance (400-800nm). 8.2% apparent quantum efficiency has achieved in lactic acid. ⇒ Heterojunction of CNS: S-Se-Gr resulted in an improved optical absorption, oxidation potential, surface area, interfacial charge transfer and charge carrier lifetime.
PSGM/rGO/CdS catalyst.[24]	The catalyst was dispersed in aqueous solution containing 0.5 M Na_2SO_3 and 0.5 M Na_2S as sacrificial reagents. Then it exposed to a simulated solar light irradiation ($\lambda > 400$ nm).	⇒ A hydrogen evolution rate of 175 μmol/ h. The quantum efficiency of the 3.99% at 420 nm was obtained. ⇒ Graphene acted as electron acceptor and H_2 evolution sites. ⇒ The catalyst showed high absorption in both ultraviolet and visible region. After 20 h reaction, the catalyst still kept high H_2 production ⇒ The heterojunction formed between CdS and graphene facilitates electrons transfer from CdS to graphene and reacted with protons on the active sites on graphene. ⇒ The recombination reaction was suppressed due to the heterojunction of this hybrid.
TiO_2-GQDs heterostructures .[25] (Graphene quantum dots = (**GQDs)**	The catalyst worked as WE while Pt as CE, a saturated Ag/AgCl electrode was used as the RE, aqueous solution (0.5 M) of Na_2SO_4 was used as the electrolyte and the pH of the solution was 5.9. The electrolyte was bubbled with nitrogen gas for 30 min. Illuminated using a 300W Xe lamp.	⇒ The absorbance has increased at both UV and visible region up to 600 nm. ⇒ The photocharge carriers generated at both TiO_2 and GQDs so both valence band of GQD and TiO_2 involves in water oxidation. Graphene may have a role as sensitizer and catalyst. ⇒ The hybrid system worked as an O_2 evolution system. Current density of 0.18 mA/cm^2 was obtained after GQDs sensitization
Graphene-intercalated Fe_2O_3/TiO_2.[26]	Solar light simulator was applied as light source. The sample was kept in a 3 electrode PEC cell with 0.1 M NaOH electrolyte. External potential of 1.23 V *vs* RHE was used as RE	⇒ The presence of graphene oxide improves the photocatalytic effect. ⇒ Higher photocurrent density (0.85 mA/ cm^2) was achieved at 1.23 V *vs* RHE and shifted the onset potential for water splitting was shifted by 0.25V *vs* RHE toward lower value. ⇒ Graphene acted as a charge acceptor and a charge transfer material. ⇒ Graphene-intercalated Fe_2O_3/TiO_2 exhibits noticeably reduced recombination of the generated e^- and h^+.
$(Bi_2S_3/rGO)_5/TiO_2$.[27]	The light source was 300 W Xe lamp with a UV cut-off filter (420 nm). While the catalyst acted as WE, Pt foil as a CE and saturated calomel electrode (SCE) as a reference electrode A mixture of 0.35 M Na_2SO_3 and 0.25 M Na_2S at pH 12.4 was used as an electrolyte. Bias of 0.0V *vs* SCE was applied.	⇒ rGO has increases visible absorbance especially at the range 400nm to 800nm and the photocurrent density reached 2.0 mA/cm^2. ⇒ Graphene facilitated charge transfer from Bi_2S_3 to TiO_2 with high resistance to the recombination reaction. ⇒ A conversion efficiency of 1.2 % at 0.47 V (*vs* RHE) under visible light ($\lambda > 420$ nm which it was higher than different structures made from these components by 4-5 times). rGO and Bi_2S_3 act as a charge transporter and sensitizer respectively. ⇒ EIS measurements on $Bi_2S_3/rGO)_5$ /TiO_2 worked as a semiconductor.

Hydrogenated graphene /TiO_{2-x} composites.[28]	Solar light simulator equipped with $CuSO_4$ pass filter in range (310 nm < λ < 625 nm) was used as a light source. 0.01 M $AgNO_3$ were used as a sacrificial agent. Bias of 1.25 V *vs* Ag/AgCl reference was applied. Ag/AgCl electrode and Pt were applied as RE and CE respectively. 0.1 M $HClO_4$ was used as an electrolyte.	⇒ The system was working for both O_2 and H_2 evolution and wide light absorption in range 300-800 nm. ⇒ Photocurrent density reached 0.055 mA/cm^2 at 1.25 V *vs* Ag/AgCl. ⇒ The rate of H_2 production was determined to be 3.5μmol/h. Quantum efficiency was calculated to be 0.068 %. ⇒ Graphene acted as interfacial electron transport material and efficiently retards the charge recombination. ⇒ H_2 evolution rate was 15.6 μmol m^2/ h and O_2 evolution rate at 4.2 μmol m^2/h with a lesser value.
Mo-doped $BiMo_{0.03}V_{0.97}O_4$ (BiMoVO)/Graphene.[29]	Solar light simulator with cut filter at 420 nm was used as a light source. The thin-film catalyst was applied as a WE, Pt as a CE and Ag/AgCl electrode as a CE. External bias of 1.0 V was apllied. 0.1 M Na_2SO_4 neutral solution was used as an electrolyte.	⇒ Increased visible absorption from 520-700 nm and the photocurrent density reached 3.5 mA/cm^2. ⇒ Graphene acted as an electrons acceptor from BiMoVO and electron transfer material. ⇒ The system worked for H_2 evolution only and photocurrent decreased by 8.6 % after 10 hours. ⇒ The presence of graphene decreases the recombination reaction resulting in increase of the lifetime of photo-induced electrons. ⇒ The conversion efficiency of BiMoVO /Graphene was 50% higher than BiMoVO alone under the incident light illumination of 440 nm.
SnS on N-reduced graphene (N-rGr) sheets.[30]	The catalyst was loaded on GCE and applied as a WE. While Ag/AgCl electrode and Pt were applied as RE and CE respectively. Mixture of 0.5 M H_2SO_4 used as electrolyte. Finally, external bias of 1.0 V was applied. No light applied in this system.	⇒ The electrocatalyst had high activity in acidic, neutral and alkaline media. ⇒ Low overpotential achieved at -125 mV and Tafel slop of 38 mv dec^{-1} with long term durability. ⇒ The system has worked for H_2 evolution reaction. ⇒ Graphene has functional group, which has strong coupling with SnS and played a role in charge transport pathway. TOF reached 0.23 /s at 125 mV ⇒ Low faradaic impedance or charge-transfer impedance reached at 98 Ω.
Novel NiO/rGO/TiO_2 *p-n* heterostructured material. [31]	A white light was used as light source. The catalyst performed as working electrode while Ag/AgCl and Pt applied as RE and CE in 1 M NaOH solution. A bias of 0.2 V *vs* Ag/AgCl was used.	⇒ rGO interfaced between *p*-type NiO and *n*-type TiO_2 resulted in enhance of photocatalyst effects. ⇒ XPS spectra of NiO/rGO/TiO_2 composite shows hierarchical hetero- structures and purely contain Ni, Ti, O and C and absence of any contaminants. ⇒ The system has worked for H_2 evolution and the rate of this gas evolution reached 240 μmol/h/g and photocurrent reached 7 μA/cm^2. ⇒ EIS spectroscopy revealed that the charge transfer resistance was smaller at the light than at the dark due to the presence of rGO. ⇒ The graphene worked as an electrical charge transfer material

rGO-$BiVO_4$ deposited on FTO. [32]	The 0.4 M potassium borate in aqueous solution was used as an electrolyte with pH 9.2. Light source was AM 1.5 G simulated sunlight (100 mW/cm^2). Catalyst film was applied as WE. Pt sheet and Hg/Hg_2Cl_2 as CE and RE respectively.	⇒ The visible absorbance was enhanced between 500-700 nm. ⇒ The system was working for both H_2 and O_2 evolution. ⇒ Charge separation efficiency of rGO-$BiVO_4$ was enhanced from 59 to 78 % at 420 nm and 1.23 $V_{RHE.}$ ⇒ The onset potential for cathodical water splitting shifted by approximately 120 mV compared to pure $BiVO_4$. ⇒ Faradaic efficiencies of H_2 and O_2 production were calculated to be 88.6 and 72.9 % respectively. ⇒ Graphene has provided an excellent electronic conductivity providing a channel for electron transport.
Nitrogen-doped graphene oxide dots (NGODs).[33]	Light source was 300-W xenon lamp with band-pass filters 420-800 nm. The catalyst was dispersed in aqueous solution of triethanolamine.	⇒ The catalyst steadily catalysed H_2 production under visible light illumination for 96 h. ⇒ Quantum yield 16.0% under 420-nm light ⇒ NGODs acted as photocatalyst for H_2 evolution. ⇒ NGO acted as charge transfer and electron media.
Co (NPs) combined with N-doped graphene film (Co@NGF.[34]	The catalyst film was applied as a WE, Hg/Hg_2Cl_2 electrode (saturated KCl) and a platinum wire were used as the RE and CE respectively. Finally, 0.5 M H_2SO_4 aqueous solution was used as the electrolyte.	⇒ Early onset potential at -14 mV (vs. RHE) with a small Tafel slope of 93.9 mV/dec. ⇒ Catalytic current remained constant after 50000 s indicating strong durability. ⇒ The photocurrent density reached over 6 mA/cm^2. ⇒ The catalyst electrode was applied for both reduction and oxidation of water. ⇒ Co@NGF based on earth-abundant elements. ⇒ Graphene doped with N atom film acted as an accepting and transferring electron material.
Nitrogen (N)-Doped Nb_2O /rGO Nanocomposite [35]	The 300 W xenon lamp with a cut off filter to obtain radiation of $\lambda >$ 420 nm was used as a light source. The catalyst was dispersed with Nafion and ethanol and loaded on ITO as WE. While SCE and coiled platinum wires were used as the RE and CE, respectively. 0.1 M sodium sulphate solution was used as the electrolyte. An external potential 1.9 V *vs* SHE was used.	⇒ The photocurrent density reached over 10 $\mu A/cm^2$ at the external potential 1.9 V. ⇒ The system has worked for H_2 evolution reaction. ⇒ rGO acted as a solid-state electron mediator.
Graphene–Pt–CdS (GP–CdS NWs) nanowires.[36]	300 W xenon lamp, cut-off filter (>400 nm)was used as a light source. The catalyst deposited on FTO as a modified WE. While Pt plate and Ag/AgCl electrodes played as CE and RE respectively. Mixture of solution of Na_2S 0.1 M and Na_2SO3 0.1 M was used as an electrolyte.	⇒ The system has worked for H_2 evolution. The H_2 rate reached a value of 3984 µmol (h.g) higher than bare CdS NWs by 4 times. ⇒ Graphene and Pt acted as cocatalyst together with modified CdS for H_2 production. ⇒ Highly active surface area achieved. It reached 19.55 m^2 /g. The photocatalytic H_2 evolution activity slightly reduced to reach 80% after four cycles (each cycle has 5 hours of operation). ⇒ The impedance plot of GP-CdS NWs has a smallest radius than other controls composites such Cds, G-Cds and Pt-CdS NW electrodes.

ZnS- GO.[37]	300 W Xe lamp, UV cut off filter ($\lambda > 420$ nm) was used as a light source in gas-enclosed circulation system, catalysts were dispersed in aqueous solution contains 0.35 m Na_2S and 0.25 M Na_2SO_3, the system was degassed under vacuum condition to remove the dissolved O_2, bias potential of 0.5 V *vs* Ag/AgCl was apllied. Ag/AgCl was used as a RE and Pt as a CE.	⇒ The system has worked for H_2 with evolution rate of 7.42 μmol/ (h. g). It was 8 times higher than ZnS. ⇒ Graphene acted as a sensitizer that absorbs photons and injects electrons in CB of ZnS. ⇒ The absorbance increased in range 500 and 700 nm. ⇒ The current density reached 0.24 mA/cm^2. ZnS-GR has 0.1% GR (w/w%) and reaches a high photocatalytic H_2 production rate.
rGO modified 3D α-Fe_2O_3.[38]	Fe_2O_3-rGO photoanodes was used as a WE. Ag/AgCl applied as RE and Pt wire as the CE. 1 M NaOH (pH 13.6) aqueous solution was used. N_2 gas was bubbled through the solution prior to the experiment to remove any dissolved O_2. No light was applied	⇒ rGO was conductive for electrons transfer in passive layers. ⇒ rGO reduces the recombination reactions increases the charge injection efficiency. ⇒ The current density raised to (1.06 mA/cm^2, at 1.23 V *vs* RHE) when the catalyst applied. ⇒ Enhanced photocurrent density to 1.06 mA/cm^2 which means 1.47 times higher than that of the pristine Fe_2O_3 at 1.23 V *vs.* RHE. ⇒ Increased UV and visible absorbance region (350 -600 nm).
$CuInS_2$(CIS)/graphene oxide nano- films.[39]	Xe light illumination of 100 mW cm^{-2} was used as a light source. The catalyst was used as WE while Pt foil as counter electrode and saturated Ag/ AgCl used as RE. Na_2S (1 mol/L) used as the electrolyte. External bias at 0.16 V *vs* Ag/ AgCl was applied.	⇒ Facile, inexpensive, and environmental friendly method. ⇒ The photocurrent density of the catalyst reached 2.47 mA/cm^2. The presence of graphene to reduce the recombination reaction of the photogenerated charge carriers. ⇒ High visible absorption, especially between 400-700 nm regions was achieved. Graphene acted as a photocatalyst semiconductor for water splitting and $CuInS_2$ as cocatalyst for H_2 evolution.
Hierarchical graphene /CdS /Ag_2S sandwiches nanofilms.[40]	Xe light illumination of 100 Mw was applied as a light source. The catalyst nanofilm applied as WE at 0.55 V *vs* saturated Ag/AgCl. Pt foil applied as a CE. Finally, Na2S was used as an electrolyte.	⇒ Photocurrent density up to 5.18 mA/cm^2. ⇒ Graphene acted as electrons acceptor. ⇒ High light harvesting due to the broaden solar absorption resulting in an increasing photo effects. ⇒ Graphene offers an excellent electron accelerator to obtain better electron-injecting efficiency between CdS and Ag_2S. ⇒ The hydrogen generation efficiencies reached a value of 4.11%. The system has worked for H_2 evolution with maximum hydrogen generation, 221 μmol/h.
Cu_2O nanoparticles/MnO–MnO_2 nanorods forms heterojunction. [41]	Solar simulator was used as a light source. 0.1 M $KHCO_3$ was used as an electrolyte. Pt film and Cu_2O/MnO_2/ Graphene/ITO are anode and cathode, and 0.6 V bias voltage. (No reference).	⇒ The catalyst was working for H_2 evolution with a high rate of 33.0 mL/min m^2. ⇒ The catalyst has absorbed only 2.3% of visible light. ⇒ Graphene acted as an electron transition pathway. ⇒ Highly efficient, low-cost, and flexible photoelectrochemical cell. ⇒ Wide absorbance for the catalyst from 500-800 nm. ⇒ Due to the heterojunction of this catalyst, the recombination reactions between h^+ and e^- were suppressed. The photocurrent was raised to reach 14 A/m^2 at bias voltage of 1.4 V and the IPCE around 7% at 400 nm.

Z-scheme system composed of (Ru-complex /$SrTiO_3$: Rh)-(RGO / BiVO4.[42]	300 W Xe lamp fitted with cut-filters allowed only to visible light in range (400-800) nm was used as alight source. The photocatalyst powder was suspended in water at pH 3.5 adjusted with H_2SO_4. The electrolyte was degassed by Ar to exclude the O_2 .	⇒ The system has worked for both H_2 and O_2 evolution under visible light irradiation (λ> 420 nm). ⇒ TON reached 450 after 8.5 h of irradiation. ⇒ Graphene acted as a solid electron mediator to construct efficient Z-scheme. ⇒ H_2 evolution rate around 70µmol and O_2 evolution rate 35 µmol during 8 h.
NiFe/rGO composite.[43]	A simulated solar light of 1.5 G filtered and calibrated to 1 sun (100 mW/cm^2) was used as light source. 1.0 M KOH used as an electrolyte. While Pt wire and Ag/AgCl used as CE and RE respectively. The catalyst was cast on carbon paper and performed as WE.	⇒ The system has worked for O_2 and H_2 evolution reaction. H_2 and O_2 evolution rates were 120 and 60 µmol during 180 minutes respectively. ⇒ Higher photocurrent of 0.95 mA cm^{-2} at 1.23 V. ⇒ The rGO was working as conductive electron pathway. ⇒ Nyquist plots recorded lower resistant charge transfer. ⇒ Practical electrocatalyst with high activity, stability, and low cost.
($Ga_{1-x}Zn_x$)($N_{1-x}Ox$)-rGO.[44]	A light source was 300W Xenon lamp was used as a light source while photocatalyst was dispersed in aqueous solution that has 10% ethanol.	⇒ Presence of rGO increased the visible absorbance especially at the range 500nm to 800nm. ⇒ The catalyst with rGO shows high surface area and more mobility for the charge carrier enhancing the photocatalytic activity. ⇒ Adding rGO more than 30% resulted in reduction of the photocatalytic activity. ⇒ ($Ga_{1-x}Zn_x$)($N_{1-x}O_x$) was responsible for water splitting and rGO was supporting and e^- conductive network. ⇒ The catalyst had higher photo- catalytical performance for H_2 production than bare ($Ga_{1-x}Zn_x$)($N_{1-x}O_x$).
[CNT + GO]/Co/Cu_2O. CNT.[45]	500 W Xe lamp was used as a light source with cut-off filter at 400 nm. The catalyst was dispersed in aqueous electrolyte of 0.6 M Na_2SO_3 and 0.1 M Na_2S	⇒ The catalyst worked for H_2 evolution with rate of 0.21 mmol after 300 min. ⇒ Apparent quantum yield was 16.6 % at 420 nm. ⇒ Economical way to produce H_2. ⇒ Some amount of graphene was formed accidently through fabrication process of CNT pre-treatment (exfoliated tube wall of CNT) (role not mentioned)
C_3N_4-rGO-WO_3 composites. C_3N_4-rGO. [46]	UV–vis lamp cut-off at 420 nm was used as a light source. The catalyst was loaded with 1 wt % of Pt then suspended on 100 mL of water with 10 mM with $AgNO_3$ as an electron acceptor. The electrolyte was purged with pure Ar to remove air.	⇒ The system showed the evolution rates of 2.84 and 1.46 µmol h^1 for H_2 and O_2 respectively. ⇒ Quantum yield obtained was of 0.9% at 420 nm. ⇒ rGO acted as an electron mediator. ⇒ High light absorbance was observed especially at beginning of visible region.
Highly ordered γ -Fe_2O_3 / rGO.[47]	UV light at 360 nm was used as a light source. Ag/AgCl and Pt were RE and CE respectively. Catalyst was mixed with carbon black and polyvinylidene fluoride (PVDF) then deposited on Cu foil as working electrode. 1.0 M NaOH buffer solution at pH 13.6 was used as an electrolyte.	⇒ Photocurrent density reached 6.74 mA/cm^2 *vs* RHE. It was 4 times higher than pristine iron oxide. ⇒ Current conversion efficiency (IPCE) of 4.7%, which is 3.7 times than pristine γ -Fe_2O_3. The catalyst has low Tafel slope of 39 mV /dec^1. ⇒ rGO acted as electrons acceptor increasing electron-hole separation and suppressing the recombination reactions.

Pt-loaded $CuGaS_2$ and rGO-TiO_2 composite Z-scheme system.[48]	A 300 W xenon arc lamp with a UV-cut-off filter $\lambda \geq 420$ nm was used as light source. Pt-loaded $CuGaS_2$ and rGO-TiO_2 dispersed in water was exposed to that light.	⇒ The system was working for H_2 and O_2 evolution rate in a stoichiometric amount of H_2 and O_2 during 12 h of operation. ⇒ rGO acted as a conductive solid-state materials enhancing transferring of electrons between photocatalyst particles in a Z-scheme system for water splitting ⇒ The quantum yield was 1.3% under 380 nm
rGO/Fe_3O_4-ZnO.[49]	Solar simulator light was used as a light source. The catalyst was loaded on carbon *via* screen-printing then applied as a WE. While carbon was used as CE, and Ag/AgCl electrode used as reference electrode. 0.1 M KOH was used as an electrolyte.	⇒ Photocurrent density increased from 520 μA/cm^2 to 850 μA/cm^2 at 1.23V with the presence of rGO. ⇒ The photocatalyst showed wide absorption in UV and visible region. ⇒ The system has worked for O_2 evolution reaction. ⇒ Graphene acted as interfacial charge transfer process from the core-shell Fe_3O_4-ZnO and prevented the charge recombination.
rGO for passive membrane (rGO-BPMs.[50] (BPMs = bipolar passive membrane)	Solar simulator light was used as light source. The catalyst was spin coated on AEL-interfacial layer sheets. At high pH condition, the system was suited for OER while at low pH conditions the system was working for HER.	⇒ The system performed for either OER or HER depending on pH conditions. ⇒ rGO worked as an electrical junction resulting in enhancement of the electrical conductivity.
Ultrathin hematite films on FTO glass.[51]	300-W xenon lamp with a cut-pass filter ($\lambda > 420$ nm) was used as a light source. The catalyst performed as WE while Pt wire as CE, and an Ag/AgCl as a RE. 1.0 M NaOH was used as an electrolyte. External bias at +1.5 V *vs* RHE was applied.	⇒ rGO acted as a co-catalyst to enhance PEC water splitting and facilitate the efficient charge transfer resulting in lower charge recombination. ⇒ The system has worked for H_2 evolution reaction with H_2 rate 45 μmol/cm^2 during 4 h. ⇒ A photocurrent of 0.61 mA/ cm^2 *vs* RHE with IPCE reached 10.4%. The catalyst has wide absorbance in 300- 600 nm.
Au–rGO/N-rGO–TiO_2 composites. [52]	300 W xenon arc lamp w.s used as a light source, Cool air circulation was apllied to keep temperature constant. The catalyst was dispersed in aqueous solution in ethanol.	⇒ H_2 evolution rate reached 525 μmol/(g.h) ⇒ Maximum apparent quantum yield (AQY) was 2.47% and without a sacrificial agent the H_2 evolution rate was reached 22 μmol/gh and the AQY reached 0.1%. ⇒ rGO played a role as electrons transporter. ⇒ Wide visible absorbance between 500-650 nm regions. ⇒ Graphene served as a catalyst with nanogold and transfered electrons from gold directly to CB of TiO_2
ZnO nanowire arrays (NAs)/rGO/$ZnIn_2S_4$ heterojunction.[53]	Solar simulator was used as a light source. The catalyst performed as a WE. 0.5 M Na_2SO_4 used as an electrolyte and purged with N_2 prior to use. Pt wire and Ag/AgCl as a CE and RE respectively.	⇒ rGO acted as high electron mobility material enhancing the electron transfer, increased the active surface area, reduced the energy barrier for water splitting resulting in enhancing PEC performance. ⇒ Photon-to-hydrogen conversion efficiency was enhanced by 200 % compared to pristine ZnO. ⇒ Photocurrent density reached over 2.2 mA/cm^2 at 1 V vs Ag/AgCl and 1.41 mA/cm^2 at 0.5 V.

Cu–TiO_2(P25)–graphene ternary composite.[54]	Solar simulator was used as light source. The catalyst was used as WE. While Pt wire as CE, and Ag/AgCl as RE. Aqueous solution with ethanol was applied as an electrolyte.	⇒ The system worked for H_2 evolution with rate of 1.90 mmol/ g^1 ⇒ The composite has high degradation rate of methyl blue (MB) under the visible light . ⇒ rGO acted as e^- acceptor, inhibiting recombination by trapping electrons to promote charge separation. ⇒ Ti-C and TiO-C bonds that are formed narrowed the band gap energy of TiO_2 improving PEC effects.
rGO/Fe_2O_3 nanostructured photoanodes. [55]	450 W Xe lamp was used as light source. The catalyst films was deposited onto the FTO substrates and used as a WE. Ag/AgCl electrode and Pt were applied as RE and respectively. NaOH at pH 13.6 was used as the electrolyte.	⇒ With rGO, the photocurrent density increased from 0.56 to 0.82 mA/ cm^2 at 1.23 V_{RHE}. ⇒ rGO reduced the recombination reaction rate. ⇒ Wide light absorption from 400-800 nm. ⇒ rGO acted as an electron transfer channel.
TiO_2/rGO composites[56]	Simulated sunlight illumination was used. The catalyst was suspended in water then exposed to the light.	⇒ The visible absorption was wider with rGO. ⇒ The photocurrent increased to reach 0.826 mA/cm^2, which it was 3.5 times higher than pristine TiO_2. ⇒ The system has worked for H_2 with an evolution rate of 889.28 µmol/g^1h^1. ⇒ rGO acted as an electrons acceptor.
Graphene coatings on nanotextured silicon. [57]	Light with 100 mW cm^{-2} (1 sun) illumination was used as light source. Pt was applied as CE and SCE applied as RE, housed in a photochemical cell with a quartz window and NaOH solution performed as an electrolyte.	⇒ The system was effective for O_2 evolution reaction. ⇒ Photocurrent density was measured to be 35 mA cm^{-2}. ⇒ 3D texturing of Si electrode surface resulted in significant enhancement of the OER performance ⇒ The presence of rGO increased the stability of the catalyst against corrosion by 50 times. ⇒ rGO acted as a stable electron transmission route.
(Graphene nanosheets) GNS-V_2O_5-TiO_2 composite. [58]	Catalyst was dispersed in aqueous solution of acridine orange (AO) dye and irradiated with direct sunlight.	⇒ The photocatalyst exhibits an efficient photocatalytic activity and very high stability. ⇒ Graphene has been accepting and transferring electrons. ⇒ The catalyst has visible absorption from 400-550 nm. ⇒ The catalyst has successfully degraded AO pollutant under sunlight (water remediation) and suggested to be successful in water splitting.
rGO–CdS–polyoxometalate nanocomposite film.[59]	Solar light simulator was applied as light source. Photocatayst's film on the ITO electrode applied as WE. While Pt foil was applied as CE and (SCE) applied as RE. Finally, Na_2S solution used as the electrolyte.	⇒ rGO acted as charge separation and electrons transporting material. ⇒ The photocurrent density with rGO was increased to o 0.35 mA/cm^2. ⇒ High light absorbance between 380-525 nm was observed
Cu–Cu_2O–graphene nanocomposites. The catalyst prepared *via* simple reflux synthesis route.[60]	Sunlight simulator using xenon arc lamp (300 W) was used as light source. The catalyst was mixed with methanol and 1 mL of H_2PtCl_6 solution and then exposed to the light.	⇒ The catalyst obtained higher absorption especially in range (200-550) and (700-800 nm). ⇒ The system has worked for H_2 evolution reaction with H_2 rate reached 16.2 µmol /hg. ⇒ rGO acted as electrons acceptor and electron transfer agent and reduced the recombination of photogenerated electrons-holes .

G-*x*/Cu_2O/Cu nanowire arrays modified with an optimized concentration of graphene.[61]	Light of AM 1.5 (100 mW cm^{-2}) was used. Ag/AgCl was applied as a RE. While Pt wire as CE. 1.0 M Na_2SO_4 solution was used as an electrolyte.	⇒ The system exhibited a highest current density of 4.8 mA/ cm^2 among other controls samples. It was two times higher than pure Cu_2O at 0 V *vs* RHE. ⇒ The solar conversion efficiency reached 3.3% at external bias - 0.55 V. ⇒ The system was bifunctional for H_2 and O_2 evolution reaction. ⇒ The faradic efficiency for H_2 evolution rate was 74 %. ⇒ The Graphene in this system suppressed both the charge recombination a photocorrosion of the composite.
Amphiphilic block copolymer poly(isoprene-*b*-acrylic acid) (PI-*b*-PAA) immobilized on CdS nanoparticles.[62]	500 W Xenon lamp was used as light source. The catalyst added to an aqueous solution of 4-nitroaniline with N_2 bubbled to degassed O_2 then the system exposed to the the light.	⇒ The system works for H_2 evolution. ⇒ Wide visible absorption gained in rang 600-750 nm.. ⇒ rGO acted as donor–acceptor systems promoting electron-transfer process.
Anatase-graphene-rutile hetero junction structure.[63]	Light source was 300 W Xe arc lamp. The catalyst was dispersed in aqueous methanol solution with H_2PtCl_6. Then the system was exposed to the light.	⇒ The catalyst worked for H_2 production with H_2 rate reached 1.714 mmol/h. ⇒ Adding 2 % of graphene, resulted in the system reached its highest photocatalyst activity. ⇒ Graphene acted as electron charge transfer agent.
TiO_2 –V_2O_5 –C nanostructure grafted by N-doped graphene (GN–TV). [64]	The light source was 300 W Xe arc lamp. Hg/Hg_2SO_4 in K_2SO_4 saturated solution was employed as the RE and Pt rod applied as CE, the catalyst deposited on FTO and applied as WE. 0.2 M Na_2SO_4 at pH 6.8 was applied as electrolyte.	⇒ The system was working for H_2 and O_2 evolution. N atom doped GO is an excellent material with uniformly interconnected interfaces. ⇒ The catalyst has wide visible absorption up to 590 nm. ⇒ EIS spectroscopy showed that the catalyst has low resistance. ⇒ Graphene in this system was not only act as multi-dimensional channels for electron transport but also has good structural stability can prolong the life of the composite.
GNS–TiO_2 and GNS–ZnO nanostructures.[65] (GNS = graphene nano sheet).	The direct sunlight was used as the light source. Photocatalyst sonicated in water with Methylene Blue (MB) and exposed to the light.	⇒ The catalyst has visible absorbance between 500-700 nm. ⇒ The graphene acted as interfacial transfer material and enhanced the charge carrier for a better conductivity and higher catalytic activity, ⇒ The graphene decreased the rate of electron–hole pair recombination as well as played a part as co-catalyst. ⇒ The system has worked for MB degradation and considered as potential material for water splitting.
Graphene (G–TiO_2) composite films. [66]	400 xenon arc lamp with light equipped with a UV cut-off filter was used as a light source. Pt wire was applied as the CE, Ag/AgCl applied as RE. 1 M NaOH was used as an electrolyte solution.	⇒ Adding 1.0 wt. % of graphene resulted in the system showed highest photocurrent density (441 μA/cm^2). This photocurrent density was higher than pure TiO_2 films by tenfold. ⇒ The presence of graphene was to suppress the recombination reactions and enhance the photocatalytic activity. ⇒ The graphene acted as electron transfer agent reducing e^--h^+ recombination. ⇒ The system has worked for O_2 and H_2 evolution.

rGO-TiO_2 nanoparticles (np) composite.[67]	100 mW cm^{-2} illumination was used. The catalyst was applied as a WE. Pt foil was applied as a CE. SCE electrode applied as a RE. 0.5 M Na_2SO_4 was used as electrolyte. A bias of 1.0 V *vs* SCE was applied.	⇒ The system has worked for H_2 generation ⇒ Both photocurrent density of the catalyst and the hydrogen generation rate increased to reach 3.4 $mAcm^{-2}$ and 127.5 mmole cm^{-2}/ h respectively. ⇒ The graphene acted as electrons scavenger and conductor. ⇒ The presence of graphene increased the visible absorbance.
rGO/$Ag_{x-1}Zn_xO$ composite.[68]	Solar light simulator was used as light source. A solution of 0.1 M NaOH was used as an electrolyte. Pt wire mesh as CE. Ag/AgCl as the RE. The catalyst was applied as WE. External bias of 0.8 V *vs* Ag/AgCl was applied.	⇒ Wide visible absorbance gained in range 400- 800 nm. ⇒ The photocurrent density increased to reach 2.48 mA/cm^2 at 0.8 V *vs* Ag/AgCl. ⇒ The graphene acted as an electron conductor transfer material, improved the charge separation and enhanced photocatalytic activity.
Au loaded on graphene and TiO_2 surface .[69]	Irradiation by high-pressure Hg lamp in the UV-visible region, the catalyst dispersed in aqueous methanol solution then exposed to the light.	⇒ The system was working for H_2 generation with the rate of 1.34 mmol /h^1 while pristine TiO_2 produced only 0.56 mmol /h^1 ⇒ The graphene in this system suppressed charge recombination reaction and accepted and transported the electrons from the excited semiconductor improving interfacial charge transfer processes, ⇒ The graphene provided much more active adsorption sites and photocatalytic reaction centres ⇒ The visible absorbance increased in range 400-650 nm.
Ta_2O_5/graphene composite. [70]	Ultraviolet irradiation *via* Xe lamp with cut off filter (200-400 nm) was used as light source. The catalyst dispersed in methanol and then exposed to the light.	⇒ The system works for H_2 evolution with a rate up to 30 mmol/ (g. h). ⇒ An apparent quantum efficiency of 33.8% at 254 nm. ⇒ The photocatalyst was durable over 5 h. ⇒ The graphene acted as interfacial charge transfer material and suppressed the recombination reactions.
Ag-TiO_2-graphene ternary nanocomposites.[71]	Xenon lamp was used as the light source. The catalyst was dispersed in aqueous solution that contains ethanol /H_2O solution. Prior to experiment, the solution was bubbled with N_2 gas and then exposed to the light.	⇒ The visible light absorption increased at 400- 800 nm range. ⇒ The system works for H_2 evolution with at rate 2.12 mmol/g. ⇒ The graphene improved the lifetime of the electrode and photo-generated electron-hole pairs and faster interfacial charge transfer rate.
ZnS/graphene/MoS_2 nanocomposite.[72]	300 W Xe lamp irradiation was used as light source. The catalyst was dispersed in aqueous solution of 0.005 M Na_2S and 0.005 M Na_2SO_3 and then the system exposed to the light.	⇒ The catalyst worked for H_2 evolution with a rate of 2258 μmol/ (h.g) ⇒ The photocurrent density of this catalyst reached 10 mA/cm^{-2} at a small overpotential of merely 0.366 V. ⇒ A small Tafel slope of ~40 mV/dec was obtained. ⇒ The graphene served as an excellent electron acceptor and transporter.
Pt/rGO–$BiVO_4$ composite.[73]	Solar light simulator. Pt gauze applied as a CE, Ag/AgCl electrode applied as RE and thin film of the catalyst as WE at 0.6 V *vs* NHE. 0.2 M Na_2SO_4 adjusted at pH 7 buffered solution was used as an electrolyte.	⇒ The maximum photocurrent value reached 200 μA/ $cm^{2.}$ ⇒ The rGO acted as electrons conductive channel (accepts and transfer electrons). ⇒ The system works for water oxidation (evolution O_2).

CeO_x/G Nanoparticulate.[74]	Sunlight simulator was used as an electrolyte. The catalyst dispersed on aqueous $AgNO_3$ and then exposed to the light.	⇒ The system works for O_2 evolution with rate reached up to 9 µmol during 240/ min. ⇒ The photocatalyst activity of this catalyst exhibits 3 times higher than commercial ceria. ⇒ The graphene role in this system was to increase the photocatalytic efficiency *via* prolong the lifetime of photogenerated electron-holes pairs.
Graphene–$Zn_xCd_{1-x}S$ composites.[75]	Sunlight simulator was used as light source. The catalyst dispersed in mixed Na_2S and Na_2SO_3 as an electrolyte, prior to use bubbled with N_2 to remove dissolved O_2.	⇒ The system worked for H_2 evolution reaction with H_2 rate reached 1.06 mmol $/h^1$ g^1. ⇒ Apparent quantum efficiency reached 19.8 %. ⇒ The visible absorption increased especially between 550-800 nm. ⇒ The photocurrent density reached up to 0.05 mA/cm^2. ⇒ The catalyst was stable over 14 h. ⇒ The graphene has an efficient role in transferring of the photogenerated charge carriers resulted in enhancing photocatalytic activity for H_2 production.
Porous $Zn_{0.5}Cd_{0.5}S$ nano sheets /rGO composites.[76]	Light source was Xe lamp of 300 W with a UV cut-pass filter (λ > 420 nm). Pt foil applied as CE and (SCE) applied as RE. The photocatalyst was casted on ITO glass and applied as WE. A solution of 0.1 M Na_2S and 0.1 M Na_2SO_3 applied as the electrolyte. Bias of 0.6 V *vs* SCE was applied.	⇒ The system has worked for H_2 production with a rate of 12.05 µmol/ (h.cm^2)and has high stability. ⇒ The photocurrent reached around 0.3 mA/cm^2.It was 7 times higher than pure $Zn_{0.5}Cd_{0.5}S$. ⇒ The EIS spectroscopy showed smaller resistant activity in comparison with the catalyst. ⇒ The rGO accepts and transfers electrons. ⇒ Adding 5 wt% of rGO resulted in showed highest photocatalyst activity with 7 times higher than pristine $Zn_{0.5}Cd_{0.5}S$.
G@MnO_2 NWs. [77]	SCE electrode applied as the RE, Pt foil applied as CE. The catalyst was mixed with Nafion, deposited on GC, and applied as the WE. A solution of 1 M KOH and 0.25 M K_2SO_4 solutions as the electrolyte. No light was used.	⇒ The maximum current density of this catalyst reached 5.9 mA/ cm^2 which it was 1.8 times higher that of the commercial Pt/C catalyst. ⇒ TOF value increased to 0.017/ S at 0.44 vs. SCE. ⇒ The system works for water oxidation. ⇒ The graphene acted as charge transport as well as enhanced stability and dispersion of MnO_2 nanostructures.
α-Fe_2O_3/GIO electrode.[78] (GIO = graphene inverse opal)	Solar light simulator applied as light source. Potential range between 0.6 to 2.0 V *vs* RHE. Ag/AgCl electrode and a Pt mesh were used as RE and CE respectively. 1 M NaOH solution was used as an electrolyte	⇒ The photocurrent density increased to 1.17 mA/cm^2 at a bias of 1.5 V *vs* RHE. It was higher by 1.4 times than α-Fe_2O_3. ⇒ The EIS spectroscopy showed that the catalyst has low resistance with 36 Ω due to the high conductivity of the catalyst. ⇒ A high visible absorbance between 550-750 nm. ⇒ The graphene accepts and transfers electrons. ⇒ IPCE exhibits maximum value of 42% at 320 nm.

TiO_2 nanotubes (NTs) modified with electro chemically reduced graphene oxide (ErGO). [79]	500 W xenon lamp was used as light source. The catalyst was applied as WE. 1 M KOH was used as an electrolyte, N_2 was purged prior to experiment. The photo electrode, a SCE and twisted Pt wire acted as the WE reference and CE electrode respectively.	⇒ The maximum photocurrent density reached 1.44 mA/ cm^2 at 1.23 V *vs*. RHE. It was higher than pure TiO_2 NP by 1.4 times. ⇒ A wide visible absorption between 400-800 nm. ⇒ The system works for both H_2 and O_2 evolution. O_2 rate reached 70 µmol during 250 min and H_2 rate reached 52.80 µmol/h. ⇒ The photocatalyst had higher stability. ⇒ rGO acted as electron charge transfer agent. ⇒ The EIS spectroscopy revealed that the ErGO–TiO_2 NTs electrode has a smaller semicircular diameter than other control samples. Which means it was more conductive and better catalytic activity.
VS_4/reduced graphene oxide (VS_4/rGO) composites. [80]	The light source was 500 W Xe lamp equipped with filter to remove UV. The catalyst was dispersed in water had 0.35 mol/ L Na_2S and 0.25 mol/L Na_2SO_3 as electrolyte and then exposed to the light.	⇒ The system works for H_2 production with rate reached about 0.7 mmol /L . ⇒ The rGO in this system suppressed the recombination reaction and accelerated of VS_4 nucleation. ⇒ A wide absorbance from 400-660 nm.
TiO_2–rGO thin film. [81]	150-W halogen lamp was used as the light source. Ag/AgCl applied as the RE and a Pt wire applied as CE. The catalyst film was used as the WE. A solution of Na_2SO_4 was acted as the electrolyte.	⇒ The maximum photocurrent increased to reach 80 µA while pure TiO_2 reached barely 13.1 mA/cm^2. ⇒ The film has better stability after 1000 voltametric cycles in Na_2SO_4 electrolyte. ⇒ The rGO acted as electron transparency material and minimized the charge recombination process. ⇒ The catalyst that had 5 % wt. of rGO exhibited the highest H_2 activity than other ratios.
$La_2Ti_2O_7$/graphene nanocomposite. [82]	500 W Xe lamp was used as source of light. The catalyst was suspended in aqueous solution that contains methanol. Then the cell exposed to the light source.	⇒ The UV-visible absorbance increased in range 300-800 nm. ⇒ The system has worked for H_2 evolution with the highest rate reached over 60 µmol/g^1h^1 (catalyst had 5% wt. of graphene). ⇒ The Graphene transferred the photo-generated electrons and prolonged lifetime of the charge carriers resulted in enhancing photocatalytic effect of H_2 production. ⇒ The EIS results showed that the catalyst has smallest charge transfer resistance, which meant it was more conductive
$NaTaO_3$ loaded with 0.2 wt% Au and rGO. [83]	150 W medium pressure mercury lamp was used as light source. The catalyst was suspended in a solution of (H_2O: MeOH) and Au (from dissolved H $[AuCl_4]\cdot 4H_2O$) then exposed to the light source.	⇒ The system works for H_2 evolution reaction higher by 28 than others such as pure $NaTaO_3$ or $NaTaO_3$ ⇒ H_2 evolution rate higher by 41 times than that of the $NaTaO_3$. ⇒ The rGO facilitated transfer of electrons and also acted as co-catalyst for H_2 evolution.
GO wrapped Ag_3PO_4 sub-micro particles. [84]	500 W Xenon lamp equipped with a 420 nm cut-off filter was used as light source. The catalyst were dispersed in an aqueous solution that has Methyl Orange (MO) dye and exposed to the light.	⇒ Increased light absorption till 520 nm. ⇒ The system has successfully worked for MO degradation and suggested to be useful for water splitting. ⇒ The Graphene acted as super electron acceptor.

rGO/TiO_2 nanowire microsphere composites. [85]	500 W Xe lamp was used as light source. The photo catalyst dispersed in aqueous methanol had $H_2PtCl_6.6H_2O$. Then the cell purged with N_2 and exposed to the light source.	⇒ The system works for H_2 evolution with rate reached 43.8 µmol /h which is 1.6 higher than pristine TiO_2. ⇒ The UV-visible light absorption had increased till 460 nm. ⇒ The rGO in this system was accepting and transferring electrons.
Fe_2O_3– graphene nanoplates (GNP). [86]	Solar light simulator was used as light source. The catalyst used as WE. SCE electrode was applied as RE, Pt mesh was applied as CE. 1 M NaOH was used as an electrolyte.	⇒ The photocurrent density increased up to 2.5 mA cm^{-2} at 0.75 V *vs* SCE. ⇒ The visible absorbance was increased in range 500-750 nm. ⇒ The Graphene role was as an electron transport pathway and reduced the recombination reaction. ⇒ The solar to H_2 conversion efficiency reached 1.8 % at 0.75 V *vs* SCE. ⇒ The EIS showed that the catalyst has the lowest charge resistance at 177.3 Ω cm^2.
GO-(Ta_2O_5) hybrid. GO [87]	A xenon arc lamp (300 W) with cut off-filter at λ> 400 nm. The catalyst was dispersed in aqueous solution that has $AgNO_3$ as a sacrificial agent and then it was exposed to the light.	⇒ The system works for H_2 evolution with rate of 140 µmol/h. ⇒ The photocatalytic activity increased by 35 times than pristine Ta_2O_5. ⇒ The Graphene was accepting and transferring electrons.
NiTi-double layered hydroxide (NiTi-DLH) nanosheets to the surface of (rGO) (NiTi-DLH/rGO) catalysts.[88] (DLH= double-layer hydroxide)	300 W Xenon lamp. Photocatalyst film acted WE Pt wire and as Ag/AgCl electrode were applied as CE and RE respectively. A solution of (0.01 mol/L $LiClO_4$ was used as the electrolyte.	⇒ The system work for O_2 evolution with a rate of 1.968 mmol/ (g.h). ⇒ Adding rGO enhanced the visible absorption. ⇒ Apparent quantum efficiencies reached 61.2 % at 500 nm. ⇒ The rGO served as an electron acceptor with an accelerating carrier mobility.
SiC-graphene composite.[89]	300 W Xe lamp (λ>420 nm filter) was used as light source. The catalyst dispersed in distilled water and then exposed to the light.	⇒ Increased visible light absorbance. ⇒ The graphene was accepting and transferring electrons. ⇒ The system has worked for H_2 evolution with H_2 rate reached 87.52 µL/(g.h). ⇒ The system was stable till 12 h.
ZnSe·xN_2H_4/GS and (ZnSe/NGS) nano composites.[90] (GS = Grapghene sheet)	500W Xe arc lamp equipped with a UV cutoff filter (λ < 400 nm) was used as light source. The catalyst was diapered in MB dye solution and then exposed to the light.	⇒ A high visible absorption especially at range of 570-700 nm. ⇒ The system works for O_2 evolution reaction. ⇒ The graphene sheet (GS) acted as an electrons acceptor and transfer material
GQD/CdS/TiO_2-NAs (NAs = arrays).[91]	300 W Xenon lamp was used as the light source. The catalyst performed as WE, Pt foil was applied as CE, Ag/AgCl electrode was applied as RE. Mixture solution of 0.1 M Na_2S and 0.1 m Na_2SO_3 acted as a sacrificial reagents. .	⇒ The visible absorption was improved. ⇒ The system works for H_2 evolution reaction with rate of 18.3 µmol/ h. While the control sample CdS/TiO_2-NA exhibited around 14 µmol/ h^1. ⇒ Graphene played a role in charge transferring and separation. ⇒ The light visible absorbance increased in range 500-600 nm.
(GQDs) functionalized ZnO (GQDs@ZnO NWs). [92]	Solar light simulator was used as light source. The PEC cells performed with two electrodes. The catalyst was applied as WE and Pt plate as the CE. A solution of 0.5 M Na_2SO_4.	⇒ The system was working for both O_2 and H_2 evolution. ⇒ IPCE of the photocatalyst without any bias was 0.42% at 450 nm. Increased to 3.18% with an applied bias of 0.6 V, ⇒ The graphene here acted as a dye sensitized solar cell. ⇒ The H_2 evolution rate obtained 2.13 µmol / h.

CuO/TiO_2-GR. [93]	500 W Xe arc lamp was used as light source. The catalyst was dispersed in methanol and exposed to light.	⇒ The system works photocatalyst for H_2 evolution with a H_2 rate of 905.60 µmol/ (h.g). It was higher by 20.2 times higher than pure TiO_2. ⇒ A higher visible absorption obtained in range in rang 400 -800 nm. ⇒ The Graphene accepted and transferred electrons.
Titanate nanotube /graphene (TNT)/GR) photocatalyst.[94]	300 W Xe-lamp as the source of light. The catalyst was dispersed in water: methanol then it was exposed to the light.	⇒ The system works for H_2 generation with rate reached 12.1 µmol/h. It was higher by 4 times than TNT alone. ⇒ The visible absorption increased in range 400-800 nm. ⇒ The rGO acted electron-transport material due to its superior electrical conductivity, which can transfer/accept electrons efficiently.
CuInZnS-decorated graphene nanosheets.[95]	800 W Xe-Hg lamp as light source. The catalyst dispersed in 0.2 M Na_2SO_3 and 0.1 M Na_2S that served as sacrificial reagents and then it was exposed to the light.	⇒ The system works for H_2 evolution with rate of 3.8 mmol/ (h. g). It was 1.84 times higher than pure CuInZnS ⇒ The Graphene acted as supporting layer for CuInZnS nanospheres, reduced the charge recombination, enhanced the interfacial charge transfer and increased photocatalytic reaction sites. ⇒ The absorbance increased in the range 400 -700 nm.
α-Fe_2O_3 on the graphene /FTO.[96]	Solar light simulator was used Pt wire and Ag/AgCl as CEr and RE respectively. A solution of 1 M NaOH as the electrolyte	⇒ Maximum photocurrent density reached to 4 mA/cm^2. ⇒ The EIS study showed less charge transfer resistance for the catalyst around 100 Ω. ⇒ The visible absorbance was up 600 nm. ⇒ IPCE was 12.5 % at 500 nm. ⇒ H_2 and O_2 gases were not analysed in this study. ⇒ The Graphene in this provided a channel for electron transferring and reducing the recombination reactions.
$RuO_2/TiSi_2$/graphene composite.[97]	Solar light simulator was used. The catalyst dispersed in water. Then system was de-aerated by bubbling argon and exposed to the light. For electrochemical measurements an aqueous of Na_2SO_4 solution (pH = 7) was used as electrolyte and Pt and SCE as CE and RE and the catalyst loaded on ITO as the WE.	⇒ The system has worked for H_2 evolution with H_2 rate of over 65 µmol during 5 h. ⇒ The photocurrent increased to 0.4 $\mu A/cm^2$ when ⇒ The Graphene accepted and transferred electrons. ⇒ The EIS confirmed a low charge resistance by the catalyst and better photocatalytic activity than other control films.
GO/SiC composite.[98]	300 W Xe arc lamp with cut-off at λ> 400 nm was used as the light source The catalyst was dispersed in aqueous solution that had 0.3 mol KI as a sacrificial reagent..	⇒ The system works for HER with H_2 evolution rate reached up to 95µL/h with 1% Wt of GO. It was higher by 1.3 times pristine SiC (NP). ⇒ The Graphene acted as electron collector and transporter.
α-Fe_2O_3 Nanorods /GO $BiV_{1-x}MoO_4$ Core/Shell Heterojunction Array.[99]	Solar light simulator. Pt foil acted as CE, and Ag/AgCl electrode as RE.0.01 M Na_2SO_4 purged with N_2 was used as electrolyte.	⇒ Photocurrent density of ~1.97 mA/cm^2 at 1 V *vs* Ag/AgCl ⇒ The photoconversion efficiency of ~0.53% at - 0.04 V *vs* Ag/AgCl. ⇒ The visible absorption enhanced in range 400-600 nm.
$[Ru(bipy)3]^{2+}$ @GO.[100]	The catalyst was irradiated using a λ=532 nm laser. The catalyst was dispersed in water / methanol solution then it was exposed to the light source.	⇒ The maximum photocurrent reached 0.3 mA/cm^2 ⇒ The system works for H_2 evolution with rate of 3290 µmol/ (h. g). ⇒ Graphene works as a photocatalyst. ⇒ The visible range absorbance increased up to 700 nm.

rGO-$Zn_{0.8}Cd_{0.2}S$. [101]	Solar light simulator. The photocatalyst was dispersed in aqueous solution that has 0.35 M Na_2S and 0.25 M Na_2SO_3 and it was exposed to the light.	⇒ The system works for H_2 evolution with rate reached 1824 µmol/ (h.g). ⇒ Apparent quantum efficiency of 23.4% at 420 nm. ⇒ The photocurrent reached over 0.8 mA/cm^2. ⇒ The rGO acted as excellent support material for the catalyst $Zn_{0.8}Cd_{0.2}S$ and excellent electron collector and transporter.
G/CdSe.[102]	Solar light simulator was used. The catalyst was suspended in mixture solution of 0.1 M Na_2S and 0.1 M Na_2SO_4. The system was purged with N_2 then exposed to the light source.	⇒ The system works for H_2 evolution with rate reached 5.35 µmol/h. ⇒ The Graphene increased mobility of electrons through the system. ⇒ The visible light absorbance increased in range 550-750 nm.
rGO-CdS@TaON composite.[103]	Visible light irradiation was used as light source. The catalysts was dispersed in 0.1 mol/L Na_2S and 0.04 mol/L Na_2SO_3. Then system was purged with Ar and exposed to the light source.	⇒ The system works for H_2 evolution with rate reached 633 µmol/ h. ⇒ The rGO provide high charge carrier mobility. ⇒ The apparent quantum efficiency reached 31% at 420 nm that equals to 141 times higher than that of pristine TaON crystal. ⇒ The visible absorbance increased in the range 550 -800 nm.
rGO-CdS-Pt nanocomposites.[104]	400 W high-pressure Hg lamp was used as the light source. The catalyst was suspended in an aqueous solution of ethanol. The system was deaerated by N_2 gas purging prior to expose to the light.	⇒ The system works for H_2 evolution with rate of 123 mol/ (h. g). ⇒ The catalyst was stable for 16 h. ⇒ The rGO accepted and transferred electrons resulted in enhance of photocatalytic effect. ⇒ The rGO stabled the catalyst against photocorrosion and prolonged the lifetime of electron – hole pairs.
TiO_2(P25)/GS composite photocatalysts.[105]	500 W Xe lamp was used as the light source. The catalyst was suspended in 0.1 M Na_2S and 0.04 M Na_2SO_4. The system was deaerated with N_2 before exposed to the light.	⇒ The system works for H_2 evolution with rate of 5.4 µmol/ h. It was 1.6 times than TiO_2 ⇒ Graphene enhances excellent electron transfer and conductivity of system. ⇒ Adding GS resulted in better dispersion of TiO_2 catalyst which improve H_2 performance activity.
rGO:$MnFe_2O_4$.[106]	100 watt Hg lamp has cut UV cut off filter was used as light source. The nano composite was act as WE while SCE and Pt plate were used as RE and CE respectively. 0.2 M Na_2SO_3 and 0.1 M Phosphate buffer solution (pH 6.9) was used as an electrolyte.	⇒ The ratio 1:1 rGO: Mn has recorded the highest photocurrent of 0.760 mA/cm^2 with quantum efficiency reached 29 %. ⇒ O_2 and H_2 evolution rates were ordinary stoichiometric evolved for 10 h. (H_2 evolution rate was 0.168 mmol/h while O2 evolution rate was 0.080 mml/h)) ⇒ The increase of rGO ratios resulted in enhanced the absorption especially between 400-800 nm. ⇒ The rGO suggested to work as electron acceptors resulting an of increase charge transfer.
Graphene-Mo_2C rods.[107]	The catalyst was mixed with isopropanol and Nafion. Then a drop was placed on a GC as WE while Ag/AgCl electrode and graphite rod were applied as RE and CE respectively. 0.5 M H_2SO_4 was used as an electrolyte.	⇒ The system was work for H_2 evolution reaction. The current density increased to 125 mA /cm^2 at 400 mv *vs* RHE. ⇒ The system has long stability reached 15 hrs. ⇒ A low Tafel slope of 67 mV/dec was observed. The rGO has a high catalytic activity support hydrogen evolution reaction. ⇒ Adding rGO increased the electrical conductivity of the catalyst.

TiO_2/rGO/Sb_2S_3 electrode. [108]	Light source 300 Watt Xenon lamp. The composite deposited on FTO and performed as WE while Ag/ AgCl electrode and Pt performed as RE and CE respectively. 0.5 M Na_2SO_4 at pH 7 acted as an electrolyte.	⇒ The Maximum photocurrent increased to (0.96 mA/cm^2) compared to 0.75 and 0.15 mA/cm^2 for TiO_2/Sb_2S_3 and TiO_2 respectively. ⇒ Adding rGO layer has an important role on the conductivity of the system and provides two-dimensional bases for Sb_2S_3 network growth. ⇒ TiO_2/rGO/Sb_2S_3 has wide visible absorbance until 750 nm.
MoS_2/sulfur and nitrogen co-doped reduced graphene oxide (SNG).[109]	An amount of composite was mixed with Nafion and water-ethanol and drop catting onto a GCE. 0.5 M H_2SO4 performed as electrolyte and Ag/AgCl electrode and Pt foil were performed as RE and CE respectively. No light used.	⇒ The system was work for HER only. ⇒ The current density increased to 33.5 mA/cm^2 at 0.3 V. It was almost two times than MoS_2/rGO. A low Tofel slope achieved of 45 mV/dec. ⇒ The catalyst was stabile even after 1000 cycles. ⇒ When S and N atoms incorporated into graphene networks, the conductivity dramatically increased.
3D porous rGO-TiO_2.[110]	Light source was 300WXe lamp. The composite was spin coated on ITO and perfumed as WE. 0.1 M KH_2PO_4 adjusted to pH 7 was used as an electrolyte. Ag/AgCl electrode and Pt performed as RE and CE respectively.	⇒ The composite yielded highest photocurrent density of 2.59 mA/cm^2 at a low bias of 0.6 V *vs* Ag/AgCl. ⇒ The solar to hydrogen conversion efficiency of 0.5%. ⇒ The role rGO was electron transport *via* multi-channel conductive network. ⇒ Absorbing incident light *via* photocatalyst had been increased.
$FeSe_2$/GO composite.[111]	The sample loaded on GCE and used as WE. Ag/AgCl electrode and Pt performed as RE and CE respectively. 0.5 M of H_2SO_4 electrolyte was used as an electrolyte. Light source was 300WXe lamp.	⇒ The system was Electrocatalyst works for HER by water splitting. ⇒ A high cathodic current density reached up to 9.68 mA/cm^2 at -250 mV. ⇒ A low Tafel slope of 64 mV/dec if compared to pure $FeSe_2$ and other composite electrocatalysts. ⇒ The system is cheap alternative to the noble material for clean energy. ⇒ The composite had high synergistic effect towards HER activity due to the electrochemical active sites and low charge transfer resistance that provided *via* the synergetic effect of rGO.
Au@rGO/rNGO-LaNi-LDH composite.[112]	The nanocomposite catalyst was applied as WE. Pt and Ag/AgCl electrode were applied as RE and CE respectively 0.5 M H_2SO_4 was applied as an electrolyte. The sample loaded on GCE and Ag/AgCl electrode and Pt performed as reference and counter restively.	⇒ The system works for H_2 evolution. ⇒ The exchange current density increased to 10 mA cm^2 reported at onset potential of – 0.80 mV *vs* RHE ⇒ The result confirmed the stability of the electrocatalyst for HER after 1000 cycles and 120 hrs working. ⇒ The rGO increased the accessible active sites for H_2 evolution activity. ⇒ A small Tafel slope of 60 mV/ dec was achieved for generation reactions.
rGO loaded on $LaFeO_3$ nano sphere.[113]	Light source was 125 W medium pressure Hg visible lamp ($\lambda \geq 420$ nm). Photocatalytic activity was studied in a batch reactor include; mixing the photo- catalyst with ethanol for HER or $AgNO_3$ for OER solution for study H_2 or O_2 evolution.	⇒ The hydrogen evolution rate has increased by loading 1% Wt of rGO to reached 611.3 mmol/(h.g) similarly oxygen evolution rate increased up to 316.24 mmol/ (h.g). ⇒ The rGO had a super interfacial interaction with the $LaFeO_3$ nano sphere enhanced the photogenerated charge carrier and also as played a role as an electron sink. ⇒ The visible absorbance increased in range 400-460 nm. ⇒ Loading 1 wt. % of rGO resulted in the system exhibited highest stability of the photocatalyst nanostructured.

rGO-M_O, rGO-TiO_2, rGO-ZnO and rGO-CeO_2.[114]	300 Xenon lamp source. An amount of the photocatalyst was dispersed on methanol and the suspension purged with N_2 before exposed to the light.	⇒ The system was work for H_2 evolution reaction only. ⇒ The visible absorbance increased especially in range 560 -610 nm. ⇒ The highest H_2 production gained 1200 µmol/(h.g) from rGO-TiO_2 photocatalyst and the lowered H_2 production gained 120 $\mu mol/h^1g^1$ *via* rGO-GeO_2. ⇒ rGO played role as photocatalyst, minimized the charge recombination and increased lifetime of the photogenerated charge carriers.
Au/rGO/hydrogenated TiO_2 nano tube arrays Au/ rGO/H-TNTs).[115]	Xe lamp 300 watt equipped with optical filter ($\lambda \geq 400$ nm) was used as light source. Platinum foil and Ag/AgCl electrode applied as CE and RE respectively. External bias of 1.23 V *vs* RHE was used. 1 M KOH was used as an electrolyte.	⇒ The system works for H_2 and O_2 with stoichiometric evolution ratios of 2: 1.(H:O). ⇒ The photocurrent density reached 224 $\mu A/cm^2$ higher than pristine H-TNTs. ⇒ The rGO played excellent electron transport and reduced the recombination reaction. ⇒ The light absorbance increased in range 450-700 nm. ⇒ The value of IPCE reached 5.8% at 580 nm.
GO/ZnO triangles.[116]	360-nm UV light illumination was used as light source. 1 M NaOH acted as an electrolyte. Ag/AgCl and Pt mesh as RE and CE respectively. The composite loaded on Copper foil as WE.	⇒ The system was work for O_2 evolution reaction. ⇒ The photocurrent density increased to 1.5 mA/cm^2 at 1.45 V *vs* RHE. ⇒ IPCE reached 10.4% at 360 nm, which it was 3.3 times higher than pristine ZnO. ⇒ The GO surface played crucial role in formation of oxygen vacancies in the ZnO nanocomposites which resulted in enhance OER activity.
P25–rGO–Co.[117]	250 Watt high pressure mercury lamp as a source of light was used as light source. Photocatalytic experiments sampled in Sealed quartz flask (150 mL) with a flat window. For HER the catalyst dispersed in ethanol-aqueous solution while in O_2 OER the catalyst dispersed in a solution has $AgNO_3$ and La_2O_3	⇒ Both evolutions rates of H_2 and O_2 were increased up to 190 and 80.8 µmol/h respectively. ⇒ The visible absorbance enhanced in range 400- 800 nm. ⇒ Graphene acted as catalytic reaction and enhance photogenerated charge carrier separation.
NiS_2/rGO. [118]	The catalyst dispersed in Nafion and isopropanol solution and loaded on GCE and then it was applied as WE. 0.5 M H_2SO_4 was used as electrolyte. Ag/AgCl and graphite rod were used as RE and CE respectively.	⇒ The system has worked for H_2 evolution reaction. ⇒ The current density increased to 10 mA cm^{-2} at −200 mV *vs* RHE. ⇒ A slow Tafel slope of 52 mV/dec was obtained. ⇒ The rGO acts as excellent medium for transporting electrons.
rG/Cu_2S/rGO/GO.[119]	100 watt xenon lamp was used as light source. Ag/AgCl and Pt foil as RE and CE respectively. ITO which contained the nanofilms as WR. 0.1 M Na_2S was used as an electrolyte.	⇒ The film was resisting the photocorrosion for more than 20 LSV cycles. ⇒ Maximum photocurrent of 1.8 mA/cm^2 was achieved at 0.16 V ⇒ The rGO accepted and transferred electrons.

MoSSe@rGO heterostructures.[120]	The catalyst was loaded on Glassy carbon disk and performed as WE while Ag/AgCl electrode and a Pt mesh applied as RE and CE respectively. 0.4 M H_2SO_4 performed as an electrolyte.	⇒ Maximum current density reached 5mA/cm^2 at only 135 mV. ⇒ A low Tafel slope was obtained of 51 mV / dec. ⇒ The rGO act as excellent electrically conductive performer. ⇒ The catalyst was durable for more than 5000 LSV cycles.
Fe_2O_3/ITO nanowire arrays wrapped with rGO.[121]	Solar light simulator was used as light. The catalyst was applied as WE. While SCE and Pt foil were applied as RE and CE respectively. 1 M NaOH at pH 12.8 was applied as electrolyte.	⇒ Maximum photocurrent density reached to 5.38 mA/cm^2 at 0.6 V *vs* SCE. It was higher ITO@Fe_2O_3 and Fe_2O_3 by 3.5 and 10 times respectively. ⇒ The visible light absorbance enhanced in range 400-60 nm. ⇒ The IPCE reached around 6 % at 500 nm in a 0.4 V *vs* SCE while photon-to-current efficiency (ABPE) reached 1.13% at 0.89V *vs* RHE. ⇒ The rGO worked as electrocatalyst and excellent electron transport ability.
rGO-TiO_2 composite [122]	300 W Xe arc lamp as a source of light. The catalyst was part of Z-scheme for O_2-evolving combined with hexagonal - and trigonal-$CuLi_{1/3}Ti_{2/3}O_2$ loaded Pt	⇒ The O_2 and H_2 gas evolution were stoichiometric ratios reached around 4.5 µmol/h and 0.75 µmol/h respectively. ⇒ The rGO played as an electron mediator
Co/Co_9S_8@S,N-doped porous graphene sheets..[123]	The catalyst was treated with alumina and then dispersed with Nafion and ethanol then it was loaded on GC and performed as WE. Ag/AgCl electrode and Pt performed as RE and CE respectively. 0.1 M KOH saturated with N_2 gas was applied as an electrolyte.	⇒ The system was works for O_2 and H_2 evolution. ⇒ The O_2 evolution rate reached 22.5 µmol/h while H_2 evolution rate reached 292.2 µmol/ h at 1.58 V *vs* RHE. ⇒ In OER study, the maximum current density reached 10 mA/cm^2 at 290 mV and in HER study the reached 20 mA/cm^2 at 350 V *vs* RHE ⇒ The composite exhibits highest surface area of 249.6 m^2/g after treatment with graphene oxide. ⇒ The GO was rich with O-atom functional groups used as substrate to adequately adsorb Co^{+2}. ⇒ The synergetic effects of S and N atoms in graphene sheet enhanced its properties as dual organic ligands assembled Co^{+2}
MoS_2/rGO/PPD/O-MW-CNT.[124]	The catalyst dispersed with nation and ethanol then loaded on GCE. Then it was applied as WE. SCE and Pt slice were performed as RE and CE respectively. 0.5 M H_2SO_4 as an electrolyte.	⇒ The current density increased to 47.6 mA/cm^{-2} at 200 mV. ⇒ The catalyst showed excellent stability during 1000 cycles in CV. ⇒ A low Tafel slope of 48 mV/dec was achieved. ⇒ The role of rGO participated with O-MWCNT to increase electron transport and conductivity.
Si/CNT/GO. [125]	The photocatalyst was applied as WE. Pt wire and Ag/AgCl electrode (saturated) were applied as CE, and RE, respectively. 1 M KOH as an electrolyte.	⇒ The system has worked for O_2 evolution. ⇒ The Photocurrent density raised to 1.2 mA/cm^2 at 1.73 V versus ⇒ The GO played both protected CNT film in the catalyst and acted as a hole exchange layer with the electrolyte. ⇒ The CV study showed that adding GO and CNT enhanced the performance of the photocatalyst by double. ⇒ In CV, the system was work also for OER in H_2SO_4 solution and the photocurrent reached 2 mA/cm^2 at 1.8 V *vs* RHE.

TiO_2-GO heterostructures.[126]	300 W xenon was used as light source. The catalyst dispersed in methanol solution then chloroplatinic acid hexa hydrate and aqueous solution contained Pt were added to final solution. Then the cell exposed to the light source.	⇒ The system works for HER with H_2 evolution rate H_2 reached rate up to 16 mmol/(h.g). ⇒ The quantum efficiency reached 1.84 % at 405 nm. ⇒ The GO/rGO enhances charge transportation and depresses recombination of electron−hole pairs. ⇒ The visible absorbance increased in range 500-800 nm.
TiO_2/rGO composite films.[127]	An Oriel Xe (Hg) 250 W lamp was used as light source. The catalyst loaded on FTO and performed as WE while Ag/AgCl electrode and Pt wire as RE and CE respectively. 0.5 M H_2SO_4 was acted as an electrolyte.	⇒ Photocurrent density increased to 0.20 mA cm^{-2} at 1.23V *vs* RHE. It was higher if compared with pristine TiO_2 (0.11 mA/cm^2). ⇒ The rGO accepted and transferred electrons with more efficiency. As well as increased photogenerated charge lifetime.
Soft-oxometalate (SOM)[Na_{17} [Mn_6 $P_3W_{24}O_{94}$ $(H_2O)_2$].43H_2O@GO.[128]	UV lamp (λ max = 373 nm) was used as light source. The composite as prepared in dispersion put in closed system with N_2 purging and then exposed to light to detect O_2 gas *via* optical sensor.	⇒ The system works for OER. ⇒ Apparent quantum yield was 16.6 % at 420nm. ⇒ The O_2 evolution rate yield was 19.2 µmol at pH 8 in phosphate buffer. ⇒ The GO sheet acted as electron acceptors.
CoQD/rGO nanocomposite.[129] (QD = Quantum Dots)	The composite dispersed with Nafion and loaded on GC then it was used as WE. While Ag/AgCl electrode and Pt performed were applied as RE and CE respectively. 0.1 M KOH was acted as an electrolyte	⇒ The system works for OER only. ⇒ The maximum electrocatalyst current reached up to 32.13 mA/cm^2 at 1.86 V and 10 mA/cm^2 at 0.37 *vs* RHE. ⇒ The Tofel slope exhibited a slow value of 37 mV/ dec. ⇒ The rGO increased the conductivity of the catalyst which resulted in enhance OER performance.
CoP/rGO.[130]	Ag/AgCl electrode and Pt were RE and CE respectively. The catalyst loaded on rotating disk electrode (RDE). For HER study, the electrolyte a solution 0.5 M H_2SO_4 was performed while for OER study a solution of 1 M KOH was performed.	⇒ The system was for either HER or OER depending operating conditions. ⇒ The Electrocurrent density of HER reached 10 mA/cm^2 at 105 mV *vs* RHE and for OER study the current also gained 10 mA/cm^2 in -150 mV. ⇒ The current density for HER and OER were stable for 20 h. ⇒ In HER study, the catalyst had a low Tafel slope of 38 mV/ dec. While in OER study it reached 66 mV/ dec. ⇒ Both OER and HER systems were durable for 3000 cycles *via* CV. ⇒ The rGO a suggested to be a conductor.
Two-dimensional TaC nano sheets on a rGO hybrid.[131]	The catalyst was dispersed in mixture of ethanol and Nafion. Then it loaded on GCE and it was applied as WE. 0.5 M H_2SO_4 was applied as the electrolyte. Piece of graphite and RHE applied as the CE and RE respectively.	⇒ The system was working for HER only. ⇒ A small Tafel slope of 58 mV/ dec was achieved. ⇒ The electrocurrent density was stable over 50 h of working and achieved around -4 and -10.7 mA/cm^2 at 150 and 200 mV *vs* RHE respectively. ⇒ Through CV, study there no obvious degradation after 1000 cycles. ⇒ The rGO facilitated electron transfer and ensure high durability of the catalyst system.

CdS/rGO-MoS_2@CoP photocatalyst.[132]	Solar light simulator was used as light source. The photocatalyst put in in water with lactic acid as sacrificial agent. The system bubbled with Ar. While the photoelectrochemical measurement, Ag/AgCl electrode and Pt wire were used as CE and RE. The photocatalyst on ITO and it was applied as WE. An aqueous solution of Na_2SO_4 was used as an electrolyte.	⇒ The system worked for HER with H_2 evolution rate of 83907 μmol/ h^1 g^1 far exceeding other control samples. ⇒ The apparent quantum efficiency of 22.5%. ⇒ The rGO played as good electron accepter and transporter. ⇒ the visible light absorption increased in range 500-625 nm. ⇒ The photocurrent density increased to reach 0.8 μA/cm^2. ⇒
SiNWs/rGO.[133]	A 300 W Xenon arc lamp was used as light source. Ag/AgCl electrode and Pt wire were applied as RE and CE respectively. A mixture solution of 0.1 M H_2SO4 and 0.5 M K_2SO_4 acted as an electrolyte. The catalyst loaded on Si and the applied as WE.	⇒ The system was performed for HER. ⇒ The maximum photocurrent density reached -5.22 mA cm^{-2} at −0.5 V *vs* RHE. It was higher than SiNWs by 29 times. ⇒ The photocurrent density also showed 0.6 mA/cm^2 at 0 V (without bias) *vs* RHE. ⇒ The rGO increased the conductivity of and improved separation of the photogenerated charge carriers.
NiMn-rGO.[134]	The catalyst dispersed in propanol and Nafion then loaded on GCE. Then it was applied as WE. A 1.0 M KOH was applied as an electrolyte. Pt wire and Ag/AgCl electrode acted as CE and reference respectively.	⇒ The system was work for OER ⇒ A low Tafel slope reached 46 mV/ dec if compared with other control samples. ⇒ The maximum photocurrent density of 10 mA/ cm^2 at 1.59 V *vs*. RHE. ⇒ The rGO shortened diffusion path and accelerating the transfer of electrons.
rGO/CuI/PANI) hetero structures nano composites.[135]	Xe light with nominal cut-off λ< 420 nm was used as light source. The catalyst dispersed in methanol in sealed system and purged with N_2 before exposed to the light.	⇒ The system works for HER. ⇒ The absorbance increased in range 300-500. ⇒ H_2 evolution rate reached 295 μmol/ (h.g). ⇒ The rGO acts as electron transfer channel and supressed the recombination reaction of photogenerated charge carriers.
Bi_2WO_6/RGO composite nano fibers.[136] **Polyvinyl pyrrolidone (PVP)**	300 watt (Xenon lamp) was used as light source as light source. The photocatalyst dispersed in methyl alcohol. Then the suspension degassed *via* evacuation.	⇒ The system works for HER with H_2-evolution rate up to 935μmol/ h. It was higher pure Bi_2WO_6 nanofibers by 5.8 times ⇒ The composite has high absorbance until 400 nm and be slightly high in visible region. ⇒ The rGO exhibits an excellent conductivity transfers electrons rabidly and hindered the recombination of electrons and hole
MoS_2 nanotubes/rGO nano composite.[137]	The catalyst dispersed on isopropanol and Nafion then loaded on GCE. Then it was performed as WE. Ag/AgCl electrode and Pt wire acted as RE and CE respectively. 0.5 M H_2SO_4 was applied as an electrolyte.	⇒ The system works for HER ⇒ The current density increased to 38.91 mA/ cm^{-2} at an overpotential of 300 mA *vs* RHE. ⇒ A low Tafel slope reached of 69 mV/ dec was achieved. ⇒ The rGO increased conductivity enhancing electron transport.
CoP_2 nanoparticles on rGO sheets.[138]	The catalyst was dispersed in Nafion and ethanol then loaded on GCE and performed as working electrode. Pt foil and SCE acted as CE and RE respectively. A solution of 1 M KOH was applied as an electrolyte	⇒ the system was cheap earth abundant and alternative to nobles metal for OER ⇒ The maximum current density reached 10 mA/cm^2 at 1.56 V *vs* RHE. ⇒ The catalyst was durable over 1000 CV cycles. ⇒ The rGO an excellent conductivity and supporting charge transfer. ⇒ The amount of O_2 and H_2 that collected after 8000 second was 0.015 and 0.03 mM respectively.

NGODs. [139] **(**NGODs = nitrogen-doped graphene oxide dots).	300 W xenon lamp. The photocatalyst dispersed in aqueous solution of triethanolamine before it was exposed to the light.	⇒ The system works for HER with evolution rate increased up to 150 µmol after 12 h. ⇒ The visible absorption in range 400-800 nm. ⇒ N –conjugated with GO increases the lifetime of photogenerated electro enhancing HER perform
$Ni_{2-x}Co_xP$ /rGO hybrids.[140]	Two of NiCoP/rGO electrodes were applied as cathode and anode for HER and OER respectively. 1 M KOH electrolyte was applied as an electrolyte.	⇒ The system was works for O_2 and H_2 ⇒ The current density increased to 10 mA/ cm^2 at 1.59 V over 75 h without an obvious degradation. ⇒ Interfacing rGO with the catalyst effectively providing more active sites, accelerating the charge transfer.
α-Fe_2O_3/rGO. [141]	50 W Xe lamp was applied as light source. Pt wire and a mercurous sulfate were applied as CE and RE respectively. A solution of 0.1 M Na_2SO_4. The photocatalyst loaded on ITO then dispersed with Nafion and alcohol and it was applied as WE.	⇒ The system works for OER. ⇒ The maximum photocurrent density increased up to 1.63 mA /cm^2 at 1.8 V versus RHE. It was 4.39 times higher than pure α-Fe_2O_3 electrode. ⇒ The rGO act as charge collectors increase lifetime of photogenerated holes.
$RhCrO_x/LaMg_{1/3}Ta_{2/3}O_2N$)/(rGO)/$BiVO_4$:Mo sheet.[142]	The catalyst acted as Z-scheme system put in distilled water and evacuated then irradiated by 300 W xenon lamp ($\lambda \geq 300$ nm as light source	⇒ The rGO combined $RhCrO_x/LaMg_{1/3}Ta_{2/3}O_2N$ and $BiVO_4$:Mo particles ⇒ The rGO acts as solid mediator enhancing charge transfer. ⇒ The H_2 and O_2 evolution rates were stoichiometric ratios. ⇒ Incorporated rGO in Z-sheme raise the activity for water splitting by 3.5 times.
MoS_2/N-RGO.[143]	The electrocatalyst was dispersed in Nafion then loaded in GCE. Then it was applied as WE. While SCE electrode and a Pt wire were applied as RE and RE respectively. 0.5 M H_2SO_4 performed as an electrolyte.	⇒ The electrocatalyst works for HER ⇒ The catalyst showed small Tofel slope of 41.3 mV/dec. ⇒ The current density increased to reach 7.4 × 10^{-4} A/cm^2 at -5 mV *vs* RHE. Tt was stable over 5000 cycles ⇒ Simple method for HER with a low cost compared with noble metal ⇒ The rGO increased the conductivity and provide high active surface area for HER.
(MPSA/GO) self-assembled melamine,phytic acid, and graphene oxide.[144]	The catalyst dispersed with Nafion and distilled water. Then it was performed as WE. Ag/AgCl electrode and Pt/C (20 wt%) were performed as RE and CE respectively. A solution of either 0.5 M H_2SO_4 or 0.1 M KOH was used as an electrolyte for HER and ORR respectively.	⇒ The system is cheap and metal free electrocatalyst for both HER and ORR respectively. ⇒ A Low Tofel slope of 89 mV/dec was achieved ⇒ The current density increased to 30 mA/cm^2 at -0.21 V. It was better than MPSA alone. ⇒ The electrocatalyst was similar to Pt/C electrode in case of HER. ⇒ it was better ORR performance with high selectivity. ⇒ Doping N and P with GO structure enhanced electron transport and increased HER and ORR activities.
GO-PANi 31-FP. (FP = phosphorous, and fluorine while 31 refers to initial mass ratio of GO-PANi).[145]	The catalyst dispersed with Nafion and distilled water and then it performed as WE. Ag/AgCl electrode Pt/C (20 wt%) electrode RE and CE respectively. 0.1 M KOH were used as an electrolyte.	⇒ The electrocatalyst works for both HER and OER with H_2 and O_2 evolution rates of 8.26 x 10^{-6} mL/ and 4.23 mL/h, respectively. ⇒ The maximum current density increased to 13 mA/cm^2 at 1.8 V *vs* RHE. ⇒ A low Tafel slope of 136 mV/dec was obtained. It was lower than other control samples. Doping GO enhanced electron transfer resulted in enhancing electrocatalytic activity.

NiO-$NiFe_2O_4$/rGO.[146]	The catalyst dispersed in Nafion solution then loaded on GCE. Then it was acted as WE. Pt foil and Hg/HgO were performed as CE and RE respectively. 0.1 M KOH was applied as an electrolyte.	⇒ The electrocatalyst system works for OER. ⇒ The catalyst showed low overpotential of 296 mV at J= 10 $mAcm^{-2}$ ⇒ A small Tafel slope was achieved (43 mV/dec) if compared with other control samples such NiO-$NiFe_2O_4$ or NiFe-LDH. ⇒ The rGO act as electron transport channel enhancing the electrocatalyst performance.
Co_3O_4/N-rGO Composites. [147]	The electrocatalyst was loaded on GCE electrode. Pt wire and SCE used as CE and RE respectively. For ORR study, the electrolyte was 0.1 M KOH and for OER the electrolyte was 1 M KOH.	⇒ The electrocatalyst applied for ORR and OER. ⇒ In OER study, the LSV obtained 45 mA/cm^2 at 1.65 V *vs* RHE. ⇒ In OER study, the electrocatalyst exhibits low over-potential of 330 mV at 10 mA/cm^2 with low Tofel Slope of 68 mV /dec. ⇒ The rGO exhibits super conductivity for electron transfer.
ERGO/UM/CdS).[148] **ERGO is Ultra-thin MoS_2 (UM) layers on exfoliated reduced graphene oxide (ERGO).**	Solar light simulator was applied as light source. For H_2 evolution, the catalyst dispersed in lactic acid solution in sealed system and then irradiated with light. While the Photoelectro chemical measurement, the photocatalyst was loaded in ITO and applied as WE. Pt wire and Ag/AgCl electrode was applied as CE and RE respectively. Na_2SO_4 solution was applied as electrolyte.	⇒ Photocatayst for HER with evolution rate reached up to ~234 mmol/ (h .g). ⇒ The visible absorbance has been improved in range 500-650 nm. ⇒ The ErGO high participated in electron mobility. ⇒ The ERGO accepted and transferred the photogenerated electrons.
rGQDs/Fe_2O_3 electrode.[149]	Solar light simulator was applied as light source. The Photocatalyst was loaded on FTO then and applied as WE. While Ag/AgCl and Pt plate as RE and CE respectively. The electrolyte was a solution of 1 M NaOH.	⇒ The system worked for O_2 generation. ⇒ The photocurrent density increased to reach 2.5 mA/cm^2 at 1.6 V *vs* RHE. It was raised by 8 times than pristine Fe_2O_3. ⇒ The rGO had an effective role in charge transfer. ⇒ The visible light absorbance enhanced in range 450-600 nm.
GO-modified Cu_2O nano sphere.[150]	Visible light with irradiation (λ > 400 nm) used as a light source. The catalyst was dispersed in methanol solution in sealed system with window to expose to the light source.	⇒ The photocatalyst for HER with evolution gas of 118.3 mmol collected after 7000 min which was more than 2.6 time than pristine Cu_2O. ⇒ The XRD approved that GO partially reduced. GO played a role in the transfer of the electrons under irradiation.
WO_3-assisted multi-junction cell. [151]	Solat light simulator was used as light source. The photocatalyst was loaded on carbon electrode and applied as WE. While Pt wire and Ag/AgCl electrode were used as CE and RE respectively. A solution of KOH was used as an electrolyte.	⇒ The system worked for O_2 ⇒ The visible absorbance increased in range 400-700 nm. ⇒ The photocurrent exceeded 900 $\mu A/cm^2$. ⇒ The presence of rGO enhances the PEC activity for OER and increases the stability of the photocatalyst. ⇒ The rGO layer protected the photocatalyst against water penetration and photo-corrosion during the oxidation of water. ⇒ The rGO provide the catalyst with good transport properties *via* its holes that increase the OER activity.

3D Ag_3PO_4/GAs. Ag_3PO_4. [152]	300 W Xe lamp was used as light source. The catalyst was dispersed in aqueous solution of $AgNO_3$. . For PEC measurement, the photo catalyst dispersed with Nafion and loaded on GCE and was applied as WE while Pt wire and Ag/AgCl electrode used as CE and RE respectively. 0.02 M Na_3PO_4 was used as an electrolyte.	⇒ The photocatalyst works for OER with evolution rate 250 µmol /h ⇒ The photocatalyst increased to 2.5 µA/cm^2 showing enhancement of 40 % than pristine Ag_3PO_4. ⇒ rGO provides electrical conductive channels for anchored Ag_3PO_4NPs, increased the life time of the hole resulting in enhance photocatalyst activity.
Ta_2O_5/graphene composite.[153]	Xe lamp, cut off filter (200-400 nm) was used as light source. The catalyst was dispersed with methanol before exposed to the light source.	⇒ The system works for H_2 evolution with a rate up to 30mmol/(g.h) ⇒ The apparent quantum efficiency reached 33.8% at 254 nm. ⇒ The photocatalyst was durable over 5 h. ⇒ The graphene acted as interfacial charge transfer material and suppressed the recombination reactions.
rGO/Pt-TiO_2 nano composite. [154]	300 W Xe lamp was used as light source. For H_2 evolution test, the catalyst dispersed in an aqueous solution of Triethanolamine. Then it exposed to light source. For PEC measurements, 0.5 M Na_2SO_4 was performed as electrolyte. While Ag/AgCl electrode and a Pt foil was applied acted as RE and CE respectively. The catalyst sonicated with ethanol and Nafion then deposited on ITO glass and used as WE.	⇒ The system works for H_2 evolution with a rate up to (1075.68 µmol/ (h. g). ⇒ Doping 2 % of rGO resulted in the H_2 evolution rate increased by 81 and 5 times than bare TiO_2 and Pt/TiO_2 samples. ⇒ The current density increased to 1 µA/cm^2 at 1.2 V *vs* RHE. ⇒ The rGO acted as "superhighway" for electrons transport.
rGO/ZnO nanowire arrays. [155]	Solar light simulator was used as light source. Ag/AgCl electrode and a Pt were applied as RE reference and CE respectively. 0.5 M Na_2SO_4 was applied as an electrolyte. The catalyst was used as WE.	⇒ The catalyst works for OER ⇒ In LSV, a photocatalyst showed higher photocurrent density reached 2.5 mA/cm^2 at 1 V *vs* Ag/AgCl. ⇒ In amperometric study the current density was steadily decreases from 1.7 to 1.5 mA//cm^2 after 1200 Sec. at bias of 0.25 V *vs* Ag/AgCl. ⇒ the UV absorbance in range 300-400 nm ⇒ rGO acted as electron trap minimizing e^--h^+ recombination reactions and enhancing overall PEC.
rGO/ZnO film.[156]	Solar light simulator was used as light source. Pt and Ag/AgCl electrode were performed as CE and RE respectively. The catalyst films was acted as WE. 0.1 KOH used as electrolyte.	⇒ The system works for OER. ⇒ The photocurrent density increased up to 1.8 mA/cm^2 at 0.7V *vs* Ag/AgCl. ⇒ In amperometric study, the photocurrent density reached 0.45 mA/cm^2 without external bias. ⇒ The visible absorbance enhanced in range 450-650 nm. ⇒ The rGO was an effective charge carriers by formation of heterostructures with ZnO catalyst.
TiO_2@rGO@Au hybrid. [157]	Solar light simulator was used as light source. . Pt and Ag/AgCl electrode were performed as CE and RE respectively. 0.5 M Na_2SO_4 were used as an electrolyte. The hybrid was loaded FTO and performed as working electrode.	⇒ The system worked for HER and OER. ⇒ The evolution rates of H_2 and O_2 were 17.8 and 8.7 µmol /cm^2) at 1.23 V *vs* RHE respectively, so the gasses evolution ratio was has stoichiometric. ⇒ The rGO was an effective super charge transfer. ⇒ The IPCE was higher than pristine TiO_2 by 2.5 times. ⇒ The visible absorbance enhanced in range 450-600 nm.

Bi_2MoO_6/rGO composite nanofibers. [158]	The photo catalyst dispersed in methyl alcohol and water and exposed to 300 W xenon lamp as a source of light.	⇒ The system works for H_2 evolution reaction with H_2 rate reached 794.72 µmol/h .It was 2.86 times than pristine Bi_2MoO_6 nanofibers. ⇒ The absorbance increased especially in range 300 -450 nm.
rGO/Cu_2O/Cu .[159]	500 W halogen tungsten lampwasa used as light source .Pt and Ag/AgCl were performed as CE and RE respectively. A solution of Na_2SO_4 at pH 6.5 was acted as an electrolyte.	⇒ The system has worked for HER. ⇒ The visible absorbance increased especially in range 500-600 nm. ⇒ The photocurrent reached -2.54 mA/cm^2 at 0 bias and was higher than Cu_2O/Cu by 3 times. ⇒ The rGO accepted and transferred of photogenerated electrons and will as played as protective layer.
Co nanoflake modified with carbon based nano composites.[160]	The catalyst was applied as WE. Pt and Ag/AgCl were performed as CE and RE respectively. 1 M KOH applied as an electrolyte.	⇒ The electrocatalyst was for water oxidation. ⇒ In LSV study, the lowest overpotential required for water electrolysis was at 244.4 mV. ⇒ The rGO acted as conductive backbone for electron transfer as well as provided significant effective surface for catalytic sites
CoO@Co/N-rGO hybrid.[161]	The catalyst was dispersed in Nafion, loaded in GCE, and used as WE. Pt and Ag/AgCl were performed as CE and RE respectively. For ORR study, O_2 saturated 0.1 M KOH solution acted as electrolyte. For HER activity, N_2-saturated 0.5 M H_2SO_4 or N_2-saturated 0.1 M KOH was applied as an electrolyte. For O_2-saturated 0.1 M KOH was an electrolyte.	⇒ The system works for HER, OER and ORR. ⇒ In HER study, low overpotential of140 mV for 10 mA/ cm^2 in 0.5 M H_2SO_4 and 237 mV in 0.1 M KOH ⇒ In OER study, a current density of 10 mA/ cm^2 with a small overpotential of 1.67 V in 0.1 M KOH ⇒ In HER study, the catalyst was durable even after 1000 of CV Cycles. While in OER study, the catalyst was stable till 5000 cycles. ⇒ In ORR study, the catalyst a very smaller onset potential of 0.95 obtained and smaller Tafel slope of 46 mV/dec was gained. ⇒ Doping N atom in rGO can generating synergetic effects for better coupling CoO@Co which resulted in enhanced the catalyst performed.
Co/Co_3O_4-Gr.[162]	Free standing Co/Co_3O_4-Gr was acted as WE while Pt and Ag/AgCl electrode were performed as CE and RE respectively. 0.1 KOH performed as an electrolyte.	⇒ The system worked for H_2 and O_2 evolution in alkaline media at a low onset potential. ⇒ In OER study, the system exhibited low onset potential of 1.38 V and at the potential of 1.66 V the current density reached 10 mA/ cm^2. These potentials values were comparable to Ru. ⇒ In HER, study the system exhibited current density of -22.5 at -0.8 *vs* RHE. ⇒ The rGO acted as enhanced the electrons transfer and sustained the stability of the

Co_9S_8/N, S-G Electro catalyst. [163]	Pt plate and (SCE) were employed as CE and RE respectively. The catalyst was dispersed in ethanol had 20 % Pt/C and 5% Nafion solution then loaded in GCE and acted as WE. For ORR O_2-saturated 0.1 M KOH medium was performed as an electrolyte. For OER O_2-saturated 1.0 M KOH medium was acted as an electrolyte.	⇒ The system works for OER and ORR. ⇒ The system was superior OER catalytic performance achieved a low overpotential of 411 mV at a current density of 10 mA/cm^2. ⇒ In OER study a low Tafel slope of 60 mV/dec was obtained. ⇒ Better ORR catalyst with low onset potential of 0.931V and half-wave potential of 0.811V *vs* RHE and the current density reached 5.207 mA/cm^2 at a potential of 0.212 V vs RHE with long stability for 10000 Sec. ⇒ Doping rGO with N, S an atoms, the resulting catalyst had high conductivity, large surface area and faster electrons and mass transfer ability.
Fe_2O_3 modified with a graphene–carbon nanotube (CNT) composite.[164]	300 W xenon lamp was used as light source. A Pt mesh and Ag/AgCl electrode were applied as CE and RE respectively. 1 M NaOH was used as an electrolyte. The catalyst was deposited onto a FTO and used as WE.	⇒ The system has worked for water oxidation. ⇒ The photocurrent increase of 530% compared with to pristine Fe_2O_3 photoanode at 1.23 V *vs* RHE. ⇒ The visible absorption increased up to 550 nm. ⇒ The Graphene and CNT acted as excellent conducting materials. ⇒ The Intrinsic conducting abilities of graphene and CNT as approved via EIS study.
TiO_2/MoS_2/graphene composite.[165]	350 W Xe arc lamp was used as light source. The catalyst suspended in suspended in aqueous solution of ethanol with ratio 4:1 (H_2O: ethanol V/V)	⇒ The system works for H_2 evolution with rate reached 165.3 µmol/ h. ⇒ The quantum efficiency reached 9.7% at 365 nm. ⇒ The graphene acted as electron transfer and co-catalysts for H_2 reduction.

References of Appendices

1. Gustafson, M. P.; Matsumoto, K.; MacFarlane, D. R.; Winther-Jensen, B. An Investigation of the Properties of Conducting Polymer Alloys for Water Oxidation. *Electrochim. Acta* **2014**, *122*, 166-172.
2. Duan, C.; Wang, H.; Ou, X.; Li, F.; Zhang, X. Efficient Visible Light Photocatalyst Fabricated by Depositing Plasmonic Ag Nanoparticles on Conductive Polymer-Protected Si Nanowire Arrays for Photoelectrochemical Hydrogen Generation. *ACS Appl. Mater. Interfaces* **2014**, *6* (12), 9742-9750.
3. Chowdhury, A. D.; Agnihotri, N.; Sen, P.; De, A. Conducting $CoMn_2O_4$ - PEDOT nanocomposites as catalyst in oxygen reduction reaction. *Electrochim. Acta* **2014**, *118*, 81-87.
4. Srinivasan, N.; Shiga, Y.; Atarashi, D.; Sakai, E.; Miyauchi, M. A PEDOT-coated Quantum Dot as Efficient Visible Light Harvester for Photocatalytic Hydrogen Production. *Appl. Catal. B: Environ.* **2015**, *179*, 113-121.
5. Jaafar, S. N. H.; Minggu, L. J.; Kassim, M. B.; Daud, W. R. W. In *Improvement of Photoelectrochemical Water Splitting with Natural Dye of Pitaya Peel*, 3rd IET International Conference on Clean Energy and Technology (CEAT) 2014, 24-26 Nov. 2014; **2014**; pp 1-6.
6. Boskovic, D.; Balakrishnan, S.; Wagner, P.; Swiegers, G. F. Demetallatation of Electrochemically Polymerised Mn Porphyrin Anion/PEDOT Composites under Light-Illumination. *Synth. Met.* **2017**, *228*, 58-63.
7. Yangqin, G.; M., L. C. V.; Alexandre, G.; Marios, N.; Abdul, H. M.; Kazuhiro, T.; M., B. P. Homo-Tandem Polymer Solar Cells with VOC >1.8 V for Efficient PV-Driven Water Splitting. *Adv. Mater.* **2016**, *28* (17), 3366-3373.
8. Xiao, X.; Engelbrekt, C.; Zhang, M.; Li, Z.; Ulstrup, J.; Zhang, J.; Si, P. A straight Forward Approach to Electrodeposit Tungsten Disulfide/Poly(3,4-ethylenedioxy thiophene) Composites Onto Nanoporous Gold for the Hydrogen Evolution Reaction. *Appl. Surface Sci.* **2017**, *410*, 308-314.
9. Ensafi, A. A.; Zandi-Atashbar, N.; Mohamadi, Z.; Abdolmaleki, A.; Rezaei, B. Pt-Pd Nanoparticles Decorated Sulfonated Graphene-Poly(3,4-ethylene Dioxythiophene) Nanocomposite, An Efficient HER Electrocatalyst. *Energy* **2017**, *126*, 88-96.
10. Jia, X.; Gao, S.; Liu, T.; Li, D.; Tang, P.; Feng, Y. Fabrication and Bifunctional Electrocatalytic Performance of Ternary CoNiMn Layered Double Hydroxides/ Polypyrrole/Reduced Graphene Oxide Composite for Oxygen Reduction and Evolution Reactions. *Electrochim. Acta* **2017**, *245*, 59-68.

11. Senchuan, H.; Yuying, M.; Shiman, H.; Anandarup, G.; Qili, W.; Junhao, L.; Shengfu, T.; Tewodros, A.; Mingmei, W. N-, O-, and S-Tridoped Carbon-Encapsulated Co_9S_8 Nanomaterials: Efficient Bifunctional Electrocatalysts for Overall Water Splitting. *Adv. Funct. Mater.* **2017**, *27* (17), 1606585.
12. Luo, J.; Ma, Y.; Wang, H.; Chen, J. Preparation of Polypyrrole Sensitized TiO_2 Nanotube Arrays Hybrids for Efficient Photoelectrochemical Water Splitting. *Electrochim. Acta* **2015**, *167*, 119-125.
13. Li, J.-S.; Wang, Y.; Liu, C.-H.; Li, S.-L.; Wang, Y.-G.; Dong, L.-Z.; Dai, Z.-H.; Li, Y.-F.; Lan, Y.-Q. Coupled Molybdenum Carbide and Reduced Graphene Oxide Electrocatalysts for Efficient hydrogen Evolution. *Nat. Commun.* **2016**, *7*, 11204 (1-8).
14. Ng, C. H.; Winther-Jensen, O.; Kolodziejczyk, B.; Ohlin, C. A.; Winther-Jensen, B. Photo-Electrocatalytic H_2 Evolution on Poly(2,2′-bithiophene) at Neutral pH. *Int. J. Hydrogen Energy* **2014**, *39* (32), 18230-18234.
15. Kim, H.; Kim, Y.; Noh, Y.; Lee, S.; Sung, J.; Kim Won, B. Thermally Converted CoO Nanoparticles Embedded into N-Doped Carbon Layers as Highly Efficient Bifunctional Electrocatalysts for Oxygen Reduction and Oxygen Evolution Reactions. *ChemCatChem* **2017**, *9* (8), 1503-1510.
16. Lattach, Y.; Fortage, J.; Deronzier, A.; Moutet, J.-C. Polypyrrole-Ru(2,2′-bi pyridine)$_3^{2+}$/MoS_x Structured Composite Film As a Photocathode for the Hydrogen Evolution Reaction. *ACS Appl. Mater. Interfaces* **2015**, *7* (8), 4476-4480.
17. Zong, X.; Miao, X.; Hua, S.; An, L.; Gao, X.; Jiang, W.; Qu, D.; Zhou, Z.; Liu, X.; Sun, Z. Structure Defects Assisted Photocatalytic H_2 Production for Polythiophene Nanofibers. *Appl. Catal. B: Environ.* **2017**, *211*, 98-105.
18. Fan, W.; Chen, C.; Bai, H.; Luo, B.; Shen, H.; Shi, W. Photosensitive Polymer and Semiconductors Bridged by Au Plasmon for Photoelectrochemical Water Splitting. *Appl. Catal. B: Environ.* **2016**, *195*, 9-15.
19. Kalyani, R.; Gurunathan, K. PTh-rGO-TiO_2 nanocomposite for photocatalytic hydrogen production and dye degradation. *J. Photochem. Photobiol. A: Chem.* **2016**, *329*, 105-112.
20. Kalyani, R.; Gurunathan, K. Metal Ions Doped and Polythiophene Coated nanophotocatalysts: Synthesis and spectroscopic characterization for H_2 production and dye degradation. *Optik - Int. J. Light Electron Optics* **2016**, *127* (11), 4741-4745.
21. Jia, Y.; Xu, W.; Bo, L.; Liang, M.; Lei, S.; Yujie, X.; Hangxun, X. Novel Iron/Cobalt-Containing Polypyrrole Hydrogel-Derived Trifunctional Electrocatalyst for Self-Powered Overall Water Splitting. *Adv. Funct. Mater.* **2017**, *27* (17), 1606497 (1-11).

22. Yu, X.; Du, R.; Li, B.; Zhang, Y.; Liu, H.; Qu, J.; An, X. Biomolecule-Assisted Self-Assembly of CdS/MoS_2/Graphene Hollow Spheres as High-Efficiency Photocatalysts for Hydrogen Evolution Without Noble Metals. *Appl. Catal.B: Environ.* **2016**, *182*, 504-512.
23. Shinde, S. S.; Sami, A.; Lee, J.-H. Sulfur Mediated Graphitic Carbon Nitride/S-Se-Graphene as a Metal-Free Hybrid Photocatalyst for Pollutant Degradation and Water Splitting. *Carbon* **2016**, *96*, 929-936.
24. Xu, J.; Wang, L.; Cao, X. Polymer Supported Graphene–CdS Composite Catalyst with Enhanced Photocatalytic Hydrogen Production From Water Splitting under Visible Light. *Chem. Eng. J.* **2016**, *283*, 816-825.
25. Sudhagar, P.; Herraiz-Cardona, I.; Park, H.; Song, T.; Noh, S. H.; Gimenez, S.; Sero, I. M.; Fabregat-Santiago, F.; Bisquert, J.; Terashima, C.; Paik, U.; Kang, Y. S.; Fujishima, A.; Han, T. H. Exploring Graphene Quantum Dots/TiO_2 Interface in Photoelectrochemical Reactions: Solar to Fuel Conversion. *Electrochim. Acta* **2016**, *187*, 249-255.
26. Kaouk, A.; Ruoko, T. P.; Gonullu, Y.; Kaunisto, K.; Mettenborger, A.; Gurevich, E.; Lemmetyinen, H.; Ostendorf, A.; Mathur, S. Graphene-Intercalated Fe_2O_3/TiO_2 Heterojunctions for Efficient Photoelectrolysis of Water. *RSC Adv.* **2015**, *5* (123), 101401-101407.
27. Wang, X.; Xie, J.; Li, C. M. Architecting smart "umbrella" Bi_2S_3/rGO-Modified TiO_2 Nanorod Array Structures at The Nanoscale for Efficient Photoelectrocatalysis under Visible Light. *J. Mater. Chem. A* **2015**, *3* (3), 1235-1242.
28. Nguyen-Phan, T.-D.; Luo, S.; Liu, Z.; Gamalski, A. D.; Tao, J.; Xu, W.; Stach, E. A.; Polyansky, D. E.; Senanayake, S. D.; Fujita, E.; Rodriguez, J. A. Striving Toward Noble-Metal-Free Photocatalytic Water Splitting: The Hydrogenated-Graphene–TiO_2 Prototype. *Chem. Mater.* **2015**, *27* (18), 6282-6296.
29. Li, W.; Yue, J.; Bu, Y.; Chen, Z. Graphene-Modified $BiMo_{0.03}V_{0.97}O_4$ Thin-Film Photoanode for Enhanced Photoelectrochemical Water Splitting Performance. *RSC Adv.* **2015**, *5* (95), 77823-77830.
30. Shinde, S. S.; Sami, A.; Kim, D.-H.; Lee, J.-H. Nanostructured SnS-N-Doped Graphene as an Advanced Electrocatalyst for the Hydrogen Evolution Reaction. *Chem. Commun.* **2015**, *51* (86), 15716-15719.
31. Yu, X.; Zhang, J.; Zhao, Z.; Guo, W.; Qiu, J.; Mou, X.; Li, A.; Claverie, J. P.; Liu, H. NiO–TiO_2 p–n Heterostructured Nanocables Bridged by Zero-Bandgap rGO for Highly Efficient Photocatalytic Water Splitting. *Nano Energy* **2015**, *16*, 207-217.
32. Yingfei, H.; Yao, S.; Huiting, H.; Qinfeng, Q.; Zhongjie, G.; Jianyong, F.; Zhaosheng, L.; Zhigang, Z. Enhancement of Photoelectrochemical Performance in Water

Oxidation over Bismuth Vanadate Photoanodes by Incorporation with Reduced Graphene Oxide. *ChemCatChem* **2015**, *7* (18), 2979-2985.

33. Te-Fu, Y.; Chiao-Yi, T.; Shean-Jen, C.; Hsisheng, T. Nitrogen-Doped Graphene Oxide Quantum Dots as Photocatalysts for Overall Water-Splitting under Visible Light Illumination. *Adv. Mater.* **2014**, *26* (20), 3297-3303.
34. Hou, D.; Zhou, W.; Zhou, K.; Zhou, Y.; Zhong, J.; Yang, L.; Lu, J.; Li, G.; Chen, S. Flexible and Prous Catalyst Electrodes Constructed by Co Nanoparticles@Nitrogen-Doped Graphene Films for Highly Efficient Hydrogen Evolution. *J. Mater. Chem. A* **2015**, *3* (31), 15962-15968.
35. Qamar, M.; Abdalwadoud, M.; Ahmed, M. I.; Azad, A. M.; Merzougui, B.; Bukola, S.; Yamani, Z. H.; Siddiqui, M. N. Single-Pot Synthesis of ⟨001⟩-Faceted N-Doped Nb_2O_5/Reduced Graphene Oxide Nanocomposite for Efficient Photoelectrochemical Water Splitting. *ACS Appl. Mater. Interfaces* **2015**, *7* (32), 17954-17962.
36. Cao, M.; Wang, P.; Ao, Y.; Wang, C.; Hou, J.; Qian, J. Investigation on Graphene and Pt Co-modified CdS Nanowires with Enhanced Photocatalytic Hydrogen Evolution Activity under Visible Light Irradiation. *Dalton Trans.* **2015**, *44* (37), 16372-16382.
37. Faze, W.; Maojun, Z.; Changqing, Z.; Bin, Z.; Wen, C.; Li, M.; Wenzhong, S. Visible Light Photocatalytic H_2-Production Activity of Wide Band Gap ZnS Nanoparticles Based on the Photosensitization of Graphene. *Nanotechnol.* **2015**, *26* (34), 345402 (1-8).
38. Tamirat, A. G.; Su, W.-N.; Dubale, A. A.; Pan, C.-J.; Chen, H.-M.; Ayele, D. W.; Lee, J.-F.; Hwang, B.-J. Efficient Photoelectrochemical Water Splitting Using Three Dimensional Urchin-Like Hematite Nanostructure Modified with Reduced Graphene Oxide. *J. Power Sources* **2015**, *287*, 119-128.
39. Bo, W.; Liu, Z.; Hong, T.; Han, J.; Guo, K.; Zhang, X.; Chen, D. Trilaminar Graphene /Tremella-like $CuInS_2$/Graphene Oxide Nanofilms and the Enhanced Activity for Photoelectrochemical Water Splitting. *J. Nanopart. Res.* **2015**, *17* (7), 295 (2-8).
40. Wang, B.; Liu, Z.; Han, J.; Hong, T.; Zhang, J.; Li, Y.; Cui, T. Hierarchical Graphene /CdS/Ag_2S Sandwiched Nanofilms for Photoelectrochemical Water Splitting. *Electrochim. Acta* **2015**, *176*, 334-343.
41. Su, Y.-H.; Huang, S.-H.; Kung, P.-Y.; Shen, T.-W.; Wang, W.-L. Hydrogen Generation of Cu_2O Nanoparticles/MnO–MnO_2 Nanorods Heterojunction Supported on Sonochemical-Assisted Synthesized Few-Layer Graphene in Water-Splitting Photocathode. *ACS Sust. Chem. Eng.* **2015**, *3* (9), 1965-1973.
42. Suzuki, T. M.; Iwase, A.; Tanaka, H.; Sato, S.; Kudo, A.; Morikawa, T. Z-Scheme Water Splitting under Visible Light Irradiation over Powdered Metal-Complex

/Semiconductor Hybrid Photocatalysts Mediated by Reduced Graphene Oxide. *J. Mater. Chem. A* **2015**, *3* (25), 13283-13290.

43. Youn, D. H.; Park, Y. B.; Kim, J. Y.; Magesh, G.; Jang, Y. J.; Lee, J. S. One-Pot Synthesis of NiFe Layered Double Hydroxide/Reduced Graphene Oxide Composite as an Efficient Electrocatalyst for Electrochemical and Photoelectrochemical Water Oxidation. *J. Power Sources* **2015**, *294*, 437-443.
44. Li, X.; Zhang, Q.; Wang, H.; Li, Y. $(Ga_{1-x}Zn_x)(N_{1-x}O_x)$–rGO Composites with Enhanced Photocatalytic Performance for Visible-Light Driven Water Splitting. *Appl. Surface Sci.* **2015**, *358*, 57-62.
45. Li, C.; Wang, J.; Jiang, Z.; Hu, P. Co/Cu_2O Assisted Growth of Graphene Oxide on Carbon Nanotubes and its Water Splitting Activities. *New J. Chem.* **2015**, *39* (6), 4562-4567.
46. Zhao, G.; Huang, X.; Fina, F.; Zhang, G.; Irvine, J. T. S. Facile Structure Design Based on C_3N_4 for Mediator-Free Z-Scheme Water Splitting under Visible Light. *Catal. Sci. Technol.* **2015**, *5* (6), 3416-3422.
47. Chandrasekaran, S.; Hur, S. H.; Kim, E. J.; Rajagopalan, B.; Babu, K. F.; Senthilkumar, V.; Chung, J. S.; Choi, W. M.; Kim, Y. S. Highly-Ordered Maghemite /Reduced Graphene Oxide Nanocomposites for High-Performance Photo electro chemical Water Splitting. *RSC Adv.* **2015**, *5* (37), 29159-29166.
48. Iwashina, K.; Iwase, A.; Ng, Y. H.; Amal, R.; Kudo, A. Z-Schematic Water Splitting into H_2 and O_2 Using Metal Sulfide as a Hydrogen-Evolving Photocatalyst and Reduced Graphene Oxide as a Solid-State Electron Mediator. *J. Am. Chem. Soc.* 2**015**, *137* (2), 604-607.
49. Yusoff, N.; Kumar, S. V.; Pandikumar, A.; Huang, N. M.; Marlinda, A. R.; An'amt, M. N. Core-shell Fe_3O_4-ZnO Nanoparticles Decorated on Reduced Graphene Oxide for Enhanced Photoelectrochemical Water Splitting. *Ceram. Int.* **2015**, *41* (3, Part B), 5117-5128.
50. B., M. M.; P., B. J.; Kevin, M.; S., F. M. Reduced Graphene Oxide Bipolar Membranes for Integrated Solar Water Splitting in Optimal pH. *ChemSusChem* **2015**, *8* (16), 2645-2654.
51. Wu, Q.; Zhao, J.; Liu, K.; Wang, H.; Sun, Z.; Li, P.; Xue, S. Ultrathin Hematite Film for Photoelectrochemical Water Splitting Enhanced with Reducing Graphene Oxide. *Int. J. Hydrogen Energy* **2015**, *40* (21), 6763-6770.
52. Bharad, P. A.; Sivaranjani, K.; Gopinath, C. S. A Rational Approach Towards Enhancing Solar Water Splitting: A Case Study of Au-RGO/N-RGO-TiO_2. *Nanoscale* **2015**, *7* (25), 11206-11215.

53. Bai, Z.; Yan, X.; Kang, Z.; Hu, Y.; Zhang, X.; Zhang, Y. Photoelectrochemical Performance Enhancement of ZnO Photoanodes From $ZnIn_2S_4$ Nanosheets Coating. *Nano Energy* **2015**, *14*, 392-400.
54. Jin, Z.; Duan, W.; Liu, B.; Chen, X.; Yang, F.; Guo, J. Fabrication of Efficient Visible Light Activated Cu–P25–Graphene Ternary Composite for Photocatalytic Degradation of Methyl Blue. *Appl. Surface Sci.* **2015**, *356*, 707-718.
55. Saulo, d. A. C.; L., S. F.; F., N. A. Enhancing Hematite Photoanode Activity for Water Oxidation by Incorporation of Reduced Graphene Oxide. *ChemPhysChem* **2016**, *17* (1), 170-177.
56. Kong, D.; Zhao, M.; Li, S.; Huang, F.; Song, J.; Yuan, Y.; Shen, Y.; Xie, A. Synthesis of TiO_2/rGO Nanocomposites with Enhanced Photoelectrochemical Performance and Photocatalytic Activity. *Nano* **2016**, *11* (01), 1650006 (1-9).
57. Carter, R.; Chatterjee, S.; Gordon, E.; Share, K.; Erwin, W. R.; Cohn, A. P.; Bardhan, R.; Pint, C. L. Corrosion Resistant Three-Dimensional Nanotextured Silicon for Water Photo-Oxidation. *Nanoscale* **2015**, *7* (40), 16755-16762.
58. Ajay Rakkesh, R.; Durgalakshmi, D.; Balakumar, S. Nanostructuring of a GNS-V_2O_5-TiO_2 Core-Shell Photocatalyst for Water Remediation Applications under Sun-Light Irradiation. *RSC Adv.* **2015**, *5* (24), 18633-18641.
59. Wang, M.; Shang, X.; Yu, X.; Liu, R.; Xie, Y.; Zhao, H.; Cao, H.; Zhang, G. Graphene-CdS Quantum Dots-Polyoxometalate Composite Films for Efficient Photoelectrochemical Water Splitting and Pollutant Degradation. *Phys. Chem. Chem. Phys.* **2014**, *16* (47), 26016-26023.
60. Zhang, D.; Wei, D.; Cui, Z.; Wang, S.; Yang, S.; Cao, M.; Hu, C. Improving Water Splitting Performance of Cu_2O Through a Synergistic "Two-Way Transfer" Process of Cu and Graphene. *Phys. Chem. Chem. Phys.* **2014**, *16* (46), 25531-25536.
61. Dubale, A. A.; Su, W.-N.; Tamirat, A. G.; Pan, C.-J.; Aragaw, B. A.; Chen, H.-M.; Chen, C.-H.; Hwang, B.-J. The Synergetic Effect of Graphene on Cu_2O Nanowire Arrays as a Highly Efficient Hydrogen Evolution Photocathode in Water Splitting. *J. Mater. Chem. A* **2014**, *2* (43), 18383-18397.
62. Skaltsas, T.; Karousis, N.; Pispas, S.; Tagmatarchis, N. Photocatalytic Applications with CdS • block Copolymer/Exfoliated Graphene Nanoensembles: Hydrogen Generation and Degradation of Rhodamine B. *Nanotechnol.* **2014**, *25* (44), 445404.
63. Yan, Y.; Wang, C.; Yan, X.; Xiao, L.; He, J.; Gu, W.; Shi, W. Graphene Acting as Surface Phase Junction in Anatase–Graphene–Rutile Heterojunction Photocatalysts for H_2 Production From Water Splitting. *J. Phys. Chem. C* **2014**, *118* (41), 23519-23526.

64. Qin, G.; Wu, X.; Zhang, H. Rational design of TiO_2-V_2O5-C Nanostructure Grafted by N-Doped Graphene with Enhanced Photocatalysis and Lithium Ion Store Performances. *RSC Adv.* **2014**, *4* (94), 52438-52450.
65. Rakkesh, R. A.; Durgalakshmi, D.; Balakumar, S. Efficient Sunlight-Driven Photocatalytic Activity of Chemically Bonded GNS-TiO_2 and GNS-ZnO Heterostructures. *J. Mater. Chem. C* **2014**, *2* (33), 6827-6834.
66. Jong-Gun, L.; Do-Yeon, K.; Jung-Jae, P.; You-Hong, C.; Y., Y. J.; Sang, J. H.; Koun, M. B.; T., S. M.; Sungho, J.; S., A. D. S.; S., Y. S. Graphene–Titania Hybrid Photoanodes by Supersonic Kinetic Spraying for Solar Water Splitting. *J. A. Ceram. Soc.* **2014**, *97* (11), 3660-3668.
67. Dubey, P. K.; Tripathi, P.; Tiwari, R. S.; Sinha, A. S. K.; Srivastava, O. N. Synthesis of Reduced Graphene Oxide–TiO_2 Nanoparticle Composite Systems and its Application in Hydrogen Production. *Int. J. Hydrogen Energy* **2014**, *39* (29), 16282-16292.
68. Upadhyay, S.; Bagheri, S.; Abd Hamid, S. B. Enhanced Photoelectrochemical Response of Reduced-Graphene Oxide/$Zn_{1-x}Ag_xO$ Nanocomposite in Visible-Light Region. *Int. J. Hydrogen Energy* **2014**, *39* (21), 11027-11034.
69. Singh, G. P.; Shrestha, K. M.; Nepal, A.; Klabunde, K. J.; Sorensen, C. M. Graphene supported plasmonic photocatalyst for hydrogen evolution in photocatalytic water splitting. *Nanotechnol.* **2014**, *25* (26), 265701.
70. Lin, M.; Shenmin, Z.; Jun, M.; Dian, S.; Yixin, C.; Zhixin, C.; Chao, Y.; Yao, L.; Di, Z. Superior H_2 Production by Hydrophilic Ultrafine Ta_2O_5 Engineered Covalently on Graphene. *Nanotechnol.* **2014**, *25* (21), 215401.
71. Yang, Y.; Liu, E.; Dai, H.; Kang, L.; Wu, H.; Fan, J.; Hu, X.; Liu, H. Photocatalytic Activity of Ag–TiO_2-Graphene Ternary Nanocomposites and Application in Hydrogen Evolution by Water Splitting. *Int. J. Hydrogen Energy* **2014**, *39* (15), 7664-7671.
72. Zhu, B.; Lin, B.; Zhou, Y.; Sun, P.; Yao, Q.; Chen, Y.; Gao, B. Enhanced Photocatalytic H_2 Evolution on ZnS Loaded with Graphene and MoS_2 Nanosheets as Cocatalysts. *J. Mater. Chem. A* **2014**, *2* (11), 3819-3827.
73. Park, H. S.; Ha, H.-W.; Ruoff, R. S.; Bard, A. J. On the Improvement of Photoelectro chemical Performance and Finite Eement Analysis of Reduced Graphene Oxide–$BiVO_4$ Composite Electrodes. *J. Electroanal. Chem.* **2014**, *716*, 8-15.
74. Lavorato, C.; Primo, A.; Molinari, R.; García, H. Natural Alginate as a Graphene Precursor and Template in the Synthesis of Nanoparticulate Ceria/Graphene Water Oxidation Photocatalysts. *ACS Catal.* **2014**, *4* (2), 497-504.

75. Qin, L.; Huan, M.; Jiaguo, Y.; Wei, X.; Yingqiu, Z.; Juan, W. Enhanced Photocatalytic Hydrogen-Production Performance of Graphene–$Zn_xCd_{1-x}S$ Compo sites by Using an Organic S Source. *Chem. A Eur. J.* **2014**, *20* (4), 1176-1185.
76. Zhang, J.; Zhao, W.; Xu, Y.; Xu, H.; Zhang, B. In-situ Photo-Reducing Graphene Oxide to Create $Zn_{0.5C}d_{0.5}S$ Porous Nanosheets/RGO Composites as Highly Stable and Efficient Photoelectrocatalysts for Visible-Light-Driven Water Splitting. *Int. J. Hydrogen Energy* **2014**, *39* (2), 702-710.
77. Yuan, W.; Shen, P. K.; Jiang, S. P. Controllable Synthesis of Graphene Supported MnO_2 Nanowires via Self-Assembly for Enhanced Water Oxidation inBoth Akaline and Neutral Solutions. *J. Mater. Chem. A* **2014**, *2* (1), 123-129.
78. Yoon, K.-Y.; Lee, J.-S.; Kim, K.; Bak, C. H.; Kim, S.-I.; Kim, J.-B.; Jang, J.-H. Hematite-Based Photoelectrochemical Water Splitting Supported by Inverse Opal Structures of Graphene. *ACS Appl. Mater. Interfaces* **2014**, *6* (24), 22634-22639.
79. Zhang, X.; Zhang, B.; Huang, D.; Yuan, H.; Wang, M.; Shen, Y. TiO_2 Nanotubes Modified with Electrochemically Reduced Graphene Oxide for Photoelectrochemical Water Splitting. *Carbon* **2014**, *80*, 591-598.
80. Guo, W.; Wu, D. Facile synthesis of VS_4/Graphene Nanocomposites and Their Visible-Light-Driven Photocatalytic Water Splitting Activities. *Int. J. Hydrogen Energy* **2014**, *39* (30), 16832-16840.
81. Fa, J.; Hn, L.; Z, Z.; Nm, H.; A, P. Titanium Dioxide-Reduced Graphene Oxide Thin Film for Photoelectrochemical Water Splitting. *Ceram. Int.* **2014**, *40* (9, Part B), 15159-15165.
82. Hu, S.; Chi, B.; Pu, J.; Jian, L. Surface Charge Modification for Improvement of Photocatalytic H_2 Production over a $La_2Ti_2O_7$/Graphene Nanocomposite. *RSC Adv.* **2014**, *4* (105), 60437-60444.
83. Meyer, T.; Priebe, J. B.; da Silva, R. O.; Peppel, T.; Junge, H.; Beller, M.; Brückner, A.; Wohlrab, S. Advanced Charge Utilization From $NaTaO_3$ Photocatalysts by Multilayer Reduced Graphene Oxide. *Chem. Mater.* **2014**, *26* (16), 4705-4711.
84. Xiu, Z.; Wu, Y.; Hao, X.; Lu, Q.; Liu, S. Graphene oxide wrapped Ag_3PO_4 Sub-Microparticles with Highly Enhanced Photocatalytic Activity and Stability under Visible Light Irradiation. *Mater. Res. Bullet.* **2014**, *59*, 192-198.
85. Li, H.; Cui, X. A Hydrothermal Route for Constructing Reduced Graphene Oxide /TiO_2 Nanocomposites: Enhanced Photocatalytic Activity for Hydrogen Evolution. *Int. J. Hydrogen Energy* **2014**, *39* (35), 19877-19886.
86. Rai, S.; Ikram, A.; Sahai, S.; Dass, S.; Shrivastav, R.; Satsangi, V. R. Morphological, Optical and Photoelectrochemical Properties of Fe_2O_3-GNP Composite Thin Films. *RSC Adv.* **2014**, *4* (34), 17671-17679.

87. Cherevan, A. S.; Gebhardt, P.; Shearer, C. J.; Matsukawa, M.; Domen, K.; Eder, D. Interface Engineering in Nanocarbon-Ta_2O_5 Hybrid Photocatalysts. *Energy Environ. Sci.* **2014**, *7* (2), 791-796.

88. Li, B.; Zhao, Y.; Zhang, S.; Gao, W.; Wei, M. Visible-Light-Responsive Photo catalysts Toward Water Oxidation Based on NiTi-Layered Double Hydroxide /Reduced Graphene Oxide Composite Materials. *ACS Appl. Mater. Interfaces* **2013**, *5* (20), 10233-10239.

89. Wang, Y.; Guo, X.; Dong, L.; Jin, G.; Wang, Y.; Guo, X.-Y. Enhanced Photocatalytic Performance of Chemically Bonded SiC-Graphene Composites for Visible-Light-Driven Overall Water Splitting. *Int. J. Hydrogen Energy* **2013**, *38* (29), 12733-12738.

90. Liu, B.; Tian, L.; Wang, Y. One-Pot Solvothermal Synthesis of $ZnSe_{\cdot x}N_2H_4$/GS and ZnSe/N-GS and Enhanced Visible-Light Photocatalysis. *ACS Appl. Mater. Interfaces* **2013**, *5* (17), 8414-8422.

91. Yu, Y.; Ren, J.; Meng, M. Photocatalytic Hydrogen Evolution on Graphene Quantum Dots Anchored TiO_2 Nanotubes-Array. *Int. J. Hydrogen Energy* **2013**, *38* (28), 12266-12272.

92. Xian, G. C.; Yongqiang, D.; Bin, Y. H.; Ming, L. C. Graphene Quantum Dots as a Green Sensitizer to Functionalize ZnO Nanowire Arrays on F-Doped SnO_2 Glass for Enhanced Photoelectrochemical Water Splitting. *Adv. Energy Mater.* **2013**, *3* (8), 997-1003.

93. Wang, B.; Sun, Q.; Liu, S.; Li, Y. Synergetic catalysis of CuO and Graphene Additives on TiO_2 for Photocatalytic Water Splitting. *Int. J. Hydrogen Energy* **2013**, *38* (18), 7232-7240.

94. Dang, H.; Dong, X.; Dong, Y.; Huang, J. Facile and Green Synthesis of Titanate Nanotube/Graphene Nanocomposites for Photocatalytic H_2 Generation From Water. *Int. J. Hydrogen Energy* **2013**, *38* (22), 9178-9185.

95. Tang, X.; Tay, Q.; Chen, Z.; Chen, Y.; Goh, G. K. L.; Xue, J. CuInZnS-Decorated Graphene Nanosheets for Highly Efficient Visible-Light-Driven Photocatalytic Hydrogen Production. *J. Mater. Chem. A* **2013**, *1* (21), 6359-6365.

96. Zhang, K.; Shi, X.; Kim, J. K.; Lee, J. S.; Park, J. H. Inverse Opal Structured α-Fe_2O_3 on Graphene Thin Films: Enhanced Photo-Assisted Water Splitting. *Nanoscale* **2013**, *5* (5), 1939-1944.

97. Mou, Z.; Yin, S.; Zhu, M.; Du, Y.; Wang, X.; Yang, P.; Zheng, J.; Lu, C. RuO_2/ $TiSi_2$/Graphene Composite for Enhanced Photocatalytic Hydrogen Generation under Visible Light Irradiation. *Phys. Chem. Chem. Phys.* **2013**, *15* (8), 2793-2799.

98. Yang, J.; Zeng, X.; Chen, L.; Yuan, W. Photocatalytic Water Splitting to Hydrogen Production of Reduced Graphene Oxide/SiC under Visible Light. *Appl. Phys. Lett.* **2013**, *102* (8).

99. Hou, Y.; Zuo, F.; Dagg, A.; Feng, P. Visible Light-Driven α-Fe_2O_3 Nanorod/ Graphene/$BiV_{1-x}Mo_xO_4$ Core/Shell Heterojunction Array for Efficient Photoelectro chemical Water Splitting. *Nano Lett.* **2012**, *12* (12), 6464-6473.

100. Marcos, L. S.; Cristina, L.; Marta, P.; Vicente, F.; Raffaele, M.; Hermenegildo, G. Visible-Light Photocatalytic Hydrogen Generation by Using Dye-Sensitized Graphene Oxide as a Photocatalyst. *Chem. A Eur. J.* **2012**, *18* (52), 16774-16783.

101. Zhang, J.; Yu, J.; Jaroniec, M.; Gong, J. R. Noble Metal-Free Reduced Graphene Oxide-$Zn_xCd_{1-x}S$ Nanocomposite with Enhanced Solar Photocatalytic H_2-Production Performance. *Nano Lett.* **2012**, *12* (9), 4584-4589.

102. Kim, Y. K.; Park, H. How and to What Extent do Carbon Materials Catalyze Solar Hydrogen Production From Water? *Appl. Catal. B: Environ.* **2012**, *125*, 530-537.

103. Hou, J.; Wang, Z.; Kan, W.; Jiao, S.; Zhu, H.; Kumar, R. V. Efficient Visible-Light-Driven Photocatalytic Hydrogen Production Using CdS@TaON Core–Shell Composites Coupled with Graphene Oxide Nanosheets. *J. Mater. Chem.* **2012**, *22* (15) 7291-7299.

104. Gao, P.; Liu, J.; Lee, S.; Zhang, T.; Sun, D. D. High Quality Graphene Oxide–CdS–Pt Nanocomposites for Efficient Photocatalytic Hydrogen Evolution. *J. Mater. Chem.* **2012**, *22* (5), 2292-2298.

105. Zhang, X.; Sun, Y.; Cui, X.; Jiang, Z. A Green and Facile Synthesis of TiO_2/Graphene Nanocomposites and Their Photocatalytic Activity for Hydrogen Evolution. *Int. J. Hydrogen Energy* **2012**, *37* (1), 811-815.

106. Mohamed, M. M.; Ibrahim, I.; Salama, T. M. Rational Design of Manganese Ferrite-Graphene Hybrid Photocatalysts: Efficient Water Splitting and Effective Elimination of Organic Pollutants. *Appl. Catal. A: General* **2016**, *524*, 182-191.

107. Ojha, K.; Saha, S.; Kolev, H.; Kumar, B.; Ganguli, A. K. Composites of Graphene-Mo_2C Rods: Highly Active and Stable Electrocatalyst for Hydrogen Evolution Reaction. *Electrochim. Acta* **2016**, *193*, 268-274.

108. Song, Y.-T.; Lin, L.-Y.; Hong, J.-Y. Enhanced Visible-light Response and Conductivity of the TiO_2/Reduced Graphene Oxide/Sb_2S_3 Heterojunction for Photoelectrochemical Water Oxidation. *Electrochim. Acta* **2016**, *211*, 576-585.

109. Ren, X.; Ren, X.; Pang, L.; Zhang, Y.; Ma, Q.; Fan, H.; Liu, S. MoS_2/Sulfur and Nitrogen Co-doped Reduced Graphene Oxide Nanocomposite for Enhanced Electrocatalytic Hydrogen Evolution. *Int. J. Hydrogen Energy* **2016**, *41* (2), 916-923.

110. Xu, X.; Feng, B.; Zhou, G.; Bao, Z.; Hu, J. Efficient Photon Harvesting and Charge Collection in 3D Porous RGO-TiO_2 Photoanode for Solar Water Splitting. *Mater. Design* **2016**, *101*, 95-101.
111. Theerthagiri, J.; Sudha, R.; Premnath, K.; Arunachalam, P.; Madhavan, J.; Al-Mayouf, A. M. Growth of Iron Diselenide Nanorods on Graphene Oxide Nanosheets as Advanced Electrocatalyst for Hydrogen Evolution Reaction. *Int. J. Hydrogen Energy* **2017**, *42* (18), 13020-13030.
112. Ensafi, A. A.; Nabiyan, A.; Jafari-Asl, M.; Dinari, M.; Farrokhpour, H.; Rezaei, B. Galvanic Exchange at Layered Doubled Hydroxide/N-Doped Graphene as an in-Situ Method to Fabricate Powerful Electrocatalysts for Hydrogen Evolution Reaction. *Energy* **2016**, *116*, 1087-1096.
113. Acharya, S.; Padhi, D. K.; Parida, K. M. Visible Light Driven $LaFeO_3$ Nano Sphere/RGO Composite Photocatalysts for Efficient Water Decomposition Reaction. *Catal. Today* **2017**.
114. Samal, A.; Das, D. P. Transfiguring UV Light Active "Metal Oxides" to Visible Light Active Photocatayst by Reduced Graphene Oxide Hypostatization. *Catal.Today* **2018**, *300*, 124-135.
115. Luo, J.; Li, D.; Yang, Y.; Liu, H.; Chen, J.; Wang, H. Preparation of Au/Reduced Graphene Oxide/Hydrogenated TiO_2 Nanotube Arrays Ternary Composites for Visible-Light-Driven Photoelectrochemical Water Splitting. *J. Alloys Compd* **2016**, *661*, 380-388.
116. Chandrasekaran, S.; Chung, J. S.; Kim, E. J.; Hur, S. H. Exploring Complex Structural Evolution of Graphene Oxide/ZnO Triangles and its Impact on Photoelectrochemical Water Splitting. *Chem. Eng. J.* **2016**, *290*, 465-476.
117. Min, S.; Wang, F.; Lu, G. Graphene-Induced Spatial Charge Separation for Selective Water Splitting over TiO_2 Photocatalyst. *Catal. Commun.* **2016**, *80*, 28-32.
118. Chen, R.; Song, Y.; Wang, Z.; Gao, Y.; Sheng, Y.; Shu, Z.; Zhang, J.; Li, X. a. Porous Nickel Disulfide/Reduced Graphene Oxide Nanohybrids with Improved Electrocatalytic Performance for Hydrogen Evolution. *Catal. Commun.* **2016**, *85*, 26-29.
119. Li, J.; Zhang, X.; Song, L.; Zhang, M.; Zhang, B. Double Laminated Reduced Graphene/Cu_2S/Reduced Graphene/Graphene Oxide Nanofilms and Their Photoelectrochemical Properties. *J. Energy Chem.* **2016**, *25* (4), 654-658.
120. Konkena, B.; Masa, J.; Xia, W.; Muhler, M.; Schuhmann, W. MoSSe@Reduced Graphene Oxide Nanocomposite Heterostructures as Efficient and Stable Electro catalysts for the Hydrogen Evolution Reaction. *Nano Energy* **2016**, *29*, 46-53.

121. Zhang, Z.; Gao, C.; Li, Y.; Han, W.; Fu, W.; He, Y.; Xie, E. Enhanced Charge Separation and Transfer Through Fe_2O_3/ITO Nanowire Arrays Wrapped with Reduced Graphene Oxide for Water-Splitting. *Nano Energy* **2016**, *30*, 892-899.
122. Iwashina, K.; Iwase, A.; Nozawa, S.; Adachi, S.-i.; Kudo, A. Visible-Light-Responsive $CuLi_{1/3}Ti_{2/3}O_2$ Powders Prepared by a Molten CuCl Treatment of Li_2TiO_3 for Photocatalytic H_2 Evolution and Z-Schematic Water Splitting. *Chem. Mater.* **2016**, *28* (13), 4677-4685.
123. Zhang, X.; Liu, S.; Zang, Y.; Liu, R.; Liu, G.; Wang, G.; Zhang, Y.; Zhang, H.; Zhao, H. Co/Co_9S_8@S,N-Doped Porous Graphene Sheets Derived From S, N Dual Organic Ligands Assembled Co-MOFs as Superior Electrocatalysts for Full Water Splitting in Alkaline Media. *Nano Energy* **2016**, *30*, 93-102.
124. Li, Z.; Dai, X.; Du, K.; Ma, Y.; Liu, M.; Sun, H.; Ma, X.; Zhang, X. Reduced Graphene Oxide/O-MWCNT Hybrids Functionalized with p-Phenylenediamine as High-Performance MoS_2 Electrocatalyst Support for Hydrogen Evolution Reaction. *J. Phys. Chem. C* **2016**, *120* (3), 1478-1487.
125. Yoon, K.; Lee, J. H.; Kang, J.; Kang, J.; Moody, M. J.; Hersam, M. C.; Lauhon, L. J. Metal-Free Carbon-Based Nanomaterial Coatings Protect Silicon Photoanodes in Solar Water-Splitting. *Nano Lett.* **2016**, *16* (12), 7370-7375.
126. Li, L.; Yu, L.; Lin, Z.; Yang, G. Reduced TiO_2-Graphene Oxide Heterostructure As Broad Spectrum-Driven Efficient Water-Splitting Photocatalysts. *ACS Appl. Mater. Interfaces* **2016**, *8* (13), 8536-8545.
127. Morais, A.; Longo, C.; Araujo, J. R.; Barroso, M.; Durrant, J. R.; Nogueira, A. F. Nanocrystalline Anatase TiO_2/Reduced Graphene Oxide Composite Films As Photoanodes for Photoelectrochemical Water Splitting Studies: The Role of Reduced Graphene Oxide. *Phys. Chem. Chem. Phys.* **2016**, *18* (4), 2608-2616.
128. Das, S.; Misra, A.; Roy, S. Enhancement of Photochemical Heterogeneous Water Oxidation by a Manganese Based Soft Oxometalate Immobilized on a Graphene Oxide Matrix. *New J. Chem.* **2016**, *40* (2), 994-1003.
129. Govindhan, M.; Mao, B.; Chen, A. Novel Cobalt Quantum Dot/Graphene Nanocomposites as Highly Efficient Electrocatalysts for Water Splitting. *Nanoscale* **2016**, *8* (3), 1485-1492.
130. Jiao, L.; Zhou, Y.-X.; Jiang, H.-L. Metal-Organic Framework-Based CoP/Reduced Graphene Oxide: High-Performance Bifunctional Electrocatalyst for Overall Water Splitting. *Chem. Sci.* **2016**, *7* (3), 1690-1695.
131. He, C.; Tao, J. Two-Dimensional TaC Nanosheets on a Reduced Graphene Oxide Hybrid as an Efficient and Stable Electrocatalyst for Water Splitting. *Chem. Commun.* **2016**, *52* (57), 8810-8813.

132. Reddy, D. A.; Choi, J.; Lee, S.; Kim, Y.; Hong, S.; Kumar, D. P.; Kim, T. K. Hierarchical Dandelion-Flower-Like Cobalt-Phosphide Modified CdS/Reduced Graphene Oxide-MoS_2 Nanocomposites as a Noble-Metal-Free Catalyst for Efficient Hydrogen Evolution From Water. *Catal. Sci. Technol.* **2016**, *6* (16), 6197-6206.
133. Meng, H.; Fan, K.; Low, J.; Yu, J. Electrochemically Reduced Graphene Oxide on Silicon Nanowire Arrays for Enhanced Photoelectrochemical Hydrogen Evolution. *Dalton Trans.* **2016**, *45* (35), 13717-13725.
134. Ma, W.; Ma, R.; Wu, J.; Sun, P.; Liu, X.; Zhou, K.; Sasaki, T. Development of Efficient Electrocatalysts via Molecular Hybridization of NiMn Layered Double Hydroxide Nanosheets and Graphene. *Nanoscale* **2016**, *8* (19), 10425-10432.
135. Wang, X.; Zhang, J.; Zhang, K.; Zou, W.; Chen, S. Facile Fabrication of Reduced Graphene Oxide/CuI/PANI Nanocomposites with Enhanced Visible-Light Photo catalytic Activity. *RSC Adv.* **2016**, *6* (50), 44851-44858.
136. Zhao, J.; Yang, Y.; Dong, X.; Ma, Q.; Yu, W.; Wang, J.; Liu, G. Electrospinning Construction of Bi_2WO_6/RGO Composite Nanofibers with Significantly Enhanced Photocatalytic Water Splitting Activity. *RSC Adv.* **2016**, *6* (69), 64741-64748.
137. Song, L.; Zhao, M.; Li, X.; Zhang, Z.; Qu, L. Solution-Processed MoS_2 Nanotubes/ Reduced Graphene Oxide Nanocomposite as an Active Electrocatalyst Toward the Hydrogen Evolution Eeaction. *RSC Adv.* **2016**, *6* (75), 70740-70746.
138. Wang, J.; Yang, W.; Liu, J. CoP_2 Nanoparticles on Reduced Graphene Oxide Sheets as a Super-Efficient Bifunctional Electrocatalyst for Full Water Splitting. *J. Mater. Chem. A* **2016**, *4* (13), 4686-4690.
139. Chen, L.-C.; Yeh, T.-F.; Lee, Y.-L.; Teng, H. Incorporating Nitrogen-Doped Graphene Oxide Dots with Graphene Oxide Sheets for Stable and Effective Hydrogen Production Through Photocatalytic Water Decomposition. *Appl. Catal. A: General* **2016**, *521*, 118-124.
140. Jiayuan, L.; Ming, Y.; Xuemei, Z.; Zheng-Qing, H.; Zhaoming, X.; Chun-Ran, C.; Yuanyuan, M.; Yongquan, Q. Mechanistic Insights on Ternary $Ni_{2-x}Co_xP$ for Hydrogen Evolution and Their Hybrids with Graphene as Highly Efficient and Robust Catalysts for Overall Water Splitting. *Adv. Funct. Mater.* **2016**, *26* (37), 6785-6796.
141. Shaoxiong, L.; Lingxia, Z.; Pingping, Y.; Sancan, H.; Xiaosheng, F. Novel Composites of α-Fe_2O_3 Tetrakaidecahedron and Graphene Oxide as an Effective Photoelectrode with Enhanced Photocurrent Performances. *Adv. Funct. Mater.* **2016**, *26* (19), 3331-3339.
142. Zhenhua, P.; Takashi, H.; Qian, W.; Shanshan, C.; Akihide, I.; Mamiko, N.; Naoya, S.; Tsuyoshi, T.; Masao, K.; Tsutomu, M.; Akihiko, K.; Kazunari, D. Photoreduced

Graphene Oxide as a Conductive Binder to Improve the Water Splitting Activity of Photocatalyst Sheets. *Adv. Funct. Mater.* **2016**, *26* (38), 7011-7019.

143. Yu-Jia, T.; Yu, W.; Xiao-Li, W.; Shun-Li, L.; Wei, H.; Long-Zhang, D.; Chun-Hui, L.; Ya-Fei, L.; Ya-Qian, L. Molybdenum Disulfide/Nitrogen-Doped Reduced Graphene Oxide Nanocomposite with Enlarged Interlayer Spacing for Electro catalytic Hydrogen Evolution. *Adv. Energy Mater.* **2016**, *6* (12), 1600116.
144. Jintao, Z.; Liangti, Q.; Gaoquan, S.; Jiangyong, L.; Jianfeng, C.; Liming, D. N,P-Codoped Carbon Networks as Efficient Metal-Free Bifunctional Catalysts for Oxygen Reduction and Hydrogen Evolution Reactions. *Angew. Chem. Int. Ed.* **2016**, *55* (6), 2230-2234.
145. Jintao, Z.; Liming, D. Nitrogen, Phosphorus, and Fluorine Tri-Doped Graphene as a Multifunctional Catalyst for Self-Powered Electrochemical Water Splitting. *Angew. Chem. Int. Ed.* **2016**, *55* (42), 13296-13300.
146. Guoquan, Z.; Yanfang, L.; Yufei, Z.; Fenglin, Y. NiFe Layered-Double-Hydroxide-Derived NiO-$NiFe_2O_4$/Reduced Graphene Oxide Architectures for Enhanced Electrocatalysis of Alkaline Water Splitting. *ChemElectroChem* **2016**, *3* (11), 1927-1936.
147. Jia, X.; Gao, S.; Liu, T.; Li, D.; Tang, P.; Feng, Y. Controllable Synthesis and Bi-functional Electrocatalytic Performance towards Oxygen Electrode Reactions of Co_3O_4/N-RGO Composites. *Electrochim. Acta* **2017**, *226*, 104-112.
148. Kumar, D. P.; Hong, S.; Reddy, D. A.; Kim, T. K. Ultrathin MoS_2 Layers Anchored Exfoliated Reduced Graphene Oxide Nanosheet Hybrid as a Highly Efficient Cocatalyst for CdS Nanorods Towards Enhanced Photocatalytic Hydrogen Production. *Appl. Catal. B: Environ.* **2017**, *212*, 7-14.
149. Xie, J.; Chen, J.; Li, C. M. Self-Assembling Reduced Graphene Quantum Dots on Hematite Photoanode for Passivating Surface States Toward Significantly Improved Water Splitting. *Int. J. Hydrogen Energy* **2017**, *42* (10), 7158-7165.
150. Huang, Y.; Yan, C.-F.; Guo, C.-Q.; Lu, Z.-X.; Shi, Y.; Wang, Z.-D. Synthesis of GO-Modified Cu_2O Nanosphere and the Photocatalytic Mechanism of Water Splitting for Hydrogen Production. *Int. J. Hydrogen Energy* **2017**, *42* (7), 4007-4016.
151. Park, S.-Y.; Kim, M.-g.; Jung, J.; Heo, J.; Hong, E. M.; Choi, S. M.; Lee, J.-Y.; Cho, S.; Hong, K.; Lim, D. C. Stable Organic-Inorganic Hybrid Multilayered Photoelectrochemical Cells. *J. Power Sources* **2017**, *341*, 411-418.
152. Cui, C.; Li, S.; Qiu, Y.; Hu, H.; Li, X.; Li, C.; Gao, J.; Tang, W. Fast Assembly of Ag_3PO_4 Nanoparticles Within Three-Dimensional Graphene Aerogels for Efficient Photocatalytic Oxygen Evolution From Water Splitting under Visible Light. *Appl.Catal. B: Environ.* **2017**, *200*, 666-672.

153. Lin, M.; Shenmin, Z.; Jun, M.; Dian, S.; Yixin, C.; Zhixin, C.; Chao, Y.; Yao, L.; Di, Z. Superior H_2 Production by Hydrophilic Ultrafine Ta_2O_5 Engineered Covalently on Graphene. *Nanotechnol.* **2014**, *25* (21), 215401 (1-9).

154. Wang, P.; Zhan, S.; Xia, Y.; Ma, S.; Zhou, Q.; Li, Y. The Fundamental Role and Mechanism of Reduced Graphene Oxide in rGO/Pt-TiO_2 Nanocomposite for High-Performance Photocatalytic Water Splitting. *Appl. Catal. B: Environ.* **2017**, *207*, 335-346.

155. Khan, I.; Ibrahim, A. A. M.; Sohail, M.; Qurashi, A. SonochemicalAssisted Synthesis of RGO/ZnO Nanowire Arrays for Photoelectrochemical Water Splitting. *Ultrason. Sonochem.* **2017**, *37*, 669-675.

156. Hamid, S. B. A.; Teh, S. J.; Lai, C. W.; Perathoner, S.; Centi, G. Applied Bias Photon-to-Current Conversion Efficiency of ZnO Enhanced by Hybridization with Reduced Graphene Oxide. *J. Energy Chem.* **2017**, *26* (2), 302-308.

157. Boppella, R.; Kochuveedu, S. T.; Kim, H.; Jeong, M. J.; Marques Mota, F.; Park, J. H.; Kim, D. H. Plasmon-Sensitized Graphene/TiO_2 Inverse Opal Nanostructures with Enhanced Charge Collection Efficiency for Water Splitting. *ACS Appl. Mater. Interfaces* **2017**, *9* (8), 7075-7083.

158. Zhao, J.; Yang, Y.; Yu, W.; Ma, Q.; Dong, X.; Wang, X.; Wang, J.; Liu, G. Bi_2MoO_6/RGO Composite Nanofibers: Facile Electrospinning Fabrication, Structure, and Significantly Improved Photocatalytic Water Splitting Activity. *J. Mater. Sci.: Mater. Electron.* **2017**, *28* (1), 543-552.

159. Ghayeb, Y.; Momeni, M. M.; Menati, M. Reduced graphene oxide/Cu_2O Nanostructure Composite Films as an Effective and Stable Hydrogen Evolution Photocathode for Water Splitting. *J. Mater. Sci.: Mater. Electron.* **2017**, *28* (11), 7650-7659.

160. Naseri, N.; Solaymani, S.; Ghaderi, A.; Bramowicz, M.; Kulesza, S.; Ţălu, Ş.; Pourreza, M.; Ghasemi, S. Microstructure, Morphology and Electrochemical Proper ties of Co Nanoflake Water Oxidation Electrocatalyst at Micro- and Nanoscale. *RSC Adv*. **2017**, *7* (21), 12923-12930.

161. Liu, X. X.; Zang, J. B.; Chen, L.; Chen, L. B.; Chen, X.; Wu, P.; Zhou, S. Y.; Wang, Y. H. A microwave-Assisted Synthesis of CoO@Co Core-Shell Structures Coupled with N-doped Reduced Graphene Oxide Used as a Superior Multi-Functional Electrocatalyst for Hydrogen Evolution, Oxygen Reduction and Oxygen Evolution Reactions. *J. Mater. Chem. A* **2017**, *5* (12), 5865-5872.

162. Monirul, I. M.; Nayeem, F. S.; Taslima, A.; Kumar, R. A.; I., M. A.; Konstantin, K.; Xue, D. S. Liquid-Crystal-Mediated 3D Macrostructured Composite of Co/Co_3O_4

Embedded in Graphene: Free-Standing Electrode for Efficient Water Splitting. *Part. Part. Syst.Charact.* **2017**, *34* (9), 1600386 (1-6).

163. Ma, X. X.; Su, Y.; He, X. Q. Use of Cobalt Polyphthalocyanine and Graphene as Precursors to Construct an Efficient Co9S8/N,S-G Electrocatalyst for the Oxygen Electrode Reaction in Harsh Media. *ChemCatChem* **2016**, *9* (2), 308-315.
164. Young Kim, J.; Jang, J.-W.; Hyun Youn, D.; Yul Kim, J.; Sun Kim, E.; Sung Lee, J. Graphene-Carbon Nanotube Composite as an Effective Conducting Scaffold to Enhance the Photoelectrochemical Water Oxidation Activity of a Hematite Film. *RSC Adv.* **2012**, *2* (25), 9415-9422.
165. Xiang, Q.; Yu, J.; Jaroniec, M. Synergetic Effect of MoS_2 and Graphene as Cocatalysts for Enhanced Photocatalytic H_2 Production Activity of TiO_2 Nanoparticles. *J. Am. Chem. Soc.* **2012**, *134* (15), 6575-6578.